Developing the Theory of Critical Distances for practical integrity assessment of real-life structural components

Richard Louks

This thesis is submitted as partial fulfilment of the requirements for the degree of Doctor of Philosophy in

The Department of Civil and Structural Engineering

At the University of Sheffield

24th May 2016

Supervisors

Professor Luca Susmel

Professor Harm Askes

Executive Summary

This PhD thesis details the research conducted to answer three questions in the field of fracture and fatigue engineering. The opening chapters provide fracture and fatigue background theory as well as a more comprehensive review of the Theory of Critical Distances (TCD), a theory proven to be successful in the assessment of components containing stress concentration features.

Chapter 4 details an engineering approach based on the TCD for the static assessment of engineering components containing stress concentrators made of brittle, quasi-brittle and ductile materials; and loaded by any combination of static forces. To validate the method, 1744 experimental data was taken from technical literature is provided in Annex A. Each data was modelled using FE software, the extracted stress data was then post-processed using this reformulation of the TCD. The results obtained were compared to the commonly used Hot-Spot-Stress-Method, across the same set of data there was an order of magnitude improvement in accuracy, the TCD Point Method giving an average error less than 30% whilst the HSSM gave an average error greater than 300%.

Chapter 5 is concerned with the use of the linear-elastic TCD to assess notched metallic components in the high-cycle fatigue regime at elevated temperatures. Full details of two experimental programmes are provided, notched samples of a low carbon steel C45 and an aluminium alloy A319-T7 was tested, the results are provided in Annex C. Additional experimental data was taken from technical literature to further validate the method. The results showed that the approach was highly accurate with errors falling within $\pm20\%$.

The 6th Chapter gives account of a study into the combined use of the TCD and the Modified Wöhler Curve Method (MWCM to accurately and efficiently assess metal engineering components

containing complex 3D stress raisers experiencing complex load histories that resulted in fatigue failures in the medium- and high-cycle fatigue regime. The method is based on critical plane theory which assumes that fatigue cracks initiate on the material plane experiencing the maximum shear stress amplitude. The method was proven to be successful independent of the stress raiser geometry and the complexity of the load history, typically returning errors of $\pm 20\%$.

Chapters 4-6 each have their individual conclusions and suggestions for further work, chapter 7 gives a summary of the conclusions and chapter 8 provides some suggestions for further work.

Publications

4 journal publications have been produced from the work contained in this thesis.

On the multiaxial fatigue assessment of complex three-dimensional stress concentrators

Louks R, Gerin B, Draper J, Askes H, Susmel L

International Journal of Fatigue, Vol 63, P12-24, 2014

Static assessment of brittle/ductile notched materials: An engineering approach based on the Theory of Critical Distances

Louks R, Askes H, Susmel L

Frattura ed Integrita Strutturale, Vol 30, P23-30, 2014

The linear-elastic Theory of Critical Distances to estimate high-cycle fatigue strength of notched metallic materials at elevated temperatures

Louks R, Susmel L

Fatigue & Fracture of Engineering Materials & Structures, Vol 38, P629-640, 2015

A generalised approach to rapid finite element design of notched materials against static loading using the Theory of Critical Distances

Louks R, Askes H, Susmel L

Materials & Design, Vol 108, P769-779, 2016

Acknowledgements

Contents

List of Figures

List of Tables

1. Introduction

This thesis provides details of research carried out to support a PhD, the research aims to formalise a novel unifying numerical method based on the Theory of Critical Distances (TCD) to design notched components subjected to different types of in-service systems of forces/moments. The TCD postulates that the damage extent can be estimated by directly post-processing the entire linear-elastic stress field acting on the material in the vicinity of the crack initiation locations. The key feature of this theory is that the assessment is based on a scale length parameter which is assumed to be a material property.

During this PhD project three different situations were planned to be investigated as follows:

(i) Notched brittle and ductile materials subjected to both uniaxial and multiaxial static loading.

(ii) Notched metallic materials subjected to fatigue loading at high-temperature.

(iii) Three-dimensional stress concentrators subjected to multiaxial fatigue loading.

The aforementioned investigations have been planned to answer the three industrial questions posed by the industrial partner Safetechnology Ltd who have funded this project jointly with the University of Sheffield through the EPSRC. The outcomes of these investigations are planned to be incorporated into engineering software by Dassualt Systemes, Abaqus®.

Initially, a systematic bibliographical investigation was performed in order to select a large number of experimental results generated by testing notched/cracked specimens under both static and high-

cycle fatigue loading. With regard to the static tests, samples made of both ductile and brittle material will be considered, whereas for the fatigue case solely results obtained by testing metallic specimens have been collected. Finally, independently of the type of addressed problem (i.e., either static or fatigue situations), failures generated under both Mode I, Mode II, Mode III as well as Mixed Mode I/II and I/III loading will be investigated.

Due to a lack of suitable data available in the technical literature and industrial reasoning, a number of experimental results were generated under axial loading by testing, at 150 °C and 250 °C, notched specimens of cast alloy A319-T7 and carbon steel C45, respectively. The experimental results are then used to accurately determine the respective material length parameter suitable for correctly applying the TCD governing equations. Finally, by solving conventional linear-elastic FE models, the accuracy of the TCD in estimating the static and high-cycle fatigue strength of the selected experimental results will be investigated systematically to formalise a novel unifying design procedure.

2. A review of failure theory:

The engineering field employed to understand and prevent the unexpected failure of engineering components is commonly referred to as structural integrity engineering. Engineering from a general perspective makes use of knowledge to design and manufacture new improved structures and machines through innovative use of knowledge. Throughout history engineering knowledge and research has been systematically recorded, in more recent decades the introduction of the Internet has facilitated the efficient sharing of knowledge and research helping to prevent the repetition of researching known knowledge. Structures and machines are constructed from engineering components assembled to form a structure or machine capable of performing the designed functions. Over the last century the developments in engineering knowledge has made it possible for design engineers to create more complex and efficient structures and machines. Despite significant improvements in knowledge, component failures still occur, either due to unexpected overloading or by inadequate design, this results in social and/or economic loses.

An investigation into the state of the art reveals that the so called Theory of Critical Distances (TCD) is a theory that is capable of accurate prediction of failure independent of loading conditions and geometry of the component being assessed. The TCD will be discussed at length in Chapter 3. Before discussing the details of the TCD, some of the basic fracture and fatigue theory will be reviewed.

2.1. Static Failure Theory

2.1.1. Stress and Stress-Strain diagrams

Consider first an elementary portion of material, as a result of some applied forces and appropriate boundary conditions, such as that depicted in *Figure 1* but assume that the forces are constant over the time domain and therefore creating a monotonic load, the stress state at 0 can be described through a Cauchy stress tensor:

$$[\sigma] = \begin{bmatrix} \sigma_x & \tau_{xy} & \tau_{xz} \\ \tau_{xy} & \sigma_y & \tau_{yz} \\ \tau_{xz} & \tau_{yz} & \sigma_z \end{bmatrix} \tag{1}$$

where σ_x, σ_y and σ_z are the normal and τ_{xy}, τ_{xz} and τ_{yz} are the shear stress components. The stress state within a body of material that is complex in its geometry will have a change in stress state from one point to the next, importantly if we consider a point within the body the numerical values of the normal and shear stress components vary as the orientation of the frame of reference changes.
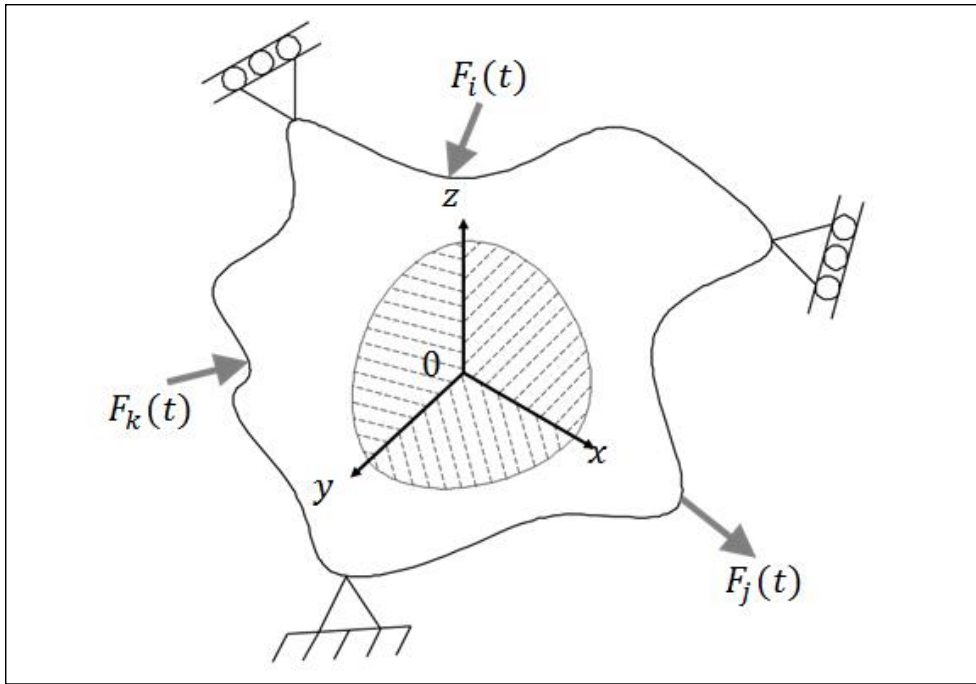
Figure 1: Generic body of material with a time dependent set of forces

Consider a sample of material that has a uniform cross-section and is loaded in simple tension, most engineering materials will produce, when plotted on a stress-strain diagram such as that depicted in *Figure 2,* a region of linear-elastic behaviour. At any point in the linear-elastic region if the load is removed the material will return to its original form, if the loaded sample fails within this linear-elastic region then the resulting fracture is considered to be brittle, importantly after breakage occurs the two parts can be placed back together and it will still resemble the original geometry. If however, the stress-strain response starts to deviate from this linear region due to increasing load, then the material is said to display plasticity, assuming the load is reduced then the stress-strain response will return along a similar gradient to the elastic region but will display some permanent deformations. The stress-strain results are typically recorded in two ways; in terms of engineering stress-strain or by true stress-strain, throughout this thesis stress-strain curves will refer to Engineering stress-strain i.e. only considering the original geometry.

When engineering materials are tested monotonically the failure can be characterised by either brittle or ductile characteristics which can be seen in the stress-strain curves of *Figure 2*, stress-strain curves are normally generated by the gradual application of an axial extension, i.e. under displacement control, applied to a plain sample of the investigated material. The stress-strain characteristic differences between brittle and ductile materials monotonic load to failures are schematically represented in *Figure 2*.
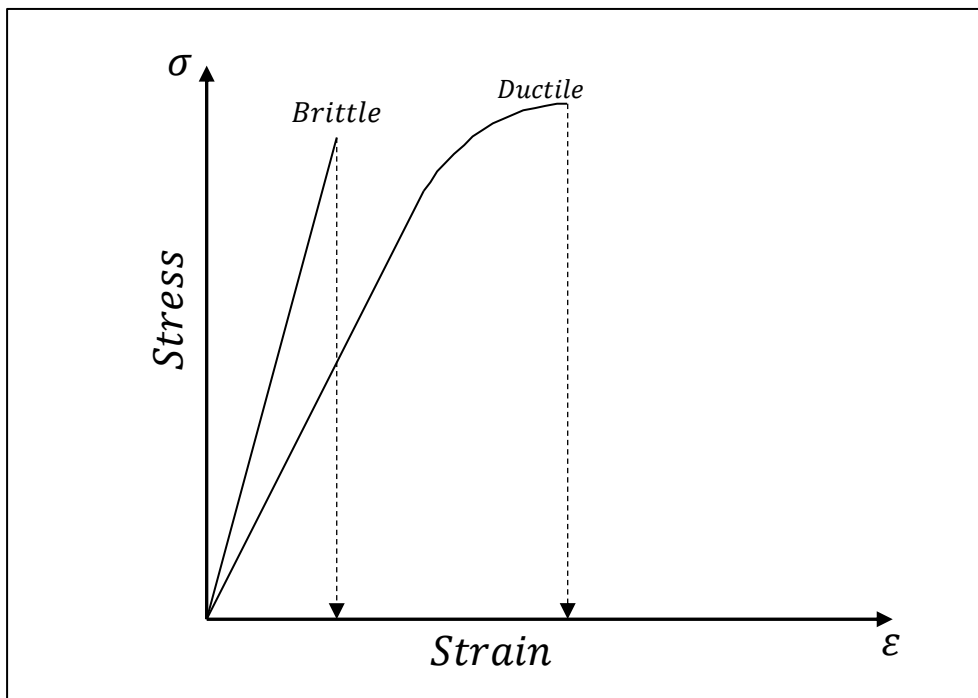
Figure 2: Engineering Stress-Strain curves

The majority of structural and mechanical engineering materials follow a predictable region of elastic Stress-Strain, if the load is removed the sample will return to its original geometry, at a material dependent level, yielding occurs, beyond this point plasticity starts to permanently deform ductile materials. If the material fractures in the elastic region the two parts will fit back together almost perfectly creating the original material geometry. When a material exhibits plasticity prior to failure, permanent deformations will have occurred and on joining the two parts the original geometry has thinned or necked around the vicinity of final fracture. The stress-strain curve of a material will be

influenced by the temperature at which the test is performed, for example, materials that show ductility prior to failure at room temperature will have at a lower temperature a ductile-brittle transition, at which point the micro-mechanisms of failure can change, at the other end of the temperature range, some materials that exhibit brittle failure at room temperature, when tested at elevated temperature will generally exhibit more plasticity.

Having defined stress and strain quantities such as yield or ultimate stresses that are material properties, a design engineer can use this information to design real components by calculating an equivalent stress quantity resulting from complex systems of forces and moments applied to a component. In the following sub-sections different equivalent stress quantities are discussed. Before moving on to some definitions of equivalent stress quantities, the Maximum Principal Stress and Von Mises stress could also expressed in terms of strains, however, this thesis is only concerned with stress based analysis. Although it is unnecessary to validate the use of stress over strain one can side with stress based analysis as it transcends between solids and fluids.

2.1.2. Principal Stresses and Maximum Principal Stress Theory

The Maximum Principal Stress (MPS) theory is considered to be suitable for determining the static fracture of components made of brittle materials. Brittle materials by their nature are likely to fail by means of fast fracture when any point within the component experiences a principal stress equal to the materials ultimate tensile strength, brittle materials typically fail by an opening micro-mechanism.

Consider first the Maximum principal stress of a simple 2D system, which can be expressed as:

$$\sigma_{max} = \frac{(\sigma_{11} + \sigma_{22})}{2} + \sqrt{\left\{ \left[\frac{(\sigma_{11} - \sigma_{22})}{2} \right]^2 + \sigma_{12}^2 \right\}} \qquad (2)$$

The principal stresses and principal directions relate to a particular frame of reference whose axes are called principal axes, on the material planes perpendicular to each of these axes the shear stress components are invariably equal to zero.

To extend the maximum principal stress theory to a 3D state of stress, the 3D principal stress tensor is as follows:

$$[\sigma_P] = \begin{bmatrix} \sigma_1 & 0 & 0 \\ 0 & \sigma_2 & 0 \\ 0 & 0 & \sigma_3 \end{bmatrix} \qquad (3)$$

Here σ_1, σ_2 and σ_3 are the principal stresses which are conventionally ordered so that $\sigma_1 \geq \sigma_2 \geq \sigma_3$. The stress components σ_1, σ_2 and σ_3 can be determined as follows. Assume that the unit vector $\boldsymbol{n}(n_x, n_y, n_z)$ defines the orientation of a known principal direction. The principal stress, σ_n, parallel to vector $\boldsymbol{n}$ can be calculated by imposing the determinant of the first matrix on the left hand side of the following equation is equal to zero which implies a homogeneous system:

$$\begin{bmatrix} (\sigma_x - \sigma_n) & \tau_{xy} & \tau_{xz} \\ \tau_{xy} & (\sigma_y - \sigma_n) & \tau_{yz} \\ \tau_{xz} & \tau_{yz} & (\sigma_z - \sigma_n) \end{bmatrix} \begin{pmatrix} n_x \\ n_y \\ n_z \end{pmatrix} = \begin{pmatrix} 0 \\ 0 \\ 0 \end{pmatrix} \qquad (4)$$

So that:

$$\sigma_n^3 - I_1\sigma_n^2 - I_2\sigma_n - I_3 = 0 \qquad (5)$$

8

In the equation above the first, second and third stress invariants are defined as:

$$I_1 = \sigma_x + \sigma_y + \sigma_z$$

$$I_2 = \tau_{xy}^2 + \tau_{xz}^2 + \tau_{yz}^2 - \left(\sigma_x \sigma_y + \sigma_x \sigma_z + \sigma_y \sigma_z\right) \tag{6}$$

$$I_3 = \sigma_x \sigma_y \sigma_z + 2\tau_{xy}\tau_{xz}\tau_{yz} - \sigma_x \tau_{xy}^2 - \sigma_y \tau_{xz}^2 - \sigma_z \tau_{yz}^2 = det[\sigma]$$

By solving the stress invariant equations the three solutions are the three principal stresses and are the eigenvalues of matrix $[\sigma]$ with the corresponding eigenvectors giving the orientation of the three principal directions or axes.

2.1.3. Von Mises Stress Theory

This subsection briefly reports on a theory which is suitable for assessing ductile materials that fail with the presence of plastic deformation which occurs beyond the yield strength of the material but before reaching the materials ultimate tensile strength.

Von Mises stress theory also commonly referred to as Distortion Energy Theory was developed by Richard von Mises, the essence of this theory is that a structural material will perform its desired function provided the calculated distortion energy is lower than the distortion energy needed to cause yielding in a tensile test specimen of the same material. Materials that have a crystalline structure such as face centered cubic (FCC) will fail by a shearing micro-mechanism. The Von Mises criterion can be expressed in terms of stress or strains as a result of assuming that the material is

isotropic, as previously mentioned this thesis only considers the stress form. The conventional application of the Von Mises criterion assumes that failure by yielding will occur when the energy of distortion reaches the energy required to yield the same material in a uniaxial tension test.

The use of Von Mises stress in this thesis is as a fracture criterion and therefore we assume that failure will occur when $\sigma_{VMS} = \sigma_{UTS}$. Where σ_{VMS} is calculated in the plane strain conditions as;

$$\frac{1}{2}\sqrt{[(\sigma_1 - \sigma_2)^2 + (\sigma_2 - \sigma_3)^2 + (\sigma_3 - \sigma_1)^2]} = \sigma_{VMS} \qquad (7)$$

In situations where the third principal stress is equal to zero, then plane stress conditions exist and the above condition reduces to:

$$\sqrt{\sigma_1{}^2 - \sigma_1\sigma_2 + \sigma_2{}^2} = \sigma_{VMS} \qquad (8)$$

The use of Von Mises stress in this thesis is as a fracture criterion and therefore we assume that failure will occur when $\sigma_{VMS} = \sigma_{UTS}$.

2.1.4. Plain Materials

When designing simple components against static loads the designer needs to consider if the material is brittle or ductile and therefore ensure that either the Maximum Principal Stress or the von Mises stress with respect to the nominal cross section is lower than the corresponding failure strength. However the majority of engineering components require notches or keyways to fit them in place, in a more broad sense, components can have a stress raising feature as part of the

geometrical design or as part of the manufacturing process such as casting inclusions, additionally components can become cracked, these situations are discussed in the next sections.

2.1.5. Notched components

Mechanical and Structural engineering components will invariably contain a variety of geometrical features which cause a stress concentration phenomena. It is important for engineers to account for the detrimental effects of stress concentrations, uniformly loaded components with abrupt changes in cross-section can fail even when the average stress is lower than the materials ultimate tensile strength, a method used to account for stress raisers is the stress concentration factor. Consider the U-notched plate in *Figure 3* (a) which is subjected to a tensile force, the stress raising feature has a local effect on the Principal Stress profile ahead of the stress raising feature apex *Figure 3* (b) which decreases as the distance from the notch apex increases.

The application of a force to a component with a stress raising feature results in three states of stress, see *Figure 3* (a, b), the gross stress which ignores the presence of a stress raiser such as a crack, the net stress which is calculated from the minimum cross sectional area but without accounting for geometrical effects, and thirdly, the local linear-elastic stress field that does take account of the geometry. The elastic peak stress can be calculated from analytical solutions or by means of FE analysis, the value of the peak stress ahead of a stress raiser is influenced mostly by the sharpness and depth of the geometrical feature.
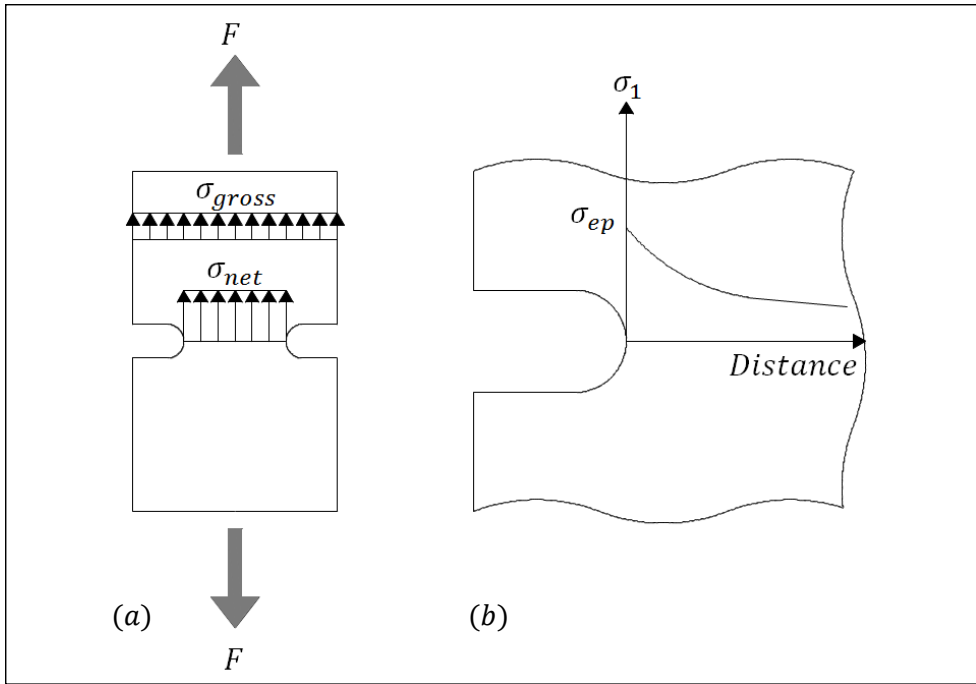
Figure 3: Gross and net stress (a), Elastic peak stress (b)

The geometrical features' effect on the linear-elastic stress field distribution can be summarised through the stress concentration factor, K_t, as proposed by Peterson [1].

$$K_t = \frac{\sigma_{max}}{\sigma_{net}}$$

(9)

where $\sigma_{max} = \sigma_{ep}$ and is the linear-elastic peak stress caused *Figure 3* by tension or bending. Similarly, in situations of torsion the stress concentration factor can be expressed as:

$$K_{ts} = \frac{\tau_{max}}{\tau_{net}}$$

(10)

The stress concentration factor can be calculated with respect to either the nominal-net or the nominal- gross section *Figure 3*.

The gradient of the local linear-elastic stress ahead of a stress raising feature is seen to have a significant effect on the strength of the component. The peak value of the linear-elastic stress can be high but if the gradient is so great that by a certain distance away from the notch tip the linear-elastic stress is significantly lower, then the stress raising feature could be considered to be non-damaging. The problems related to singular linear-elastic stress fields are discussed in the next section.

2.1.6. The problem of singular stress fields, LEFM

The previous section explains how notches or more broadly speaking geometrical features with a finite radius apex can affect the stress field through the stress concentration factor, K_t. In situations where the stress raising feature apex root radius tends towards zero we have a crack or crack like feature where in this scenario the stress field according to linear elastic laws produces a singular stress field. In what follows is a brief review of fracture mechanics and stress intensity factors, for more detailed explanations there exist various handbooks such as [2][3].

The field of fracture mechanics explains the cracking behaviour of bodies of material containing pre-existing cracks, assuming that the cracked material obeys linear –elastic constitutive laws then we are in the specific field of Linear-Elastic Fracture Mechanics (LEFM). In this section LEFM is described for the situation where brittle static fracture occurs, however it should be briefly mentioned that LEFM also has applications in fatigue loading scenarios which are discussed in section 2.2.7.

In structural and mechanical engineering the forces or loads acting on a cracked component are split into three different Modes, as shown in *Figure 4*, Mode I is the opening mode resulting from a

tensile load, Mode II is the in-plane shear mode and Mode III is the out-of-plane / anti-plane shear or tearing mode.
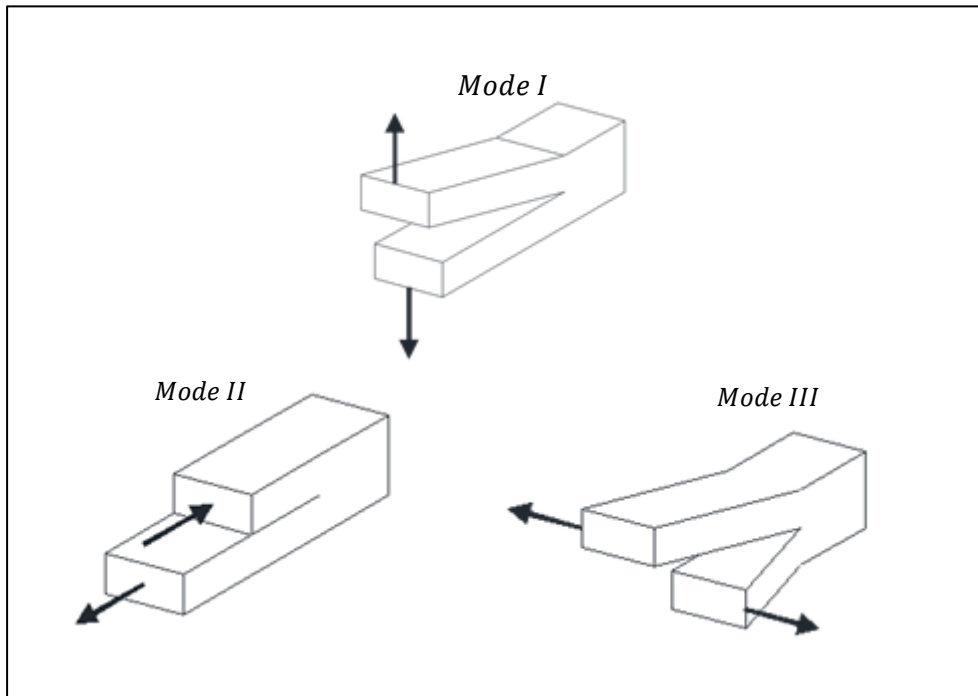
Figure 4: Loading Modes

The stress intensity factor story starts with Griffiths work on glass [4], during his research he discovered the paradoxical conclusion that at a crack tip the stress according to the theory of elasticity would tend towards infinity and therefore any cracked component couldn't withstand any load. Later Irwin modified Griffiths theory to deal with such a phenomenon [5], consider the component shown in *Figure 5* a through thickness central crack in a finite width plate with a crack of length $2a$, however, for now, consider the plate to be infinite, then the area of material close to crack tip can be described by the first order stress equations in terms of direct and shear stress:

$$\sigma_x = \sigma\sqrt{\frac{a}{2r}}\cos\frac{\theta}{2}\left(1 - \sin\frac{\theta}{2}\sin\frac{3\theta}{2}\right) + Higher\ order\ terms$$

$$\sigma_y = \sigma\sqrt{\frac{a}{2r}}\cos\frac{\theta}{2}\left(1 + \sin\frac{\theta}{2}\sin\frac{3\theta}{2}\right) + Higher\ order\ terms \qquad (11)$$

$$\tau_{xy} = \sigma\sqrt{\frac{a}{2r}}\sin\frac{\theta}{2}\cos\frac{\theta}{2}\cos\frac{3\theta}{2} + Higher\ order\ terms$$

The higher order terms in the expansion series do not contain the $1/r^{0.5}$ term which causes the singularity at the crack tip, $r \to 0, \sigma \to \infty$. In a Williams-type expansion the second term or first higher order term of the crack tip stress equation is the T-stress which affects the shape and extent of the crack tip plasticity. Ahead of the crack tip where $\theta = 0$ is the plane where the fracture processes take place, equations (11) above reduce to:

$$\sigma_{ij} = \sigma\sqrt{\frac{a}{r}} \qquad (12)$$

Irwin defined the numerator as the stress intensity factor, K, from which he could relate it to the strain energy argument, Irwin showed that at some critical value i.e. when $K_I = K_{Ic}$ fracture would occur. The plane strain fracture toughness, K_{Ic}, is a material property that should be appropriately determined by following a standard such as ASTM E399. Common tests involve testing samples such as the compact tension or bend specimens with a pre-crack of a specific length. Once the materials plane strain fracture toughness is known, a cracked component can then be assessed and declared safe providing $K_I < K_{Ic}$.

Returning to the plate of finite width, Irwins stress intensity factor, K, can be described as:

$$K = Y\sigma\sqrt{\pi a} \qquad\qquad (13)$$

Where Y is a shape factor which is used when the length of the crack is no longer small in comparison to the size of the plate and will take a value greater than unity. Traditionally the shape factor is denoted $F\left(\frac{a}{b}\right)$ for a central crack of length $2a$ in a finite width plate equal to $2b$, various analytical solutions exist for determining the appropriate shape factor with respect to the loading mode [6].
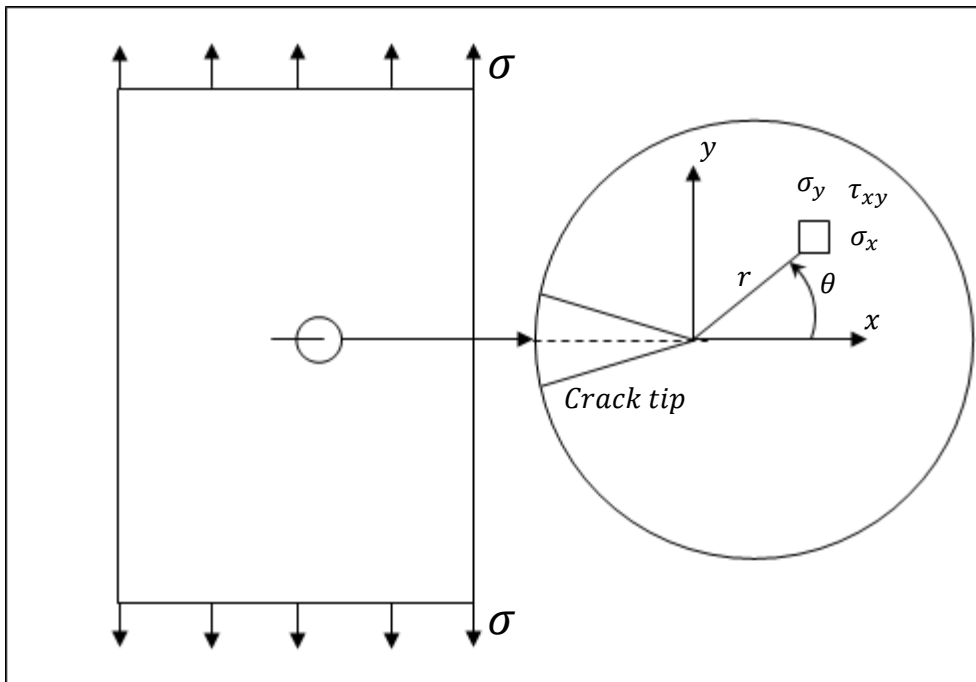
Figure 5: A through thickness central crack loaded in tension and crack tip stress notation

The more common notation of Irwins equations to describe the stress conditions in *Figure 5* and by assuming that it is a plane stress scenario i.e. $\sigma_z = 0$ are[7]:

$$\sigma_x = \frac{K_I}{\sqrt{2\pi r}} \cos\frac{\theta}{2}\left(1 - \sin\frac{\theta}{2}\sin\frac{3\theta}{2}\right) + Higher\ order\ terms$$

$$\sigma_y = \frac{K_I}{\sqrt{2\pi r}} \cos\frac{\theta}{2}\left(1 + \sin\frac{\theta}{2}\sin\frac{3\theta}{2}\right) + Higher\ order\ terms \qquad (14)$$

$$\tau_{xy} = \frac{K_I}{\sqrt{2\pi r}} \sin\frac{\theta}{2}\cos\frac{\theta}{2}\cos\frac{3\theta}{2} + Higher\ order\ terms$$

When the plate is in plane strain conditions the use of Poissons' ratio, v, gives:

$$\sigma_z = \frac{2vK_I}{\sqrt{2\pi r}} \cos\frac{\theta}{2} \qquad (15)$$

The transition from plane stress to plane strain occurs as specimen thickness increases this is seen to have an effect on the fracture toughness, K_{IC}, the condition for plane strain conditions is given as:

$$Thickness \geq 2.5\frac{K_{IC}}{\sigma} \qquad (16)$$

This chapter has so far considered the Mode I loading condition but as mentioned at the end of the last sub-section there are three loading modes, Mode II and Mode II loading have their own corresponding stress intensity factors, K_{II} and K_{III} which can be defined according to the frame of reference in *Figure 6* as:

Mode II

$$\sigma_x = \frac{K_{II}}{\sqrt{2\pi r}} \sin\frac{\theta}{2}\left(2 + \cos\frac{\theta}{2}\cos\frac{3\theta}{2}\right) + Higher\ order\ terms$$

$$\sigma_y = \frac{K_{II}}{\sqrt{2\pi r}} \sin\frac{\theta}{2}\cos\frac{\theta}{2}\cos\frac{3\theta}{2} + Higher\ order\ terms \qquad (17)$$

$$\tau_{xy} = \frac{K_{II}}{\sqrt{2\pi r}} \cos\frac{\theta}{2}\left(1 - \sin\frac{\theta}{2}\sin\frac{3\theta}{2}\right) + Higher\ order\ terms$$

Mode III

$$\tau_{xz} = -\frac{K_{III}}{\sqrt{2\pi r}} \sin\frac{\theta}{2} + Higher\ order\ terms$$

$$\tau_{yz} = \frac{K_{III}}{\sqrt{2\pi r}} \cos\frac{\theta}{2} + Higher\ order\ terms \qquad (18)$$

$$\sigma_x = \sigma_y = \sigma_z = \tau_{xy} = 0$$

Having shown Irwins equations for the stress intensity factors for each load mode i.e. K_I, K_{II} and K_{III}, convenient relations which are consistent with the governing equations which describe the linear-elastic stress in the vicinity of the crack tip and the subsequent definition of the three, K , values are as follows:

$$\begin{Bmatrix} K_I \\ K_{II} \\ K_{III} \end{Bmatrix} = \lim_{r \to 0} \sqrt{2\pi} \begin{Bmatrix} \sigma_y \\ \tau_{xy} \\ \tau_{yz} \end{Bmatrix} \qquad (19)$$
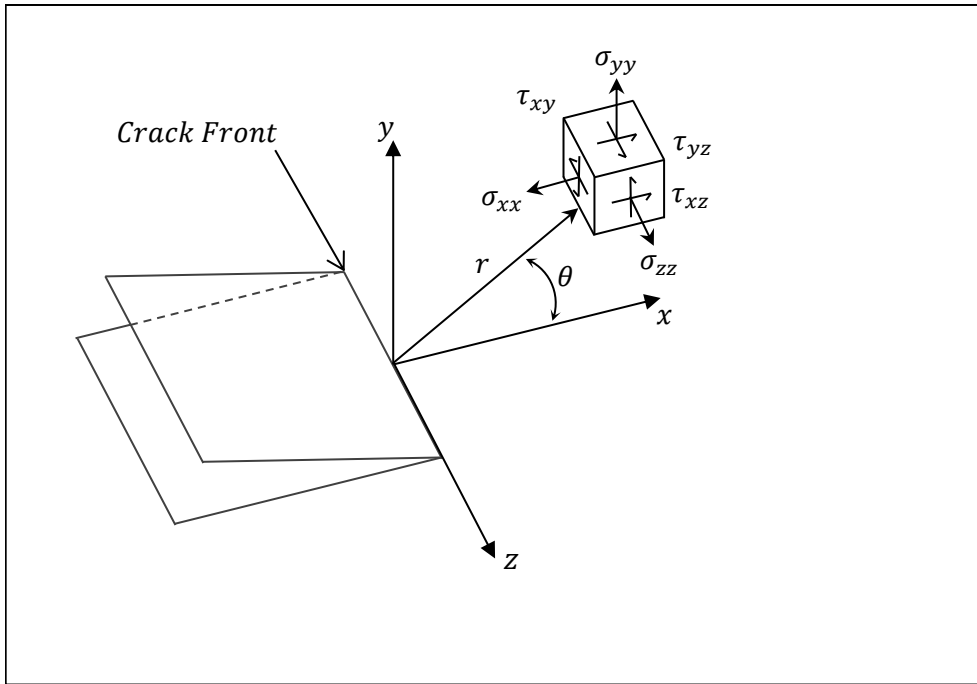
Figure 6: 3D stress components in the crack tip stress field

2.2. Metal Fatigue Theory and Assessment

During the industrial revolution, it was observed that metallic components could become *tired* or *fatigued*. Metal lifting chains, rail axels and other such mechanical components experiencing cyclic loading would fail at load's much lower than the materials static tensile strength. The cyclic loading-un-loading was seen to have a severe detrimental effect on these components, after a period of time the metallic components develop micro-cracks that are seen to grow a very small amount with each cycle. Once the crack has grown to a critical length, the component is then seen to fail, often with catastrophic consequences. Since these early observations, a tremendous amount of effort has been given from the science and engineering community to develop sound engineering methods so that fatigue failures do not occur.

Fatigue is a complex engineering problem which has to be properly addressed during the design of structural and mechanical components so to avoid fatigue failures. The fatigue behaviour of materials in their plain form is seen to be influenced by various factors, such as, the materials production and treatments, characteristic defects such as inclusions, surface finishes i.e. machined, ground or polished, external environment including temperature or chemical. To further complicate the situation, real components will almost always contain geometrical features, such as notches or key ways, these changes in cross section act as stress concentrators which promote crack initiation leading to component failure.

2.2.1. Crack initiation and growth in metallic materials

Fatigue damage in metallic materials is highly complex and is affected by many conditions, firstly a crack must initiate or form , under certain conditions it is possible for cracks to initiate and then stop, whereas once the crack starts to propagate if the cyclic load signal is unchanged it will propagate until complete fracture occurs. In this context, metallic materials are commonly understood to be made up of grains which are joined together through mutual grain boundaries. Each grain is made of closely packed atoms that display some order, amongst the order however exist atomic defects in the packing, and these defects promote what is commonly understood as slip planes or slip bands. If a cyclic load is applied to a single grain or crystal a persistent slip band or easy glide plane will form, it is along this plane that crack initiation occurs. Crack initiation will commonly form in a crystal whose easy glide plane orientation is at 45° to the applied load i.e. the direction experiencing the maximum shear stress. Typically, stage 1 crack will grow through a few grain boundaries at 45° before changing direction and propagating perpendicular to the applied load, once the change of direction occurs, stage 2 crack growth will then propagate through the material at a certain rate depending on the applied force until the crack reaches a certain length and conditions for fast fracture to occur.

2.2.2. Uniaxial cyclic loading definitions

Consider the generic body of material that has a system of forces that change with time, see *Figure 1*, the point 0 is the origin of a convenient reference system, $0xyz$, at such a point the stress state can be characterised by the following stress tensor:

$$[\sigma(t)] = \begin{bmatrix} \sigma_x(t) & \tau_{xy}(t) & \tau_{xz}(t) \\ \tau_{xy}(t) & \sigma_y(t) & \tau_{yz}(t) \\ \tau_{xz}(t) & \tau_{yz}(t) & \sigma_z(t) \end{bmatrix} \tag{20}$$

Assume that the stress component, $\sigma_x(t)$, is the only non-zero stress quantity i.e. the component has a uniaxial load applied, and that it varies cyclically, the definition of a fatigue cycle is a sequence of changing stress state which on completion of each cycle returns to the initial one *Figure 7*. The minimum and maximum values of stress component in each cycle take on the following values;

$$\sigma_{x,min} = \sigma_{x,m} - \sigma_{x,a} \tag{21}$$

$$\sigma_{x,max} = \sigma_{x,m} + \sigma_{x,a} \tag{22}$$

Where $\sigma_{x,m}$ and $\sigma_{x,a}$ are the mean value and the amplitude of the applied stress cycle.
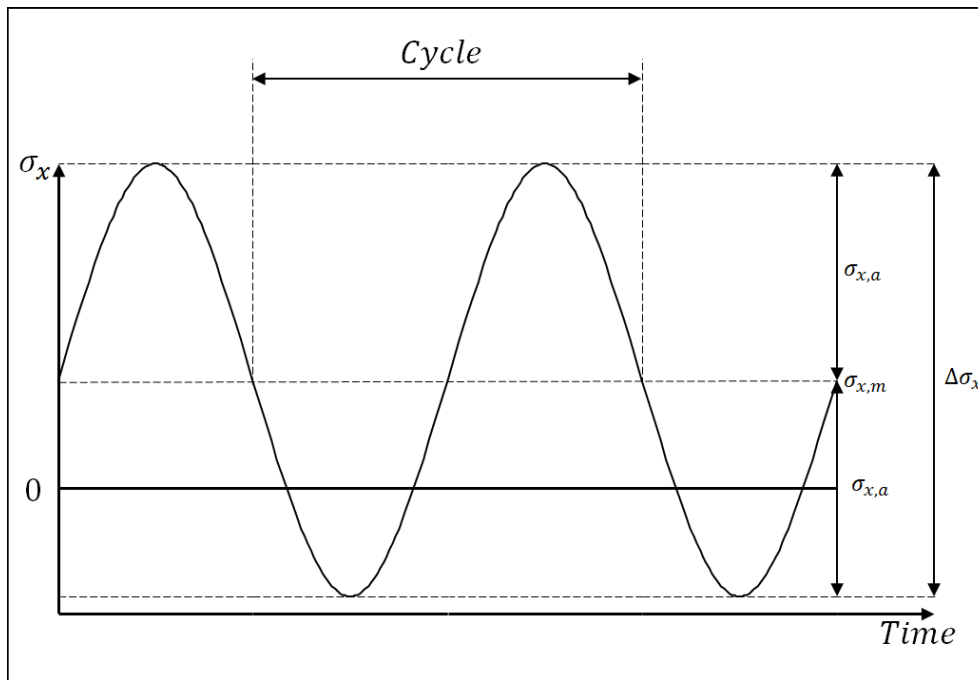
Figure 7: Schematic of a constant amplitude fatigue load cycle

Having defined the maximum and minimum stress, the load ratio, R, of the considered fatigue cycle is defined as;

$$R = \frac{\sigma_{x,min}}{\sigma_{x,max}} \qquad (23)$$

Two common load ratios are, $R = -1$, which can occur due to rotating bending i.e. axels, shafts, etc. and $R = 0$, which occurs in lifting gear i.e. load-unload. In the scenario where $R > -1$, we have a positive mean stress, this can have a detrimental effect on components where the material is sensitive to such conditions.

2.2.3. Wöhler curves

Early fatigue investigations used test data obtained by testing real components. In the 1830s, Wilhelm Albert [8] built the first fatigue test machine and published the results by testing real components instead of samples of the same material. In the 1860s, August Wöhler [9] published his results of fatigue testing on railway axles, tests which were carried out *in situ* when rail carriages were in service. His investigations revealed that stress amplitudes were the most detrimental parameter to fatigue life and that a tensile mean stress also has a detrimental influence. Wöhler was the first to take note of the phenomenon of crack propagation, noticing that hairline cracks, in particular those that are radial on the train axels, after years in service would grow, eventually resulting in the breakage of the axles themselves. A few years later Ludwig Spangenberg [10] plotted Wöhler's fatigue data in graphical form but he used a linear scale for the abscissa and ordinate. Subsequently Basquin showed the fatigue results on a log-log graph which is the fundamental layout of a Wöhler diagram as used up till recent advances which better improve the accuracy [11].

Taking a closer look at the traditional method of assessing the fatigue strength of engineering materials, in the Wöhler diagrams of *Figure 8*, also commonly referred to as S-N diagrams, the amplitude of the applied stress, $\sigma_{x,a}$, is plotted against the number of cycles to failure, N_f. In the diagrams of *Figure 8* the curves are determined under the hypothesis of a log-normal distribution of experimental results obtained by testing under fully reversed loading, the statistical determination of fatigue curves is discussed in section 2.2.8.   The fatigue curve of *Figure 8* (a) describes the typical fatigue behaviour of ferrous metal materials such as low carbon steels, such as that of En3B [12], up to a certain stress amplitude, σ_0 , below this threshold value the specimen will theoretically last forever, this threshold is referred to as the *Fatigue Limit*. Contrary to the fatigue limit, the fatigue curves of *Figure 8* (b and c) describes the typical fatigue behaviour of non-ferrous metal materials such as aluminium alloys, these materials do not display, when tested, a conventional fatigue limit, to design components made of such materials they must be designed for finite life. This requires the determination of a so called *Endurance Limit*, σ_A, the value of the endurance limit stress amplitude is extrapolated in the high cycle fatigue regime, taken as a number of cycles to failure, N_A , in the interval $10^6 \leftrightarrow 10^8$. In some non-ferrous materials the fatigue curve that describes the medium-cycle regime will be steeper than the curve obtained by plotting the failure results which occur in the high-cycle fatigue regime *Figure 8* (c) [13].
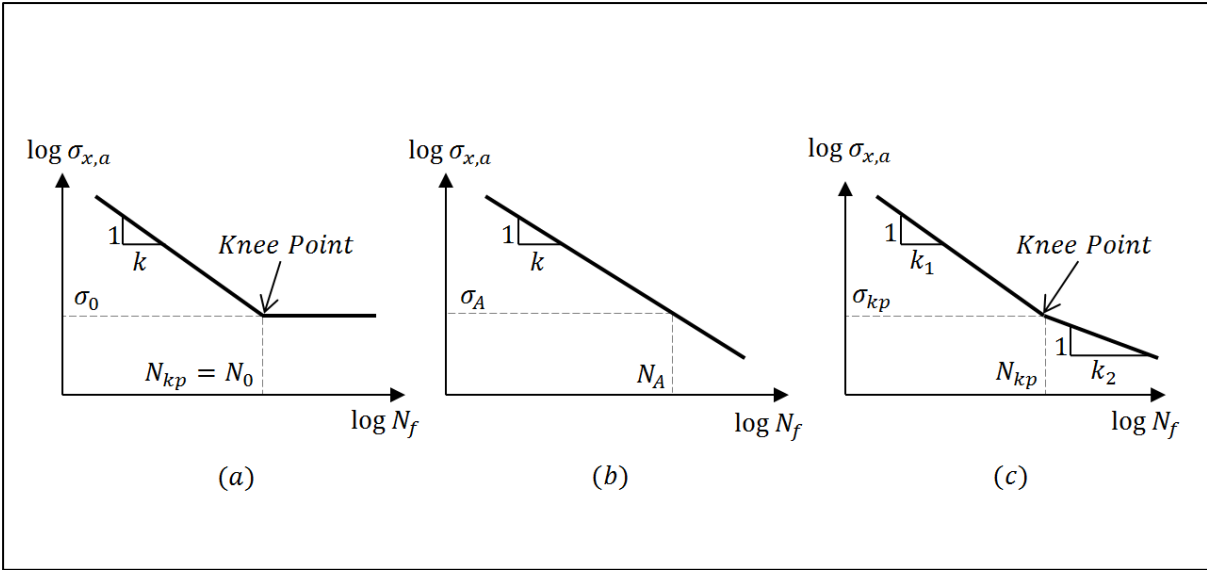
Figure 8: Traditional Wöhler S-N curves for ferrous and non-ferrous materials, defining the Fatigue Limit and the Endurance Limit

Wöhler curves are characterised by the negative inverse slope, k, and the reference stress amplitude, σ_A, extrapolated at a given number of cycles to failure, N_A. From *Figure 8* the $\sigma_{x,a}$ vs. N_f relationship can be described mathematically as;

$$\sigma_{x,a}^k \cdot N_f = \sigma_0^k \cdot N_0 = \sigma_A^k \cdot N_A = Constant \tag{24}$$

If the tested material exhibits characteristics similar to that shown schematically in *Figure 8* (c), the Wöhler curves are described as follows:

$$\sigma_{x,a}^{k_1} \cdot N_f = \sigma_{kp}^{k_1} \cdot N_{kp} \qquad for \ N_f \leq N_{kp}$$

$$\tag{25}$$

$$\sigma_{x,a}^{k_2} \cdot N_f = \sigma_{kp}^{k_2} \cdot N_{kp} \qquad for \ N_f \geq N_{kp}$$

An important aspect of using fatigue curves characterised by a knee point is the position of said knee point. To accurately determine the position of the knee point can be costly in term of time and money, however, recommendations of appropriate values for the position of the knee point have been determined by Sonsino [13].

To conclude this sub-section, it has been stated that the finite life region of Wöhler curves are established by plotting failure data, which raises the question, *When has the sample failed?* It is commonly understood and reported in text books such as [14] that fatigue life can be split into three phases: initiation, propagation and final fracture. One may use the relative length of the crack to define the failure criteria, like Socie and Co-workers in the 1980's [15][16]. Alternatively final failure can be based on stiffness reduction criterion i.e. as the crack gets bigger the stiffness reduces, this criterion has been presented by [17] and [12]. In both these adopted failure criterion there are potential drawbacks highlighting the importance of defining the failure criteria since no universal accepted criterion exists.

2.2.4. Non-zero mean stress effects in fatigue

A load history characterised by non-zero mean stresses can have a significant effect on the position of the Wöhler curve, under uniaxial fatigue loading the fatigue damage is seen to increase as the superimposed static stress, $\sigma_{x,m}$ increases, as shown in *Figure 9* (a). *Figure 9* (b) shows the similar effects obtained by changing the load ratio, R. As well as moving the Wöhler curve up and down, by changing the load ratio or mean stress is seen to influence the position of the knee point.
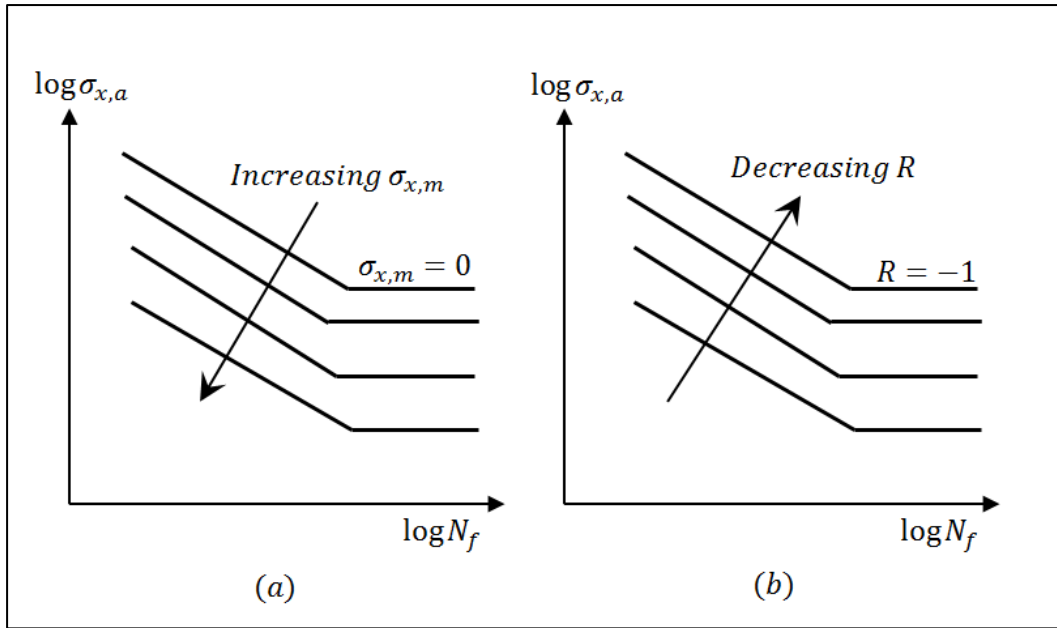
Figure 9: Effects of non-zero mean stresses on the Wöhler curves

There have been many attempts to propose sound engineering methodologies to accurately account for the effects of mean stresses in fatigue. The majority of the proposed criteria can be summarised by using the Marin's general equation [18]:

$$\left(\frac{\sigma_0}{\sigma_{0,R=-1}}\right)^n + \left(f\frac{\sigma_{x,m}}{\sigma_{UTS}}\right)^m = 1 \tag{26}$$

where $\sigma_{0,R=-1}$ denotes the fatigue limit obtained under fully reversed loading, σ_{UTS} is the ultimate tensile strength, σ_0 is the stress amplitude at the fatigue limit considering the presence of a positive mean stress, $\sigma_{x,m}$. The parameters f, n and m are constants which take a value of 1 or 2 depending on the considered model, the adopted criteria can be derived as follows [19]:

Soderberg's relationship uses $n = 1, m = 1$ and $f = \sigma_{UTS}/\sigma_Y$ where σ_Y is the yield stress:

$$\frac{\sigma_0}{\sigma_{0,R=-1}} + \frac{\sigma_{x,m}}{\sigma_Y} = 1 \;\rightarrow\; \sigma_0 = \sigma_{0,R=-1}\left(1 - \frac{\sigma_{x,m}}{\sigma_Y}\right) \tag{27}$$

Goodman's relationship uses $n = 1, m = 1$ and $f = 1$:

$$\frac{\sigma_0}{\sigma_{0,R=-1}} + \frac{\sigma_{x,m}}{\sigma_{UTS}} = 1 \;\rightarrow\; \sigma_0 = \sigma_{0,R=-1}\left(1 - \frac{\sigma_{x,m}}{\sigma_{UTS}}\right) \tag{28}$$

Gerber's parabola uses $n = 1, m = 2$ and $f = 1$:

$$\frac{\sigma_0}{\sigma_{0,R=-1}} + \left(\frac{\sigma_{x,m}}{\sigma_{UTS}}\right)^2 = 1 \;\rightarrow\; \sigma_0 = \sigma_{0,R=-1}\left(1 - \left(\frac{\sigma_{x,m}}{\sigma_{UTS}}\right)^2\right) \tag{29}$$

Dietman's parabola uses $n = 2, m = 1$ and $f = 1$:

$$\left(\frac{\sigma_0}{\sigma_{0,R=-1}}\right)^2 + \frac{\sigma_{x,m}}{\sigma_{UTS}} = 1 \;\rightarrow\; \sigma_0 = \sigma_{0,R=-1}\sqrt{1 - \frac{\sigma_{x,m}}{\sigma_{UTS}}} \tag{30}$$

The so called elliptical relationship uses $n = 2, m = 2$ and $f = 1$:

$$\left(\frac{\sigma_0}{\sigma_{0,R=-1}}\right)^2 + \left(\frac{\sigma_{x,m}}{\sigma_{UTS}}\right)^2 = 1 \;\rightarrow\; \sigma_0 = \sigma_{0,R=-1}\sqrt{1 - \left(\frac{\sigma_{x,m}}{\sigma_{UTS}}\right)^2} \tag{31}$$

These criteria can be plotted in a unique non-dimensional chart, where the abscissa plots the ratio of $\sigma_{x,m}$ to σ_{UTS} and the ordinate plots the ratio of σ_0 to $\sigma_{0,R=-1}$, as shown in *Figure 10*. In reality experimental data obtained by testing plane samples with superimposed static mean stresses will generally fall within the two extremes of the Soderberg and the Ellipse relationships which was shown in [19] by plotting data taken from [20]. When designing components made of materials

whose sensitivity to non-zero mean cyclic stresses, the use of Goodman's criterion will provide an adequate margin of safety. Additionally Susmel [19] showed that these classical expressions designed to assess the mean stress effect in uniaxial fatigue scenarios can be re-interpreted in terms of the critical plane approach with limited success, this will be discussed further in section 2.2.9.
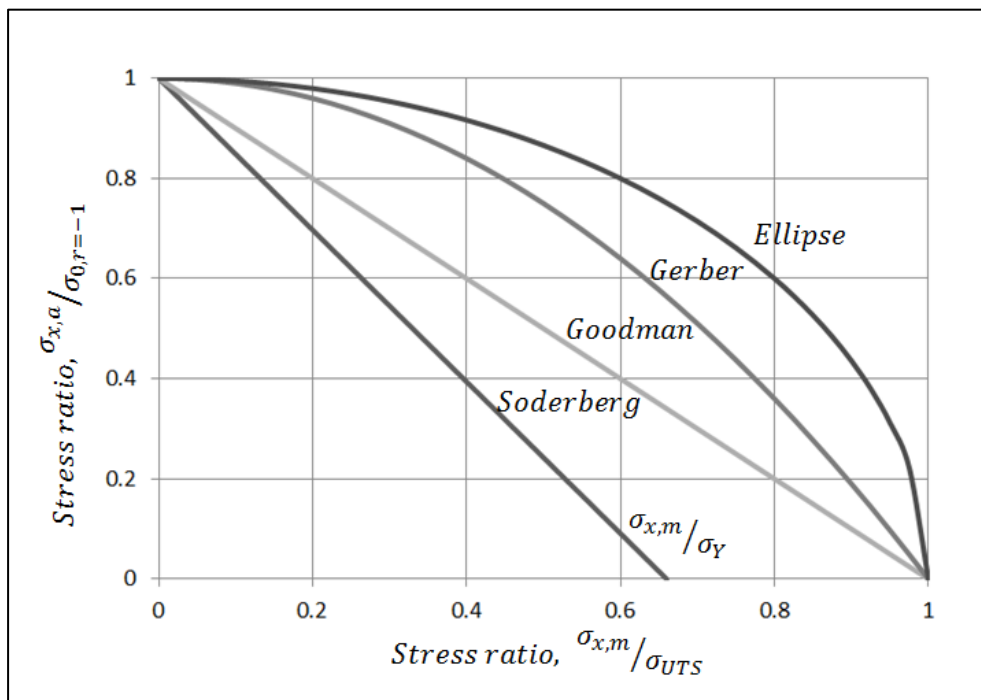
Figure 10: Mean stress effect on uniaxial fatigue strength

2.2.5. Elevated temperature effects in fatigue

The fatigue properties of metallic components experiencing in-service elevated temperatures can be difficult to predict due to the intrinsic complexities associated with such increases in energy into the fatigue process. Engineers that design components need to properly account for the effects, elevated in service temperatures have on the components fatigue performance. A few examples of particular industries where temperature can play a significant role are in the transportation industry, for example engine components such as jet engine blades. In the energy sector, for example

pressure vessels and turbines in nuclear and conventional power plants. And in manufacturing for example metal working (hot rolling of metals).

Around the middle of the last century, the scientific community was engaged with understanding metallic materials behaviour at elevated temperature. Based on the ideas of Bauschinger [11], Manson [21] and Coffin [22][23] pioneered work in the field of Low-Cycle Fatigue (LCF), since these early works [24]–[27] and the references therein, show that tremendous efforts have been made to understand and model the mechanical behaviour as well as being able to accurately predict the lifetime of components subject to time variable load histories at elevated temperatures.

A state of the art publication [28] suggested that such an intractable problem has generally been addressed in terms of strain, the fatigue crack initiation at elevated temperatures being mostly attributed to the plastic part of the total cyclic deformation. Due to the fact that real components often contain complex geometrical features there have been numerous experimental and theoretical investigations, these investigations being designed to quantify the effect of stress-strain concentrators on the overall fatigue behaviour of metallic materials experiencing elevated in-service temperatures, see for instance [29]–[35] and the references reported therein. Single-crystal superalloy components play significant roles in the energy and aerospace sectors and because of the important role played by single-crystal metallic materials, the effect of stress/strain concentrators have been studied in depth, see for instance [36],[37] and the references reported therein.

Nisitani [38] extended his linear notch mechanics approach for assessing the high-cycle fatigue performance of notched components at room temperature to situations involving elevated temperatures. His work on Inconel 718 demonstrated that the use of simpler linear assessment

methods were capable of producing accurate predictions of samples containing stress raising features and failing in the high-cycle fatigue regime whilst experiencing elevated temperatures.

This section has given a brief review of what is a very complex engineering problem and provides in part, the motivation to conduct the experimental investigation detailed in chapter 5 which proposes a simplified approach to this complex problem.

2.2.6. Notch fatigue

The detrimental effects of stress raising features in real components on the fatigue performance have been extensively investigated over the last century, the results of such research confirm that structural/mechanical engineers engaged in designing components must take into account of such features in order to provide safe reliable design. This section provides a brief review of two fundamental methods that have direct links to the theory used in this thesis, namely, Neubers average stress method and Petersons point stress method.

Section 2.1.5 introduced stress concentrations from a static point of view. This concept will now be applied to fatigue scenarios. Consider then a body of homogenous and isotropic linear-elastic material, firstly if the material is made into a plain component i.e. without a stress raising feature, as already discussed the tested plain samples will produce a Wöhler curve which can be referred to as the plain fatigue curve *Figure 11 (1),* the second curve of *Figure 11* is generated by testing under the same loading conditions samples made of the same material but containing a stress raising feature and calculated with respect to the nominal net section, finally the third curve is scaled from the second simply by the same ration of the net to gross nominal sections.

According to Peterson [39] the problem addressed in terms of nominal net stresses, the detrimental effect of a notch in the considered material can be quantified through the fatigue strength reduction factor, K_f .

$$K_f = \frac{\sigma_0}{\sigma_{0n}}$$ (32)

where σ_{0n} is the fatigue limit for a notched component, see Figure 11.

To use the fatigue strength reduction factor, it should be always determined by running appropriate experiments and maintaining the same test conditions, as it is seen to be sensitive to the load ratio.
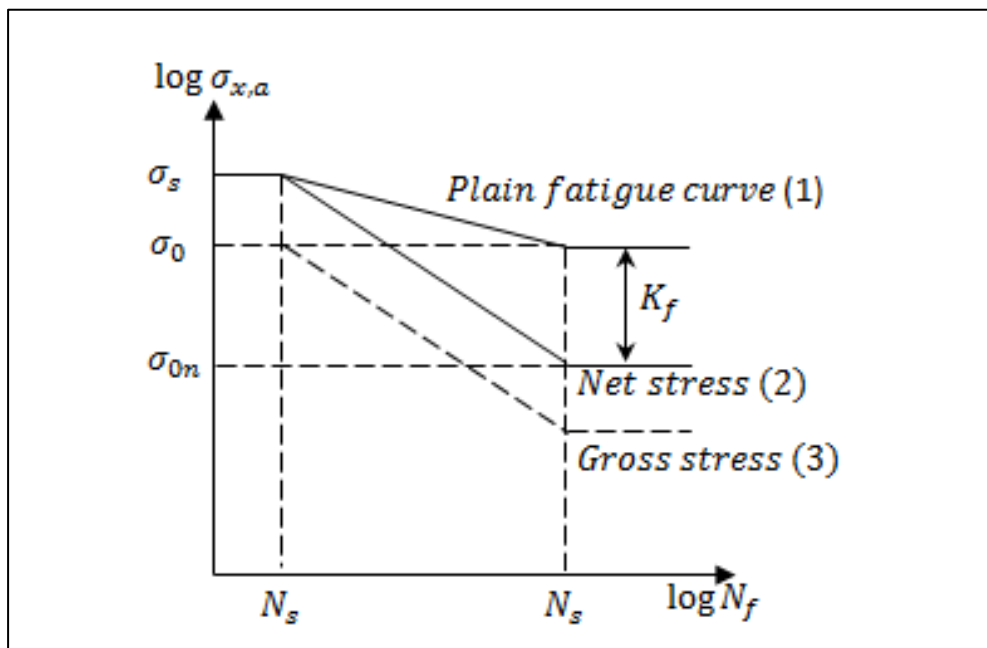
Figure 11: Plain and notch curves defining the fatigue strength reduction factor,

The first of the two methods devised for predicting the fatigue strength reduction factor is that presented by Neuber [40], in particular Neuber suggested that K_f could be predicted using the following formula:

$$K_f = 1 + \frac{K_t - 1}{1 + \sqrt{\frac{a_N}{\rho}}}$$

(33)

where a_N is a critical distance calculated using the materials ultimate tensile strength, K_t is the stress concentration factor and ρ is the notch root radius. In more detail, Neuber believed that the stress at the stress raising feature apex could not reach those predicted by continuum mechanics and suggested instead that the stress field ahead of a stress raising feature should be averaged over a line coincidental with the notch bisector, the length of line being related to the critical distance which is assumed to be a material parameter.

Using a similar strategy to Neuber, Peterson also assumed that the notch root radius was the most important geometrical factor and suggested that K_f could be predicted using the following formula [39]:

$$K_f = 1 + \frac{K_t - 1}{1 + \frac{a_p}{\rho}}$$

(34)

Where a_P is a critical distance which after a systematic experimental investigation was assumed to be a material parameter. Where Neuber averaged the linear-elastic stress over a line, Peterson suggested taking the reference stress at a point along the notch bisector, these methods are later

referred to as the Line Method and Point Method and discussed in great detail in Chapter 3 and shown in *Figure 22* and *Figure 25*.

In situations where the notch root radius tends towards zero the continuum mechanics approaches tend to give increasingly inaccurate results. In situations involving very sharp notches that are somewhat crack like the use of fracture mechanics prevail, as will be discussed in the next section.

2.2.7. Linear Elastic Fracture Mechanics and Fatigue

Section 2.1.6 introduced the concept of Linear-Elastic Fracture Mechanics (LEFM). This section will provide a review of the basic concepts of the application of LEFM in fatigue. It is evident from the previous section that when the root radius of a notch approaches zero, continuum approaches can no longer be used as the linear-elastic peak stress tends towards infinity, resulting in stress concentration factors also equal to infinity.

Shown in *Figure 5,* is a component loaded in tension, if the load is cyclic, then according to Irwin the stress field damaging the material close to the crack tip is a function of the Mode I stress intensity factor range, ΔK_I, defining the stress components as:

$$\Delta\sigma_x = \frac{\Delta K_I}{\sqrt{2\pi r}} \cos\frac{\theta}{2}\left(1 - \sin\frac{\theta}{2}\sin\frac{3\theta}{2}\right) + Higher\ order\ terms$$

$$\Delta\sigma_y = \frac{\Delta K_I}{\sqrt{2\pi r}} \cos\frac{\theta}{2}\left(1 + \sin\frac{\theta}{2}\sin\frac{3\theta}{2}\right) + Higher\ order\ terms \tag{35}$$

$$\Delta\tau_{xy} = \frac{\Delta K_I}{\sqrt{2\pi r}} \sin\frac{\theta}{2}\cos\frac{\theta}{2}\cos\frac{3\theta}{2} + Higher\ order\ terms$$

Where ΔK_I can be calculated as follows:

$$\Delta K_I = F \cdot \Delta\sigma_{gross} \cdot \sqrt{\pi a} \tag{36}$$

where $\Delta\sigma_{gross}$ is the range of stress applied to the gross section and a is the half crack length. These equations make it evident that ΔK_I is a very useful stress quantity that can be used to estimate fatigue damage in cracked components experiencing cyclic loading by describing the stress state ahead of the crack tip in the direction of crack growth. To show how ΔK_I can be used to address crack growth problems, consider a finite plate containing a crack of length, $2a$, is loaded cyclically by a tensile force, assuming that the initial semi-crack length, a, is long enough and the range of the applied force is great enough to induce crack propagation. Then we can refer to the starting semi-crack length as, a_i, as shown in *Figure 12 (a).* In this condition the crack will propagate by an amount each cycle and the new semi-crack length can be plotted against the number of cycles producing a curve. If we consider two force ranges on two like samples with $a_{i,a} = a_{i,b}$ but $\Delta\sigma_a > \Delta\sigma_b$, the onset of static fracture will occur not only in fewer cycles but also at a shorter semi-crack length i.e. $a_{f,a} < a_{f,b}$ and $n_a < n_b$. At any semi-crack length, the crack growth rate can be determined i.e. da/dn. For a given material and load rate it is then possible to plot the crack growth rate against the calculated ΔK_I onto a log-log graph, as shown in *Figure 12 (b),* which is the well-known Paris diagram.
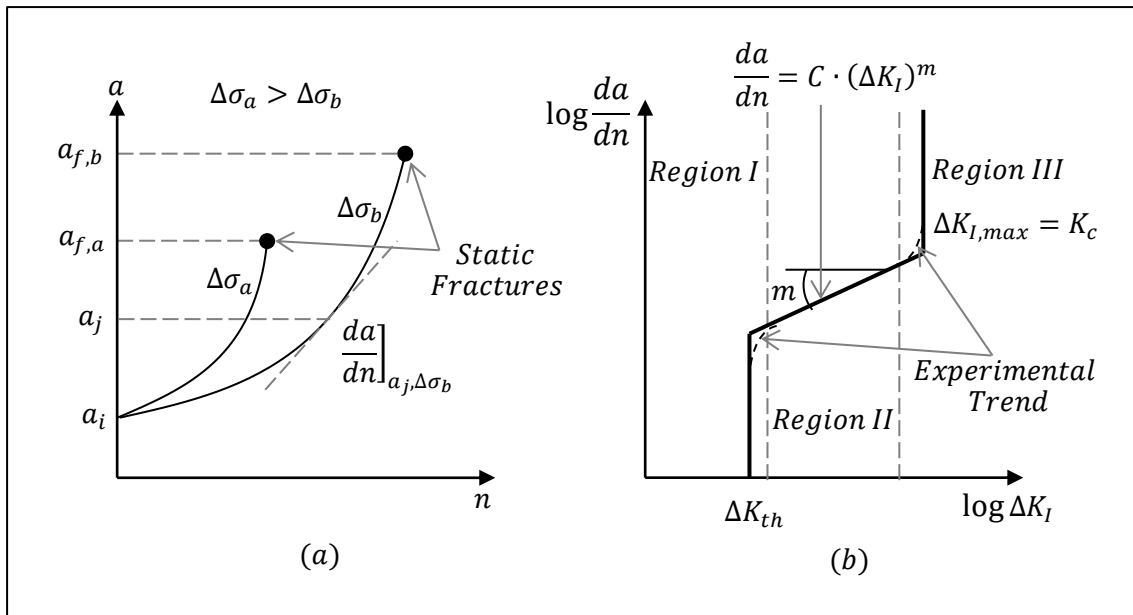
Figure 12: Crack growth curves (a) and Paris diagram (b)

Such a diagram is split into three regions, which correspond to the different stages of fatigue damage, namely, initiation, propagation and final fracture. The points that separate the regions are of fundamental importance to fatigue assessment.

First consider region one. This is where a component spends the majority of its fatigue life. This region is governed by the microstructure, mean stress and working environment. The border between Region I and Region II is characterised by the value referred to as the threshold value of stress intensity factor, ΔK_{th}, and is considered to be a material property which changes for different materials and different load ratios but is independent of sample thickness. If the value of $\Delta K_I > \Delta K_{th}$ then crack propagation will occur. To determine the material property, ΔK_{th}, an appropriate experimental program should be conducted in accordance with the procedures stated by a relevant code of practice, such as ASTM E647. In region two, the crack propagation curve can be described by the Paris equation, as shown in *Figure 12 (b),* where the values for the constants C and m are determined experimentally for each material and load ratio. Finally Region III describes the condition of fast unstable fracture which occurs when $\Delta K_{I,max} > K_C$, the value of K_C is influenced by the

thickness of the tested specimens, therefore, the static assessment of any cracked component, is recommended to be done by using the plane-strain fracture toughness, K_{IC} , for the assessed material.

2.2.8. Statistical evaluation of fatigue data

To assess the finite life region of a fatigue curve firstly the curve is estimated from a series of experimental results. The experimental results are generated by testing n number of samples experiencing different stress amplitudes. By plotting the results on a log-log chart, the fatigue curves can be characterised by a straight line *Figure 8*, the straight line is commonly calculated through the least squares linear regression assuming the hypothesis of a log-normal distribution of the cycles to failure at any given stress level. The scheme of *Figure 13* and the assumption that any stress amplitude produces a log-normal distribution of the fatigue life will be used during this thesis.
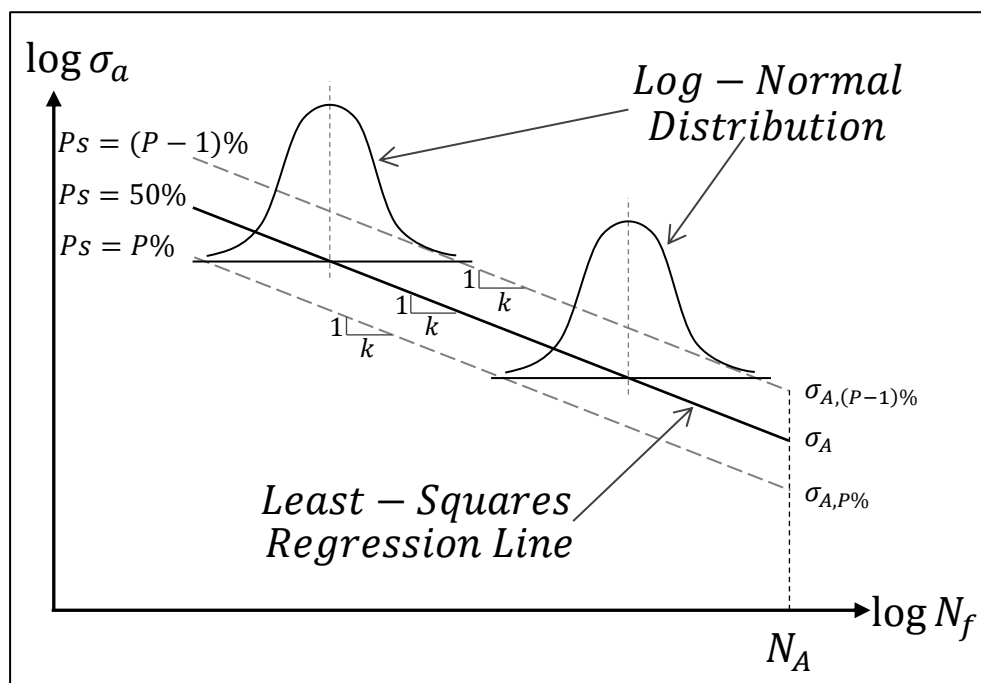
Figure 13: Log-Normal distribution and associated scatter bands

Having obtained a set of finite lifetime fatigue experimental results, the data can be used to estimate the Wöhler curve having a probability of survival, Ps, equal to 50%, for this purpose the linear regression function can be expressed as:

$$y(x) = c_0 + c_1 \cdot x \quad \rightarrow \quad \log(N_f) = c_0 + c_1 \cdot \log(\sigma_a) \tag{37}$$

where x is the independent variable corresponding to the stress amplitude in this specific problem and y is the dependent variable corresponding to the number of cycles to failure. The constants c_0 and c_1 in equation (38) take into consideration the number of experimental data points, n, generated by testing the i_{th} sample ($i = 1,2,\dots,n$) at a stress amplitude equal to $x_i = \log(\sigma_{a,i})$ giving the corresponding experimental number of cycles to failure as $y_i = \log(N_{f,i})$. In accordance with the least squares method, [41] suggest calculating constants c_0 and c_1 as:

$$c_1 = \frac{\sum_{i=1}^{n}(x_i - x_m) \cdot (y_i - y_m)}{\sum_{i=1}^{n}(x_i - x_m)^2} = \frac{\sum_{i=1}^{n}\left[\log(\sigma_{a,i}) - x_m\right] \cdot \left[\log(N_{f,i}) - y_m\right]}{\sum_{i=1}^{n}\left[\log(\sigma_{a,i}) - x_m\right]^2} \tag{38}$$

$$c_0 = y_m - c_1 \cdot x_m \tag{39}$$

Where

$$x_m = \frac{\sum_i^n x_i}{n} = \frac{\sum_i^n \log(\sigma_{a,i})}{n} \tag{40}$$

$$y_m = \frac{\sum_i^n y_i}{n} = \frac{\sum_i^n \log(N_{f,i})}{n} \tag{41}$$

Once constants c_0 and c_1 are calculated, the governing equation of the Wöhler curve Equation (24) can be equated to Equation (43) and (44) to obtain the negative inverse slope and the amplitude of the reference stress at the reference cycles to failure, of the Wöhler curve having $Ps = 50\%$, expressed as:

$$k = -c_1 \tag{42}$$

$$\sigma_A = \left(\frac{10^{c_0}}{N_A}\right)^{\frac{1}{k}} \tag{43}$$

After calculating the necessary constants in the least squares regression model, it becomes possible to derive the associated scatter band allowing the appropriate design curve to be obtained. Thus far we have used, n, experimental results to determine constants c_0 and c_1, therefore the corresponding standard deviation has to be estimated as follows:

$$s = \sqrt{\frac{\sum_{i=1}^{n}[y_i - y(x_i)]^2}{n-1}} = \sqrt{\frac{\sum_{i=1}^{n}\left\{log(N_{f,i}) - log\left[N_A \cdot \left(\frac{\sigma_A}{\sigma_{a,i}}\right)^k\right]\right\}^2}{n-1}} \tag{44}$$

It then follows, the reference stress amplitude $\sigma_{A,P\%}$ and $\sigma_{A,(1-P)\%}$ at N_A cycles to failure which accounts for the probability of survival, Ps, equal to P% and (1-P)% can be expressed through the following equations:

$$\sigma_{A,P\%} = \sigma_A \left[\frac{N_A}{10^{log(N_A)+q\cdot s}} \right]^{\frac{1}{k}} \tag{45}$$

$$\sigma_{A,(1-P)\%} = \sigma_A \left[\frac{N_A}{10^{log(N_A)-q\cdot s}} \right]^{\frac{1}{k}} \tag{46}$$

The encapsulating scatter bands are then characterised by the two reference stress amplitudes and share the same inverse slope, k, as the Ps=50%. In equations (19) and (20), the value of q depends on both the confidence level, the probability of survival and the number of data points, n. A sample of q values are provided in Table 1 [42].

Table 1: Values of index q for a confidence level equal to 95% for different probabilities of survival [42]

	q			
n	Ps=90%	Ps=95%	Ps=99%	Ps=99.9%
4	4.163	5.145	7.042	9.215
6	3.006	3.707	5.062	6.612
8	2.582	3.188	4.353	5.686
10	2.355	2.911	3.981	5.203
12	2.21	2.736	3.747	4.9
14	2.108	2.614	3.585	4.69
16	2.032	2.523	3.463	4.534
18	1.974	2.453	3.37	4.415
20	1.926	2.396	3.295	4.319

To conclude this section a final value, $T\sigma$, is calculated which gives an indication of the scatter associated with the test data, where values closest to unity indicate minimal scatter.

$$T\sigma = \frac{\sigma_{A,(1-P)\%}}{\sigma_{A,P\%}} \tag{47}$$

2.2.9. Multiaxial fatigue

2.2.9.1. Multiaxial Loading

In sub-section 2.2.2 a single sinusoidal load signal is described through its amplitude, mean and range, under a multiaxial loading more than one load signal exists which cause cumulative damage and have to be properly accounted for during the design phase.

As an example, if a plane sample of material is loaded by multiaxial, tension and torsion, out-of-phase load signal, see *Figure 14,* each signal in this case is 90° out-of-phase. Each of the sinusoidal load signals can be described as:

$$\sigma_x(t) = \sigma_{x,m} + \sigma_{x,a}\sin(\omega.t)$$

$$\tag{48}$$

$$\tau_{xy}(t) = \tau_{x,m} + \tau_{xy,a}\sin(\omega.t - \delta_{xy,x})$$

where the subscripts, m and a indicate the mean and amplitude, ω is the angular velocity, t is time and $\delta_{xy,x}$ is the out-of-phase angle. Shown in *Figure 14* are two instances in time, t_1 and t_2, at the first instance the tensile stress is maximised whilst the shear stress is equal to zero and at the second instance the shear stress is maximised whilst the tensile stress is zero.
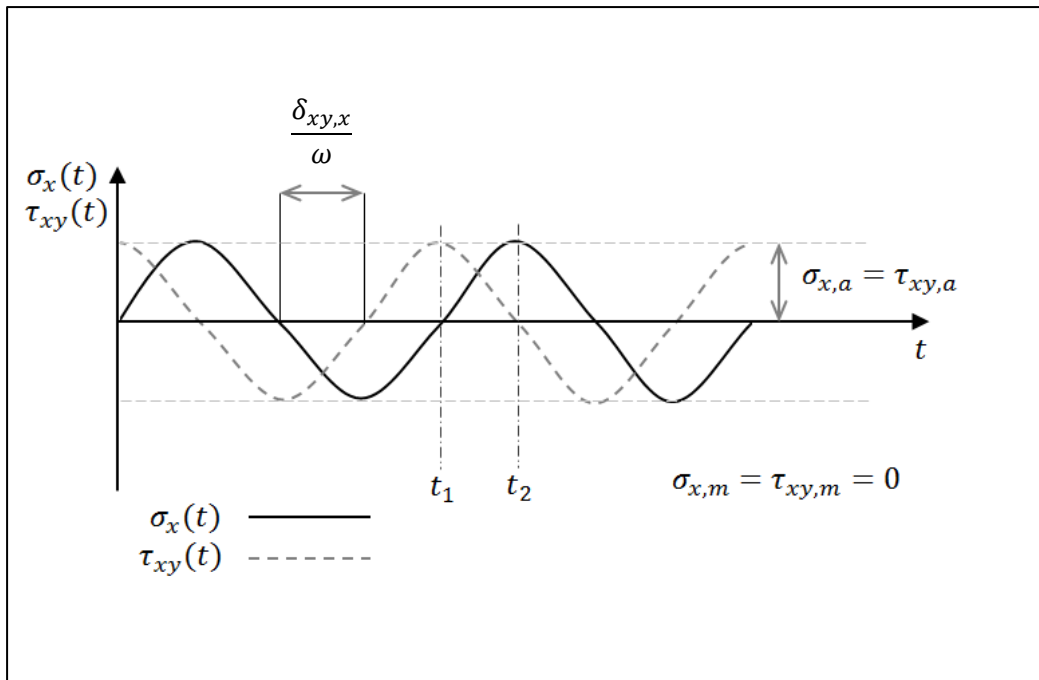
Figure 14: Out-of-Phase multiaxial load signals

In multiaxial fatigue assessment, the most accurate methods are those methods which are based on critical planes. These methods start with the assumption that fatigue cracks initiate on the plane of maximum shear stress i.e. the so called critical plane. The multiaxial fatigue criteria proposed by Matake [43]and McDiarmid [44] also take account of the normal stress relative to the critical plane, the normal stress being seen to significantly affect the propagation of cracks. The critical plane approach used in this thesis is discussed later in this chapter, before this, we must consider some material plane definitions.

Consider the frame of reference and the system of cyclic forces shown in *Figure 15* and assume that point 0 is the most critical location i.e. the point of crack initiation. This point is taken as the centre of our frame of reference, $0zxy$.
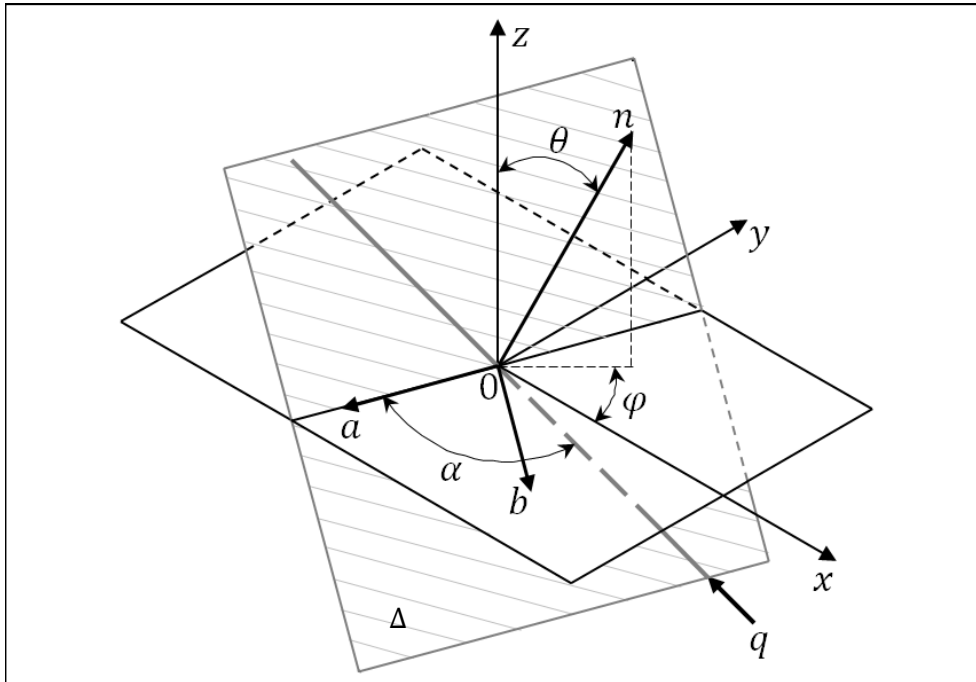
Figure 15: Definition of a generic material plane

The generic plane, indicated by the hatched area, has an orientation characterised by having normal unit vector, $\boldsymbol{n}$, and is defined through angles, φ, and θ. The angle θ is taken between the unit vector, $\boldsymbol{n}$ and the y-axis whilst the angle, φ, is taken as the angle between the x-axis and the projection of the unit vector $\boldsymbol{n}$ on the $x - y$ plane.

To calculate the stress components relative to any considered plane passing through,0, a new system of coordinates is created $0nab$. The unit vectors which define the new axes can be expresses in terms of the angles, φ, and θ [45][46].

$$\mathbf{n} = \begin{bmatrix} n_x \\ n_y \\ n_z \end{bmatrix} = \begin{bmatrix} \sin(\theta) \cdot \cos(\varphi) \\ \sin(\theta) \cdot \sin(\varphi) \\ \cos(\theta) \end{bmatrix} \tag{49}$$

$$\mathbf{a} = \begin{bmatrix} a_x \\ a_y \\ a_z \end{bmatrix} = \begin{bmatrix} \sin(\varphi) \\ -\cos(\varphi) \\ 0 \end{bmatrix} \tag{50}$$

$$\mathbf{b} = \begin{bmatrix} b_x \\ b_y \\ b_z \end{bmatrix} = \begin{bmatrix} \cos(\theta) \cdot \cos(\varphi) \\ \cos(\theta) \cdot \sin(\varphi) \\ \cos(\theta) \end{bmatrix} \tag{51}$$

Next, consider a generic direction, q, which lies on the considered plane and passes through 0, and which can be located through angle, α, which is taken between the unit vector, $\mathbf{q}$, and axis, a.

$$\mathbf{q} = \begin{bmatrix} q_x \\ q_y \\ q_z \end{bmatrix} = \begin{bmatrix} \cos\alpha \cdot \sin\varphi + \sin\alpha \cdot \cos\theta \cdot \cos\varphi \\ \cos\alpha \cdot \cos\varphi + \sin\alpha \cdot \cos\theta \cdot \sin\varphi \\ -\sin\alpha \cdot \sin\theta \end{bmatrix} \tag{52}$$

According to these definitions, the instantaneous values of the normal stress and the shear stress relative to the considered plane can be calculated, respectively, as:

$$\sigma_n(t) = \begin{bmatrix} n_x & n_y & n_z \end{bmatrix} \cdot \begin{bmatrix} \sigma_x(t) & \sigma_{xy}(t) & \sigma_{xz}(t) \\ \sigma_{xy}(t) & \sigma_y(t) & \sigma_{yz}(t) \\ \sigma_{xz}(t) & \sigma_{yz}(t) & \sigma_z(t) \end{bmatrix} \cdot \begin{bmatrix} n_x \\ n_y \\ n_z \end{bmatrix} \tag{53}$$

$$\tau_q(t) = \begin{bmatrix} q_x & q_y & q_z \end{bmatrix} \cdot \begin{bmatrix} \sigma_x(t) & \sigma_{xy}(t) & \sigma_{xz}(t) \\ \sigma_{xy}(t) & \sigma_y(t) & \sigma_{yz}(t) \\ \sigma_{xz}(t) & \sigma_{yz}(t) & \sigma_z(t) \end{bmatrix} \cdot \begin{bmatrix} n_x \\ n_y \\ n_z \end{bmatrix} \tag{54}$$

Consider the material plane shown in *Figure 16;*
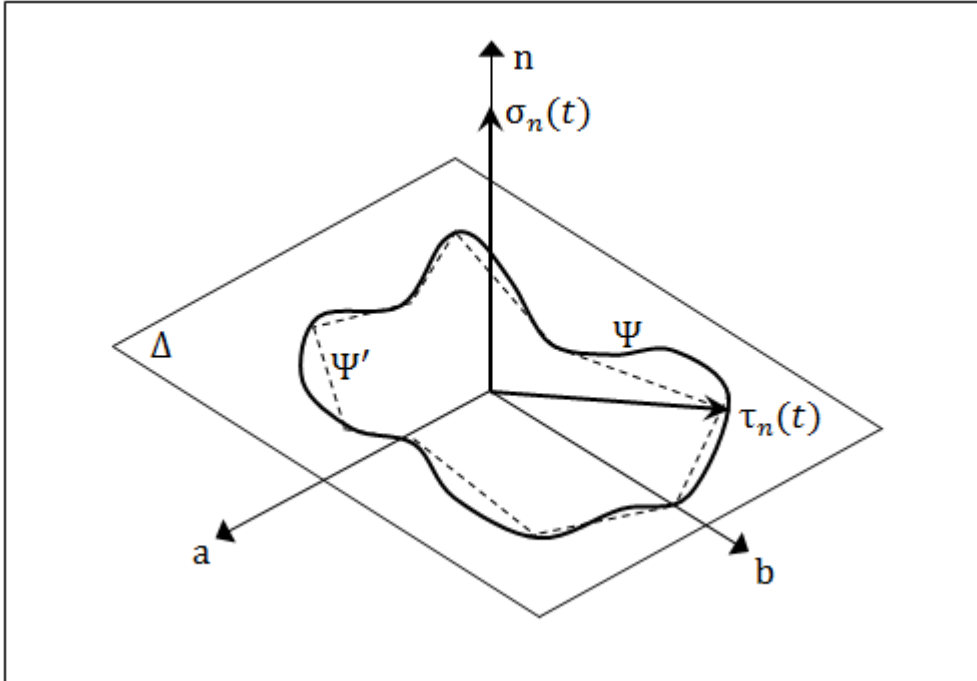
Figure 16: Normal and shear stress relative to a specific material plane

The normal stress components, in terms of amplitude and mean value, relative to a material plane are described through the following equations:

$$\sigma_{n,a} = \frac{1}{2}\left[\max_{t_1 \in T} \sigma_n(t_1) - \min_{t_1 \in T} \sigma_n(t_2)\right] \tag{55}$$

$$\sigma_{n,m} = \frac{1}{2}\left[\max_{t_1 \in T} \sigma_n(t_1) + \min_{t_1 \in T} \sigma_n(t_2)\right] \tag{56}$$

From the above it is then possible to define the maximum and minimum values of the normal stress relative to the specific plane by the following equations:

$$\sigma_{n,max} = \sigma_{n,m} + \sigma_{n,a} \tag{57}$$

$$\sigma_{n,min} = \sigma_{n,m} - \sigma_{n,a} \tag{58}$$

2.2.9.4.   Shear stress components relative to a specific material plane

In the previous sub-section the normal stress components relative to a specific material plane were determined with relative simplicity. In this sub-section the determination of the shear stress components i.e. shear stress amplitude $\tau_{n,a}$ and mean value of shear stress, $\tau_{n,m}$, will be addressed. The nature of this problem is very complex, owing to the fact that that vector $\tau_n(t)$ changes its magnitude and direction during the load cycle. Consider the material plane, Δ , shown in *Figure 16*, this schematisation proposed by Papadopoulos [45] provides a simplification in terms of calculation complexity as well as reducing the numerical effort in obtaining the final result. In more detail, the material plane, Δ , has drawn onto to it a closed curve, Ψ , which represents the shear stress amplitude throughout the cycle. If we consider n different instances within the load cycle and plot the shear stress amplitude at each instance, then curve, Ψ , can be represented by the polygon, Ψ'.

When a component is subjected to out-of-phase tension and torsion or bending and torsion the curve, Ψ , can be determined using equations proposed by Papadopoulos et al. [47] providing that the stress system is synchronous sinusoidal bending and torsion, however it was reported that this loading scenario is not really representative of the loading on real machine parts. As previously stated the shear stress vector changes its magnitude and direction throughout the load cycle, their exist various methods for estimating the important shear stress components relative to a material plane. The more commonly reported classical approaches are Longest Chord Method [48], Minimum Circumscribed Circle [45] or Minimum Circumscribed Ellipse [49][50][51].

The longest chord method is the simplest of the methods but a common feature of these methods is that to determine the orientation of the material plane that experiences the maximum shear stress amplitude is computationally inefficient according to Susmel [52]. To overcome this problem Susmel showed that the maximum variance method is computationally efficient independent of the complexity of the investigated load history. The following sub-section will provide a review of the Maximum Variance Method MVM.

2.2.9.5. *Maximum Variance Method*

A reformulation of the Maximum Variance Method (MVM) was proven to be an efficient method of identifying the critical planes orientation and shear stress amplitude relative to it. In addition to the resolved shear stress amplitude, which mostly governs stage 1 crack formation, stage 2 cracks are influenced by the normal stress relative to the critical plane and if the normal stress cycle has a non-zero mean stress. Independently of the degree of multiaxiality and non-proportionality of the load history damaging the material, the shear stress Maximum Variance Method (τ-MVM) has been proven to be an efficient method for the determination of the critical plane, a full mathematical description of this method can be found in [52] whilst validation of this approach can be found in [53].

In what follows is a review of how the problem of resolving the variance of shear stress along direction, q, $\tau_q(t)$ can be more efficiently expressed through the following scalar product:

$$\tau_q(t) = \boldsymbol{d} \cdot \boldsymbol{s}(t) \tag{59}$$

Where $\boldsymbol{d}$ is the vector of direction cosines and $\boldsymbol{s}(t)$ is a six-dimensional vector process that depends on $[\sigma(t)]$, $\boldsymbol{d}$ and $\boldsymbol{s}(t)$ defined respectively as:

$$d = [n_x q_x \quad n_y q_y \quad n_z q_z \quad n_x q_y + n_y q_x \quad n_x q_z + n_z q_x \quad n_y q_z + n_z q_y] \qquad (60)$$

$$s(t) = [\sigma_x(t) \quad \sigma_y(t) \quad \sigma_z(t) \quad \sigma_{xy}(t) \quad \sigma_{xz}(t) \quad \sigma_{yz}(t)] \qquad (61)$$

Vector **d** could also be expressed in terms of angles φ, θ and α. The quantities defined above show that the variance of the shear stress, $\tau_q(t)$, resolved along direction q can be calculated directly as:

$$Var[\tau_q(t)] = Var\left[\sum_k d_k s_k(t)\right] = \sum_i \sum_j d_i d_j Cov[s_i(t), s_j(t)] \qquad (62)$$

The identity above takes advantage of the definitions of $Var[\sigma_i(t)]$ and $Var[\sigma_j(t)]$, such that when i=j then $CoVar[\sigma_i(t), \sigma_i(t)] = Var[\sigma_i(t)]$, and when i≠ j, $CoVar[\sigma_i(t), \sigma_j(t)] = CoVar[\sigma_j(t), \sigma_i(t)]$. The equation above can be rewritten in the following simplified form:

$$Var[\tau_q(t)] = d^T[C]d \qquad (63)$$

Where [C] is a six by six symmetric square matrix that contains both the variance and covariance terms:

$$[C] = \begin{bmatrix} V_x & C_{x,y} & C_{x,z} & C_{x,xy} & C_{x,xz} & C_{x,yz} \\ C_{x,y} & V_y & C_{y,z} & C_{y,xy} & C_{y,xz} & C_{y,yz} \\ C_{x,z} & C_{y,z} & V_z & C_{z,xy} & C_{z,xz} & C_{z,yz} \\ C_{x,xy} & C_{y,xy} & C_{z,xy} & V_{xy} & C_{xy,xz} & C_{xy,yz} \\ C_{x,xz} & C_{y,xz} & C_{z,xz} & C_{xy,xz} & V_{xz} & C_{xz,yz} \\ C_{x,yz} & C_{y,yz} & C_{z,yz} & C_{xy,yz} & C_{xz,yz} & V_{yz} \end{bmatrix} \qquad (64)$$

where:

$$V_i = Var[\sigma_i(t)] \qquad for \ i = x, y, z, xy, xz, yz \qquad (65)$$

$$C_{i,j} = CoVar[\sigma_i(t), \sigma_j(t)] \quad for \ i,j = x, y, z, xy, xz, yz \qquad (66)$$

The terms above depend on the load history damaging the component and not the orientation of the considered material plane. Once the V_i and $C_{i,j}$ terms are known, the determination of the direction experiencing the maximum variance of the resolved shear stress becomes a conventional multi-variable optimisation problem that does not depend on the length of the input load history itself.

To conclude this section, the multi-variable optimisation problem was reported to get satisfactory results by adopting the so-called Gradient Ascent Method. In order to reach convergence the steps for the iterative process can be calculated as:

$$\begin{bmatrix} \varphi_{n+1} \\ \theta_{n+1} \\ \alpha_{n+1} \end{bmatrix} = \begin{bmatrix} \varphi_n \\ \theta_n \\ \alpha_n \end{bmatrix} + k \begin{bmatrix} \dfrac{\partial Var[\tau_q(t)]}{\partial \varphi}(\varphi_n, \theta_n, \alpha_n) \\ \dfrac{\partial Var[\tau_q(t)]}{\partial \theta}(\varphi_n, \theta_n, \alpha_n) \\ \dfrac{\partial Var[\tau_q(t)]}{\partial \alpha}(\varphi_n, \theta_n, \alpha_n) \end{bmatrix} \qquad (67)$$

Where subscript n denotes the solution calculated at the nth step and n+1 is the subsequent step , steps are taken in the direction proportional to the gradient function $Var[\tau_q(t)]$ and k>0 is a number which is small enough to allow the iterative process to converge.

2.2.10. Modified Wöhler Curve Method (MWCM)

The MWCM is a bi-parametric medium/high-cycle multiaxial fatigue criterion based on critical plane assumptions. The MWCM hypothesises that the material plane from which estimates on fatigue damage are made, as a result of multiaxial cyclic loading, is the plane experiencing the maximum

shear stress amplitude i.e. the assumed critical plane [46][54]–[56]. This assumption is supported by the experimental evidence provided by [57],[58] which showed the probability of predicting crack initiation is most likely to occur when considering those material planes experiencing maximum shear. Although fatigue damage, stage 1, crack initiation is mostly governed by the maximum shear stress amplitude, τ_a, the effect of the shear stress amplitude is significantly affected by the normal stress amplitude, $\sigma_{n,a}$, and the mean stress value, $\sigma_{n,m}$, of the normal stress relative to the critical plane.

The MWCM fatigue damage model has been proven to take into account of all three damaging components simultaneously through the critical plane stress ratio, ρ_{eff}, [59], and takes the form:

$$\rho_{eff} = \frac{m \cdot \sigma_{n,m} + \sigma_{n,a}}{\tau_a} \tag{68}$$

where, m, is the mean stress sensitivity index. This material parameter has been shown to accurately account for the materials sensitivity to the detrimental effects positive mean stresses can have, based on the assumption that a micro/meso crack has greater chance of propagating whilst the crack is opened i.e. during the tension part of the load cycle [60][19][59][46]. The material sensitivity index, m, will take a value between 0 and 1, if the material has $m = 1$ the material is assumed to be fully sensitive to the normal stress acting on the critical plane, on the other hand, if the material has $m = 0$ then the material is considered to be not sensitive to the superimposed static tensile stresses [61].

A significant aspect of the stress ratio, ρ_{eff}, is that the way it is defined leads to it being capable of efficiently accounting for both, the presence of superimposed static stresses and the degree of non-proportionality of the applied loading [46]. With these aspects in mind, the devised hypothesis for the MWCM is formed; for an engineering material, the extent of fatigue damage is the same

independent of the complexity of the applied load history, provided that the assumed crack initiation locations experience the same values of, ρ_{eff}, and τ_a.
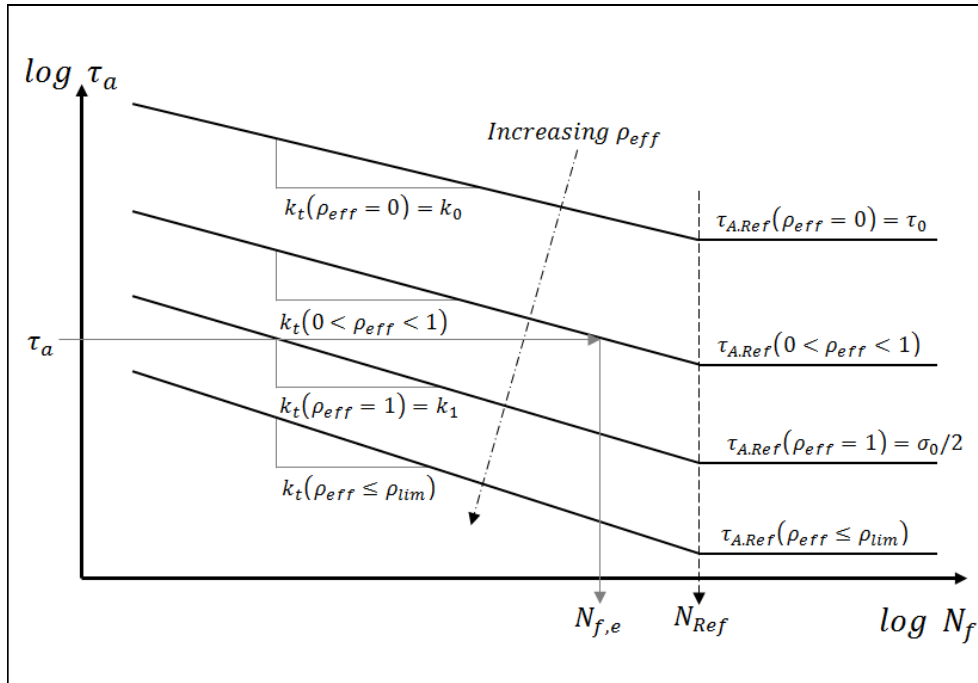
Figure 17: Modified Wöhler diagram

The MWCM assumes that fatigue damage can be quantified through modified Wöhler diagrams[54]. The diagrams plot the shear stress amplitude relative to the critical plane, τ_a, against the number of cycle to failure, N_f. The position of the modified Wöhler curve is seen to shift downwards as the value of ρ_{eff} increases, up to a limiting value of ρ_{lim}, at which point the material is fully sensitive to positive mean stress and the crack is assumed to be open throughout the load cycle. The limiting value of ρ_{lim} is described through the following relationship:

$$\rho_{eff} \leq \rho_{lim} = \frac{\tau_0}{2\tau_0 - \sigma_0} \tag{69}$$

In a practical scenario, the position of a modified Wöhler curve can be directly estimated by using the fully reversed i.e R=-1, uniaxial and torsional fatigue curve by use of the following calibration functions [54][55].

$$k_\tau(\rho_{eff}) = (k_1 - k_0) \cdot \rho_{eff} + k_0 \qquad (for\ \rho_{eff} \leq \rho_{lim}) \qquad (70)$$

$$\tau_{A,Ref}(\rho_{eff}) = \left(\frac{\sigma_0}{2} - \tau_0\right) \cdot \rho_{eff} + \tau_0 \quad (for\ \rho_{eff} \leq \rho_{lim}) \qquad (71)$$

ρ_{lim} was introduced to more accurately model the material fatigue behaviour observed under large values of ratio ρ_{eff}, and has been shown to reduce the level of conservatism characterising the critical plane approach when used in these loading situations.

Once the modified Wöhler curve is estimated for the assessed value of ρ_{eff}, the number of cycles to failure, $N_{f,e}$, can be predicted using the value of τ_a, relative to the critical plane, expressed through the following relationship:

$$N_{f,e} = N_{Ref} \cdot \left[\frac{\tau_{A,Ref}(\rho_{eff})}{\tau_a}\right]^{k_\tau(\rho_{eff})} \qquad (72)$$

When the MWCM is formulated to perform the High-Cycle Fatigue (HCF) assessment, the material is assumed to be at its endurance (fatigue) limit when the following condition is satisfied [54];

$$\tau_a \leq \tau_{A,Ref\ (\rho_{eff})} = \left(\frac{\sigma_0}{2} - \tau_0\right) \cdot \rho_{eff} + \tau_0 \qquad (73)$$

This condition is summarised in *Figure 18*, the schematic representation of τ_a vs ρ_{eff} shows that when $\rho_{eff} > \rho_{lim}$, $\tau_{A,Ref\ (\rho_{eff})}$ is recommended to be taken as $\tau_{A,Ref\ (\rho_{lim})}$[61].
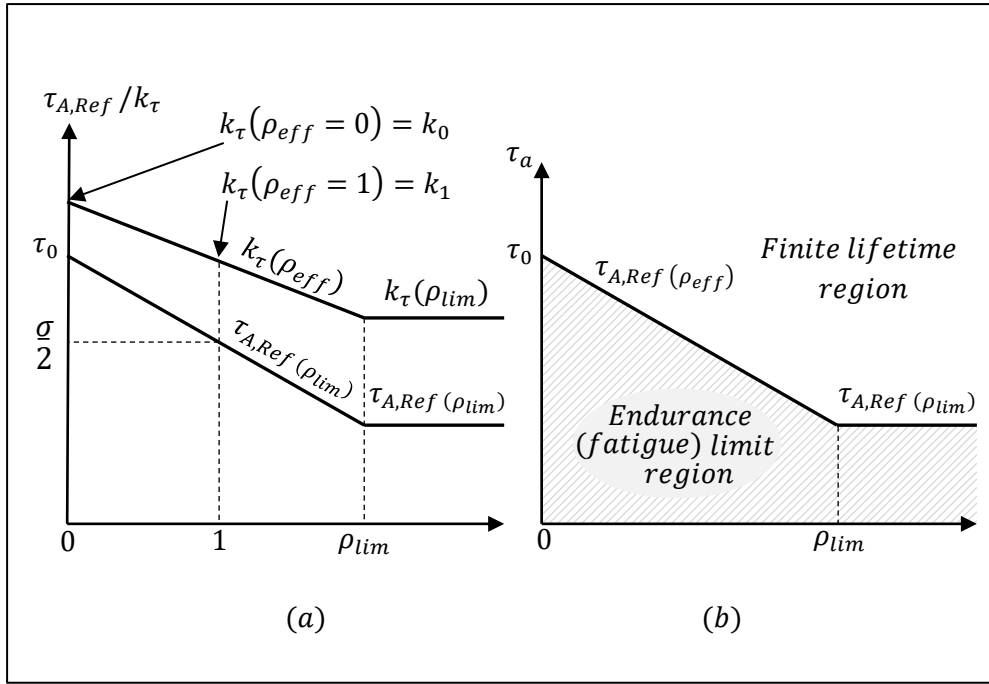
Figure 18: (a) MWCM's calibration functions, (b) Multiaxial endurance (fatigue) limit region according to the MWCM

The condition above can be re-arranged to define an equivalent shear stress amplitude, $\tau_{A,eq}$, so that;

$$\tau_{A,eq} = \tau_a + \left(\tau_0 - \frac{\sigma_0}{2}\right) \cdot \rho_{eff} \leq \tau_0 \tag{74}$$

This is useful from a fatigue design point of view since the above equivalent stress can be directly used to calculate an appropriate high-cycle multiaxial fatigue safety factor, given as;

$$\nu_{HSF} = \frac{\tau_0}{\tau_{A,eq}} \geq 1 \tag{75}$$

This completes the fundamentals of the MWCM, which has shown that this approach can accurately describe the fatigue state of the material independently of the degree of multiaxiality and non-

proportionality of the load paths damaging the components. Before moving on to considering the MWCM in situations involving stress concentration features, it should be highlighted that the MWCM has been successfully used in other fatigue engineering scenarios [46] where damage occurs due to other mechanisms such as fretting fatigue [62], and fatigue of welded joints [63][64][65] to mention just a few. The MWCM can design not only plain specimens but also capable of assessing components containing stress concentration features against fatigue loading regimes, this can be achieved in different ways; by using nominal stresses [55], Hot-Spot stress [63][62] or as is used in this thesis by using the TCD PM [66][67][68][69]. The MWCM has been proven to be highly efficient when used in conjunction with the TCD, this will be discussed in detail in the next chapter.

This concludes the review of fracture and fatigue theory relevant to the work detailed in this thesis. It has been shown that broadly speaking there exist two excellent tools for assessing engineering components performance capabilities, namely; continuum mechanics and fracture mechanics. The limitations of each approach have been discussed and at the limitations estimates can become significantly inaccurate. It was briefly mentioned in the introduction that a review of the state of the art reveals that the so called Theory of Critical Distances provides a sound link between the mechanics of component failure and will be discussed in detail in the next chapter. Beforehand it should be highlighted that one of the main reasons for why this theory has seen resurgence is due to the relative ease of obtaining accurate stress data by means of finite element analysis. The following sub-section is provided for completeness and details the assumptions made whilst creating finite elements models.

2.3. Finite Element Analysis

Throughout the investigations detailed in this thesis a set of assumptions that remain constant in the finite element modelling used to obtain stress data, these are that all considered materials obey

linear-elastic constitutive laws and the material is isotropic and homogenous. All stress data obtained by finite element methods are obtained via commercial software Ansys®. Throughout this thesis all modelled notches are assumed to be consistent in terms of the geometrical make-up. The two most common notch geometries are the V-notch and the U-notch; shown in *Figure 19* are the three most important features which characterise notches and defects. They are; the notch root radius, ρ_n, the notch depth, D_n and the notch opening angle, α_n, however, it should be mentioned that decreasing notch root radius and increasing the notch depth have more of a significant effect over the notch opening angle.
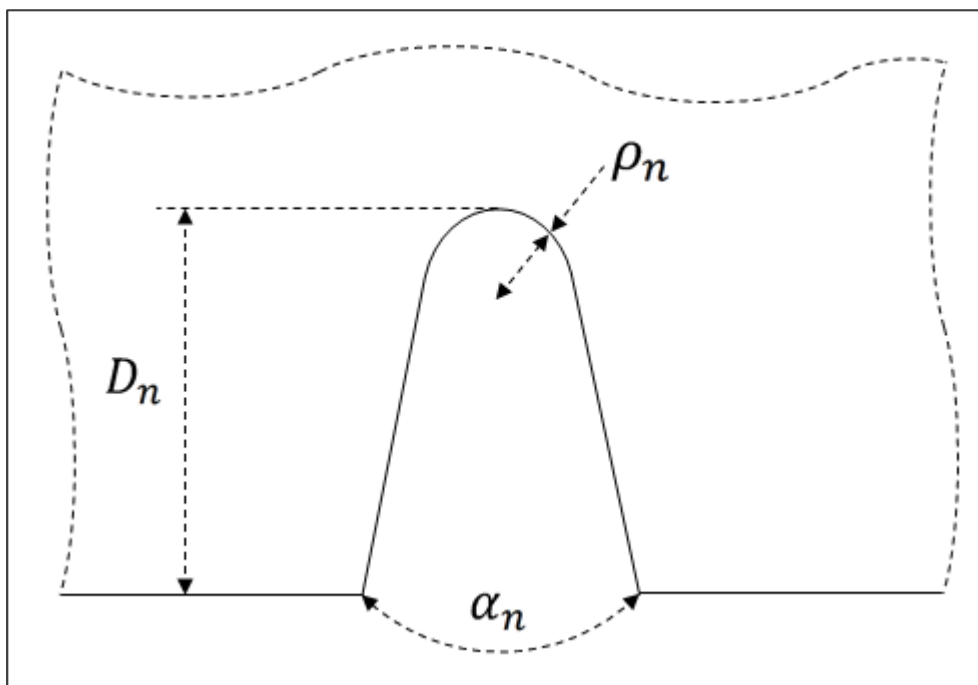
Figure 19: Basic notch or defect characterisation

The V-notch samples are commonly characterised by all three parameters i.e. the notch root radius, ρ_n, the notch opening angle, α_n, and notch depth, D_n, as shown in Figure 19 whilst U-notches are characterised by just the notch root radius and the notch depth. In both cases the sides are assumed perfectly straight, the notch root is always modelled as a perfect continuous fillet of radius equal to the notch root radius and that the notch is perfectly symmetrical about its major axis

which coincides with the notch bisector. These assumptions are used for the FEM, however, in reality the manufacturing process can cause geometrical irregularities on the surfaces of the samples such as gouging. These irregularities can have an effect on the strength of the samples, particularly if located near the point of maximum stress. The variations in the actual geometry are typically accounted for in the statistical analysis and will attribute to the level of scatter.

The FE software package Ansys like other FE packages has many different elements and modelling processes that significantly reduce the computational requirements compared to generating full 3D models. The simplest of these considers a simple block with a through thickness geometrical feature such as a notch. Modelling the block as a cut through 2D projection by using Plane elements, either 4 or 8 node, that offer plane strain conditions can significantly reduce computational time, it also allows for simpler 2D mapped meshes to be created in the area of interest.

When modelling cylindrical samples with circumferential notches loaded axially, the use of axisymmetric elements allows a simple 2D model to be created and analysed as if it's a full cylinder. The 2D model requires the central axis of the cylinder to be coincident with the y-axis at x=0 and the model has a width equal to the cylinders radius. In the loading scenario of applying a torque to a cylindrical sample the modelling is geometrically the same as above, however, the element changes to one that can offer antisymmetric loading.

When components contain complex notches, simplified 2D models are not possible, however, the TCD still requires refinement of the mesh in the vicinity of maximum stress. The level of refinement required for the stress distance curve to converge can result in a very large number of elements which can be very time consuming for most standard computers to solve. In this situation the use of solid-to-solid sub-modelling is used. In more detail, initially a global model is created and coarsely meshed, providing the computer being used can solve this in a satisfactory time, this is an appropriate starting point. The next step is to create sub-model which has approximately half the

volume of the coarse model whilst maintaining approximately the same number of elements, this process is detailed in the flow chart of *Figure 20*. The process of sub-modelling can be repeated, each time the volume is reduced and the mesh density increased, allowing convergence of the stress-distance curve extracted along the focus path.
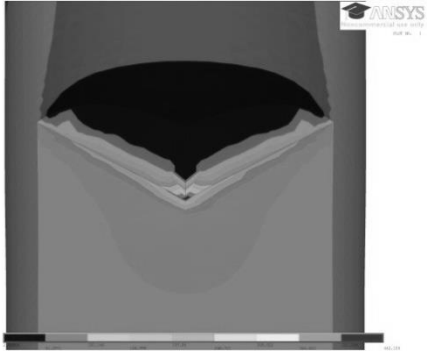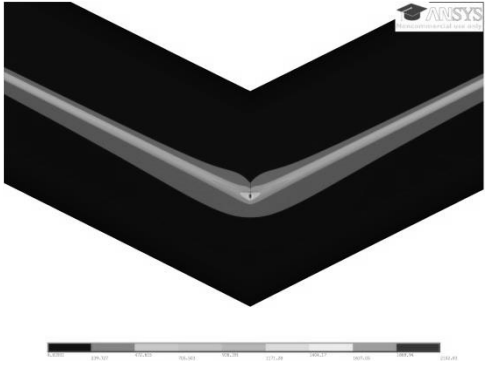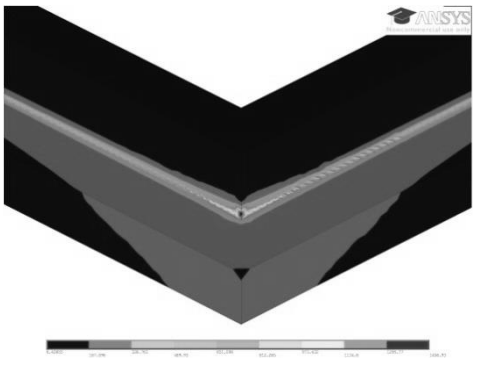
1	Launch Ansys 13 Workbench	
2	Create global geometry	
3	Apply coarse mesh	
4	Apply load and boundary conditions	
5	Analyse the coarse model and save results file	
6	Create a sub-model using the same global co-ordinate system	
7	Apply fine mesh	
8	Select nodes on common boundaries and save nodes	
9	Perform cut boundary interpolation using the save node file and the Coarse results file	
10	Select .cbdo file and apply it to the sub-model and solve	
11	Compare results between the coarse and sub-model	
12	If results comparison ok but finer mesh required repeat the process using sub-model as coarse model	

Figure 20: Flow chart of Sub-modelling procedure

3. The Theory of Critical Distances

3.1.Introduction

The so called, Theory of Critical Distances (TCD) has, since the 1990s, had a significant resurgence which is largely due to the fact that local stress data has become relatively easy to calculate due to the advancements in Finite Element Analysis (FEA) software such as Ansys ® or Abaqus® to name just two. This chapter will provide an overview of the TCD's *modus operandi* and a brief review of its proven applications. For a more thorough insight into the ways and whys the TCD works, the reader is directed to *'The Theory of Critical Distances, A New Perspective in Fracture Mechanics'* by Taylor [70].

Critical distance theories were originally proposed in the 1930s and over the last century the theory has been discovered and rediscovered by scientists and engineers researching fracture and fatigue issues in a variety of disciplines [71][72][73]. The Theory of Critical Distances is a non-mechanistic theory that takes into account through its length parameter, the highly complex processes of fracturing caused by applied loads, being either static or dynamic, on components containing stress concentration features.

As mentioned in the first chapter, Wöhler noticed a decrease in fatigue strength due to the presence of notches, however, it was the pioneering work carried out by Neuber [40] and Peterson [39] that systematically evaluated the notch effect on the fatigue performance of components. Neuber proposed to calculate an effective stress to estimate high-cycle notch fatigue strength by averaging the linear-elastic stresses over a line, this is the first account of the now referred, Line

Method. Subsequently, Peterson simplified the above approach by suggesting that the effective stress could directly be calculated by simply using the stress at a given distance from the notch apex which is the first form of the Point Method.

When it came to implementing their critical distance methods Neuber and Peterson faced two problems;

1. What value should the critical distance be for each material? Peterson hypothesised that the critical distance was related to grain size, however, this posed some measuring difficulties. Both Neuber and Peterson determined the critical distance empirically, fitting predictions to data.

2. Obtaining accurate stress-distance curves in real components. Neuber suggested various elegant solutions for some standard notch geometries but they only offer approximations when applied to real components.

In 1974 Whitney and Nuismer published their paper [72] on laminated composite materials, using test data obtained by testing samples containing varying crack lengths and holes diameters acting as stress concentrators. This limited the validity of the proposed method to through thickness circular holes and cracks, however, they hypothesized that the proposed stress criteria could be applied to any geometric discontinuity. They proposed two methods which took a very similar form to the work of Nueber and Peterson, which the TCD refers to as the LM and PM respectively. Further to this Whitney and Nuismer hypothesised that the value of the length was a material property which was related to both the materials ultimate tensile strength and the plane-strain fracture toughness through their lengths, a_0 and d_0 which are the equivalent to twice and half the TCD's, L, respectively.

The modern advancements of the TCD are in part because of the fact that it takes advantage of the relative ease of obtaining accurate stress estimations by Finite Element Analysis (FEA). Using FEA with the TCD makes it an efficient engineering design tool which is capable of predicting accurate results independent of geometry and the complexity of load history applied to the component. By post-processing the linear-elastic stress field obtained by FEA or by other analytical means and using one of the four methods of the TCD results in failure predictions typically falling within ±20% error, each of the methods all share a material dependent length parameter which is considered to be a material property. The four methods are;

- The Point Method (PM) is the simplest of the methods, taking only into consideration the stress at a single point ahead of the point of maximum stress, where the distance to the point from the surface is considered to be a material property [39][71][74].

- The Line Method (LM) assesses the average stress values along a line ahead of the point of maximum stress [40][71][74].

- The Area Method (AM) averages the stress values within a specific area in the vicinity of the maximum stress[74][75], the area usually being taken as a semicircle with a radius equal to the critical distance.

- The Volume Method (VM) averages the stress values within a specific volume in the vicinity of the maximum stress. The VM has not been used in this thesis and therefore will get no further mention, however, further details of this method can be found in reference [70] and the references therein.

The common feature in these notch fatigue assessment methods is that they all use a material characteristic length parameter. In more detail by examining state of the art fracture and fatigue theory indicates that the TCD is highly accurate and yet relatively simple, the theory uses a material dependent inherent strength and length parameter both of which are assumed to be material properties independent of geometry, for each material the parameters are conventionally

determined by experimental procedures for each type of load history i.e. monotonic or a particular fatigue load ratio, R, characteristic of the loading regime likely to be damaging the real component needing to be assessed.

The focus path is fundamentally the point where crack initiation is assumed to occur and is therefore the line of interest where the stress data is extracted from the FEA, strictly speaking this is only really relevant for the TCD PM and LM. In situations where the geometry is 2D or symmetric 3D and experiencing Mode I loading the focus path will emanate from the point of maximum stress which is coincident with the notch bisector. In situations where the loading is multiaxial, combining Mode I+II or I+III, the point of maximum stress, commonly referred to as the hot spot, will move depending on the ratio of the different loading modes, in these situations obtaining the correct focus path is not so straight forward [76]. The appropriate selection of the focus path will be discussed in more detail in chapters 4-6 but before moving on it is worth reviewing some recommendations made in recent publications as to the location and orientation of the so-called focus path.

First we will consider the suggestions in [70] which were made whilst investigating the size effect of holes loaded by a cyclic torsion load. Three focus paths were investigated each of them emanated from the linear elastic hot-spot, the first path projected along a line perpendicular to the hole surface, the second at 45° to the tangent of the hole at the hot-spot and finally the third path followed the maximum value of the shear stress resulting in a curved path. The predictions were made using the LM in conjunction with Susmel-Lazzarin critical plane method [54], interestingly the maximum error was less than 20% independent of the choice of focus path with the experimental results being between the two straight focus paths, the focus path aligned at 45° produced the most accurate results with a maximum error of 10%.

When using the TCD to assess welded connections experiencing fatigue loading. It has been suggested that the focus path be taken as the bisector of the toe of the weld bead [46] as it is

recommended that the weld bead to parent section be modelled with zero root radius. In general where the notch has a root radius approaching zero the focus path is recommended as being taken as the notch bisector [46][67].

It was suggested in [70], that the TCD would likely to be successful also in situations of contact fatigue. Since then the TCD has been applied to fretting fatigue and has been proven to be successful, achieving high levels of accuracy [77][62][78], the focus path is suggested to be located at the point of maximum stress along the contact line, it is interesting to point out that the TCD is seen to be highly accurate when applied in conjunction with the MWCM.

3.2. Linking aspects of the TCD

In the previous chapters, fundamental theory and assessment methods were presented in the form of LEFM and continuum mechanics, these methods have limitations in their use which induce ever increasing errors as the limits are reached. In more detail, the fracture mechanics approach is very effective when assessing long cracks whilst continuum mechanics methods become increasingly conservative as the notch root radius approaches zero, since *natura non facit saltus*, there must exist some form of relationship between the two, one such theory that provides sound links between these theories is the TCD.

An important feature which the TCD captures is that it can identify and correctly predict the transition of short and long cracks. In more detail, it is well documented that the Kitagawa-Takahashi [79] diagrams can show how the transition from long to short crack lengths cannot be captured by standard LEFM since LEFM would suggest that as cracks of lengths approaching microstructural grain sizes would have a higher strength than the materials ultimate tensile strength.

This particular relationship was used by Taylor [70] during his work on ceramics, in which he shows that the critical distance can be estimated by the intersection of the LEFM prediction line and the inherent strength. More recently a normalised Kitagawa-Takahashi diagram was used in the validation of the TCD PM and LM applicability in predicting the fracture strength of geological materials containing short and long cracks [80], the crack lengths recorded on the abscissa were normalised by dividing the square of the shape function multiplied by the semi-crack length by the critical distance, so that the intersection of the LEFM and Tensile strength occurs at unity.

Consider the static assessment of cracked body where the TCD provides another link with LEFM, in the situation where a component contains a notch with a root radius equal to zero i.e. a sharp crack.

Predictions can be made using both the TCD and LEFM methods. According to LEFM, brittle fracture will occur when the stress intensity factor, K_I, reaches the plane-strain fracture toughness, K_{IC}. The plane-strain fracture toughness is considered to be a material property as are the material parameters in the TCD equation for the critical distance, therefore, there must exist a relationship between them. This relationship as shown in [70] is deduced as follows, the plane-strain fracture toughness is related to the fracture stress and crack length by:

$$\sigma_f = \frac{K_{IC}}{\sqrt{\pi a}}$$ (76)

Additionally the stress ahead of such a crack, assuming that the distance ahead is much less than the crack length can be expressed as:

$$\sigma(r) = \sigma \sqrt{\frac{a}{2r}}$$ (77)

The failure condition according to the PM is $\sigma(L/2) = \sigma_0$, which if combined with the above equations results in:

$$L_S = \frac{1}{\pi} \left(\frac{K_{IC}}{\sigma_0} \right)^2$$ (78)

This equation relates the plane-strain fracture toughness from LEFM to the TCD's material properties, this equation is the primary equation for the mathematical representation the critical distance in the static case.

In high-cycle fatigue the critical distance value is seen to correspond with the intersection of the materials plain fatigue limit curve and the LEFM curve for long cracks as shown on a Kitagawa –

Takahashi diagram. Such a diagram was successfully extended by Atzori and Lazzarin [81] to create a link between the sharp crack like notches and blunt notches.

Before moving onto a more detailed review of specific proven applications of the TCD, the following schema shows how in practice the value of the critical distance varies with loading.
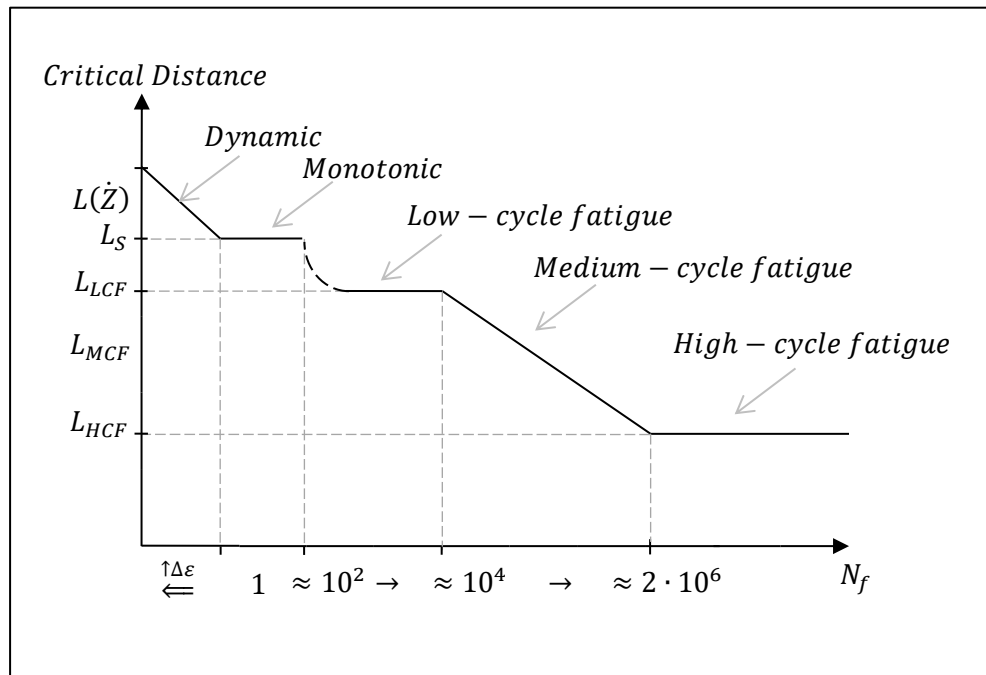
Figure 21: Schematic diagram of the critical distan ce verses loading rate

The schematic diagram of *Figure 21*, shows how the critical distance changes with loading rate or number of cycles to failure. If a critical distance theory existed that could accurately account for the change in plasticity due to loading variations, the critical distance would become a constant material property independent of loading and geometry and would truly be a material property. As it is the, the TCD is a non-mechanistic method that provides sound engineering estimates independent of geometry but the critical distance has to be determined for each loading condition since the loading condition has a significant impact on the level of plastic deformation.

The first region *Figure 21* provides a relationship for the critical distance as the dynamic strain rate increases from quasi-static loading up to high strain rate impact loading, it has been suggested by Yin et al. [82] that the dynamic critical distance can be obtained through the following formula:

$$L(\dot{Z}) = \frac{1}{\pi}\left[\frac{K_{Id}(\dot{z})}{\sigma_0(\dot{z})}\right]^2 = A \cdot \dot{Z}^B \tag{79}$$

where in the above equation $K_{Id}(\dot{z})$ and $\sigma_0(\dot{z})$ are the dynamic fracture toughness and the dynamic strength which are both dependent on the loading rate, finally the critical distance can also be represented by the power law equation on the right hand side, where constants A and B have to be determined by running appropriate experiments.

Moving into the second region of *Figure 21*, this covers the monotonic/static loading scenario, as this is only considering only one loading rate the critical distance is constant. Depending on the considered material, in general the critical distance value will increases as the level of plasticity prior to failure increases, the critical distance in this region is described by Equation (78). The static application of the TCD is discussed at great length in this chapter.

The transition from monotonic loading to low-cycle fatigue is highly complex due the large scale plasticity, in the region of Low-cycle fatigue, the critical distance remains constant [83], this being independent of cycles to failure and geometrical effects, providing that the TCD is used to post-process the elasto-plastic stress/strain field damaging the material in the assumed crack initiation sites.

The next region is the medium-cycle fatigue which represents the finite lifetime of components. In this region the critical distance is seen to be a function of the number of cycles [84]. The medium cycle fatigue assessment according to the TCD is reviewed later in this chapter.

Finally the high-cycle fatigue region has a well-defined critical distance value assuming the material in question displays a conventional fatigue limit. The high-cycle fatigue assessment according to the TCD is again discussed in detail later in this chapter.

3.3. Static assessment using the TCD

3.3.1. Uniaxial static assessment using the TCD

Taylor and Susmel have individually and collaboratively investigated the use of the TCD in situations of static brittle and ductile fracture in a variety of engineering components made of metallic and non-metallic materials containing stress concentration features [85]–[88]. In these papers the TCD is adapted to account for some plasticity prior to failure in some ductile materials, it is therefore referred to as the modified TCD, however, this form of TCD has become the convention and within this work is referred to as the conventional TCD. The modification is simply that instead of using the materials Ultimate Tensile Strength (UTS) as the material characteristic strength a material inherent strength, σ_0, is determined experimentally and is considered to be a material property.

The purpose of the static investigation, detailed in Chapter 4, was to test a simplifying hypothesis. For this reason, the AM and VM are not used in the static assessment due to the additional complexity of applying these methods in comparison to the PM and the LM. Therefore they will not be discussed further in the static loading scenarios detailed in this work. If the reader is interested in these methods more details can be found in [70]. The details of the simplifying hypotheses are discussed in Chapter 4.

In static loading scenarios the TCD adopts the frame of reference shown in *Figure 22(a)* the PM and the LM are shown in *Figure 22 (b and c)* respectively. Employing the PM, σ_{eff}, is estimated at a

certain distance from the apex of the stress raising feature, by employing the LM, σ_{eff}, is averaged over a line ahead of the apex of the stress raising feature.
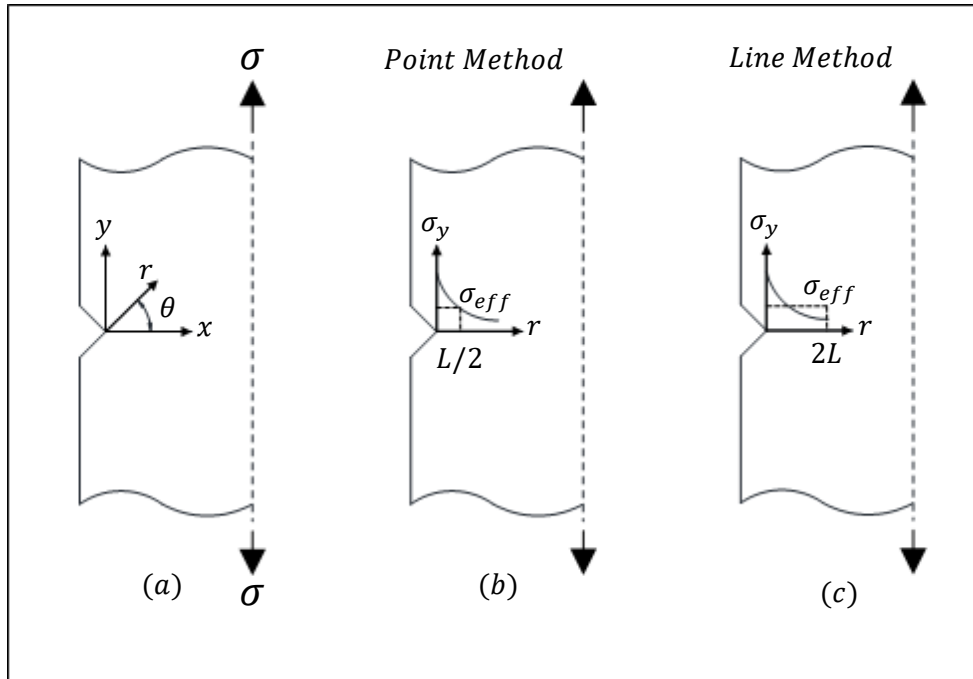
Figure 22: The TCD static frame of reference and formalisation of the PM and the LM

Using the frame of reference reported in *Figure 22*, the two different ways of determining the effective stress can be formalised as:

$$\sigma_{eff} = \sigma\left(\theta = 0, r = \frac{L}{2}\right) \tag{80}$$

$$\sigma_{eff} = \frac{1}{2L}\int_0^{2L} \sigma\left(\theta = 0, r\right)dr \tag{81}$$

According to the TCD's *modus operandi*, to predict static fracture, a component is expected to fail when the calculated effective stress reaches the materials inherent strength.

When employing the TCD to assess components made of brittle materials such as engineering ceramics or polymers at very low temperatures the materials inherent strength is taken as the materials UTS. In materials which exhibit some plasticity prior to failure, it has been shown that the materials inherent strength can be 2-3 times the UTS [87]. The required material inherent strength and critical distance are therefore not known *a priori*, meaning that these material parameters have to be determined experimentally.

The critical distance for any material loaded monotonically can be estimated by running a relatively simple set of experiments. In more detail and with reference to *Figure 23*, the critical distance can be estimated by testing two sets of samples containing two different notch geometries. The known geometries of the notches should have a significantly different notch root radii i.e. a blunt notch and a sharp notch. The linear-elastic stress distance curves are required from along the focus path which can be determined by either FEA or analytical methods. By plotting the incipient failure curves for each set the TCD suggests that in accordance with the PM, at the point where the incipient failure curves intersect corresponds with the inherent strength and half the critical distance. From a different perspective, if the fracture toughness is not known for a material, it has been shown that using the inherent strength and critical distance and rearranging Equation(78) the fracture toughness can be estimated [89].

Like in the static case, under high-cycle fatigue loading conditions, if the threshold value of stress intensity is not known for a material, it has been shown that using the inherent strength and critical distance and rearranging *Equation 88*, the fracture toughness can be estimated [89].
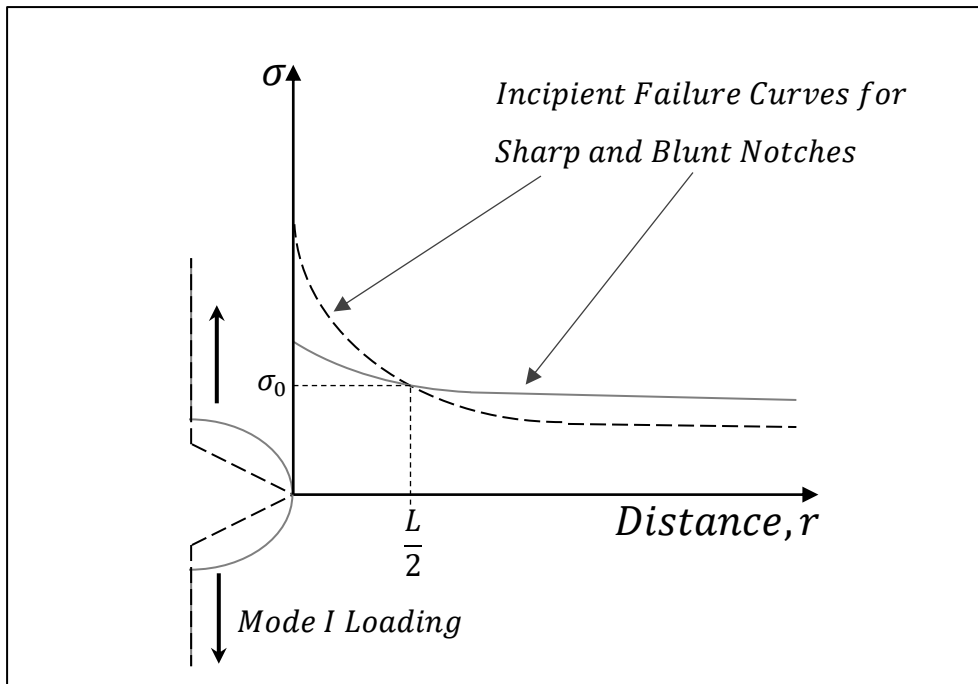
Figure 23: Local Stress-Distance curves at the incipient failure conditions for two geometrically different notches, The PM length and strength determining procedure.

3.3.2. Multiaxial Static loading

So far this static section has considered the uniaxial Mode I loading case where the focus path is unambiguously known *a priori*, and the critical distance is constant. Materials will often display a variation in the ultimate strength depending on the loading type, there exist various empirical relationships for the ultimate torsional strength to the ultimate tensile strength, for some materials the ratio is approximately $\sigma_{UTS} = \sqrt{3} \cdot \tau_{UTS}$. With this in mind, the TCD critical distance will be longer for the material if loaded in torsion than in tension.

To date the TCD has been shown to accurately predict the static strength of notched components made of both brittle and ductile materials. First, the effect of static multiaxial loading on brittle materials was investigated in [76], in which the authors suggest three hypotheses:

1. The materials inherent strength is independent of the complexity of the stress field damaging the material.

2. The value of the critical distance is dependent on the degree of multiaxiality damaging the material.

3. The propagation of small tensile cracks is responsible for the failure of the component, and occurs on the plane experiencing the maximum normal stress.

Taking a closer look at the second hypotheses, it was proposed that, in order to measure in an efficient and concise way the damaging stress fields multiaxiality within the process zone, the following stress ratio be used:

$$\rho(\delta, r) = -\frac{\sigma_3(\delta, r)}{\sigma_1(\delta, r)} \tag{82}$$

This ratio of the maximum and minimum principal stress in the above form shows that at any given distance, r, from the notch tip, the ρ value changes as the orientation, δ, of the considered material plane changes and in the same way if the orientation is kept constant the ρ value changes with change in distance from the notch tip. Once the a critical angle δ^* has been determined, it then follows that the critical distance associated with that degree of multiaxiality can be estimated by the following mathematical formulation:

$$L[\rho(\delta^*, r)] = a \cdot \rho(\delta^*, r) + b \tag{83}$$

Where in the above linear relationship material constants a and b are determined under two different ρ ratios. The simplest way to determine the constants is by testing under pure tension and pure torque where $\rho = 0$ and $\rho = 1$ respectively.

This method is considered to be highly efficient in situations of assessing brittle materials. Next, attention will be given to the way the TCD evaluates ductile materials.
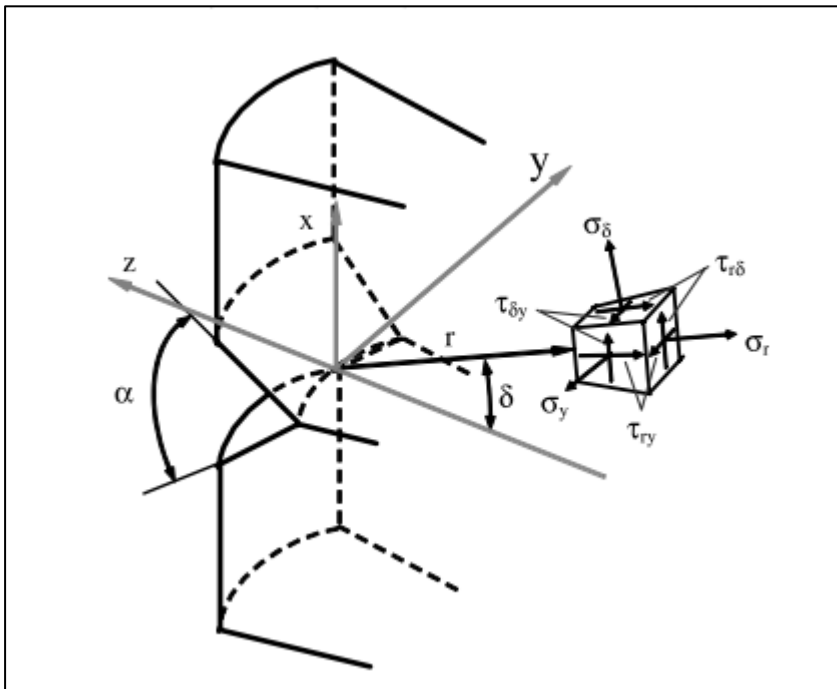
Figure 24: Frame of reference taken from [76]

In a two part paper series [90][88], the authors presented an experimental and theoretical investigation into the response of circumferentially notched samples loaded in tension, torsion and combined tension/torsion, the samples were made of a commercial aluminium alloy, Al6082, which has many applications from bridges to beer barrels. The two papers report the experimental data, load-deflection curves, observed material failure modes and with a main emphasis on the application of the TCD.

The experimental investigation revealed that samples with blunt notches loaded by Mode I tension failed by a ductile-like fracture process, contrary to this, samples which contained sharp notches and were loaded by Mode I tension failed in a brittle-like manner with final fast fracture being preceded by a period of stable crack growth. Samples loaded by Mode III torsion failed with the same characteristics independent of notch sharpness, the failures being characterised by the propagation of stable shear cracks on planes perpendicular to the specimen axis. Under mixed Mode I and III loading, the failures occurred due to a combination of the above fundamental mechanisms, the prevalent failure condition being dependent on the mutual interaction between notch sharpness and the nominal tensile stress to nominal torsional stress ratio.

In the application of the TCD to assess the static strength of the notched AL6082, the use of three different equivalent stresses were used, Von-Mises equivalent stress, Tresca's equivalent stress and the Maximum Principal stress criterion. Using the procedure shown in *Figure 23*, the PM argument for determining the critical distance value, it was shown that the Von-Mises and Tresca equivalent stress resulted in the same critical distance value. These equivalent stresses gave the least error in the overall strength predictions independent of the multiaxiality of the stress state damaging the material. The critical distance value obtained by the Maximum Principal stress criterion was more than 3 times greater than the other obtained values and had a value approximately half of the net area radius. The Maximum Principal stress criterion gave very good results when assessing Mode I loading with more accuracy than the Von-Mises or Tresca estimations, the Mode III loading scenarios are however extremely conservative when using the maximum Principal Stress, the conservatism could be attributed to the fact that a torque load on a shaft will produce a zero stress state at the central axis and since the maximum principal stress critical distance is comparable to the physical dimensions of the assessed samples, the assessed point could be affected in a more significant way by the loading rather than the notch itself. This can be seen by the increase in conservatism as the ratio of the nominal tensile stress to nominal torque stress tends towards zero, finally the

application of the LM to these samples results in assessing the stress state passing through the central axis. More will be said on this in Chapter 4 and will help define a limitation regarding Mode III loading used in proposed simplified methodology.

3.4. Fatigue assessment using the TCD

3.4.1. Uniaxial Fatigue

The TCD has been proven to be successful in predicting fatigue strength and lifetime of structural and mechanical components containing stress raising features experiencing constant and variable amplitude cyclic loading, both these regimes will be discussed after first introducing the general application of the TCD in fatigue scenarios. To introduce the TCD's *modus operandi i*n fatigue applications, first consider the frame of reference shown in *Figure 25*, the TCD as previously mentioned can be applied in four different methods but this section will only consider three, being the PM, LM and the AM, excluding the VM.

The application of the TCD requires the knowledge of material properties obtained for the like loading case, the required parameters being the critical distance itself and the plain fatigue limit, $\Delta\sigma_0$, the required parameters can be obtained by running appropriate experimental investigations, however many commonly used materials parameters are detailed in [46]. The TCD assumes that the fatigue damage resulting from stress raising features can be accounted for by using a stress quantity which is essentially an average of the entire linear-elastic stress field damaging the process zone. Moreover, a component containing a stress raising feature is assumed to be at its

fatigue limit condition when a defined effective stress, $\Delta\sigma_{eff}$, equals the materials plain fatigue

limit, $\Delta\sigma_0$, so that;

$$\Delta\sigma_{eff} = \Delta\sigma_0 \tag{84}$$

The effective stress will now be defined using three of the TCD methods.
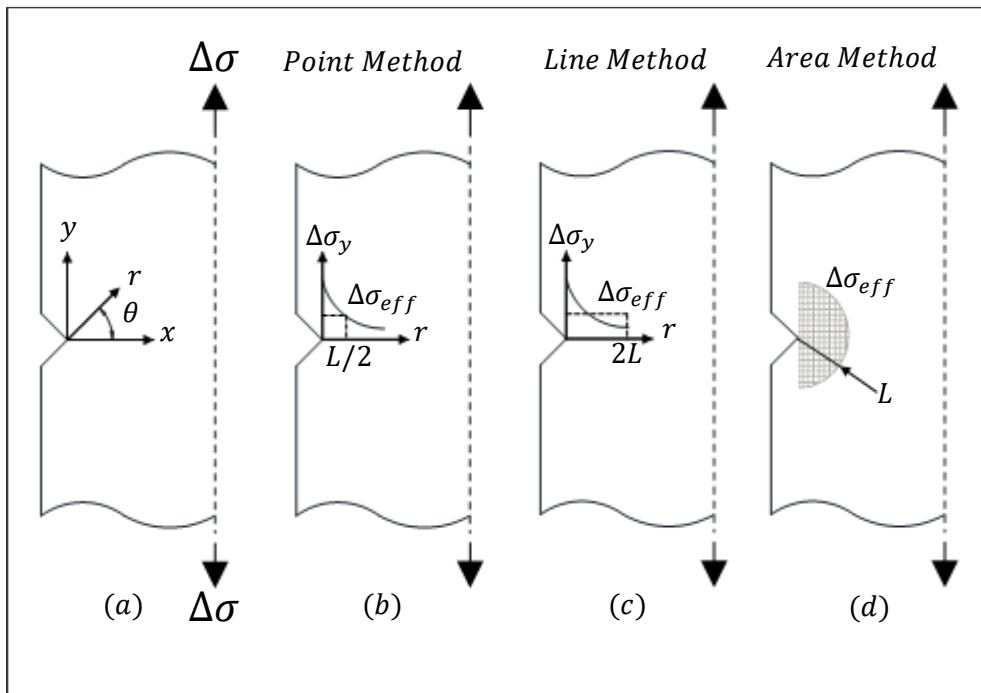
Figure 25: (a) Local system of coordinates, (b-d) the TCD formalised according to the PM, LM and AM

If the TCD is applied in the form of the PM, *Figure 25 (b),* then the component is considered to be in

its failure condition when the following condition is satisfied:

$$\Delta\sigma_{eff} = \Delta\sigma\left(\theta = 0, r = \frac{L}{2}\right) = \Delta\sigma_0 \tag{85}$$

If the TCD is applied in the form of the LM, *Figure 25 (c),* then the component is considered to be in its failure condition when the following condition is satisfied:

$$\Delta\sigma_{eff} = \frac{1}{2L} \int_0^{2L} \Delta\sigma\,(\theta = 0, r\,)dr = \Delta\sigma_0 \qquad (86)$$

If the TCD is applied in the form of the AM, *Figure 25 (d),* then the component is considered to be in its failure condition when the following condition is satisfied:

$$\Delta\sigma_{eff} = \frac{4}{\pi L} \int_{-\pi/2}^{\pi/2} \int_0^{L} \Delta\sigma\,(\theta, r\,)d\theta dr \approx \Delta\sigma_0 \qquad (87)$$

In each of the above formalisations of determining the effective stress use an assumed material property which can be defined as [70][71][73] [67][66];

$$L = \frac{1}{\pi} \left(\frac{\Delta K_{th}}{\Delta\sigma_0} \right)^2 \qquad (88)$$

where ΔK_{th} is the threshold range of stress intensity and $\Delta\sigma_0$ is the range of stress of an un-notched sample of the same material at its fatigue (endurance) limit, commonly extrapolated at $N_{Ref} = 2 \cdot 10^6$ but more importantly must be determined under the same load ratio, R.

The linear-elastic TCD has been proven to be successful in predicting fatigue limits of notched components [91][92]. In addition to the HCF success the TCD has also been successful in predicting the fatigue lifetime of components failing in the MCF regime [12]. In the MCF regime the TCD assumes that the critical distance changes as the number of cycles to failure decreases, the TCD predictions of fatigue lifetime for components containing stress raising features rely on knowledge of the L_{MCF} vs N_F relationship which is assumed to follow a power law relation [12]:

77

$$L_{MCF}(N_f) = A \cdot N_f^{\;B} \qquad\qquad (89)$$

where A and B are material dependent fatigue properties to be estimated using un-notched and notched fatigue curves generated under $R = -1$ and with knowledge of the notch geometry.

The obvious approach to calibrating the constants in the above power law relation would be to assume at one end the static expression for the critical distance whilst at the other end the HCF critical distance, however, this approach has various problems. Most importantly is that stress based approaches are seen to be unsuccessful in the LCF regime. To overcome this and other associated problems in this simplistic approach, it was suggested by Susmel and Taylor [12] that an alternative procedure based on two calibration curves be used.

In particular, the critical distance can be determined from the fatigue curve of the plain material with a fatigue curve generated by testing samples with a known geometrical feature *Figure 26*. In accordance with the PM philosophy *Figure 26 (b)* when the local stress, due to the applied gross stress, ahead of the stress raising feature reaches the plain fatigue life for that given number of cycles to failure, N_{Ref} ,the critical distance, L_{MCF}, can be estimated.

Once the L_{MCF} vs N_F relationship is known for values of N_f falling between the low/medium-cycle regime and the HCF regime, a conventional recursive procedure can then be used to estimate in the presence of any geometrical feature the fatigue lifetime, providing the component is made of the same material.
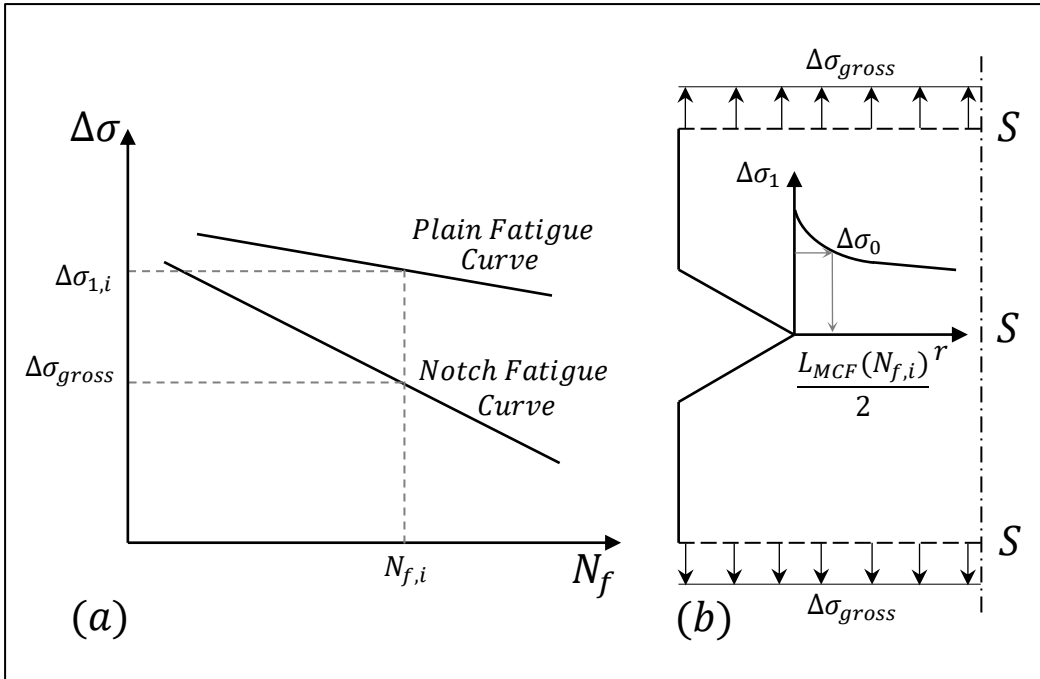
Figure 26: Determination of the critical distance value using two calibration fatigue curves

A simple recursive procedure is demonstrated through the flow chart of *Figure 27*, this being suitable for using the TCD to predict the MCF damage.
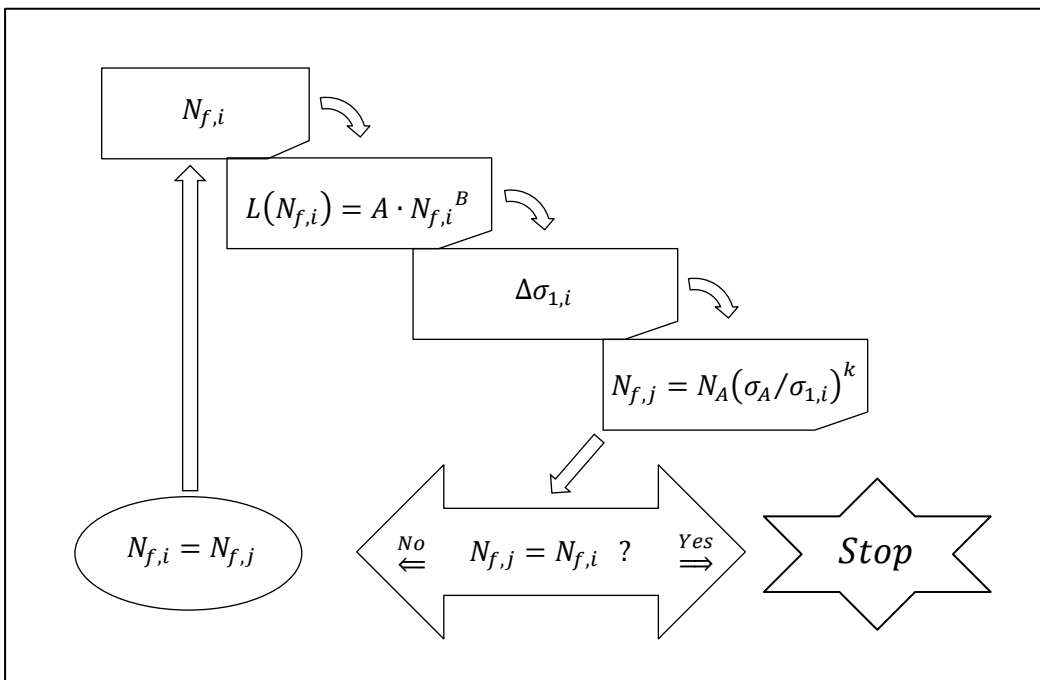
Figure 27: Recursive procedure for determining the MCF critical distance [12]

3.4.2. The MWCM applied along with the TCD PM to assess multiaxial fatigue loading

This section will provide a brief overview of a considerable amount of work and development into a methodology for multiaxial loading. Unlike other stress based methodology which have approached the multiaxial problem by extending a uniaxial criterion, this methodology considers the uniaxial case as a simple case of the more complex multiaxial case. In more detail, the MWCM applied in conjunction with the TCD PM starts with the idea that fatigue damage has to be estimated by taking account of the multiaxiality of the entire linear-elastic stresses in the vicinity of crack initiation [66][93][94][67][95]. In this coupled theory approach, the scale and stress gradient effects resulting from the stress concentration feature are accounted for by the TCD [71][74][96], whereas the degree of multiaxiality and non-proportionality of the fatigue loading damaging the fatigue process zone is efficiently accounted for by the MWCM [54][55][19][59]. The MWCM is applied in conjunction with the TCD PM for greater efficiency, since complex non-proportional multiaxial load histories are easier to handle when evaluating fatigue damage by using the stress state at a single point [66], furthermore, the critical distance is assumed to be independent of the geometry but increases as the number of cycles to failure decreases as reported in the previous section. Finally, before moving onto the specific review of the MWCM in conjunction with the TCD PM in its application to HCF and MCF, if the reader is interested in how it is applied to fretting fatigue and welded joints scenarios then they are directed to the book by Susmel '*Multiaxial Notch Fatigue, from nominal to local stress/strain quantities*'[46].

Consider the component depicted in *Figure 28*, which is subjected to a series of time dependent

forces. In order to correctly assess the HCF using the MWCM in conjunction with the TCD PM the

parameters in the following equation must be determined, namely α, β, m and ρ_{lim}:

$$\tau_{A,Ref}(\rho_{eff}) = \alpha \cdot \rho_{eff} + \beta \tag{90}$$

$$m = \frac{\tau_a^*}{\sigma_{n,m}^*}\left(2\frac{\tau_0 - \tau_a^*}{2\tau_0 - \sigma_0} - \frac{\sigma_{n,m}^*}{\tau_a^*}\right) \tag{91}$$

$$\rho_{lim} = \frac{\tau_0}{2\tau_0 - \sigma_0} \tag{92}$$

The parameters should be determined using the fatigue results obtained by testing the plain

sections of the material from which the notched components are to made from [67][66]. The critical

distance used in the HCF regime is equation 88 which is as previously mentioned a function of the

threshold value of the stress intensity factor and the range of stress at the materials plain fatigue

limit. The fatigue properties should be determined under fully reversed conditions, this is due to the

assumption that the presence of positive mean stresses are directly accounted for by the MWCM. In

addition to the above, the critical distance could also be determined using the PM argument which

requires the fully reversed plain fatigue limit and the fully reversed fatigue limit of samples

containing a known geometrical feature [70][94].

 To assess the HCF performance of a component, consider the component depicted in *Figure 28,* in

accordance with the TCD PM, the linear-elastic stress state to be post-processed is extracted at

point, 0, positioned along the focus path at a distance equal to $L/2$ from the surface. The focus path emanating from point, A, which is considered to be the point of crack initiation [67].
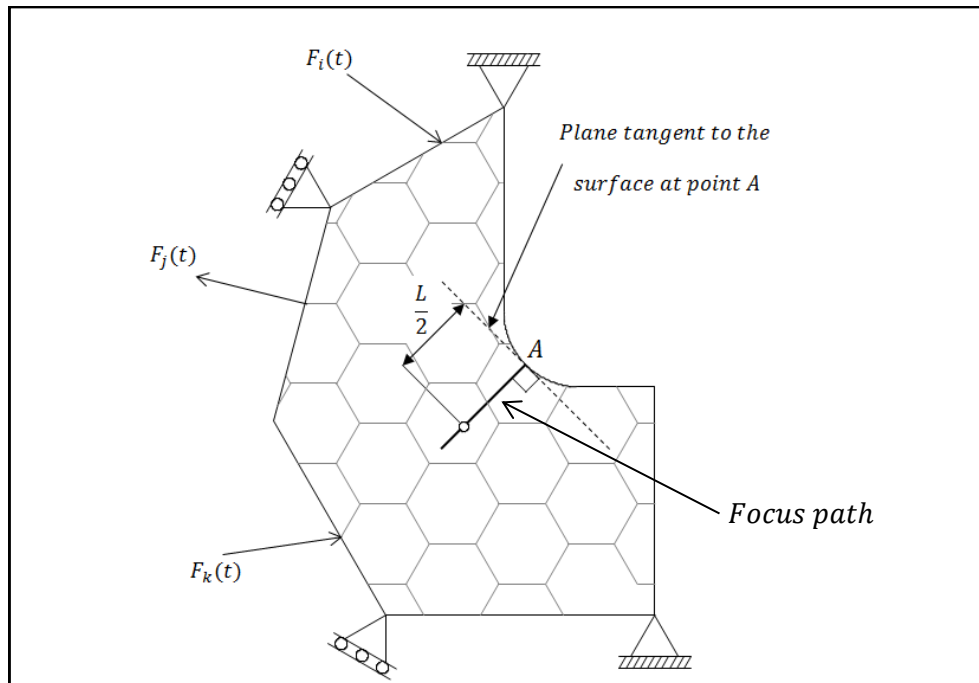
Figure 28: High-Cycle Fatigue assessment focus path definition

At point, o, *Figure 28*, if a suitable frame of reference is introduced, say $Oxyz$, then for any instance in time corresponding to some point in the cyclic load history, the linear-elastic Cauchy stress tensor can be obtained. Using the components of this stress tensor the shear stress amplitude τ_a, normal stress amplitude, $\sigma_{n,a}$, and mean value of the normal stress, $\sigma_{n,m}$, relative to the critical plane can be obtained as described in the previous chapter. Using the obtained values the effective value of the critical plane stress ratio, ρ_{eff} , can be calculated, and finally, the component being assessed is assumed to be at the fatigue limit providing that the following condition is satisfied [67]:

$$\tau_a \leq \tau_{A,Ref(\rho_{eff})} = a \cdot \rho_{eff} + b \qquad (93)$$

A significant aspect of this design approach which should be highlighted is that, when a component is being designed to withstand a complex system of time variable forces, each load can be calculated

separately. The master stress tensor can then be formed by superposing the results obtained for each of the considered forces whereby particular attention must be given to maintaining synchronicity of the load signals. By following this procedure both positive mean stresses and the presence of non-zero out-of-phase load signals can be efficiently accounted for during the design phase.

To conclude this section, the above procedure has been systematically validated by first considering uniaxial loading on both flat and cylindrical samples made of a variety of materials containing different geometrical features [67]. Additionally the method was applied to samples weakened by V-notches experiencing different ratios of Mode I and Mode II loading [66], following on from this the method was applied to V-notched cylindrical samples tested by imposing both bending and torsion load signals which were applied in- and out-of-phase. Concluding the validation the method was also applied to notched samples of En3B which were subjected to in-phase and out-of-phase tension and torsion which additionally involved superimposed positive tensile and torsional mean stresses [68]. In all of the above investigations the method returned highly accurate results, typically returning results with $\pm 20\%$, which as previously mentioned is within the original scatter bands characterising the parent materials fatigue results.

3.4.2.2. *Medium-cycle fatigue (Finite Life) using the MWCM+PM*

The previous section reviewed the MWCM applied in conjunction with the TCD PM to estimate the high-cycle fatigue limit of components containing stress raising features and experiencing simple and complex load histories, in this section the same method will be reviewed but considering components that fail in the medium-cycle fatigue regime i.e. the so called endurance limit.

To design a component that experiences medium-cycle fatigue loading in accordance with the MWCM and the TCD PM, first the following parameters a, b, α, β, m and ρ_{lim} need to be determined. Like the application of the TCD discussed in 3.4.1, the application of the MWCM with

the TCD PM starts by assuming that the most accurate estimations are achieved by adopting a material characteristic length, L_{MCF}, which as previously discussed, changes its value depending on the number of cycles to failure but independent of the components geometry [68][94], the critical distance being assumed to follow the power law relation of equation 89.

To use the MWCM in conjunction with the TCD PM to estimate MCF, consider the component depicted in *Figure 29* which is experiencing a system of cyclic loads. The first task is to obtain the linear-elastic stress distance curve along the focus path, as shown in *Figure 29*, the focus path emanates from point A along a direction perpendicular to the surface, point A is taken as the surface hot-spot and is assumes to be coincident with the point of crack initiation. In situations where the notch root radius tends towards zero, the focus path is recommended as being taken as the notch bisector [59].

Having obtained the stress data along the focus path, the maximum shear stress amplitude, τ_a, and the stress ratio, ρ_{eff}, as a function of distance, r, the relationships τ_a vs r and ρ_{eff} vs r are schematically shown in *Figure 29*. Using the calculated values of τ_a and ρ_{eff}, and incorporating them with the relationships k_τ vs ρ_{eff} and $\tau_{A,Ref}$ vs ρ_{eff}, obtained from the fatigue properties of the parent material, the modified Wöhler curve can be estimated. Now the number of cycles to failure can be considered to be a function of the distance along the focus path. Using an estimated value of the number of cycles to failure and equation 89, the method postulates that the component being assessed will fail at the number of cycles to failure when the following condition is satisfied, see *Figure 29*:

$$\frac{L_M\left(N_{f,e}\right)}{2} - r = 0 \tag{94}$$
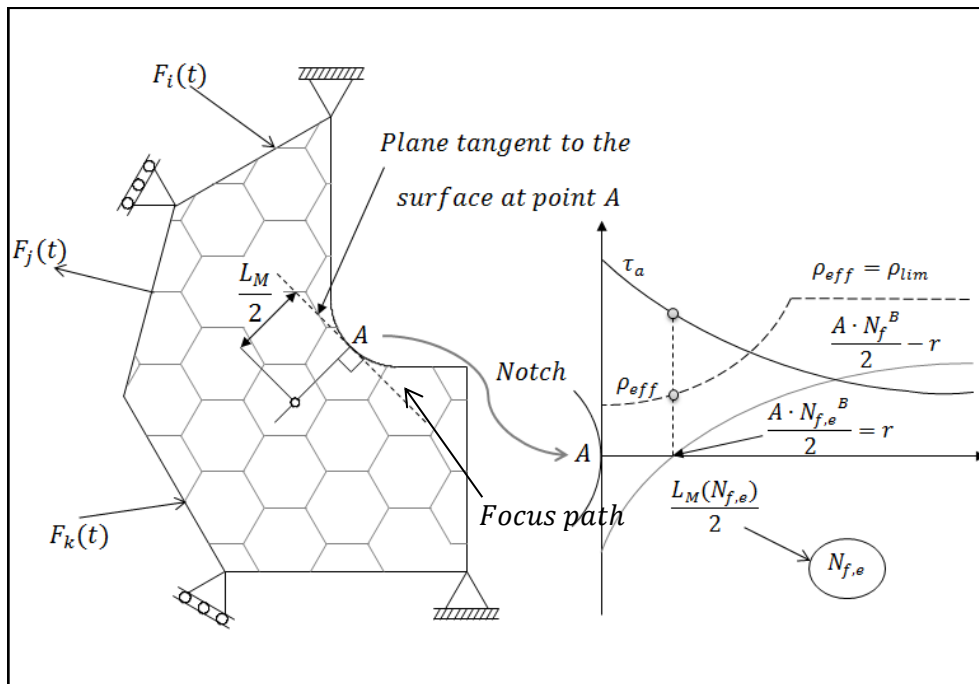
Figure 29: Definition of focus path and in-field procedure to estimate finite lifetime

The above procedure has been validated using a large number of experimental data [94][68][46], the predicted number of cycles to failure being typically within $\pm 20\%$ of the experimental results.

3.4.3. The linear-elastic TCD at elevated temperatures

Mechanical components are often required to perform in extreme environmental situations, two commonly occurring scenarios are highly corrosive environments and elevated temperature. As to the first of these, it has been discussed in [70] that the TCD could be used in scenarios such as stress-corrosion cracking where the propagation of cracks is controlled by small scale yielding and characterised by stable crack growth. In situations where the component is expected to perform during elevated in-service temperatures, the effect of these elevated temperatures can have a significant impact on the fatigue life of a component, and therefore need to be appropriately accounted for by the design engineer when components are likely to operate under such conditions.

The fatigue characteristics of metallic components become intrinsically complex as normal working temperatures are increased, this being a serious matter of concern for structural / mechanical engineers designing components that have to be assessed for their fatigue performance at elevated in service temperatures. There are numerous industries where in-service operational temperatures are elevated, for example; transportation conventionally requires an engine, either a conventional combustion engine or jet engine, in the energy sector, power plants will have components working in extreme conditions and finally in this short list the manufacturing sector such as hot-rolling of steel sections.

The assessment of notched components experiencing high-cycle fatigue loading at elevated temperature by using critical distance concepts has been considered by Yang et al. [97]. In this paper the authors investigated the accuracy of the TCD to assess notched specimens of directionally solidified superalloy DZ125 experiencing fatigue loading at 850°C. The authors concluded that for this specific material the value of the critical distance was somehow related to the geometry of the notch tip.

3.5. TCD Conclusions

The history of the TCD and the more recent developments has been discussed. In the modern use of the TCD it has been shown that to get the most accurate results, the TCD parameters are best determined by running an appropriate experimental program. In the conventional use of the TCD, required parameters are determined by experimental procedures, the required test data being relatively simple to determine by means of standard test machines. The TCD can be used in conjunction with stress analysis data obtained by standard FEA, make it a simple, effective and efficient design methodology.

Considering the problem of 3D stress raisers experiencing complex load histories, it should be highlighted that Bellet and Taylor [75][98][99] have applied the TCD to situations involving multiaxial stress fields resulting from 3D stress raising features, the resulting estimates were reported to be too conservative, they suggested that the high degree of conservatism could be due to the differences in crack shapes between bi- and tri-dimensional bodies. An ad-hoc correction factor was proposed to correct the degree of conservatism which improved the accuracy of the TCD when assessing tri-dimensional stress concentrators, this implies that there is a characteristic pattern to be found however further work is required to find it. Further work regarding this particular forms the basis of chapter 4 of this thesis.

It has been reported that when applying the TCD to components experiencing high-cycle fatigue loading at elevated temperatures, the value of the critical distance was seen to be a affected by the sharpness of the stress concentrator. In general the TCD assumes that the value of the critical distance is a material property that is independent of geometrical features, an investigation using the linear-elastic form of the TCD to assess the fatigue performance of metallic samples experiencing fatigue loading at elevated temperatures provides the grounds for chapter 5 of this thesis.

The review of the applying the TCD to the static loading cases shows that the materials inherent strength parameter is somehow related to the ductility of the material in question with the only way of obtaining the appropriate material properties being by running experimental investigations which can be costly in terms of finance and time. In the situation of assessing brittle materials the required value of the critical distance is said to be a function of the materials ultimate tensile strength and the plane-strain fracture toughness. Chapter 4 of the thesis provides details of an investigation into extending this approach of obtaining the required material critical distance to materials that exhibit quasi-brittle and relatively ductile mechanical characteristics in their plain form.

4. Can the TCD method for static assessment become more efficient and be applied independent of the components, material, geometry or loading?

4.1. Introduction:

This chapter details an investigation into a reformulation of the TCD applied to static loading scenarios. The proposed methodology will be incorporated into a software solver and works by using the material properties that are, in general, provided by engineering material manufacturers. This will enable more efficient designs in comparison with the commonly used HSSM.

Structural components often require notches or keyways that raise the magnitude of the local stresses. Accurately predicting the failure of engineering materials experiencing localised stress concentration phenomena has been the goal of many investigations during the last century, as improved accuracy leads to less unexpected failures and a more efficient usage of natural resources.

The problem of designing components containing stress concentration features against static loading is commonly addressed by adopting the so-called Hot Spot Stress Method (HSSM). This method is generally considered to be an ultra-safe design methodology potentially leading to excessive use of resources, despite this significant safety factors are to be used in conjunction with it. The method is relatively simple to use and takes advantage of FEA by taking the hot-spot stress result from the analysis. The linear-elastic stress produced in this analysis is seen to give results that increase in there conservatism as the sharpness of the stress raising feature increases.

A classic brittle material is considered to be perfectly elastic, that is, the stress-strain curve produced as a sample is loaded to failure is linear. On the other hand some engineering polymers and metallic materials in their plain form will deviate from the linear stress-strain curve prior to failure, displaying some plasticity/ductility. The presence of stress raising features in such materials can change the mechanism by which they fail and can promote brittle like failures [90] even in relatively ductile materials. This phenomenon makes it clear that the problem of designing against static loading is not a trivial one.

Chapter 3 reviewed the state of the art theory, namely the TCD, and it was shown to be successful in assessing engineering components containing stress raising features experiencing static loading. The TCD has been proven to be successful when applied to the uniaxial and multiaxial static fracture cases [70], [86][76], [85], [88], [90] and [100]. On reviewing this literature, two limitations in the applicability of the conventional TCD become apparent. These are

1. When dealing with materials that exhibit under static loading an inherent strength greater than the UTS, this raises the question, when does a notch stop acting like a notch? This situation raises the issue of employing the conventional TCD method as it would result in large non-conservative errors for very blunt notches tending towards plane material conditions.

2. In order to obtain the correct length and strength parameter, the TCD is conventionally calibrated by means of experimental investigations which can be costly and time consuming.

In order to make the TCD more attractive to the design engineers and to allow automation of the TCD to static cases, the method proposed in this chapter aims to eliminate the need for additional experimentally determined parameters. If this is achieved the efficiency of the design process could be considerably increased. Owing to the fact that many engineering materials manufacturers

provide the ultimate tensile strength, σ_{UTS}, and the plane-strain fracture toughness, K_{IC}, by using these values this would eliminate the need for additional testing.

Critical distance theory has been successfully applied to brittle materials using the value of the inherent strength equal to the materials UTS, with a good degree of success [70]. Also Whitney and Nuismer successfully used the UTS in their research on Quasi-Brittle composites [72]. However for ductile materials i.e. materials in their plain form that display signs of plasticity prior to failure, the value of the inherent strength, σ_0, is seen to be larger than the materials σ_{UTS}. It has been shown that using $\sigma_0 = \sigma_{UTS}$ to assess ductile materials does not return accurate results compared to applying the TCD rigorously [87].

4.2. Formed simplifying hypotheses

If the critical distance is calculated using the materials UTS and plane-strain fracture toughness i.e. according to equation (95), independent of the materials level of ductility and the type of static load applied;

$$L_E = \frac{1}{\pi} \left(\frac{K_{IC}}{\sigma_{UTS}} \right)^2 \tag{95}$$

It is trivial to point out that this results in a critical distance being larger than in scenarios where the TCD's inherent strength parameter would be larger than the material UTS.
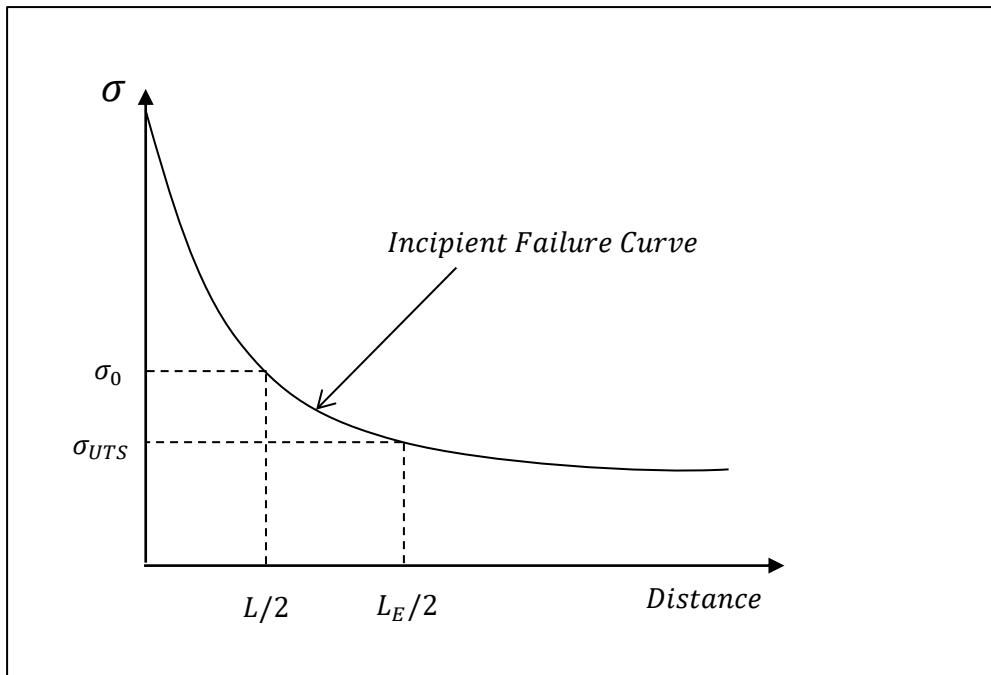
Figure 30: Reference strength and critical distance relationship

If we consider the stress-distance curve shown in *Figure 30*, and recall that the TCD is considered to account for the problem of singular stress and complex non-linear fracture processes which occurs in the presence of stress raising features. This results in the critical distance being larger than that obtained by using the conventional application of the TCD and therefore may not capture the detrimental effects of the stress raising feature, this raises the obvious and unavoidable question, *does the simplified TCD PM still work?* The only way to answer this question is by running an extensive validation investigation which will be detailed after forming the following hypotheses.

Does the TCD PM still work when;

- the critical distance is calculated using the inherent strength equal to the materials σ_{UTS} i.e. the use of equation (95)?

- the focus path is taken as the notch bisector, when Mode I and/or Mode III are applied and for very sharp notches experience any load mode?

- Alternatively for samples containing finite notch root radii and experience mixed Mode I+II the focus path is taken perpendicular to the surface at point where the maximum linear-elastic stress occurs?

4.3. Methodology

A review of technical literature detailing experimental results of static fracture was compiled. The built database was segmented into material type i.e. Brittle, Quasi-Brittle and Ductile as well as the loading Mode i.e. Mode I, Mode II, Mode III, Mixed-Mode I+II and Mixed-Mode I+III. *Table 2* provides a summary of the different materials used in the investigations reported in the literature along with where appropriate the temperature at which the material was tested. Also reported in *Table 2* are the types of loading used to test the samples i.e. three/four point bending tests, Tension Tests, half and full Brazilian disks. The samples all contained a stress concentration feature that can be categorised as internal or external U- or V-Notches, all reanalysed test samples geometry are provided in Annex A.

The range of notch sharpness characterised by the notch root radius is given in *Table 2* along with the critical distances obtained using our simplified hypothesis, i.e. equation (95). Full details of the geometries and experimental details for all the data are provided in Annex A.

The geometry of each sample was modelled in accordance with the assumptions stated in Chapter 1 using commercial FE software ANSYS®. Each model had appropriate boundary conditions applied and with the application of a unit load, the stress results obtained from each model were calculated by assuming that the materials are linear-elastic, isotropic and homogeneous. Each model ran

iteratively with increasing mesh density in the vicinity of the stress concentrator apex until convergence of the stress value occurred at the critical distance i.e. at $L_E/2$, the mesh spacing at which a sufficient accuracy was obtained at a mesh spacing equal to approximately $L_E/20$.

The local effective stress calculated according to the PM and where possible the LM was extracted from along the focus path, under Mode I loading the focus path was taken as the notch bisector which is coincident with the point of maximum stress. When considering samples failing under Mixed-Mode I+II the point of maximum stress is seen to move away from the notch bisector, in this scenario the focus path takes as its staring point the point of maximum stress in the notch root and emanates perpendicular to the surface. Further to the Mixed-Mode I+II, when considering samples with 'sharp' notches, in addition to modelling them with a finite root radius and taking the focus path as just discussed, various data sets were modelled assuming that there is no root radius and in this scenario the focus path once again being taken as the notch bisector.

For all material types the required stress-distance curves were calculated by FEA in terms of Maximum Principal Stress, where under Mode I loading the first principal stress is coincident with the maximum opening stress. Under Mode I+II loading the coordinate system in the FEA was rotated to be coincident with the focus path, this was done to check the directionality of the Maximum Principal Stress and to show that it remained consistent with the maximum opening stress which can be seen in *Figure 31*.
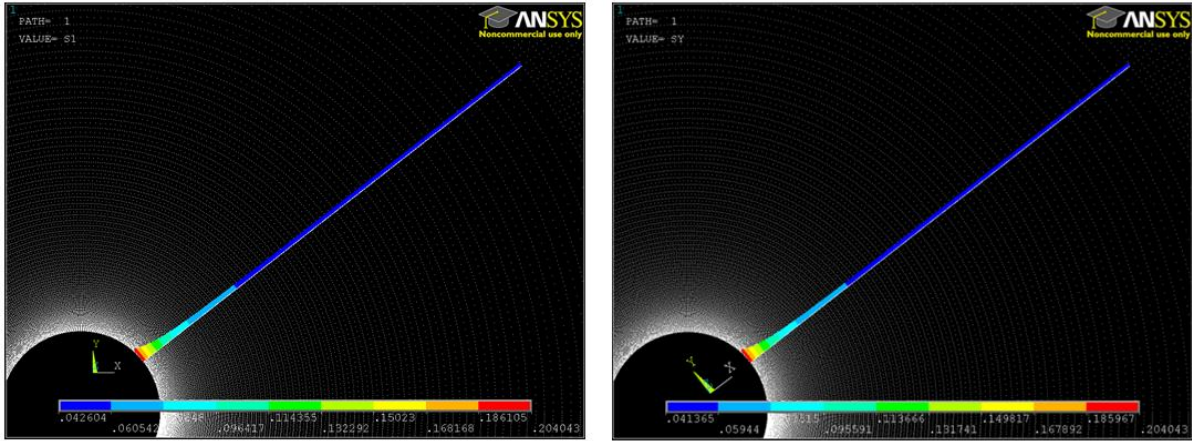
Figure 31: Directionality of Maximum Principal Stress check

In addition to post-processing the Maximum Principal Stress extracted along the focus path, for the metallic materials the Von Mises equivalent stresses were also post-processed according to the TCD PM and where possible the LM.

Finally, the failure predictions were compared with the experimental results by comparing the validation stress obtained according to the TCD PM, LM as well as the HSSM, the error was calculated by;

$$Error(\%) = \frac{\sigma_{Prediction} - \sigma_{UTS}}{\sigma_{UTS}} \cdot 100 \tag{96}$$

Where $\sigma_{Validation}$ is either the Maximum Principal Stress or Von Mises equivalent stress calculated at a distance equal to $L_E/2$, along the focus path according to the TCD PM or averaged over a distance equal to $2L_E$ according to the TCD LM, from the FEA results calculated for the failure stress for each test sample. The resulting error associated with each sample will show if the proposed methodology gives failure predictions falling on the conservative or non-conservative side by assigning either a positive or negative sign respectively.

In order to provide appropriate design safety factors, $SF_{D,i}$, the following safety factor equation provides a safety factor for each data used.

$$SF_i = \frac{\sigma_{UTS}}{\sigma_{Prediction,i}} \tag{97}$$

where i refers to the method and the equivalent stress, i.e. $SF_{PM,MPS}$ is the safety factor obtained by using the TCD PM with the Maximum Principal Stress as the effective stress. Design safety factors will then be calculated by using the mean and standard deviation of the SF_i values. The "engineers rule of thumb" or "three sigma rule" [101], albeit a simplistic statistical assessment it is said that for non-normally distributed data at least 97.7% will fall into three-sigma intervals of the mean value. Therefore the values reported later in this chapter will assume that the values of the safety factor will return at least 97.7% probability of survival.

Table 2: Compiled database of Brittle (B), Quasi-Brittle (QB) and Metallic (M) data

Reference	Material Temperature	Load Modes	Loading Type	K_{IC} (MPa.M^0.5)	σ_{UTS} (MPa)	L_E (mm)	$\Delta\rho$ (mm)
B1 [102]	PMMA -60 ˚C	I+II	TPB	1.7	128.4	0.0558	0.01→4
B2 [103]	PMMA -60 ˚C	I+II	TPB	1.7	128.4	0.0558	0.018→0.072
B3 [104]	PMMA -60 ˚C	I+II	TPB	1.7	128.4	0.0558	0.01→4
B4 [105]	PMMA -60 ˚C	I	TPB/Tension	1.7	128.4	0.0558	0.04→7.07
B5 [106]	PMMA -60 ˚C	III	Torsion	1.7	153.1	0.0392	0.1→7
B6 [107]	Polycrystalline Graphite	I	TPB/HBD/BD	1	27.5	0.4210	1→4
B7 [108]	Soda-Lime Glass	I, I+II, II	BD	0.6	14	0.5847	1→4
B8 [109]	Alumina-7%Zirconia	I	TPB/FPB	8.12*	509*	0.0810	0.031→0.1
B9 [110]	Isostatic Graphite	I, I+II	Tension	1.06	46	0.1690	0.25→4
B10 [111]	Isostatic Graphite	I, I+II	Tension	1.06	46	0.1690	0.25→4
QB1 [112]	PMMA 20 ˚C	I	TPB	1	75	0.0566	0.08
QB2 [113]	PMMA 20 ˚C	I	TPB	1	75	0.0566	0.1→4
QB3 [114]	PMMA 20 ˚C	I, I+II, II	BD	1.96	70.5	0.2460	0.05→0.07
QB4 [115]	PMMA 20 ˚C	I, I+II, II	BD	1.96	70.5	0.2460	1→4
QB5 [116]	PMMA 20 ˚C	I, II	BD	1	75	0.0566	0.5→4
QB6 [76]	PMMA 20 ˚C	I, I+III, III	TT	2.2	67	0.3432	0.2→4
QB7 [117]	PMMA 20 ˚C	I	TPB	2.03	71.95	0.2534	0.1→2.5
QB8 [118]	PMMA 20 ˚C	III	Torsion	1	67	0.0709	0.1→7
QB9 [119]	PMMA 20 ˚C	I, I+II, II	Tension	1.37	115	0.0450	0.10
QB10 [120]	PMMA 20 ˚C	I, I+III, III	Tension	1.72	70	0.0960	→0
M1 [121]	Aluminium Alloy 6061	I	Tension	25	319.8	1.9452	0.012
M2 [122]	High Strength Steel	I	TPB	33	1285	0.2099	0.1→1
M3 [87]	En3B	I	TPB	97.4	638.5	7.4071	0.1→5
M4 [123]	Martensitic Tool Steel	I+II	TPB	6.09	1482	0.0054	0.2→2
M5 [88]	Aluminium Alloy 6082	I, I+III, III	TT	35.8	367	3.0289	0.44→4
M6 [124]	Al-15%SiC	I	TPB	6	230	0.2166	0.5→2
M7 [124]	Ferritic–Pearlitic Steel-40	I	TPB	12.3	502	0.1911	0.5→1.5
TPB = Three Point Bend, FPB = Four Point Bend, BD = Brazilian Disc, HBD = Half Brazilian Disc, TT = Tension Torsion (*) Values determined using the PM							

4.4. Results:

The data sets detailed in *Table 2*,were modelled using Ansys ® FE Software, the stress data obtained was post-processed using three methods. The results are calculated according to the simplified reformulation of the TCD PM where the critical distance is the so called engineering critical distance, L_E, which is calculated according to TCD equation (95), where the critical distance is estimated by using the materials ultimate tensile strength, additionally the TCD LM was used where applicable. To provide comparison to the proposed reformulation, the data were post-processed using the so called HSSM. In each of the following sub-sections respective figures will show the error results for that sub-section with each sub-section containing a table highlighting the critical error and the mean error for each of the three assessments, the critical error being the largest non-conservative prediction error i.e. $E_{Critical}$ (%) $= E_{min}$ (%).

4.4.1. Mode I

Shown in *Figure 32 and Figure 33* are the results obtained by post-processing the linear-elastic stress fields ahead of notches in components experiencing Mode I static loads. *Figure 33* provides a more focused view of the same results shown in *Figure 32.* The solid lines represent the maximum error in each data set whilst the dashed line represents the minimum or critical error. The HSSM is represented by the grey lines, the PM is represented by the red lines and the green lines represent the LM results.

The error results obtained by employing the TCD PM and LM using the engineering critical distance, the stress-distance data was extracted in terms of Maximum Principal Stress extracted along the notch bisector which under Mode I loading is coincident with the crack initiation location.
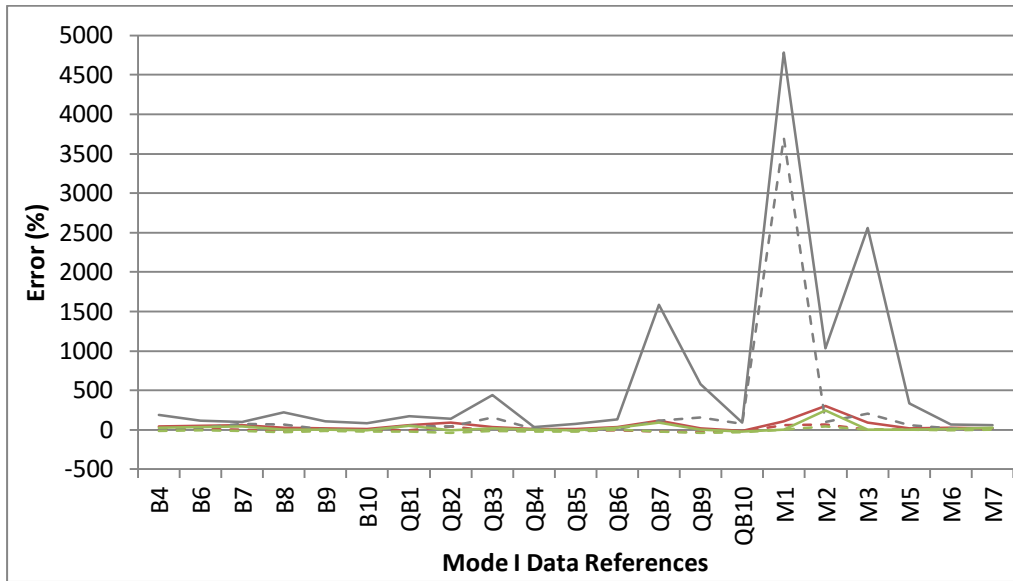
Figure 32: Mode I data (Table 2) and associated maximum (Solid line) and minimum (Dashed line) error results calculated according to the TCD PM (Red) TCD LM (Green) and the HSSM (Grey) using Maximum Principal Stress as effective stress
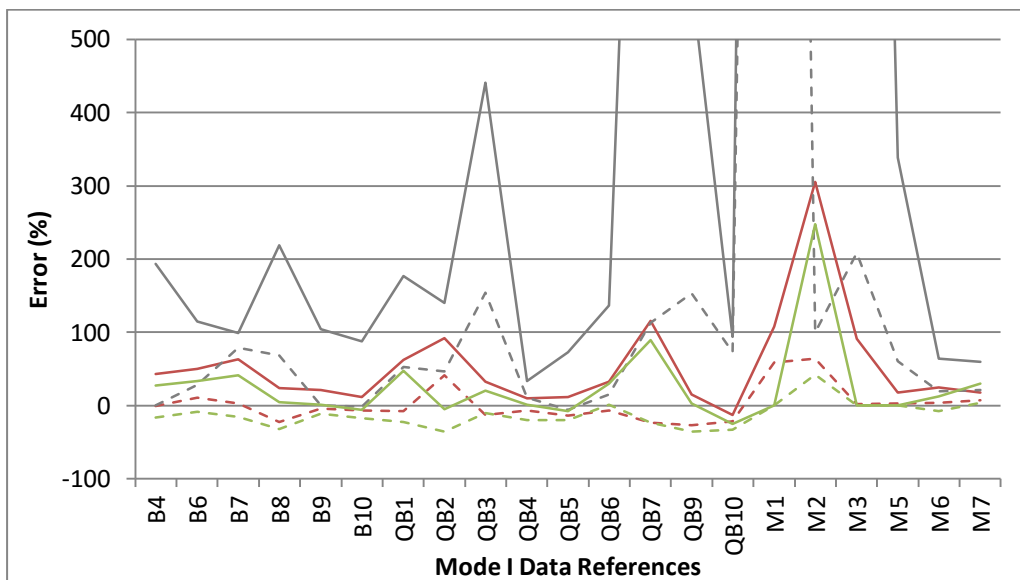
Figure 33: Mode I data (Table 2) and associated maximum (Solid line) and minimum (Dashed line) error results calculated according to the TCD PM (Red) TCD LM (Green) and the HSSM (Grey) using Maximum Principal Stress as effective stress

For sets of data M1, M3 and M5 the TCD LM was not applied as the distance equal to, $2L_E$, was either beyond the physical dimensions or encroached into stress fields resulting from other factors; as a result these data sets are excluded.

The complete error results for the three assessments are shown in Figure 107Figure 110 in Annex B. To conclude the sub-section, the critical and mean error are presented in Table 3, across the Mode I error results, the TCD PM offers a significant increase in accuracy.

Table 3: Mode I Critical and mean error for the PM, LM and HSSM using MPS

	Point Method	Line Method	HSSM
Critical Error, $E_{Critical}$	-26 %	-35 %	-6 %
Mean Error	25 %	2 %	473 %

4.4.2. Mode II

This sub-section will detail the error results obtained by post-processing the stress data for the sets of data which report pure Mode II loading, in terms of the TCD PM the TCD LM and the HSSM. The stress data is extracted from the FEA along the focus path which is taken from the point of maximum stress and projects perpendicular to the surface at that location.

Shown in *Figure 34* are the error results obtained by employing the TCD PM and the TCD LM with the engineering critical distance, under Mode II loading, the focus path was taken from the point of maximum stress in the notch root, and proceeded along a straight line perpendicular to the surface of the point in the notch root.
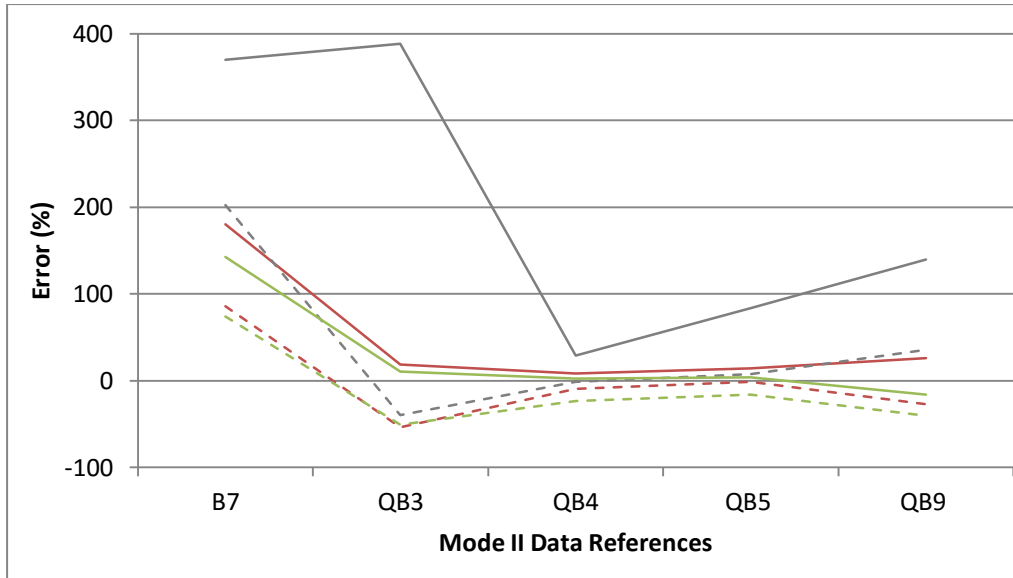
Figure 34: Mode II data (Table 2) and associated maximum (Solid line) and minimum (Dashed line) error results calculated according to the TCD PM (Red) TCD LM (Green) and the HSSM (Grey) using Maximum Principal Stress as effective stress

The complete error results for the three assessments are shown in Figure 111Figure 113. To conclude this Mode II sub-section the data sets were assessed using the HSSM, it can be seen in Table 4: Mode II Critical and mean error for the PM, LM and HSSM using MPS, that the error results for the HSSM exhibit a greater level of scatter and conservatism.

Table 4: Mode II Critical and mean error for the PM, LM and HSSM using MPS

	Point Method	Line Method	HSSM
Critical Error, $E_{Critical}$	-53 %	-51 %	-39 %
Mean Error	25 %	7 %	109 %

4.4.3. Mode III

Detailed in this sub-section are the error results obtained for test samples subjected to Mode III loading, again the error results are calculated using the TCD PM, the TCD LM and the HSSM. The PM and the LM take the focus path as the notch bisector, and the critical distance is calculated according to equation (95).

Shown in *Figure 35* are the results obtained for the test samples experiencing Mode III loading, under Mode III loading the focus path was taken as the notch bisector, the effective stress being the Maximum Principal stress. The complete error results for the three assessments are shown in *Figure 114Figure 116*.
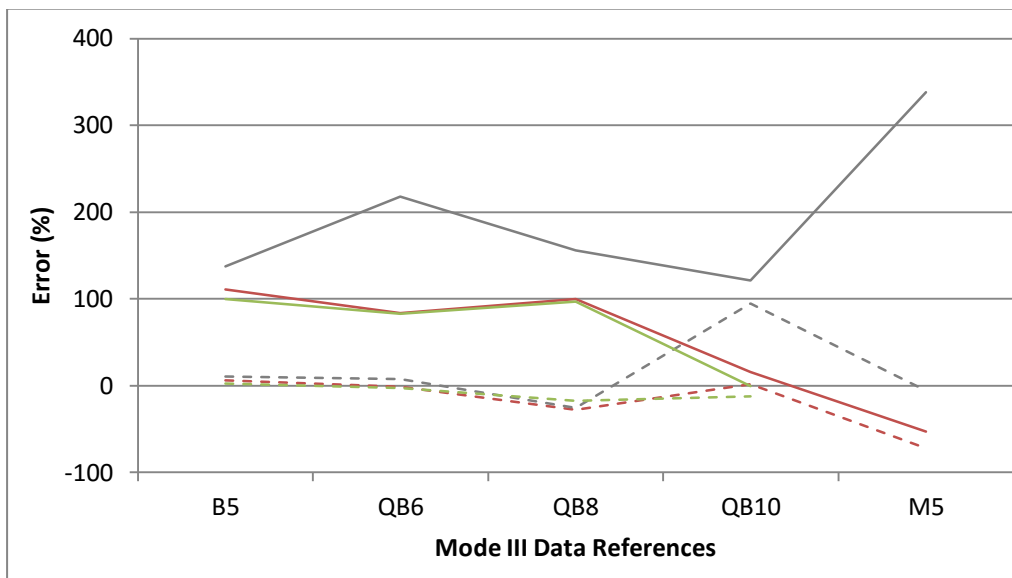
Figure 35: Mode III data (Table 2) associated maximum (Solid line) and minimum (Dashed line) error results calculated according to the TCD PM (Red) TCD LM (Green) and the HSSM (Grey) using Maximum Principal Stress as effective stress

Table 5: Mode III Critical and mean error for the PM, LM and HSSM using MPS

	Point Method	Line Method	HSSM
Critical Error, $E_{Critical}$	-73 %	-13 %	-25 %
Mean Error	23 %	45 %	92 %

4.4.4. Mixed Modes I+II and I+III

This sub-section reports on data sets obtained by testing samples under Mixed-Mode I+II and Mixed-Mode I+III loading conditions. The results obtained by using the proposed reformulations of the TCD PM, the TCD LM and the HSSM are shown in *Figure 36*. Due to the high values returned by the HSSM, *Figure 37* provides a more focused view of the results. In agreement with the previous sub-section error results the predictions made using the TCD PM and LM display considerably less scatter and a greater level of accuracy. The complete error results for the three assessments are shown in *Figure 117-Figure* 120.
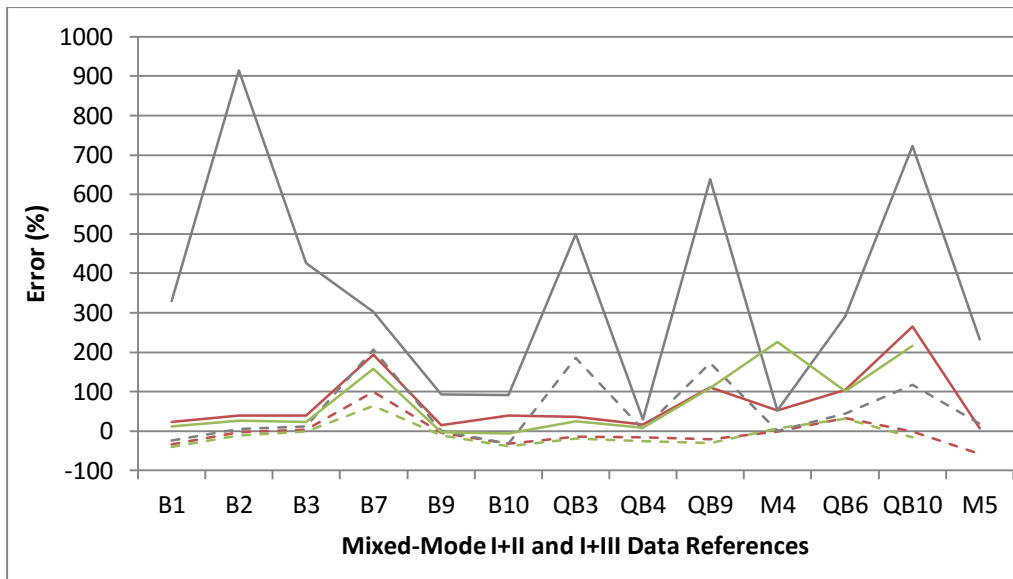
Figure 36: Mixed-Mode I+II and I+III data (Table 2) associated maximum (Solid line) and minimum (Dashed line) error results calculated according to the TCD PM (Red) TCD LM (Green) and the HSSM (Grey) using Maximum Principal Stress as effective stress

Figure 37: Mixed-Mode I+II and I+III data (Table 2) associated maximum (Solid line) and minimum (Dashed line) error results calculated according to the TCD PM (Red) TCD LM (Green) and the HSSM (Grey) using Maximum Principal Stress as effective stress

Table 6: Mixed-Mode I+II and I+III Critical and mean error for the PM, LM and HSSM using MPS

	Point Method	Line Method	HSSM
Critical Error, $E_{Critical}$	-57 %	-40 %	-24 %
Mean Error	27 %	27 %	164 %

4.4.5. Metallic samples Maximum Principal Stress and Von Mises equivalent stress

It can be seen from the figures of the previous sub-sections that there is a noticeable increase in scatter and level of conservatism for some of the metallic data sets assessed using the Maximum Principal Stress as the effective stress. The TCD has been proven to be successful in estimating the static strength of notched components made of metallic materials [88] by using the Von Mises effective stress in conjunction with the critical distance and inherent strength being determined experimentally. Additionally it was suggested in [87] that it would be interesting to see how well the TCD performs when applied using Von Mises equivalent stress, it was therefore decided to assess the metallic data sets using Von Mises equivalent stress.
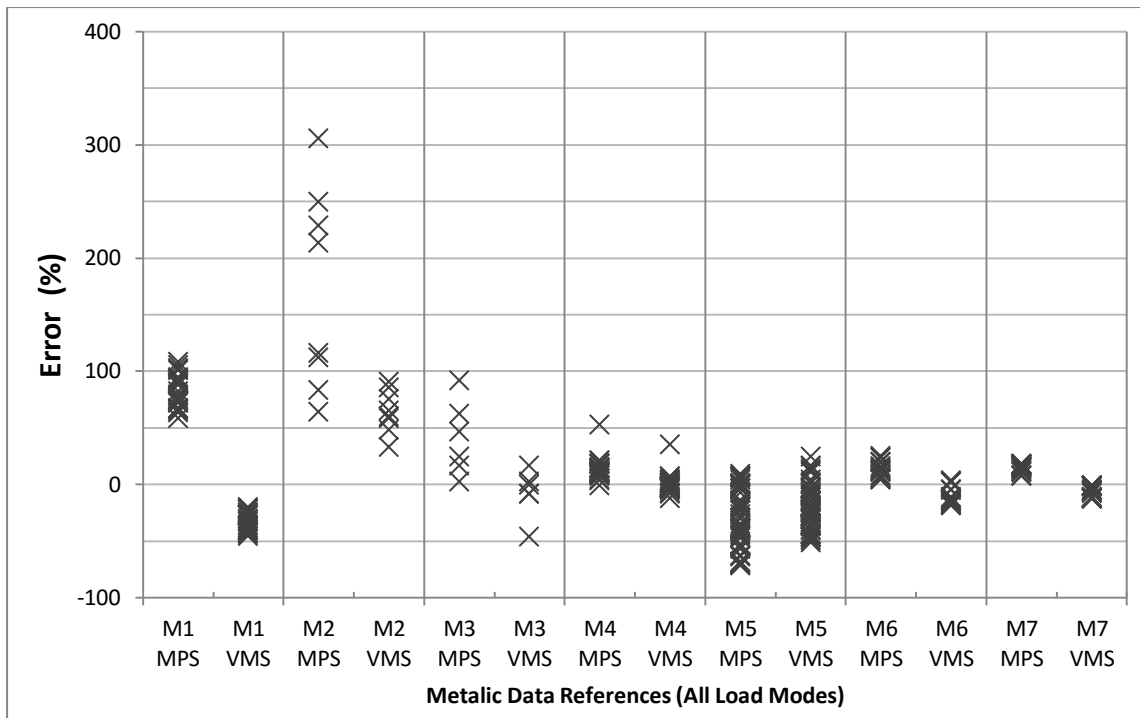
Figure 38: Metallic data (Table 2) and associated error using the TCD PM MPS (X) and VMS (+)

The error results shown in *Figure 38* were calculated in accordance with the proposed application of the TCD PM in terms of both Maximum Principal Stress and Von Mises Stress. The error results obtained by Von Mises Stress offer a reduction in the level of scatter but an increase in the level of non-conservatism except for data set M5. The complete error results for the three assessments are shown in *Figure 121Figure* 124.

The errors for the metallic samples are shown in Table 7, each of the methods being applied in terms of MPS and VMS. As previously reported, the LM was unable to be applied to all metallic data, and further suitable experimental data is required to properly validate the use of the TCD LM.

Table 7: Metallic data, Critical and mean error for the PM, LM and HSSM using MPS and VMS

	Point Method	Line Method	HSSM
	MPS (VMS)	MPS (VMS)	MPS (VMS)
Critical Error, $E_{Critical}$	-72 % (-51 %)	-7 % (-13 %)	-0 % (-11%)
Mean Error	19 % (-12 %)	22 % (8 %)	1067 % (906 %)

4.5. Discussion:

Across a variety of materials that exhibit different failure characteristics which are influenced by temperature, loading and geometrical features, the proposed methodology based on a reformulation of the TCD has returned some positive results.

Table 8: Summary of Error results

Design Methodology	Error (%)								
	Brittle Materials			Quasi-Brittle Materials			Metallic Materials		
	E_{max}	E_{min}	E_a	E_{max}	E_{min}	E_a	E_{max}	E_{min}	E_a
PM MPS	193	-33	32	116	-53	18	116	-78	2
PM VMS	-	-	-	-	-	-	91	-62	-15
HSSM MPS	915	-33	111	1588	-39	171	4329	-6	488
HSSM VMS	-	-	-	-	-	-	3699	-11	441

Where, E_{max}= Maximum error: E_{min} = Minimum error/Critical error: E_a = Average error

The results obtained for the Mode I loaded data sets by post-processing the linear elastic Maximum Principal Stress offered good predictions independent of geometry and the materials level of ductility.

The previous section reported the error results used to assess the validity of the proposed methodology, before looking at the overall validity of the method and determining appropriate safety factors, the set of data M5 [88] should be discussed. The data presented in the previous sub-sections regarding the data set M5 this data set could be highlighting a limitation of the proposed method, that is, when the critical distance is comparable to the major dimensions of the sample being assessed. It can be seen in the error results of *Figure 39,* the data is organised so that for Mode I, there are three results for each like sample which are characterised by four different notch root radii, each set starts from the sharpest to bluntest root radii.
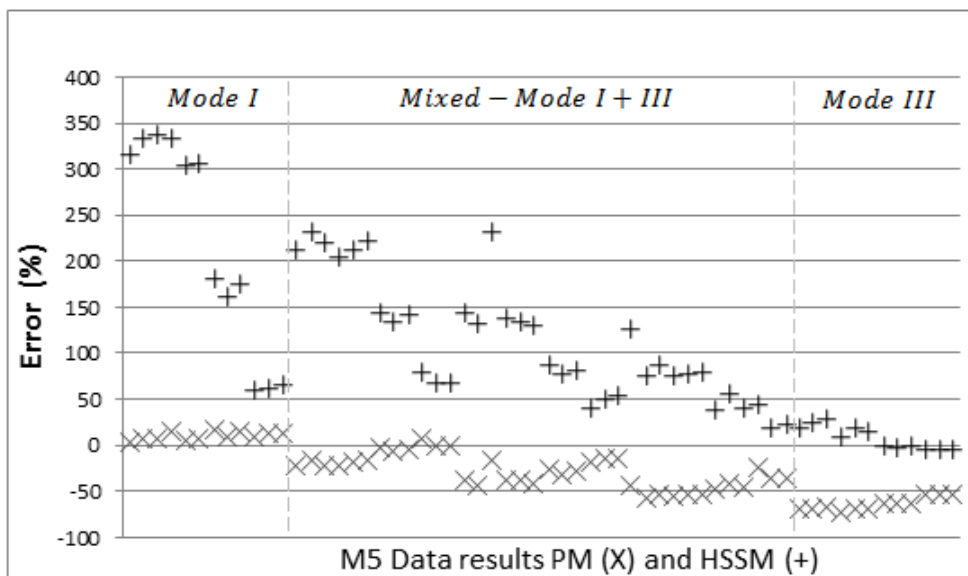
Figure 39: Error results for data set M5 from left to right, Mode I – Mixed-Mode I+III – Mode III

For each of the Mode mixity ratios shown in *Figure 39,* the level of conservatism obtained can be related to notch sharpness under Mode I loading whereas the notch sharpness appears to have less effect on the level of conservatism. The incipient failure curves for set of data characterised by

having notch root radii equal to 0.44mm are shown in *Figure 40*, the two critical distances being

calculated using equation (95) and values for K_{IC} taken from Table 4 of [88].
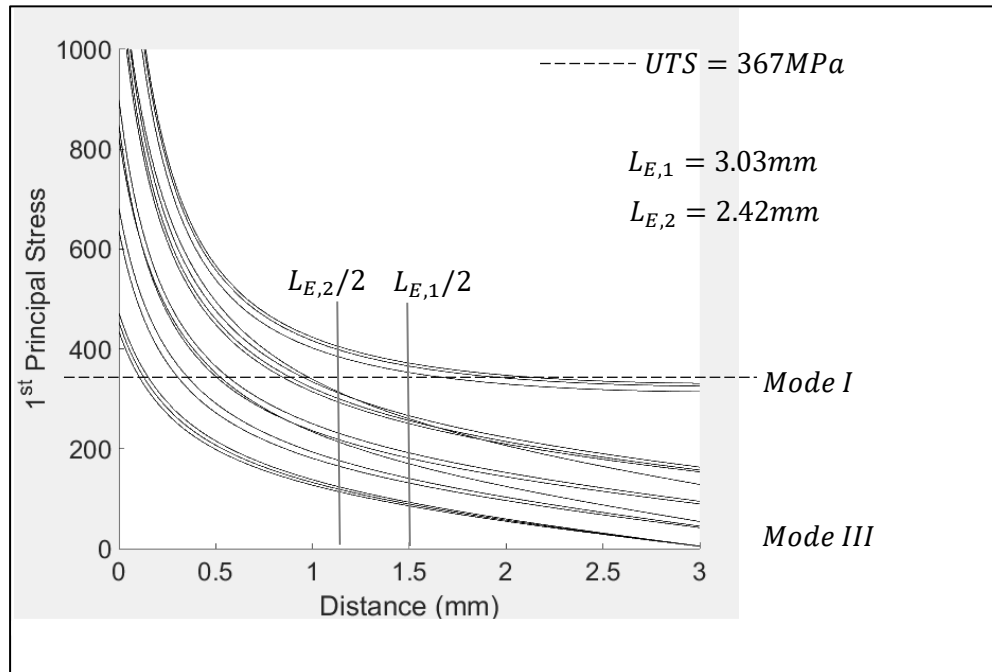
Figure 40: Incipient failure curves of data set M5 (ρ_n=0.44mm)

In *Figure 40*, the effect of the notch on the stress-distance curve is seen, under Mode I loading, to

dissipate before reaching $L_{E,1}/2$. Consider the two loading cases shown in *Figure 41*, it is trivial to

point out that under these two loading scenarios, if the samples were un-notched, the linear-elastic

stress profile would be zero at the centroid or neutral axis. The increasing level of non-conservatism

as mode mixity increases, shown in *Figure 39,* could be attributed to the fact that the critical

distance is comparable to the specimens overall dimensions. Further experimental investigations are

required to determine the validity of applying the propose methodology to ductile metals such as

mild steel and aluminium alloys. An experimental program using the technique described in [120]

but for a mild steel and/or aluminium alloy would provide greater certainty in the success of the

proposed method.

In the scenario where the elastic-stress profile passes through zero, such as those shown in *Figure 41*, the value of half the engineering critical distance i.e. calculated using equation (95), the value should be less than 1/3 the distance from the notch tip to the neutral axis as such the following condition must be satisfied:

$$\frac{L_E}{2} \leq \frac{1}{3}\bar{y} \tag{98}$$
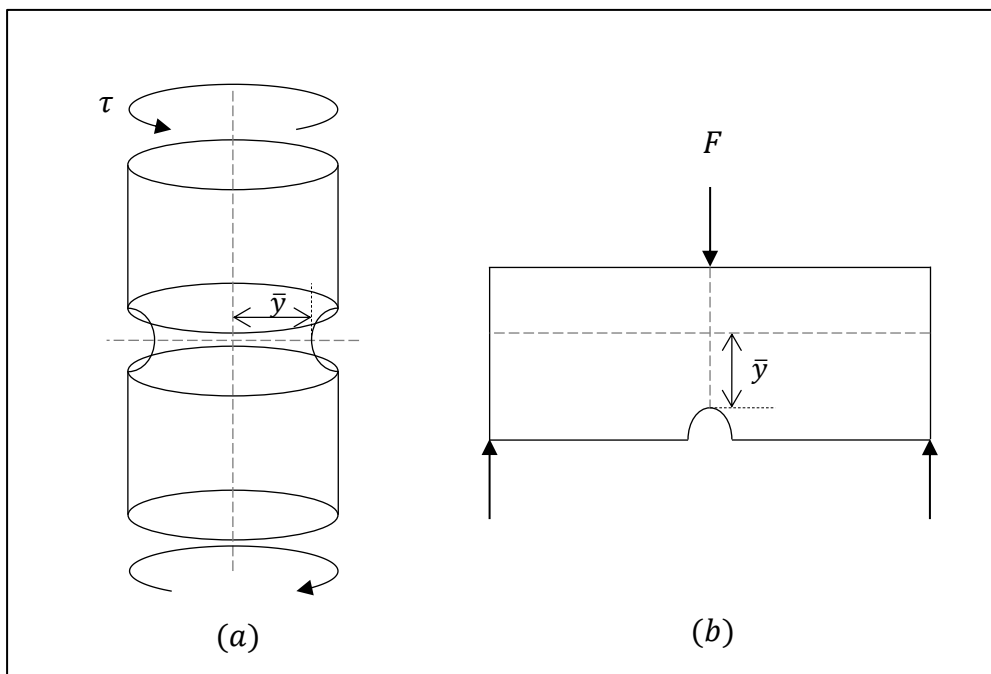
Figure 41: Limiting load cases, Torsion on a round bar (a) Bending load on a beam (b)

When assessing sharp V-notched test samples that typically have less than 0.1mm notch root radius, it can be impractical to model the finite root radii, instead the samples are modelled with no notch root radii. Set of data QB9 [119] reported the samples to have notch root radii less than 0.1mm, the

samples loaded in Mode I, Mixed-Mode I+II and Mode II. The error results shown in *Figure 42,* markers (X) indicate PM errors for the samples modelled with a notch root radius equal to 0.1mm, obtained by post-processing the MPS values extracted along the focus path which emanate perpendicular to the point on the surface where the maximum stress occurred, on the other hand, markers (+) indicate PM error for the same samples but modelled with no notch root radius, in this case the focus path being taken as the notch bisectors for all loading modes. The two sets of error results shown that in the presence of sharp notches i.e. notch root radii less than 0.1mm, samples can be modelled without explicitly modelling the exact geometry without significant loss of accuracy.
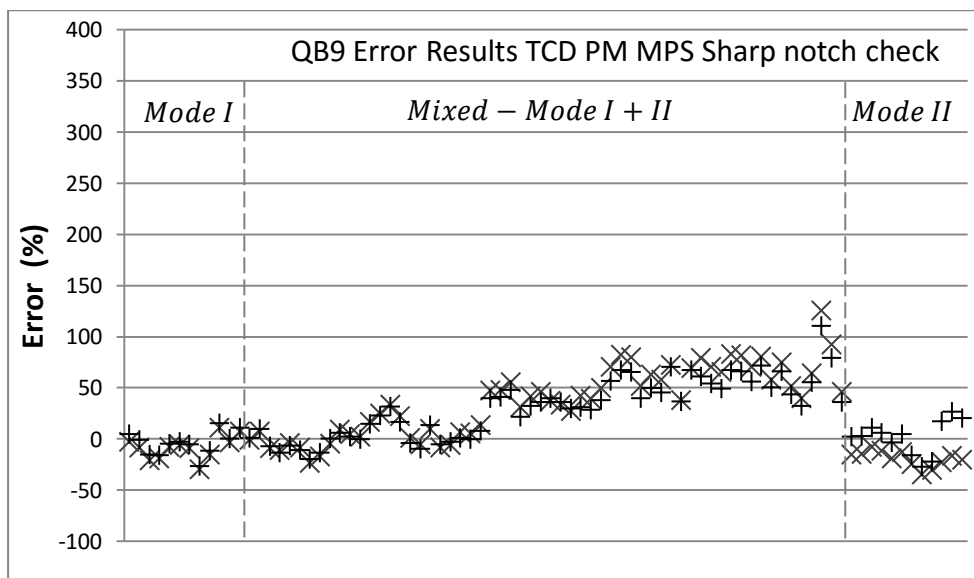
Figure 42: QB9 Error results, Sharp notch check

Shown in *Figure 43*, are the critical and mean errors for all the data sets, (b) and (d) are close-ups of (a) and (c) respectively. Having reviewed the overall accuracy of the TCD's predictions when used in conjunction with equation (95) i.e. using the simplified method of calculating the materials critical distance. The results have shown that the proposed method offers a considerable improvement in terms of the accuracy compared to the error results obtained by using the HSSM.
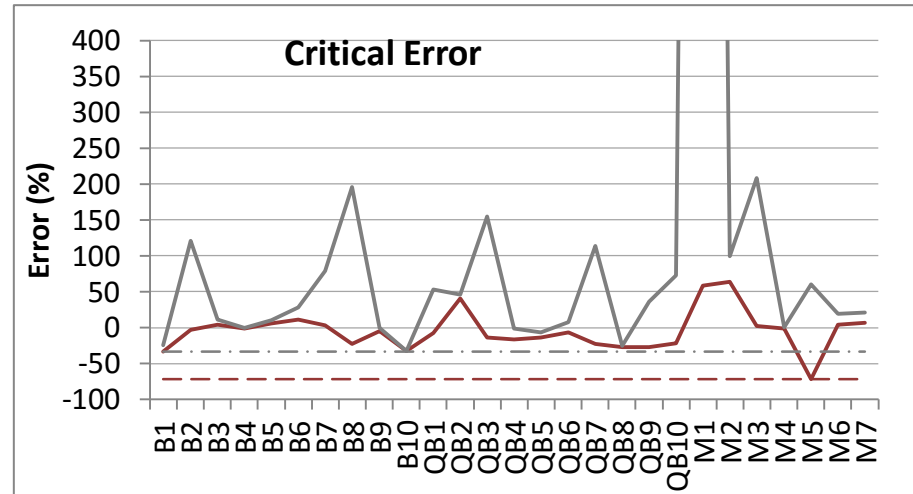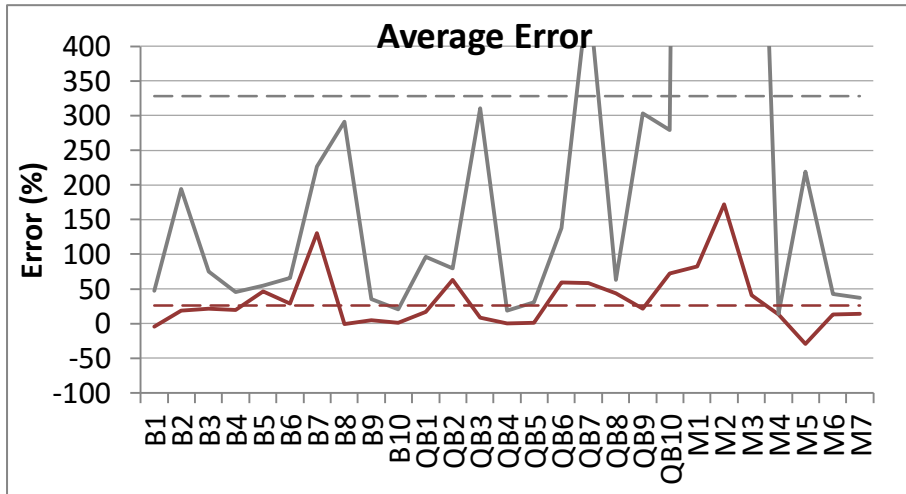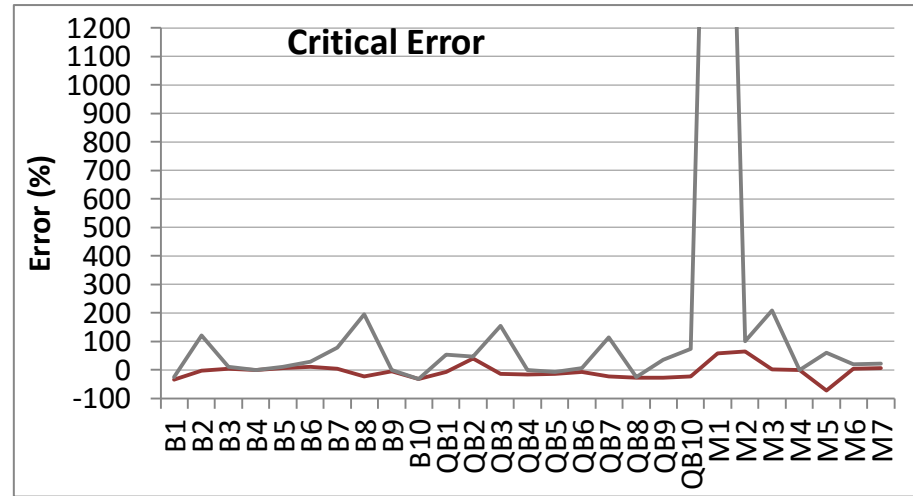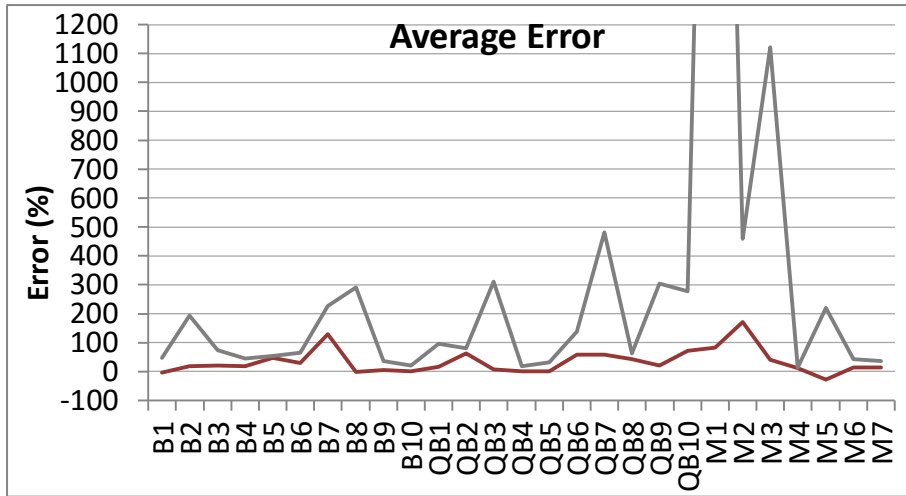
Figure 43: Average Errors (a) and (b) Critical Errors (c) and (d), red line PM and grey line HSSM.

It can be seen from the error plots, independent of loading and geometry, that when assessing notched components made from brittle and quasi-brittle materials the highest level of accuracy was achieved by using the MPS as effective stress. On the other hand, when assessing notched components made of metallic materials the greatest level of accuracy was achieved by using VonMises equivalent stress. Therefor the recommended design safety factors have been determined using MPS for the brittle and quasi-brittle materials and VMS for the metallic materials.

Due to the fact that it was not possible to apply the LM to all the metallic data, the LM will not be included in determining appropriate design safety factors, instead design safety factors will be determined using the PM and the HSSM only.

Table 9: Recommended Design Safety Factors Values

Design Methodology	Design Safety Factor, DS_F					
	Brittle and Quasi-Brittle Materials			**Metallic Materials**		
	Mean	Standard Deviation	P=97.7%	Mean	Standard Deviation	P=97.7%
PM MPS	0.9	0.2	1.5	-	-	-
PM VMS	-	-	-	1.2	0.3	2.1
HSSM MPS	0.6	0.3	1.4	-	-	-
HSSM VMS	-	-	-	0.6	0.3	1.6

The safety factors calculated using equation (97) are reported in Table 9 and shown in *Figure 44* and *Figure 45.* The calculated safety factors are plotted against the ratio of each samples notch root radius to the materials critical distance, this dimensionless abscissa plot provides assessment that is independent of the materials sensitivity to stress concentrators and the stress concentration feature itself which is considered to be effected largely due the sharpness of the notch root radius.
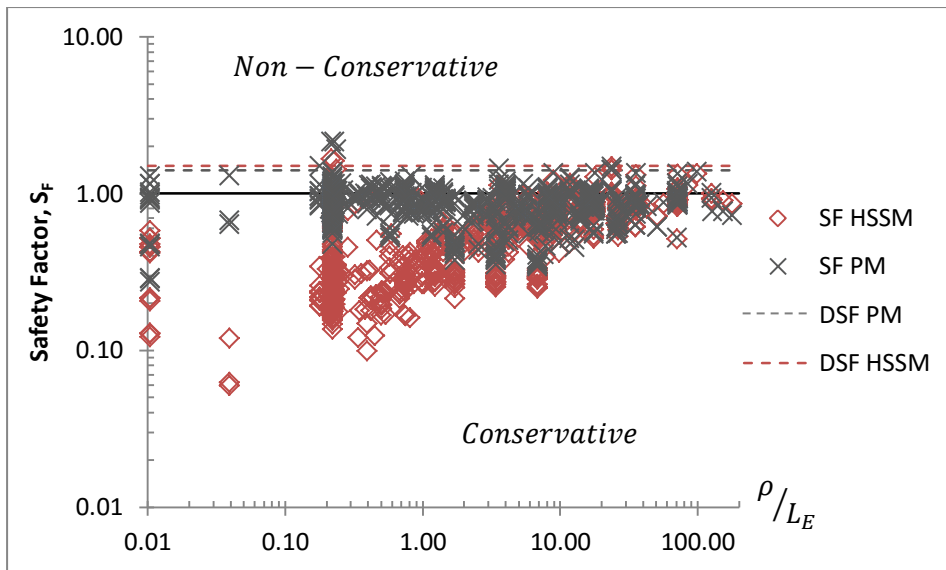
Figure 44: Brittle and Quasi-Brittle materials, Safety Factors and recommended Design Safety Factors
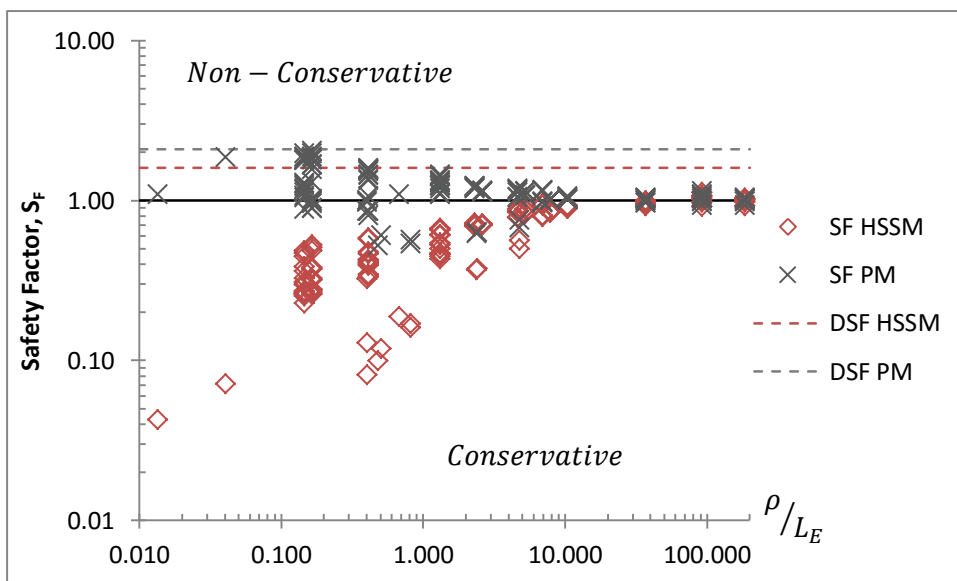
Figure 45: Metallic materials, Safety Factors and recommended Design Safety Factors

A final point should be made regarding the level of conservatism incurred by adopting the proposed methodology, that is, the engineering values that are provided by engineering materials

manufacturers are generally given as minimum whereas the values reported in technical literature are commonly given as an average. Thus by using the manufacturers values, predictions should increase in the level of conservatism, from a design engineers point of view this should achieve an additional level of safety in their design.

4.6.Conclusions:

- The reformulation of TCD equation proposed has been validated using 1744 test data taken from technical literature.

- In comparison to the conventional HSSM the simplified TCD PM predicted failures with an average error was less than 30% compare to the HSSM which had an average error greater than 300%.

- The simplified TCD PM offers an efficient methodology suitable for designing components to resist static loading by post-processing the stress data obtained by linear –elastic FEA, this holding true independent of the components materials mechanical characteristics.

- The reformulation is capable of assessing both notched and un-notched engineering components.

- A geometric check is provided for situations where the loading creates a neutral axis.

- In practical scenarios, the design of components made from Brittle or Quasi-Brittle materials is recommended to use the simplified TCD PM in conjunction with the Maximum Principal Stress and by adopting a design safety factor greater than 1.5.

- The design of metallic samples is recommended as using the simplified TCD PM along with VonMises Stress and by adopting a design safety factor of at least 2.1.

- Additional experimental results are required to further investigate the mechanical behaviour of notched metallic materials under uniaxial and multiaxial loading.

5. Can the linear-elastic TCD accurately estimate high-cycle fatigue failures of notched metallic components at elevated temperatures?

This chapter is based on an industrial investigation to determine the elevated temperature critical distance in the HCF regime of notched alloy components as well as our published paper titled: *The linear-elastic Theory of Critical Distances to estimate high-cycle fatigue strength of the notched metallic materials at elevated temperatures* by R. Louks and L. Susmel.

5.1.Introduction:

This chapter provides details of investigations into the use of the TCD in high-cycle notch fatigue at elevated temperatures. The study of notch fatigue at elevated temperature is highly complex, the aim of this chapter is to investigate whether the relatively simple linear-elastic TCD is successful in estimating high-cycle fatigue strength of notched metallic materials at elevated temperatures where the length scale parameter is treated as a material property whose value is independent of geometry i.e. independent of notch sharpness. We consider two types of material for the experimental investigation, one that is characterised by not having conventional fatigue (endurance) limit and one that does, the materials being A319-T7 and C45 respectively. To check the accuracy of the linear-elastic TCD in estimating high-cycle fatigue strength of notched metals at elevated temperatures, plain and notched samples of Alloy A319-T7 and structural steel C45 (similar to SAE 1045) were tested in the Lea Laboratory, a materials testing laboratory at the University of Sheffield.

Additionally to further validate the use of the TCD in situations of elevated temperature further data was taken from technical literature.

Examination of the state of the art suggests that the fatigue behaviour of metallic materials at elevated temperatures has been investigated mainly considering high-performance alloys. This is a consequence of the fact that the superalloy materials have superior mechanical properties are obviously used in those extreme situations involving time variable loading and elevated temperatures e.g. the blades of jet engines and turbines. The study of notch fatigue at elevated temperatures has unsurprisingly focused on the engineered superalloys which have been designed specifically to work in extreme conditions, however, there are situations of practical interest where conventional structural/mechanical steels also experience medium/high temperatures during in-service operations, such as the metallic parts of vehicle engines and engine beds.

It has been recently reported in [125] that the high-temperature notch fatigue problems have generally been investigated by mainly considering the low- to medium-cycle fatigue regime. Contrary to this, much less attention has been given to formalising and validating an appropriate design method suitable for designing against high-cycle fatigue damage in notched metallic components experiencing in-service elevated temperatures. In this context, towards the end of the last century, Nisitani and co-workers [38][126] have shown that the high-cycle fatigue strength of notched specimens of Inconel 718 experiencing elevated temperatures could be successfully estimated using conventional linear-elastic notch mechanics, the small scale yielding conditions being satisfied for this specific material also at 300, 500 and 600 °C. By performing an accurate experimental investigation, Shi et al.[127] observed that the fatigue strength at 850°C of notched DZ125 decreases as the linear-elastic stress concentration factor, K_t, increases, additionally the K_t factor was also seen to affect the ratcheting behaviour of this directionally solidified superalloy. The authors of [125][128][129][130] have investigated the fatigue characteristics of 40CrMoV13.9 as well as of a copper–cobalt–beryllium (Cu-Be) alloys, by testing plain and notched samples of these

materials the authors have proven that, for each material, the strain energy density parameter is capable of summarising in the same scatter band as the experimental results generated at the different test temperatures.

It has been shown through Chapter 3 and 4 that the room temperature notch fatigue problem can be solved by the use of the TCD, the TCD is a highly capable group of methodologies, providing a reliable engineering tool which allows notched components to be accurately designed against medium/high-cycle fatigue with most prediction errors falling in an error interval of $\pm 20\%$ which is comparable to the original data scatter bands, such a high level of accuracy is seen to be achieved independent of geometry and loading i.e. under multiaxial as well as uniaxial load signals. To briefly recall, the TCD's modus operandi, notch fatigue strength is estimated using an effective stress whose definition depends on a material critical length, the stress analysis being performed by adopting a simple linear-elastic constitutive law. According to the most general formulation of the TCD, such a theory makes use of a length scale parameter that is treated as a material property, that is, its value is assumed not to vary as the sharpness of the assessed notch changes.

Returning to the issue of high-temperature notch fatigue, in a recent paper by Yang et al. [97] they investigated the accuracy of the TCD in estimating fatigue damage in notched specimens of directionally solidified superalloy DZ125 tested, at 850°C, by axial fatigue loading. To assess their data, they applied the TCD by considering the linear-elastic [71][74] as well as the elasto-plastic [83] formalisation of this theory, the authors post-processed their experimental results, keeping to the *modus operandi* of the particular re-interpretation of the above strategies, they conclude that, for the tested material, the critical distance value was somehow affected by the notch sharpness. In a recent investigation by Leidermark et al. [131], it was shown that the critical plane method applied along with the critical distance method was successfully used to estimate lifetime of notched single-crystal superalloy MD2 experiencing uniaxial fatigue loading at 500°C.

5.2. Methodology:

5.2.1. Experimental Details

The following sections of this chapter will provide full details of the two experimental investigations, these experimental programs being designed to determine the validity of the linear-elastic form of the TCD in elevated temperature environments and the corresponding critical distance values.

5.2.1.1. Set 1. A319-T7

The first investigation was sponsored by the industrial partner Safe Technology ltd and a third party company wanting to re-evaluate their materials sensitivity to the presence of notches when experiencing in service constant amplitude medium/high-cycle fatigue loading at elevated temperature. The material is aluminium A319-T7, test specimens were extracted from larger cast sections, from which 30 specimens were machined.

- 10 Plain un-notched samples
- 10 U-notched samples, with $K_t = 3.8$
- 10 V-notched samples, with $K_t = 18.3$

The geometries of the samples machined at the University of Sheffield workshop are shown in *Figure 46*. The in-service temperature suggested by the third party was $150°C$, they provided reference material properties to design the experiments and they were: $\sigma_{UTS} = 230\ MPa$, $E = 69200\ MPa$, $\nu = 0.32$, $\Delta\sigma_0 = 200\ MPa$ @ $N_{Ref} = 10^7$ cycles to failure under $R = -1$.

5.2.1.2. Set 2. C45

The second investigation was designed to investigate if at elevated temperature the TCD could accurately predict in the presence of stress raising feature the fatigue life of components made of C45 steel. As to the expected mechanical behaviour at high- temperature of structural steel C45, by

testing under fatigue loading specimens of SAE 1045, Christ et al. [132] have observed that, given

the amplitude and mean stress of the loading cycle, fatigue damage reaches its maximum value at a

temperature in the range 200–250 °C. It was reported that beyond this temperature range the

material displayed dynamic strain aging and returned a greater fatigue life. These reasons being the

motivation behind the choice of testing commercial structural steel C45 at 250 °C.

The chosen design of samples are shown in *Figure 46*, the samples were machined by a local

engineering company, who produced:

- 10 Plain un-notched samples

- 10 Blunt U-notched samples, with $K_t = 6.9$

- 10 Sharp U-notched samples, with $K_t = 10.0$

- 10 V-notched samples, with $K_t = 26.5$

The net stress concentration factors were obtained via FE analysis. The samples were measured
using a high resolution camera in conjunction with measuring software calibrated using a graticule.
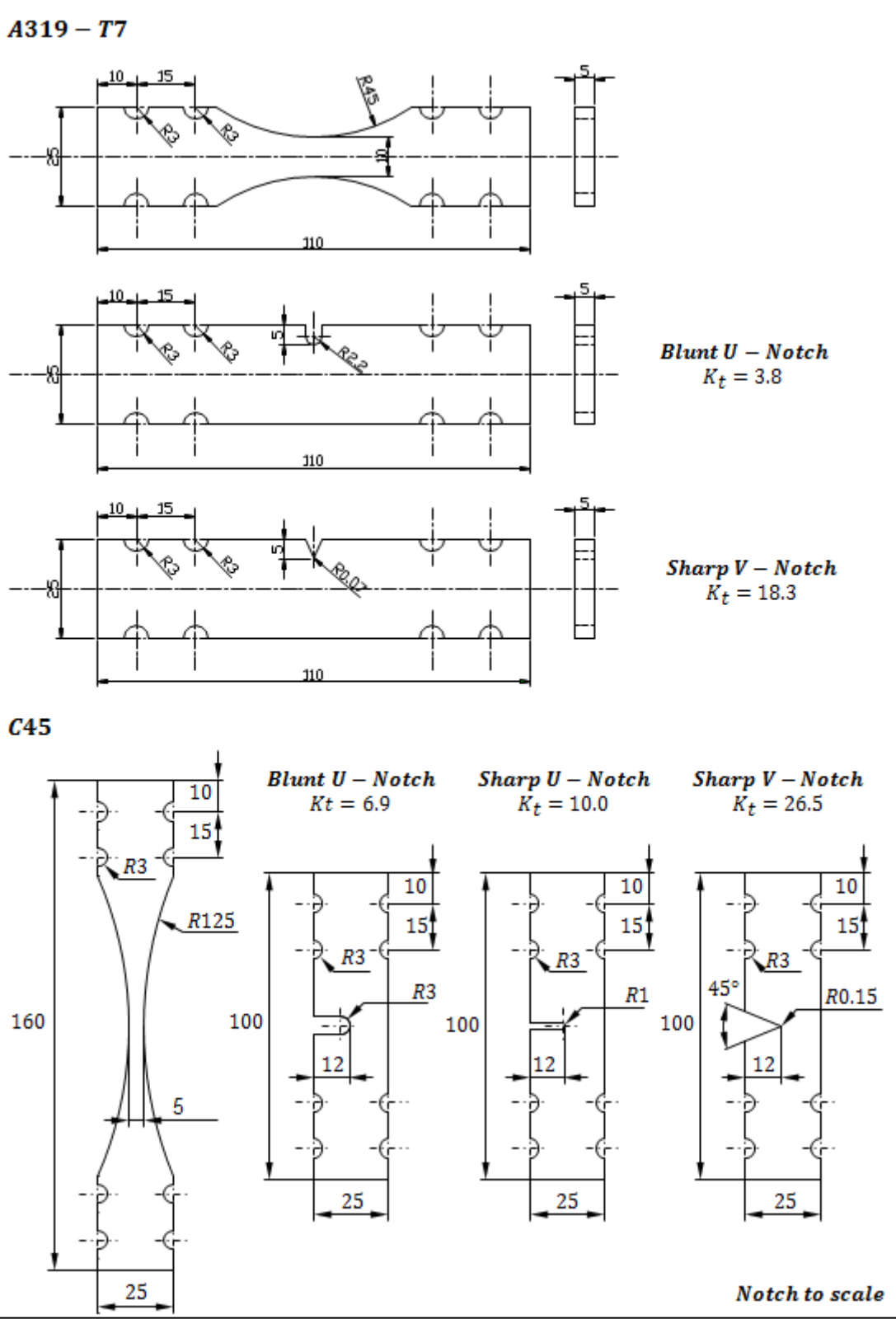
Figure 46: Elevated temperature test specimens

5.2.2. Equipment for testing

The testing apparatus used for the fatigue testing of each material is largely the same but due to the higher testing temperature of the steel a higher operating temperature furnace was used shown in *Figure 47* and *Figure 48*. Fatigue tests were performed using a servo-hydraulic $100kN$ Mayes fatigue testing machine which was controlled by a Kelsey Instruments K7500 controller.

During set-up and testing of the A319-T7 the furnace was kept at a constant temperature equal to $150°C$ this being controlled by an external controller connected to a number of thermocouples positioned inside the furnace.
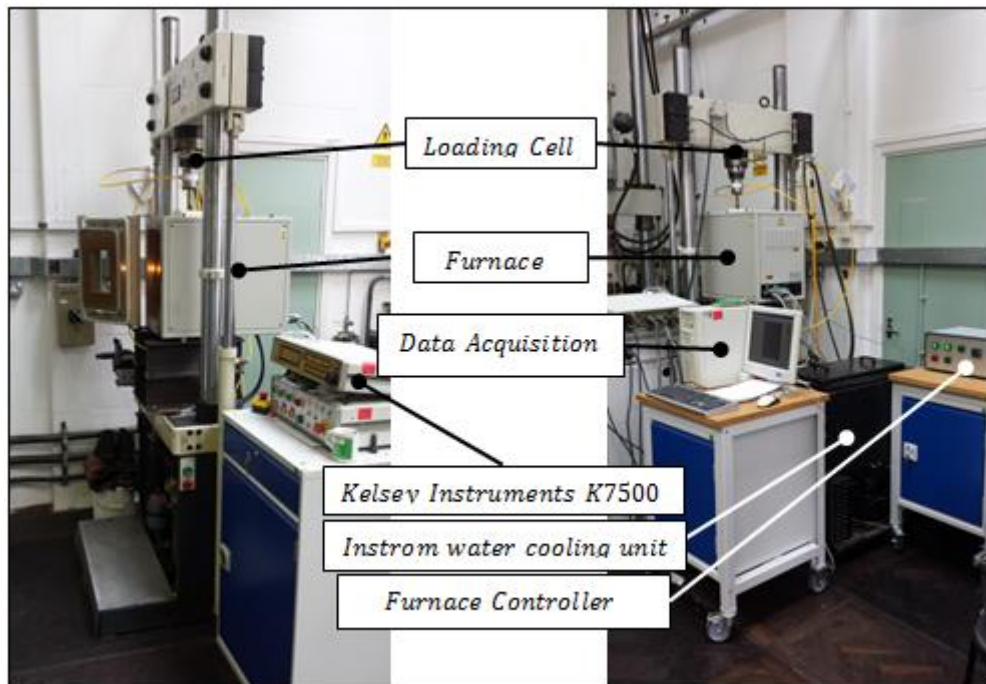
Figure 47: Experimental Apparatus

The loading cell was calibrated and certified at room temperature. Load cells are sensitive to temperature, in order to maintain the magnitude of the applied loads during high temperature fatigue testing the load cell was positioned outside of the furnace. However, simply locating the loading cell outside the furnace would not be sufficient since some tests could run for up to 7 days,

123

and therefore providing sufficient time for heat to transfer through the metal fixtures and fittings to the load cell. To overcome this problem an ad-hoc cooling system was designed, shown in *Figure 48*. The cooling system is made from high grade peak plastic, into which a water channel was machined, the channel was designed to circumvent the securing bolts, maximising the heat removal effectiveness. The water was then subsequently cooled by an external water cooling device. This ad-hoc cooling system was also fitted between the lower grip assembly and the actuator to prevent overheating of the hydraulic oil.
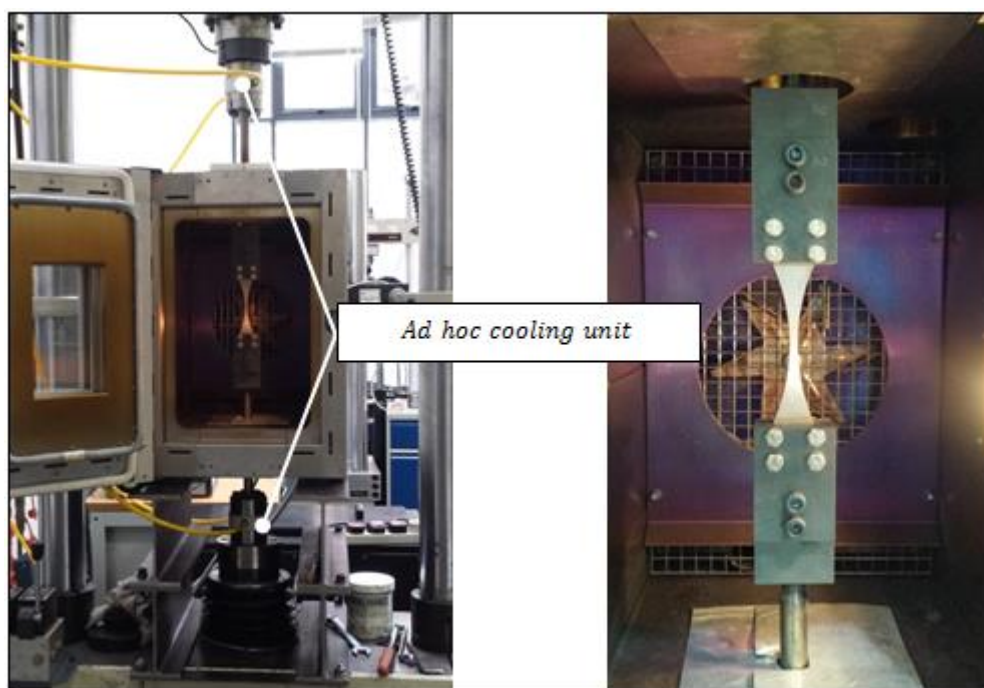
Figure 48: Cooling system and Clamped plain sample of C45

The mechanical grips shown in *Figure 49* and associated fixings were designed to ensure loads were correctly applied. The samples were held in place using A2 stainless M6 bolts with 30mm plain shanks, additionally NordLock® locking washers were fitted to ensured samples remained clamped throughout the test period.
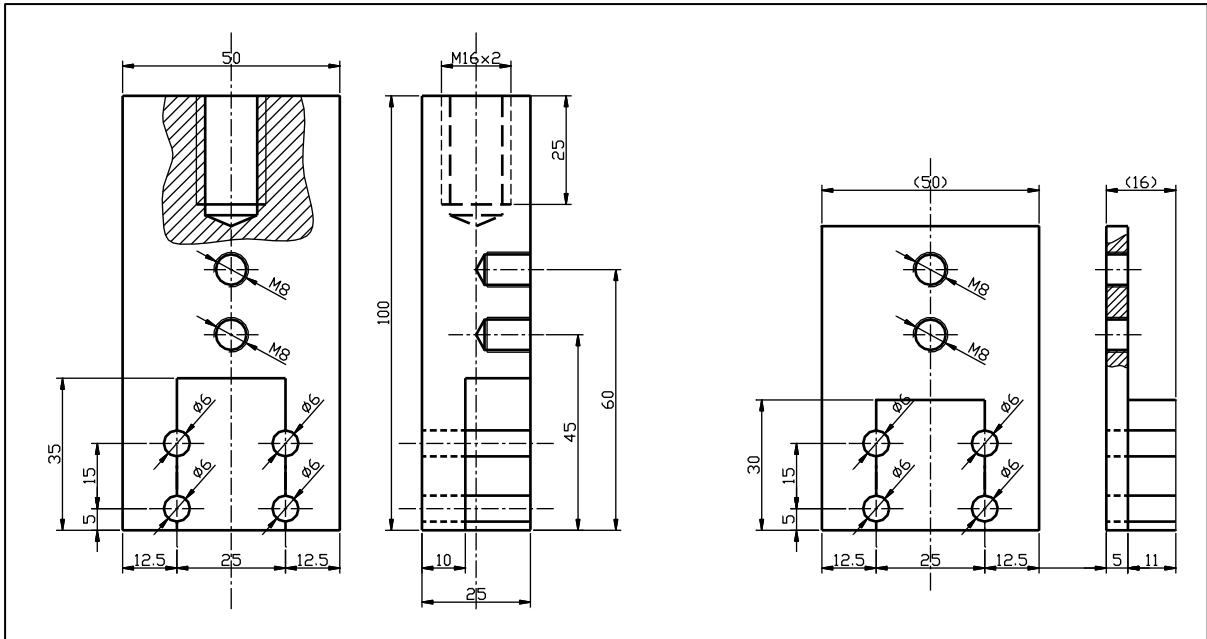
Figure 49: Mechanical Grips

5.2.3. Testing Procedure

The fatigue tests were performed according to the following experimental protocol:

- Fatigue samples were clamped in position by means of purpose built grip assembly as shown in *Figure 49*.

- With the machine in load control, so not to cause compression from thermal expansion, the furnace is set to $150°C$ and $250°C$ for the A319-T7 and the C45 respectively.

- Once the furnace had reached the set temperature, the samples were left for 30 minutes as to ensure all the thermal dilations had equalised.

- The furnace was then opened and with haste the clamping bolts were tightened to compensate for possible thermal dilations. The furnace was then left for a further 30 minutes to ensure the tested material was at the correct temperature.

- Fatigue tests were performed, using a standard sign wave function, under load ratio $R = 0.5$ and $R = 0.1$ for the A319-T7 and the C45 respectively, all at a frequency of $15 Hz$.

- Cycles to failure were recorded when complete fracture occurred.

During the set-up, temperature equalisation phase, there was no evidence of creep/relaxation phenomena.

5.3. Results and discussions:

The experimental results generated by testing each set of samples sketched in *Figure 46*, in accordance with the test protocol previously described, are provided in full in appendix B.

The first set of results obtained by testing samples of A319-T7 are plotted in *Figure 50, Figure* 51 *and Figure* 52*,* for the plain, U-notched and V-notched samples respectively, in each of these figures the Ps=50% is shown with the associated scatter bands equal to Ps=10% and Ps=90% which were calculated according to the statistical evaluation detailed in section 2.2.8, these results are also summarised in *Table 10.*
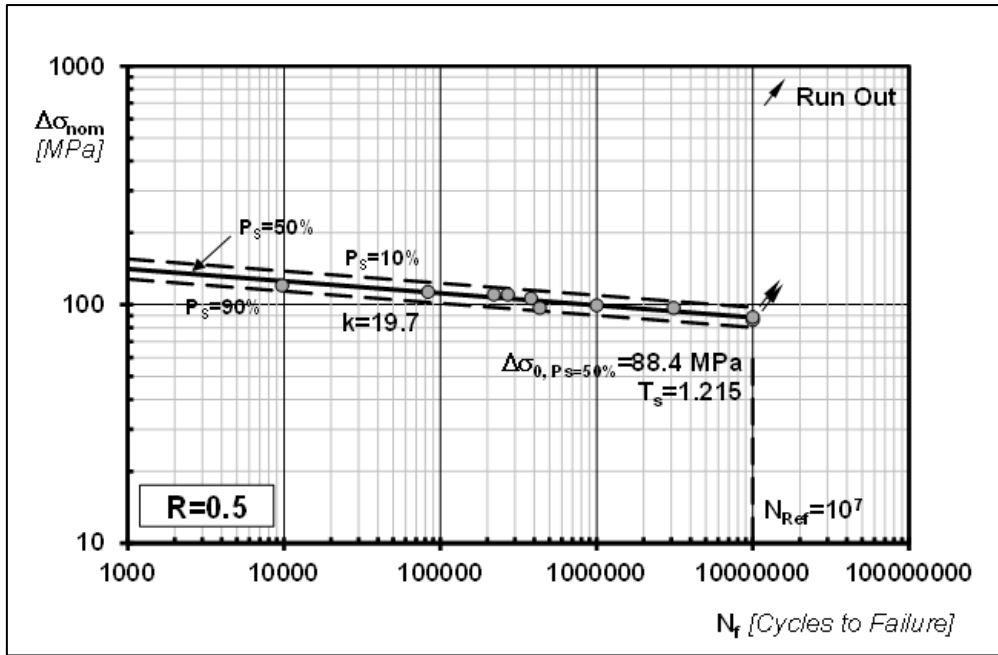
Figure 50: Wöhler curve and associated scatter band for Ps=10% and Ps=90% for the results generated by testing un-notched samples of A319-T7
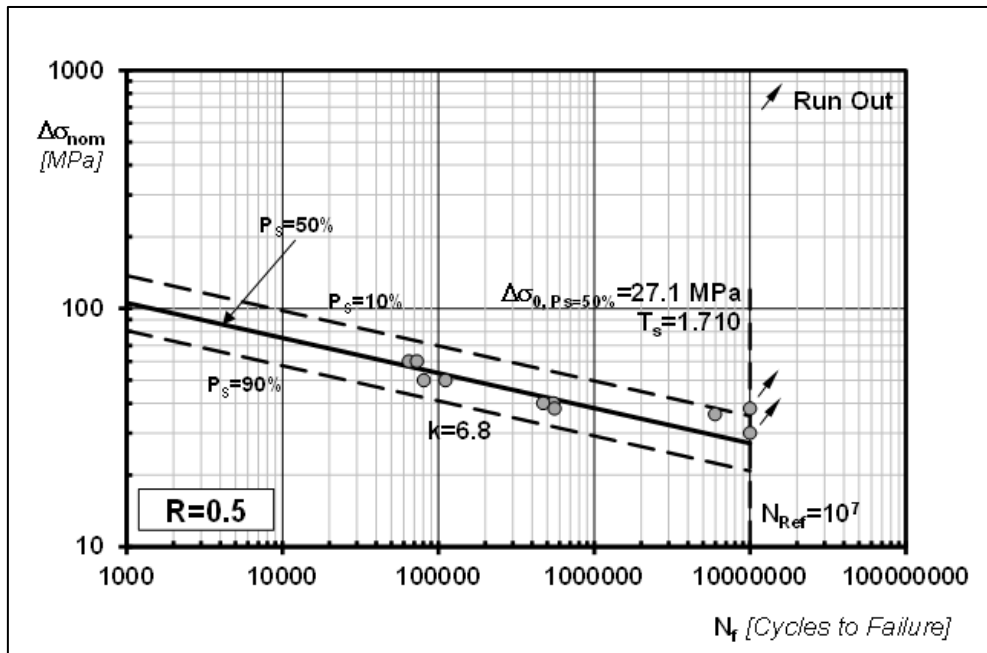
Figure 51: Wöhler curve and associated scatter band for Ps=10% and Ps=90% for the results generated by testing U-notched samples of A319-T7
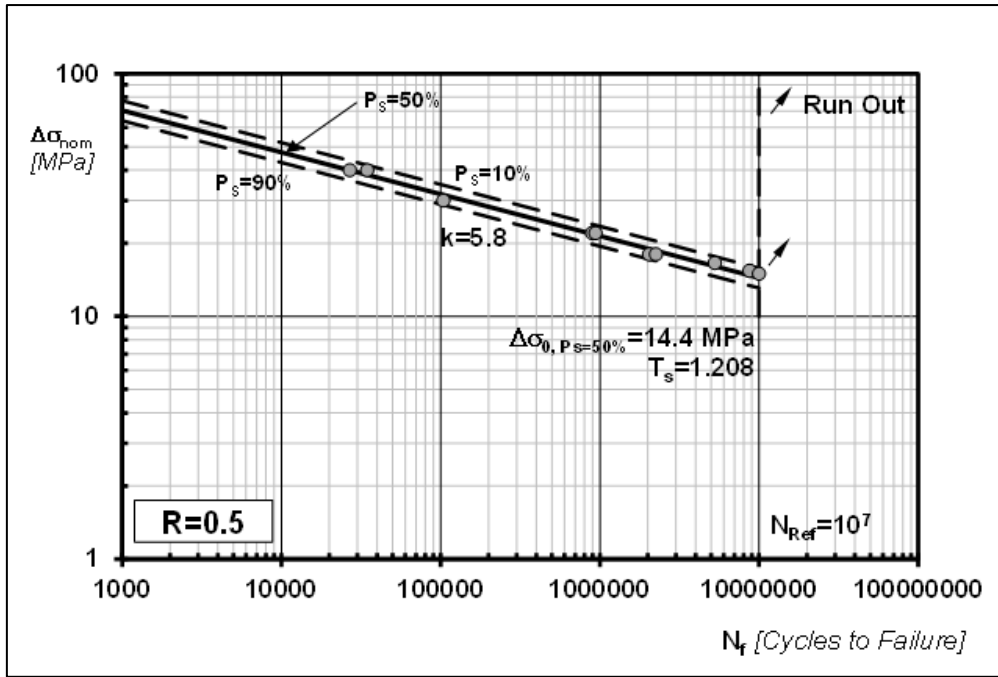
Figure 52: Wöhler curve and associated scatter band for Ps=10% and Ps=90% for the results generated by testing V-notched samples of A319-T7

Table 10: Summary of results generated by testing, at $T = 150°C$, with $N_{Ref} = 10^7$ cycles to failure for plain and notched samples of A319-T7: The accuracy of the TCD applied in the form of the PM, LM and AM

Sample	K_t	No. of samples	k	$\Delta\sigma_0{}^a$ (MPA)	$T\sigma$	$\Delta\sigma_{eff}$ PM (MPA)	LM (MPA)	AM (MPA)	Error PM (%)	LM (%)	AM (%)
Plain	1.0	8	19.7	88.3	1.215						
Blunt U-Notch	3.8	8	6.8	27.1	1.710	94.4	87.6	96.0	7.0	-1.0	9.0
Sharp V-Notch	18.3	9	5.8	14.4	1.208	79.3	72.0	85.3	-10.0	-18.0	-3

$.^a$ *Range of the nominal stress referred to the net area.*

The second set of results obtained by testing samples of C45 are plotted in *Figure 53, Figure* 54, *Figure* 55 *and Figure* 56, for the plain, Blunt U-Notched, Sharp U-Notched and V-notched samples respectively, in each of these figures the Ps=50% is shown with the associated scatter bands equal to Ps=10% and Ps=90% which were calculated according to the statistical evaluation detailed section 2.2.8, these results are also summarised in *Table 11*.
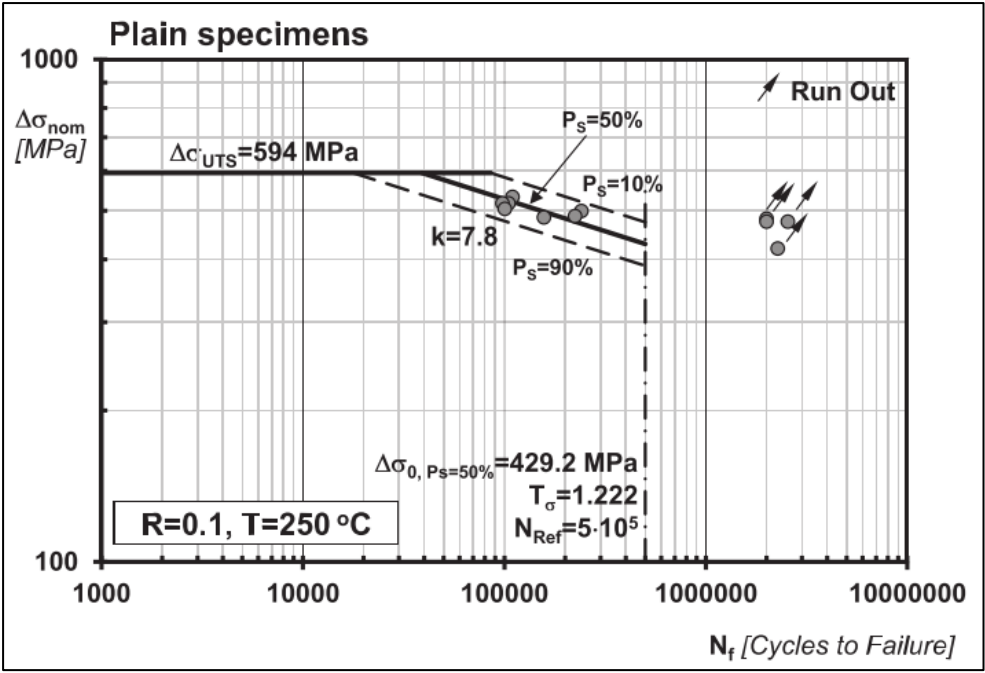
Figure 53: Wöhler curve and associated scatter band for Ps=10% and Ps=90% for the results generated by testing un-notched samples of C45
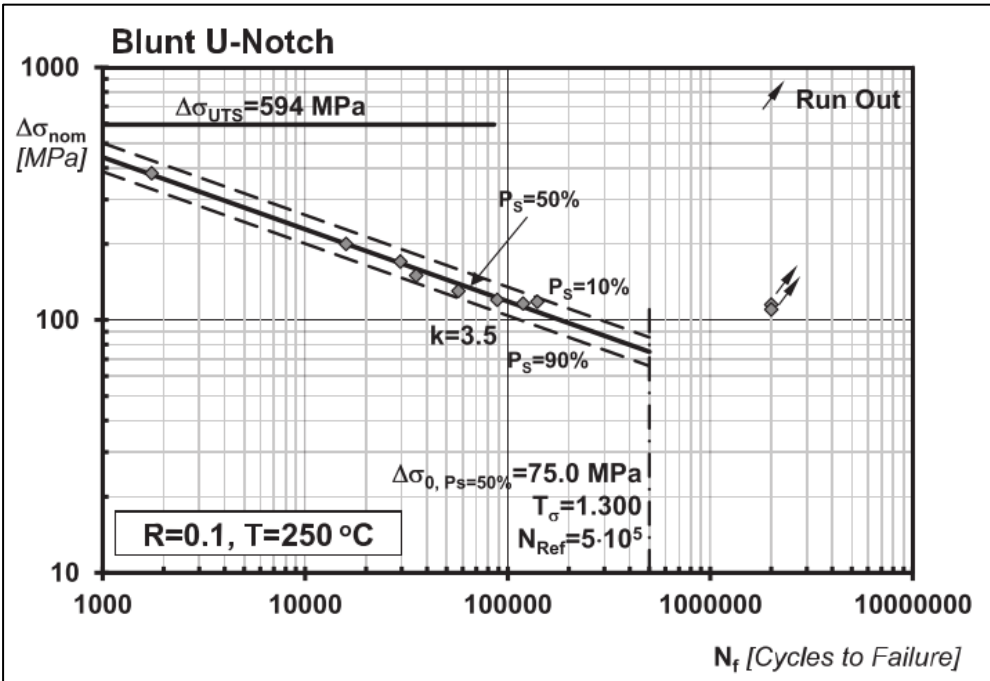
Figure 54: Wöhler curve and associated scatter band for Ps=10% and Ps=90% for the results generated by testing Blunt U-notched samples of C45
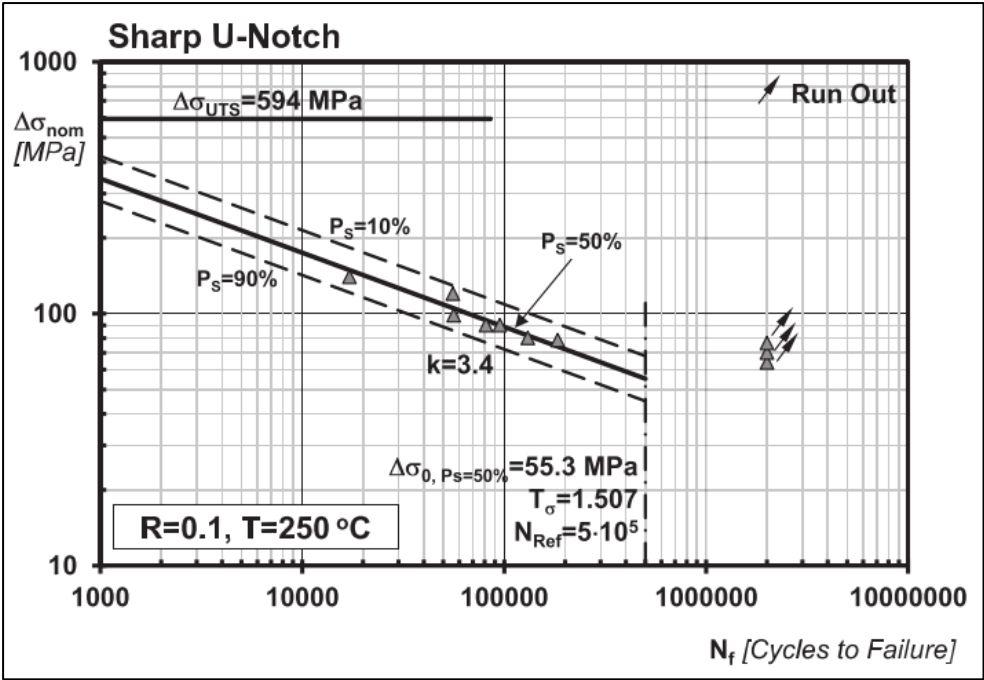
Figure 55: Wöhler curve and associated scatter band for Ps=10% and Ps=90% for the results generated by testing Sharp U-notched samples of C45
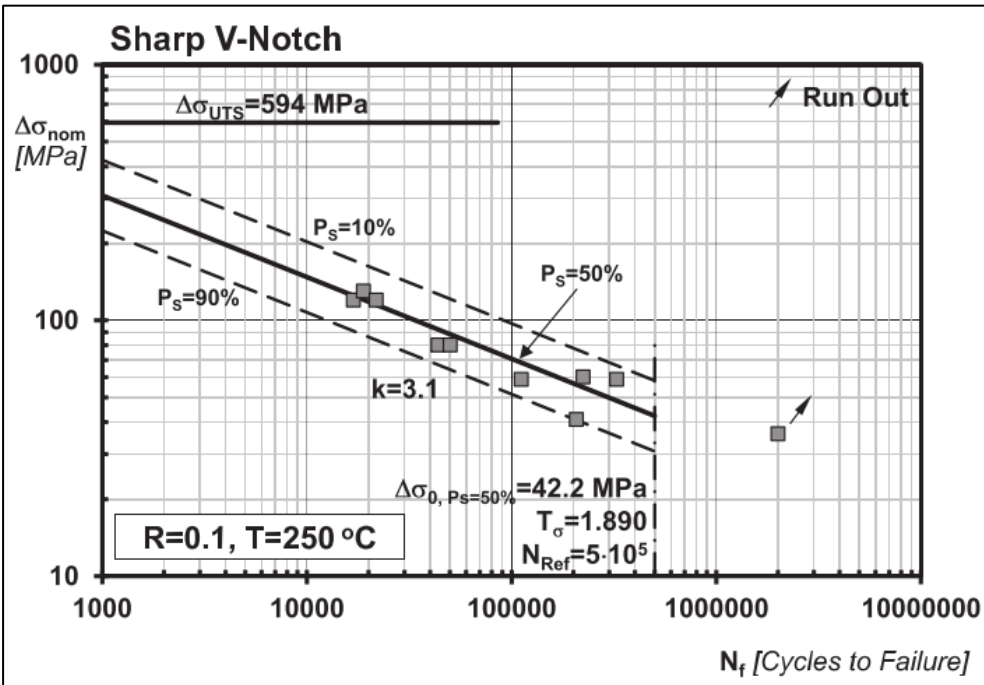
Figure 56: Wöhler curve and associated scatter band for Ps=10% and Ps=90% for the results generated by testing Sharp V-notched samples of C45

Table 11: Summary of results generated by testing, at $T = 250°C$, with $N_{Ref} = 5 \times 10^5$ [13], plain and notched samples of C45: The accuracy of the TCD applied in the form of the PM, LM and AM

Sample	K_t	No. of samples	k	$\Delta\sigma_0{}^a$ (MPa)	$T\sigma$	$\Delta\sigma_{eff}$ PM (MPA)	LM (MPA)	AM (MPA)	Error PM (%)	LM (%)	AM (%)
Plain	1.0	10	7.8	429.2	1.222						
Blunt U-Notch	6.9	9	3.5	75.0	1.300	471.0	436.4	476.6	9.7	1.7	11.1
Sharp U-Notch	10.0	9	3.4	55.2	1.496	439.8	380.0	449.1	2.5	-11.5	4.6
Sharp V-Notch	26.5	8	3.1	42.2	1.891	429.2	369.9	439.5	0.0	-13.8	2.4

$\cdot^a$ *Range of the nominal stress referred to the net area.*

The results summarised in *Table 10* and for the respective probabilities of survival, in terms of the negative inverse slope, k , range of the endurance limit, at $N_{Ref} = 10^7$ cycles to failure, as suggested by the third party company, the large reference number of cycles to failure being fully justified by the experimental results failing in this region which also highlights that this material does not have a conventional fatigue limit.

The results summarised in *Table 11,* for the respective probabilities of survival, in terms of the negative inverse slope, k , range of the endurance limit, at $N_{Ref} = 5 \cdot 10^5$ cycles to failure, for the structural steel C45 as suggested by [13], this suggestion was confirmed to be acceptable by the run out data for this test data.

To conclude this section it should be clarified that in both *Table 10* and *Table 11* as well as in *Figure 50, Figure* 51*, Figure* 52*, Figure* 53*, Figure* 54*, Figure* 55 *and Figure* 56 the range of endurance limit extrapolated at the respective N_{Ref} cycle to failure and was calculated with respect to the nominal net section.

5.4. Experimental validation:

In addition to experimental data generated as part of this project, data was also taken from technical literature as to strengthen the validity of the proposed method. To check the accuracy of the linear elastic TCD in estimating the high-cycle fatigue strength of the considered notched samples, the first thing considered was the stress analysis problem. The linear-elastic stress fields surrounding the stress concentrators were estimated using commercial finite element software ANSYS® in accordance with the assumptions stated in Chapter 2. The specimens were modelled and meshed using a 2D element Plane183. This 2D element offers greater accuracy as a higher order 8-node element, having quadratic displacement behaviour, each node has two degrees of freedom, that is, translations in the nodal x and y directions. This plane element can be used in terms of plane stress, plane strain and generalised plane strain, additionally this element can be used as an axisymmetric element. To achieve the required level of accuracy, that is, convergence at the critical distance, the mesh density in the vicinity of the stress concentrator apex was increased. The stress-distance curve was extracted at each stage of mesh density refinement, once the profile and magnitude were no longer affected by mesh density itself convergence is assumed to have occurred, this resulted in element sizes lower than 0.005mm close to the notch tip.

The sample clamps shown in *Figure 49* and connecting rods seen in *Figure 47*, were specifically designed so that, during set-up and testing, they could rotate about an axis perpendicular to the plane containing the surface of the samples and removing any possibility of static imposed torsional loading.

With regards to the A319-T7 samples, shown in *Figure 46,* it can be seen that the notch geometry can be characterised by Width/5, this resulted in stiffer samples which in turn removed the secondary bending effect. In order to accurately model these samples the following boundary

conditions were applied; on one end, all the degrees of freedom were constrained whilst on the other end, the lateral degrees of freedom were constrained i.e. pure axial loading with no secondary bending. In the case of the C45 specimens, it can be seen in *Figure 46,* that these samples have a notch depth characterised by approaching Width/2, resulting the load line running through the notch root, effectively maximising the secondary bending effect which in turn maximises the local stress concentration phenomena. The effect of secondary bending was modelled in the FEA by constraining all degrees of freedom at one end of the specimen whilst the degrees of freedom at the load end being completely unconstrained. In both cases a gross stress of -1MPa was applied to one end of the specimen, the negative sign indicating tensile load.

Estimations of the critical distance values, L, were made using the PM argument, as discussed in chapter 3. The samples made from A319-T7 were tested at $150°C$, experiencing a load ratio, $R = 0.5$. The S-D diagrams shown in *Figure 57*, summarise the obtained results for various Ps values, the S-D curves being taken from the vicinity of the notch tips and plotted along the notch bisector. The experimental investigation resulted in three pieces of information used to estimate the critical distance, the values reported in *Figure 57* and in *Table 12* were estimated by minimising the error calculated according to the error equation where the range of effective stress is calculated according to the PM, LM or AM.
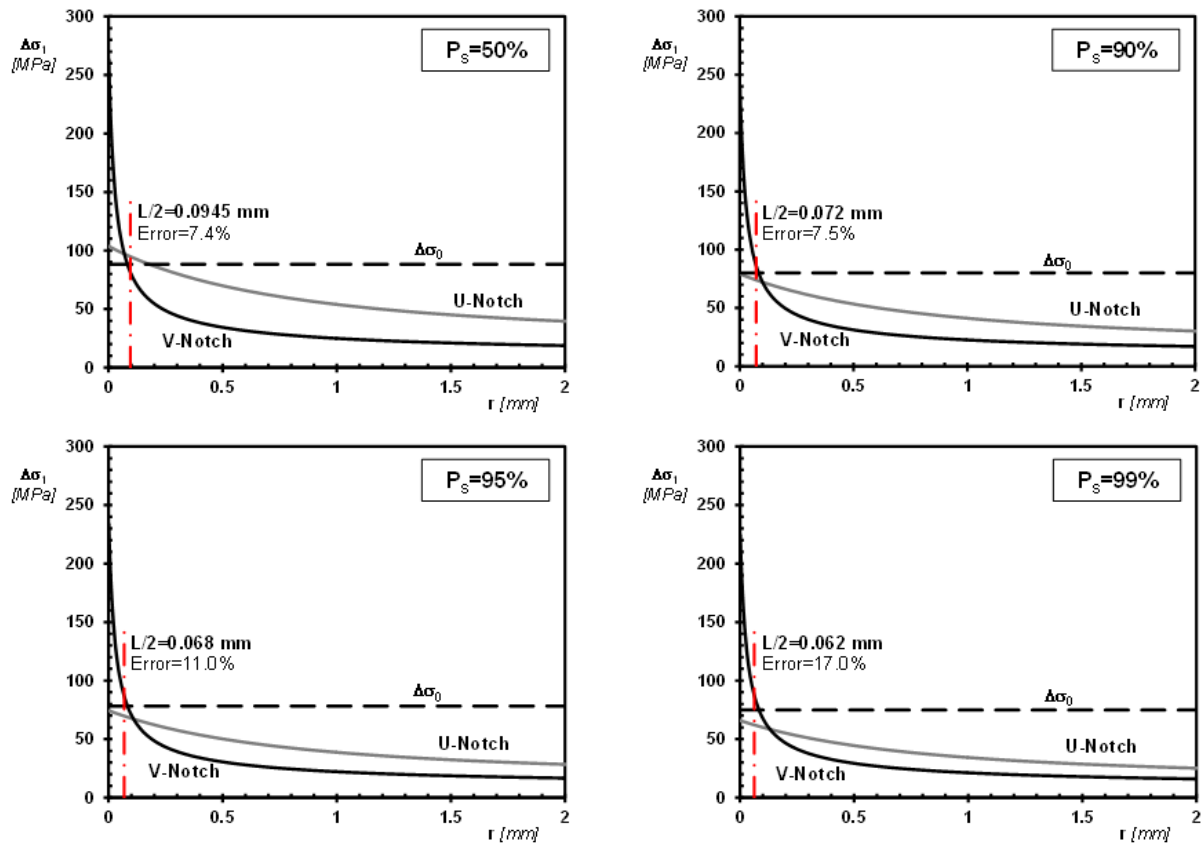
Figure 57: Stress-Distance curves and estimated values for high cycle critical distance, L – also see Table 12

The test samples of the structural steel, C45, were tested at $250°C$, experiencing a load ratio, $R = 0.1$. The resulting critical distance was estimated to be $0.252\ mm$, this being obtained from the S-D curves of *Figure 58*, in accordance with the PM argument, more specifically the estimation was made using the plain endurance limit and the linear-elastic stress field, at the endurance limit condition, ahead of the sharp V-Notch.
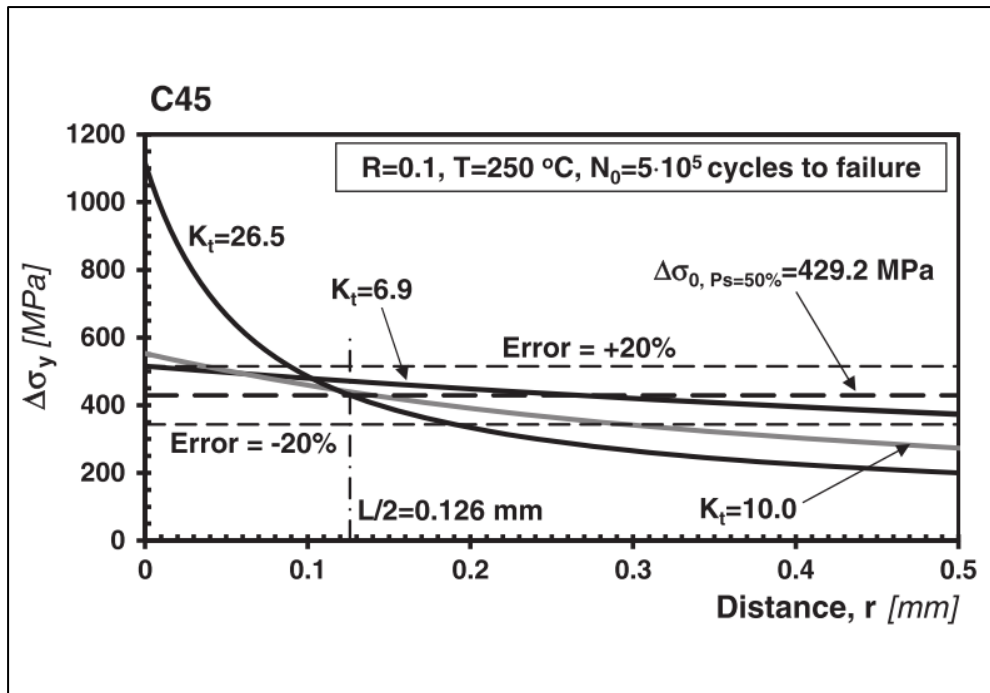
Figure 58: Linear-elastic stress-distance curves at the endurance limit for structural steel C45: Determination of critical distance according to the PM

The diagram of *Figure 58* also shows that the linear-elastic PM was highly accurate when estimating the HCF strength of both the blunt and sharp U-Notch specimens. The error being calculated using the error equation where the range of effective stress is calculated according to the PM, LM or AM.

Table 12: Summary of the endurance limits, estimated values for critical distance L at 150°C under $R = 0.5$ for different Ps values and associated Error calculated according to (EQN)

	Probability of survival			
	$Ps = 50\%$	$Ps = 90\%$	$Ps = 95\%$	$Ps = 99\%$
Plain $(\Delta\sigma_0)$	88.3	80.2	78.3	74.9
$U - Notched$ $(\Delta\sigma_0)$	27.1	20.7	19.5	17.2
$V - Notched$ $(\Delta\sigma_0)$	14.4	13.1	12.8	12.3
L (mm)	0.189	0.144	0.135	0.123
Error $(\%)$	7.4	7.5	11.0	17.0

The results summarised in *Table 10* and *Table 11* confirm that the TCD used in the form of the PM, LM or AM is capable of predicting fatigue failures falling within an error interval of $\pm 20\%$, these results being independent from the sharpness of the assessed notch. This level of accuracy is highly promising in light of the fact that when assessing fatigue data, it is not possible to distinguish between an error of $\pm 20\%$ and 0%, due to problems that often occur during testing as well as during the numerical analysis [70].

In light of the impressive level of accuracy that was obtained when using the linear-elastic TCD to post-process the results of the afore mentioned experimental investigations, it was decided that to further validate the use of the linear-elastic TCD in HCF elevated temperature scenarios, it would be checked against two data sets taken from technical literature.

The first being reported by Chen et al. [38] investigated the high-cycle fatigue behaviour of notched cylindrical specimens of Inconel 718. The samples were tested under rotating bending, as such the load can be characterised by, $R = -1$, and at a temperature of $500°C$. The details of the experimental parameters are shown in Table 13, the net diameter, w_n, of the samples was kept constant and equal to 8mm whist the gross diameter, w_g, was either 9 or 10mm. Three different values of the notch root radius were investigated, that is, $\rho = 1, 0.1 \ and \ 0.05 \ mm$.

Table 13: Summary of results generated by Chen et al. [38], at $T = 500°C$, with $N_{Ref} = 10^6$, notched cylindrical samples of Inconel 718: The accuracy of the TCD applied in the form of the PM, LM and AM

w_g	w_n	ρ		$\Delta\sigma_0{}^a$	$\Delta\sigma_{eff}$			Error		
					PM	LM	AM	PM	LM	AM
(mm)	(mm)	(mm)	K_t	(MPa)	(MPA)	(MPA)	(MPA)	(%)	(%)	(%)
9	8	1.00	2.0	460	787.3	709.5	800.0	10.9	-0.1	12.7
9	8	0.10	4.8	370	743.1	657.8	762.1	4.7	-7.4	7.3
9	8	0.05	6.7	370	718.1	668.0	748.7	1.1	-5.9	5.5
10	8	1.00	2.2	450	846.8	761.8	858.5	19.3	7.3	20.9
10	8	0.10	5.8	310	737.0	641.0	752.1	3.8	-9.7	5.9
10	8	0.05	8.0	310	710.0	650.2	747.6	0.0	-8.4	5.3

$\cdot^a$ *Range of the nominal stress referred to the net area.*

The second data set taken from literature was reported on by Shi et al. [127], they used flat samples of directionally solidified superalloy DZ125 with a single lateral notches characterised by either U or V shapes, the test specimens were tested at $850°C$. The axial cyclic force was applied parallel to the direction of solidification at a constant loading rate, $R = 0.1$. Two geometries characterised by U type notches had gross width, w_g, equal to 6mm, net width, w_n, equal to 5.4 and 5.5 with notch root radii, ρ, equal to 0.4 and 0.2 mm, respectively. Two geometries characterised by V type notches were also considered, these specimens had a notch opening angle equal to 60˚ and 120˚ had w_g, equal to 6mm, w_n, equal to 5.5 and 5.4mm, ρ, equal to 0.4 and 0.3 mm, respectively. The reference properties of the parent material were taken from a different publication [133], from the same university at a similar time and sharing an author, further justifying its use. The parent material was tested under a load ratio, $R = -1$, cylindrical samples having diameter equal to 10mm. *Table 14* summarises the considered experimental results in terms of the negative inverse slope, k, range of the endurance limit, $\Delta\sigma_0$, for Ps=50% referred to the net section and scatter ratio of the range of endurance limit for Ps=90% and Ps=10%, $T\sigma$. For the sake of consistency the reference number of cycles to failure was taken as, $N_{Ref} = 10^6$, since the experimental results used to determine the fatigue curves were mainly generated in the range $5 \cdot 10^2 \rightarrow 10^6$. Taking the statistical view point,

the experimental results were post-processed under the hypothesis of a log-normal distribution of the number of cycles to failure for each stress level and incorporating a 95% confidence level, following the fatigue data statistical assessment described in section 2.2.8.

In order to generate a populous numerous enough to be evaluated from a statistical point of view, the results obtained by testing U-notched and V-Notched samples having notch root radii equal to 0.2mm were reanalysed together. This grouping of the data is justified on the basis that there is little loss in accuracy because, the profile of the local linear-elastic in the presence of a sharp V-Notch, the notch opening angle has little influence providing the notch opening angle is less than 90˚ [134]. Therefore in this reported validation exercise the V-Notched specimens having opening angle equal to 60˚ were modelled as U-Notches having notch root radius equal to 0.2mm.

Table 14: Summary of results generated by Shi et al. [127], at $T = 850°C$, with $N_{Ref} = 10^6$, un-notched and notched samples of directionally-solidified-superalloy DZ125: The accuracy of the TCD applied in the form of the PM, LM and AM

| | | | | | | | | | $\Delta\sigma_{eff}$ | | | Error | | |
| | No. of | w_g | w_n | ρ | | | $\Delta\sigma_0{}^a$ | | PM | LM | AM | PM | LM | AM |
Ref	samples	(mm)	(mm)	(mm)	K_t	k	(MPa)	$T\sigma$	(MPA)	(MPA)	(MPA)	(%)	(%)	(%)
[133]	11	10	10		1.0	7.5	1210	1.222						
[127]	9	6	5.4	0.4	3.4	13.1	823	1.300	471.0	436.4	476.6	9.7	1.7	11.1
[127]	7	6	5.5	0.2	4.2	12.4	711	1.496	439.8	380.0	449.1	2.5	-11.5	4.6
[127]	8	6	5.4	0.3	3.7	15.1	849	1.891	429.2	369.9	439.5	0.0	-13.8	2.4

$\cdot^a$ $Range\ of\ the\ nominal\ stress\ referred\ to\ the\ net\ area.$

Table 14 highlights that the presence of a stress raising feature clearly lowers the overall strength of this material, however, the plain fatigue curve is steeper than the ones obtained by testing notched samples. This could be attributed to the probability of having a microscopic flaw is higher along the

edge of a plain sample as appose to the macroscopic flaw introduced as a stress raising feature forcing failure to occur at that location.

To determine the required linear-elastic stress fields of the investigated geometries, they were modelled using commercial FE software ANSYS®, in order to reach convergence of the stress-distance curve, the mesh density in the vicinity of the stress concentrator apices was gradually increased until convergence occurred, to improve the efficiency of this process the Ansys models were generated using a script with changeable parameters that control the mesh density. For the sake of completeness, it is worth observing here that the values reported in *Table 13* and *Table 14* for the net stress concentration factors estimated according to this standard numerical procedure were slightly different from the corresponding values reported in the original sources [38][127].

The stress-distance curves of *Figure 59* report the local stress profile at the endurance limit for the notched specimens of Inconel 718 that were tested by Chen et al [38]. The critical distance value shown in *Figure 59,* where $L = 0.154mm,$ was estimated according to the PM, shown in *Figure 23*, using the plain fatigue curve which had a calculated endurance limit, $\Delta\sigma_0 = 710MPa$, and the notch endurance limit which was determined experimentally by testing samples characterised by $K_t = 8$. The diagram of *Figure 59* and error values reported in Table 14 clearly prove the validity of using the TCD PM, returning accurate results when estimating the high-cycle fatigue strength of the other notched geometries, with estimations characterised by an error interval of $\pm20\%$, this table also indicates that the other TCD methods, to wit the LM and the AM returned similar levels of accuracy.
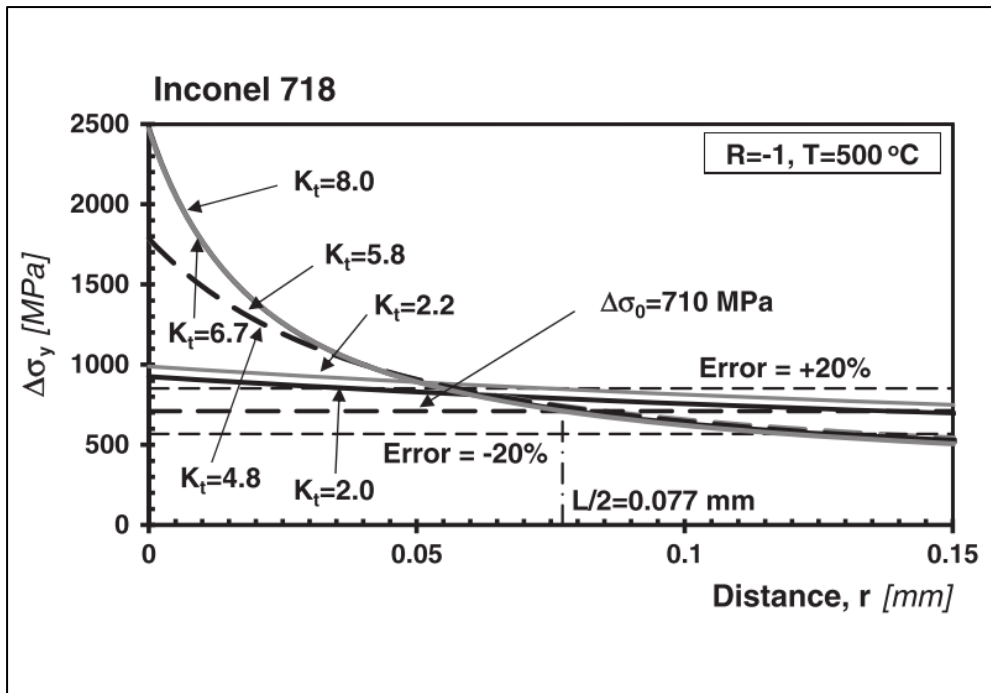
Figure 59: Linear-elastic stress-distance curves at the endurance limit for Inconel 718 [38]**: Determination of critical distance according to the PM**

The stress-distance curves of *Figure 60* were determined by post-processing the experimental results generated by Shi et al [127] by testing notched samples if directionally solidified superalloy DZ125 at 850°C. Due to the numerous assumptions made with regards to determining the fatigue curves characterised by the details of *Table 14,* for the material the critical distance was estimated using the three stress-distance curves of *Figure 60.* The value of 0.452mm was selected for the critical distance value by simply adopting a standard best fit approach. The errors listed in *Table 14* prove the validity of applying the TCD in the form of the PM, LM and AM to assess the high-cycle fatigue strength with predictions falling within an error interval of $\pm 20\%$, this level of accuracy being achieved by adopting the critical distance as a material property, under this loading condition, and independent of the notch geometry being assessed.
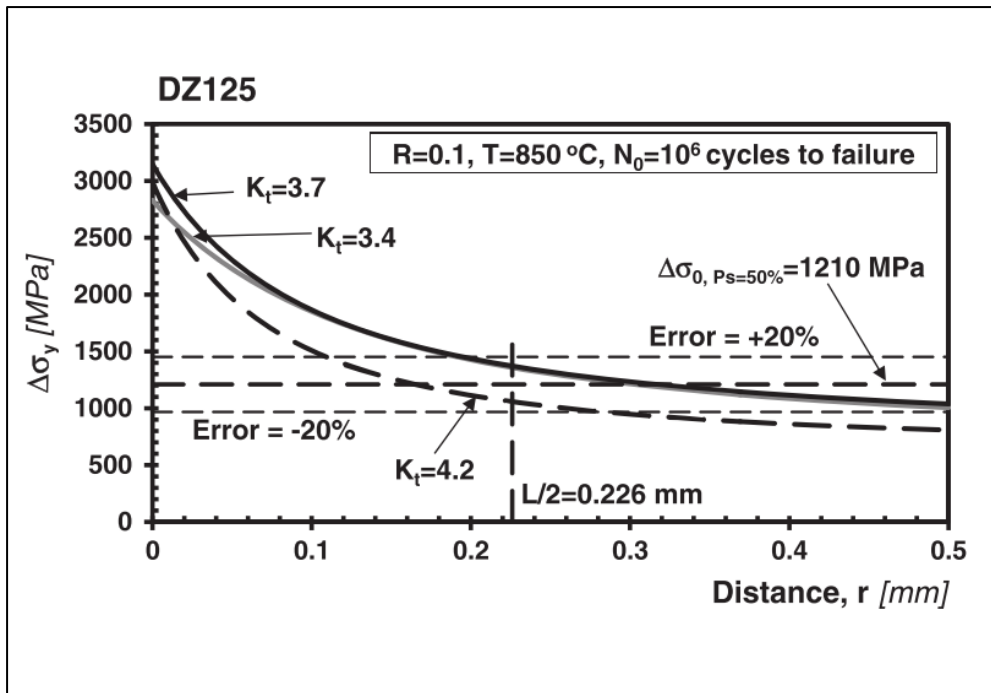
Figure 60: Linear-elastic stress-distance curves at the endurance limit for DZ125 [127][133]**: Determination of critical distance according to the PM**

To summarise this section, *Figure 61* shows the prediction errors plotted against the stress concentration factor, this shows the overall level of accuracy that was achieved by using the linear-elastic TCD to estimate the notch endurance limits at elevated temperatures. This diagram strongly supports the idea that, in the presence of a stress concentration feature and elevated in-service temperatures, accurate endurance limit fatigue assessment can be performed by continuing to adopt a linear-elastic constitutive law to model the mechanical behaviour of the material and by continuing to treat the critical distance as a material property.
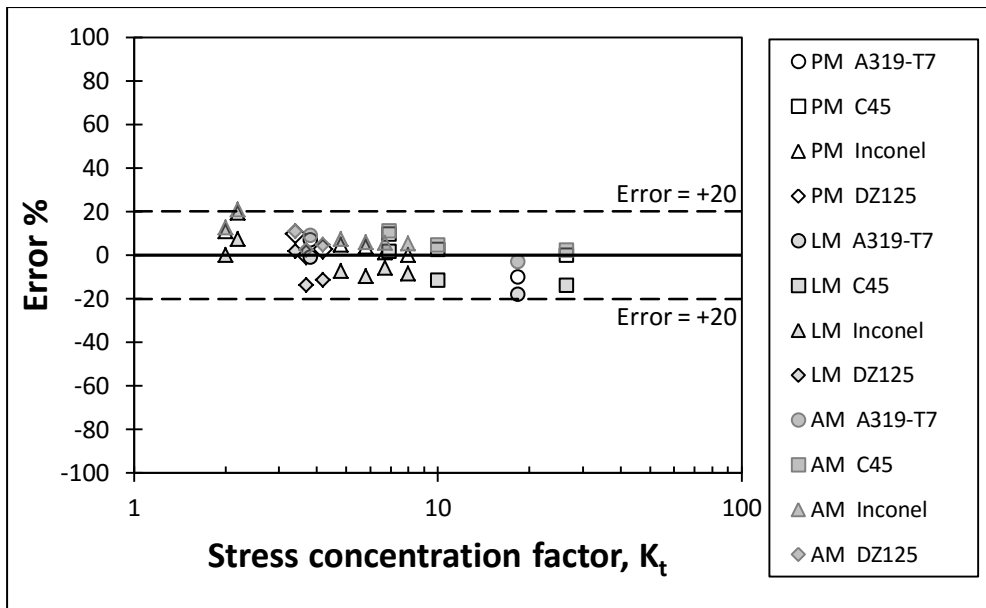
Figure 61: Overall accuracy of the TCD applied in the form of the PM, LM and the AM

5.5. Discussion:

Fatigue assessment according to the TCDs *modus operandi* is performed by post-processing the entire stress field damaging the so called process zone which is that portion of material controlling the overall fatigue strength of the component being designed [70][135]. The process zone is said to depend on three main material characteristics; the microstructural features such as grain size and boundaries, local micro-mechanical properties and also the physical mechanisms which result in the initiation of a fatigue cracks [67].

An accurate experimental investigation was conducted by Yokobori et al. [136], who tested at 650°C V-Notched samples of stainless steel SUS304. They reported their *in-situ* observations revealing that damage due to fatigue loading was localised to a small region at the notch apex which coincides with the location of crack initiation. It was reported that there was a clear change in the morphology of

the material within the process / damaged zone. These observations correlate with the idea that the TCD, when applied to high-temperature and high-cycle fatigue scenarios, is successful because the process zone provides all the engineering information required to accurately quantify the effect of the damaging mechanisms responsible for changing the materials morphology. It can be said that in contrast to the classic approach [137] which evaluates the fatigue strength by considering only the stress at the notch, the TCD instead, assumes that fatigue strength of a notched component is controlled by a finite portion of material located at the notch apex, this portion of material having dimensions in the same order of L.

With this in mind, it can be said that localised stress concentration phenomena, such as surface finishing i.e. roughness, play a secondary role in terms of damaging during fatigue loading, due to the fact that the stress field perturbation caused by a macroscopic notch is more dominant than those highly confined perturbations resulting from superficial asperities. In this context, it is evident that further validation of the TCD would be interesting, by considering the stress fields resulting from the macroscopic notch in conjunction with the localised stress gradients generated due to surface roughness of the notch walls. This combined approach could provide an explanation why in certain materials, such as aluminium alloys commonly used in aircraft construction [138], a reduction in surface roughness can significantly improve the total fatigue lifetime.

It should be highlighted that, as previously mentioned, the TCD can estimate high-cycle fatigue strength by directly post-processing the linear-elastic stress fields at the assumed crack initiation location, despite the fact that, particularly at elevated temperatures, the local mechanical behaviour of metallic materials within the process zone are known to be highly non-linear. As to this aspect, one may argue that the TCD in the linear-elastic form is still successful because when using a sophisticated energy argument, such as that presented by Lazzzarin and Zambardi [139], the linear-elastic energy is equal to the elastic-plastic energy when they are averaged over the entire fatigue process zone.

An important aspect that should not be overlooked is the effect of frequency, since the experimental work reported was carried out under the same constant frequency, to further improve the usefulness of the proposed methodology further investigation would be interesting. The Life Fraction Rule proposed by Robinson [140] suggests that at elevated temperature the design life of a component can be represented as the sum of the damage fractions φ_{LFR}, for fatigue and creep, which can be expressed as:

$$\varphi_{fatigue} + \varphi_{creep} = 1 \ (at \ failure) \tag{99}$$

Our model has been shown to produce accurate predictions of notched materials at elevated temperature, the fact that during our investigation the frequency of the applied cyclic stress was constant means that frequency effects would need further investigation to find out if our model needs further advancement to correctly account for the time/frequency effects.

Assume that the reported considerations offer an explanation for why the linear-elastic TCD is highly successful in predicting the high-cycle fatigue strength of metallic notched components experiencing high in-service temperatures, it is evident that more work is required in this area to rigorously link the TCD's *modus operandi* to the physical mechanisms taking place which result in the initiation of fatigue cracks within the process zone.

5.6. Conclusions:

The linear-elastic TCD applied in the form of the PM, LM and AM is successful in estimating high-cycle notch fatigue strength of metallic materials at elevated temperatures, returning errors within $\pm 20\%$.

The TCD allows notched components experiencing in-service high-temperature to be designed against high-cycle fatigue by directly post-processing the relevant stress fields determined through conventional linear-elastic FE models. This implies that an accurate high-cycle fatigue assessment can be performed without the need for explicitly modelling the highly non-linear mechanical behaviour displayed by metallic materials when exposed to elevated temperatures.

At high-temperature, the TCD can be used to design notched components against fatigue by treating the required critical distance as a material property whose value is not affected by the sharpness of the notch being assessed.

More work needs to be done in this area to coherently extend the use of the stress-based linear-elastic TCD to the medium-cycle fatigue regime, more work is also required to effectively take account of creep effects relating to cycle frequency.

6. Can the combined use of the MWCM and the TCD PM be used to predict fatigue strength and finite lifetime of components containing complex 3D stress concentration features?

The work presented in this chapter is based on Louks et al. "*On the multiaxial fatigue assessment of complex three-dimensional stress concentrators*" International Journal of Fatigue, Volume 63, Pages 12-24.

This chapter details an investigation into the use of the MWCM being used in conjunction with the TCD PM to assess and quantify the detrimental effects of complex three-dimensional stress raising features in components subjected to uniaxial and multiaxial fatigue loading. A selection of experimental results was taken from technical literature; the test data were generated by testing specimens containing complex geometrical features and experienced uniaxial and multiaxial constant amplitude load histories considering the effects of non-zero mean stresses as well as non-proportional loading.

The considered notched geometries and load histories showed that the position of the critical location changed as the degree of multiaxiality of the applied loading varied. The investigated linear-elastic stress fields in the vicinity of the assumed crack initiation points were calculated using the FE software ANSYS® and subsequently post-processed using the proposed use of the MWCM in conjunction with the TCD PM. The resulting predictions confirms the accuracy and reliability of our multiaxial fatigue life assessment technique, which can be efficiently used in situations of practical interest by directly post-processing the relevant linear-elastic stress fields calculated with commercial Finite Element software packages.

6.1. Introduction:

It is apparent from Chapters 1-3 that significant effort has gone into understanding the strength of engineering materials in fracture and fatigue applications, many paying particular attention to the detrimental effect of stress raisers [46][70]. As to the latter issue, examination of the state of the art suggests that, apart from a few isolated investigations , such as those detailed in [75] and [141], so far the notch fatigue issue has been addressed by mainly considering standard stress risers whose detrimental effect could directly be assessed by considering bi-dimensional geometrical configurations, the crack initiation locations being unambiguously known *a priori*. On the contrary, real components often contain complex three-dimensional (3D) geometrical features, where the position of the hot-spots is not always so obvious, this holding true especially in the presence of complex multiaxial fatigue load histories [141]. With regard to the detrimental effect of 3D stress concentrators, it is reported that current methods used to assess such geometrical features often give results that tend towards the conservative side, typically by a factor of 2 [75]. This obviously results in components which are heavier than required, unnecessarily increasing the material usage and the associated manufacturing costs.

The TCD PM and the MWCM discussed in Chapters 2 and 3 are used to answer the question proposed as the title of this chapter. In order to apply correctly the MWCM in conjunction with the PM, the first problem to be addressed is the determination of the so-called focus path, discussed in Chapter 3, the way of determining the correct focus path to design complex 3D geometrical features against fatigue can be very complex particularly when the component experiences complex multiaxial loading. A complex 3D geometrical stress raiser produces multiaxial stress fields in the material around such a feature, the stress gradient decreasing in all directions from the point experiencing the largest stress state (i.e., the so-called hot-spot). Further, given the geometry of the

component, the position of the hot-spot can shift depending on the degree of multiaxiality and non-proportionality of the loading path being applied. In this scenario, the focus path is assumed to emanate from the crack initiation point, which is assumed to be coincident with the hot-spot stress. This implies that to apply our design procedure in the presence of complex 3D stress concentrators subjected to complex multiaxial load histories, fatigue damage has to be estimated by considering several potential focus paths to find the one which experiences the maximum fatigue damage extent.

During the industrial revolution the use of metal chains and lifting gear became common place. Consequently it was noticed that these metallic components could become *tired* or *fatigued*, leading to failure of the component, often with catastrophic consequences. Complex machines and structures require components with complex geometries and that experience complex load histories, a classic example of this are in the modern combustion engine, the cam shafts and bearing journals as well as the engine casing itself. The specific study of components containing complex stress raising features experiencing multiaxial fatigue loading which starts with the pioneering work done by Gough back in the 1940s [142][143], Gough's work provided the first engineering method for the design of shafts under combined torsion and bending loads. Since then tremendous effort has been made by the scientific community to propose reliable criteria suitable for estimating fatigue damage under multiaxial fatigue loading, evidenced by various reviews of the state of the art in this field. Amongst the different methods which have been proposed and experimentally validated so far, the criteria formalised by Dang Van et al. [144], Papadopoulos [145], Liu [146], Fatemi and Socie [147], and Brown and Miller [148] deserve to be mentioned explicitly. Despite the efforts of the previously mentioned, multiaxial notch fatigue still doesn't have a globally accepted method of analysis.

As to the detrimental effects of multiaxial loading, examination of the state of the art suggests that, apart from a few isolated investigations (see, for instance, Refs [75][141]), so far the notch fatigue

effect has been addressed by mainly considering standard stress risers whose detrimental effect could directly be assessed by considering bi-dimensional geometrical configurations, the crack initiation locations being unambiguously known *a priori*, i.e. the notch bisector which is coincident with the stress hot-spot. However real components can contain complex tri-dimensional (3D) geometric features which under complex multiaxial fatigue load histories can cause the stress hot-spot to move along or around a notch fillet, making the determination of its location not so straight forward [141], the issue of locating the 'correct' part of the linear-elastic stress field is discussed in the next section.

6.2. The determination of the focus path to design complex/3D stress concentrators against fatigue

A complex 3D geometrical stress raiser produces multiaxial stress fields in the material around such a feature, the stress gradient decreasing in all directions from the point experiencing the largest stress state (i.e., the so-called hot-spot). Further, given the geometry of the component, the position of the hot-spot can shift depending on the degree of multiaxiality and non-proportionality of the loading path being applied. In this scenario, the focus path is assumed to emanate from the crack initiation point, which is assumed to be coincident with the hot-spot stress. This implies that to apply our design procedure in the presence of complex 3D stress concentrators subjected to complex multiaxial load histories, fatigue damage has to be estimated by considering several potential focus paths to find the one which experiences the maximum fatigue damage extent.

Before discussing the problem of estimating the position of the focus path, the classic experimental results obtained by Gough [143] are considered. In more detail, Gough tested under fully-reversed

pure bending and pure torsion, the filleted samples sketched in *Figure 62*. These specimens were made from a high strength steel, S65A, the mechanical properties of this material being: $\sigma_{UTS} = 1000MPa$, $\sigma_y = 946.3MPa$, $\sigma_0 = 583.5MPa$, $\tau_0 = 946.3MPa$ and a critical distance being estimated to be 0.056mm[67].

Table 15: Safety factor calculated according to the MWCM in conjunction with the TCD PM for the filleted samples of S65A tested by Gough [142] **as** $\zeta°$**angle varies – also see *Figure 62*.**

Loading type	ζ (°)	τ_a (MPa)	$\sigma_{n,a}$ (MPa)	$\sigma_{n,m}$ (MPa)	ρ_{eff}	$\tau_{A,eq}$ (MPa)	φ_{HCFSF}	Error (%)
Fully-reversed bending	0	294.2	302.2	0.0	1.027	375.1	0.99	1.2
	22.5	325.0	345.4	0.0	1.063	408.7	0.91	10.3
	45	231.0	245.2	0.0	1.061	314.6	1.18	-15.1
	67.5	112.3	118.4	0.0	1.054	195.3	1.90	-47.3
Fully-reversed torsion	0	335.6	0.0	0.0	0	335.6	1.10	-9.4
	22.5	361.7	0.0	0.0	0	361.7	1.02	-2.4
	45	312.0	0.0	0.0	0	312.0	1.19	-15.8
	67.5	236.0	0.0	0.0	0	236.0	1.57	-36.3

The safety factors, φ_{HCFSF}, calculated according to the MWCM applied in conjunction with the TCD PM, are given in *Table 15* for each orientation of the adopted focus path as shown in *Figure 62*. *Table 15* also gives the HCF error calculated by;

$$Error(\%) = \frac{\tau_{A,eq} - \tau_0}{\tau_0} \cdot 100 \qquad (100)$$

From *Table 15* it can be seen that fatigue damage is maximised along the focus paths characterised by angle, $\zeta = 22.5°$, independent of the type of loading applied i.e. bending or torsion. It is worth briefly recalling from Section 1.2 and 3, the TCD based methods are seen to be capable of HCF estimates falling within an error interval equal to approximately $\pm20\%$ [70][91][149]. The error

151

interval of ±20% is generally believed to be indistinguishable from 0% error due to the well-known problems commonly encountered during testing and during numerical analyses[91], as well as variations in the material morphology which plays a significant role in defining the physiological level of scattering commonly associated with fatigue results [46]. These considerations suggest that in Goughs' samples *Figure 62* fatigue cracks are expected to form within the fillet, in a the portion of material close to the junction of the notch fillet and the net section of the specimen, such a region is characterised by an error in the estimates of approximately ±20%. This explains the reason why in Ref. [33] accurate estimates were obtained by forming the engineering hypothesis that in shafts containing a fillet, fatigue cracks initiate at the toe of the fillet itself. This hypothesis is also supported by the cracking behaviour observed by Gough himself, who states ''*nearly all the specimens failed similarly, by a transverse crack situated at the junction of the fillet with the parallel central portion of the test-piece or slightly removed from that junction and within the fillet*'' [142].
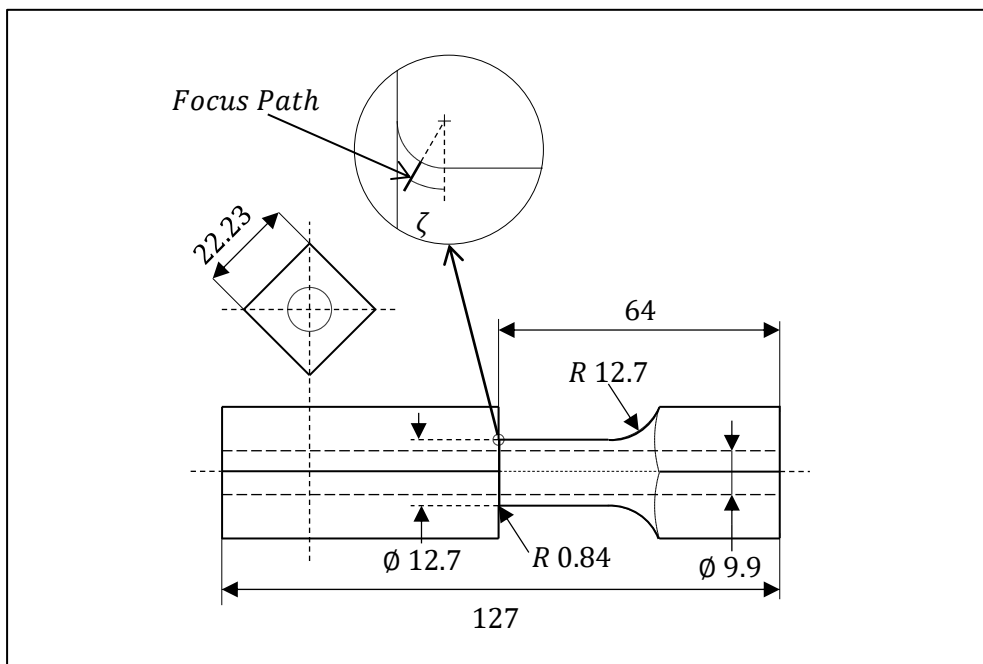
Figure 62: S65A steel samples with fillet tested by Gough [142] **, angle ζ defining the orientation of the focus path.**

The elastic stress when calculated according to Maximum Principal Stress or Von Mises is maximised when angle ζ is equal to $18°$, independent of the type of load i.e. tension or torsion, even though the fatigue cracks were seen to initiate in the fillet toe. This experimental evidence further confirms that in the presence of complex stress raisers, fatigue cracks can emanate from points on the material surface not subjected to the maximum elastic-stress value.

To summarise the determination of the focus path, from a design point of view, the safest way to perform the fatigue assessment of components containing complex stress raising features subjected to multiaxial load histories is by exploring all focus paths until the focus path experiencing the largest fatigue damage extent estimated according to the MWCM and the TCD PM is found.

6.3.Analysis of stress and strength:

To correctly post-process the experimental results collected from literature, appropriate linear-elastic stress data needed to be generated which was achieved by using the commercial finite element software ANSYS®. The finite element models were solved by assuming that the material obeys linear-elastic laws and being isotropic and homogeneous. The samples were modelled with a mapped mesh in the vicinity of the likely crack initiation, the mesh density was gradually increased until the stress around the critical distance converges, and this process resulted in elements in the process zone having sizes in the order of $2.5\mu m$. This resulted in a very large number of elements for each model and significantly increased the computational time required to solve and in some instances the model failed to solve, for this reason the models critical regions were calculated using the solid-to-solid sub-modelling technique described in Section 2.3 and shown in *Figure 63*. Elastic

stress plots were captured for the coarse model and subsequent sub-models, these are shown in

Figure 64, it can be seen that each sub-model produces a smoother stress profile.
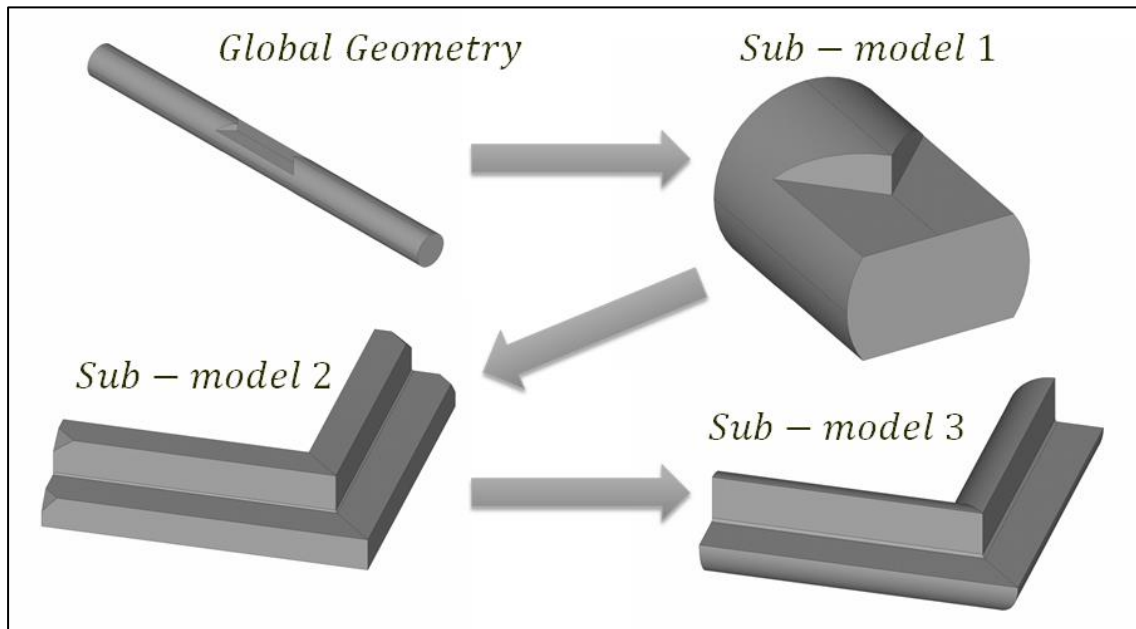
Figure 63: Solid-to-solid sub-modelling of a complex 3D notch
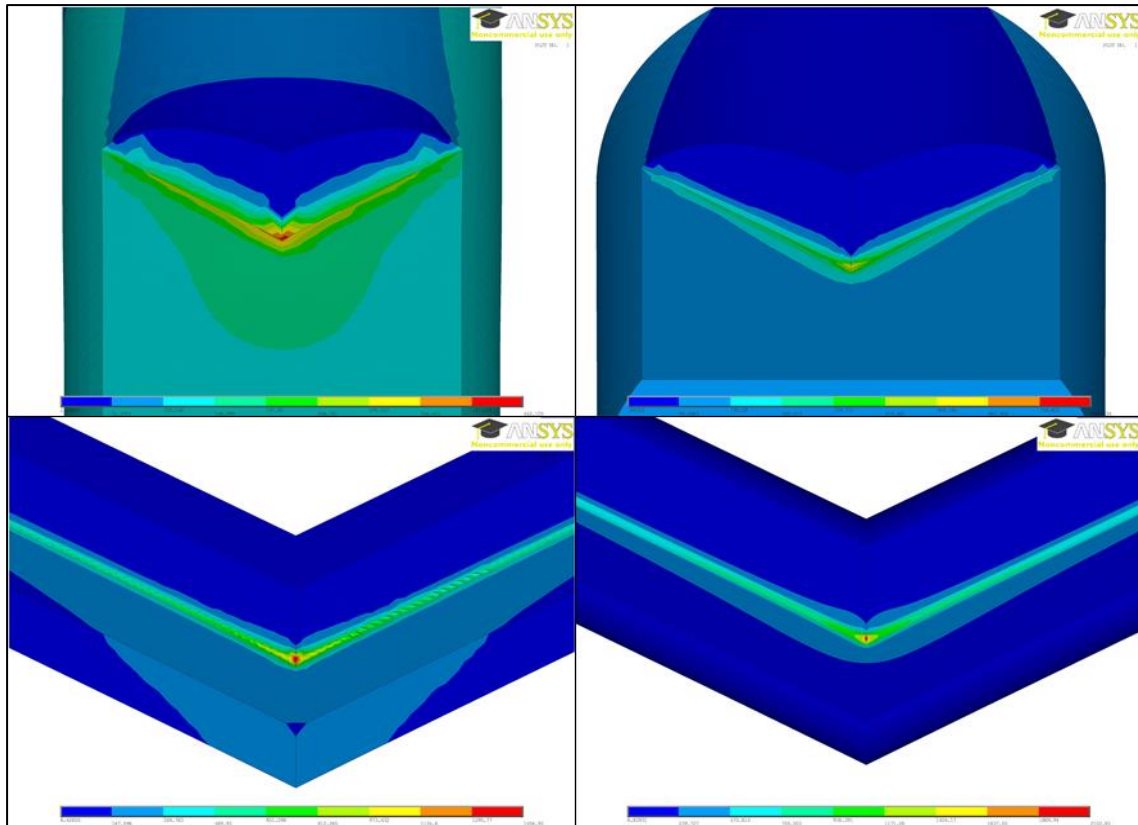
Figure 64: Smoothing of elastic stress plots in each sub-model

When considering components experiencing bi-axial loading, the linear-elastic stress fields were obtained by applying individual loads, either uniaxial tension or bending and pure torsion. Since the samples are being assessed assuming linearity, the total stress field resulting from bi-axial loading can be simply determined by taking advantage of the superposition principle. During this process it should be highlighted that particular attention should be paid so as not to lose synchronisation amongst the different nominal stress components [46]. The majority of the stress data was obtained by FEA, the exception for this being the stress fields in the vicinity of the micro-hole samples taken from [150] were instead, the stress data was determined by using the classic solution for plane stress distributions proposed by Kirsch [151].

The estimations made in this chapter, were obtained for both the HCF strength and the finite lifetime via software specifically programed for this task, the software which is now available

commercially is called Multi-FEAST©(www.multi-feast.com). This software requires the appropriate stress data obtained by means discussed in the section. Multi-FEAST is a post-processor which works by coupling three pieces of information: the stress field data in the critical locations, the load history applied to the component or which the component is likely to experience, and the fatigue response of the material. The stress state of interest i.e. in the vicinity of a geometrical feature can be calculated using any finite element package. Alternatively, the relevant stress fields can be determined from classical solid mechanics analytical solutions, for example, the use of either beam theory or the classical equations suitable for describing stress fields in the vicinity of stress raisers. The load history can be defined either analytically, a simple sinusoidal loading or some other repetitive cycle can be assumed, or constructed from a combination of varying loads. Additionally load signals can be gathered experimentally using transducers or strain gauges attached to the component surface, this idea also opens up this methodology to be implemented in real components or structures that are monitored by such devices as strain gages etc. Experimentally determined stresses or strains opens the possibilities up to data collected by photoelastic, thermoelastic or digital image correlation (DIC) methods. To conclude this section, when estimating fatigue damage, the appropriate material properties can either be determined from experiments on the material of interest, extracted from a database, or estimated using ad hoc empirical rules.

6.4. Validation by experimental data:

In order to check the validity and overall reliability of the design method proposed, experimental data was taken from technical literature. The data used was generated by testing components containing complex tri-dimensional notches under both uniaxial and multiaxial fatigue loading. The reanalysed results are grouped according to their typology and to the degree of multiaxiality of the load history.

6.4.1. Set 1, V-notched samples experiencing three-point bending:

The investigation started by considering square section beams with a through thickness V-notch, see *Figure 65*, [75][99]. The material used for these samples was En3B, a low carbon steel having mechanical and fatigue properties according to [66]: $\sigma_{UTS} = 273\ MPa$, uniaxial fatigue limit $\sigma_0 = 273 MPa\ @\ R = -1$, torsional fatigue limit $\tau_0 = 171 MPa\ @\ R = -1$, critical distance $L = 0.2\ mm$, and a mean stress sensitivity index $m = 1$.
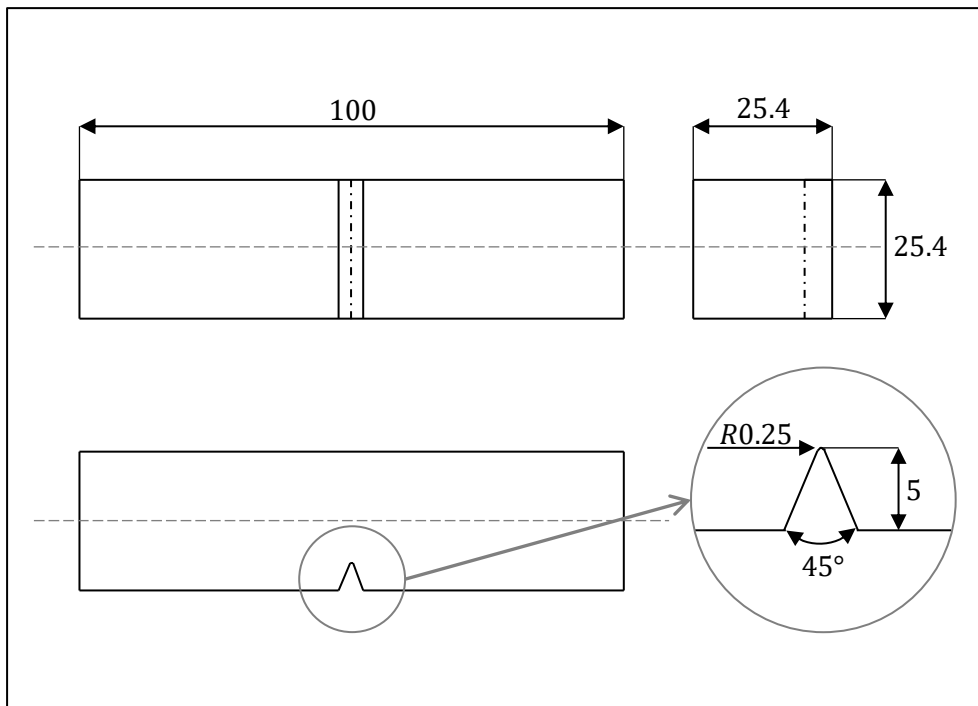
Figure 65: Geometry of the V-notched samples [75][99]

The V-notched samples were loaded by three point bending, *Figure 66*, and the load was cyclically applied under a load ratio, $R = 0.1$. As shown in *Figure 66*, the experiments considered two loading configurations, one loaded perpendicular and the second loaded parallel to the notch. The relative simplicity of the geometry allowed the crack initiation locations to be reliably guessed. In the first loading configuration (LC1) the crack initiation location and therefore focus path was taken as the notch bisector at the mid-point as this is the point experiencing the highest degree of triaxiality. The

second load configuration (LC2) where the load is applied parallel to the notch, two focus paths were investigated; the first being taken as the notch bisector and coincident with the upper surface as shown in *Figure 66*, the second being on the same plane as the notch bisector but at 45° to the upper surface.   These focus path positions and therefore the assumed crack initiation location is confirmed by the observed cracking behaviour.
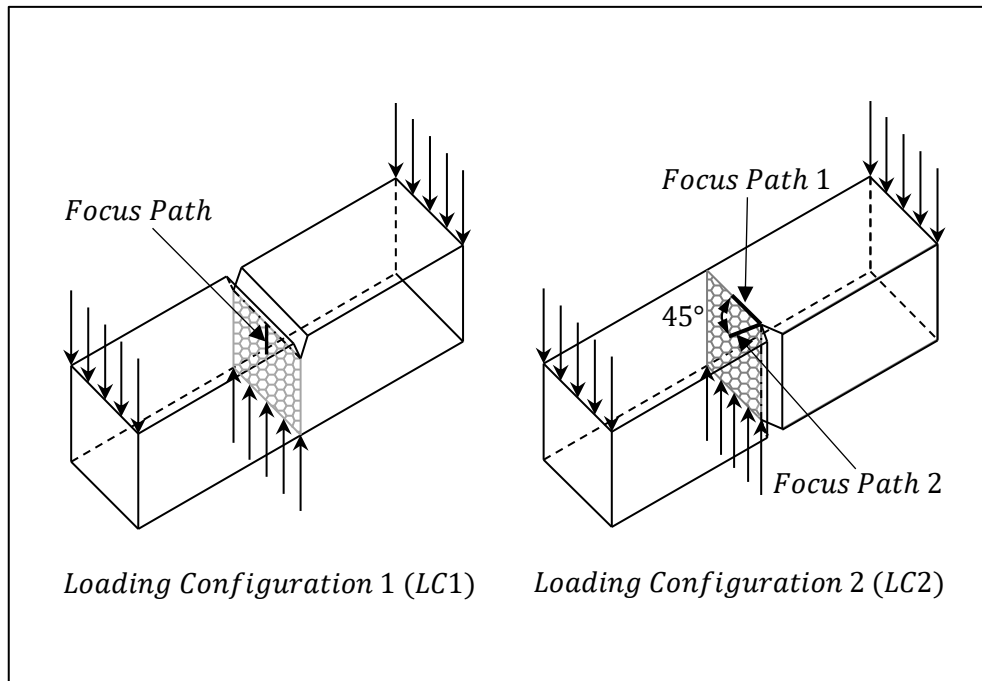
Figure 66: Three-point bend loading configurations [75][99]

The overall accuracy obtained by applying the MWCM along with the TCD PM to estimate the HCF strength of these samples, *Figure 67*, is shown in the τ_a vs ρ_{eff} diagram. The results shown in *Figure 67*, confirms that this design methodology was capable of estimating the HCF strength within an acceptable error interval of $\pm 20\%$.
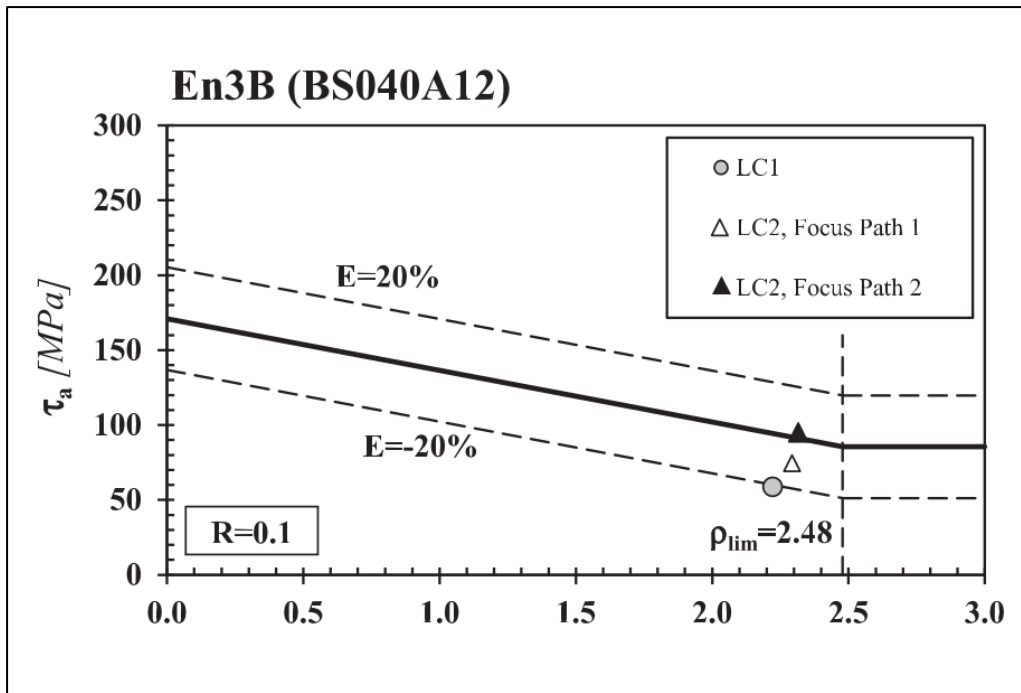
Figure 67: High-Cycle fatigue strength estimated according to the MWCM

In the case of LC2, *Figure 66*, the focus path that resulted in the largest fatigue damage was focus path 2, this in agreement with the observed cracking behaviour where cracks initiated on the upper surface at the notch tip and then propagated inwards along a direction approximately equal to 45° from the upper surface[99].
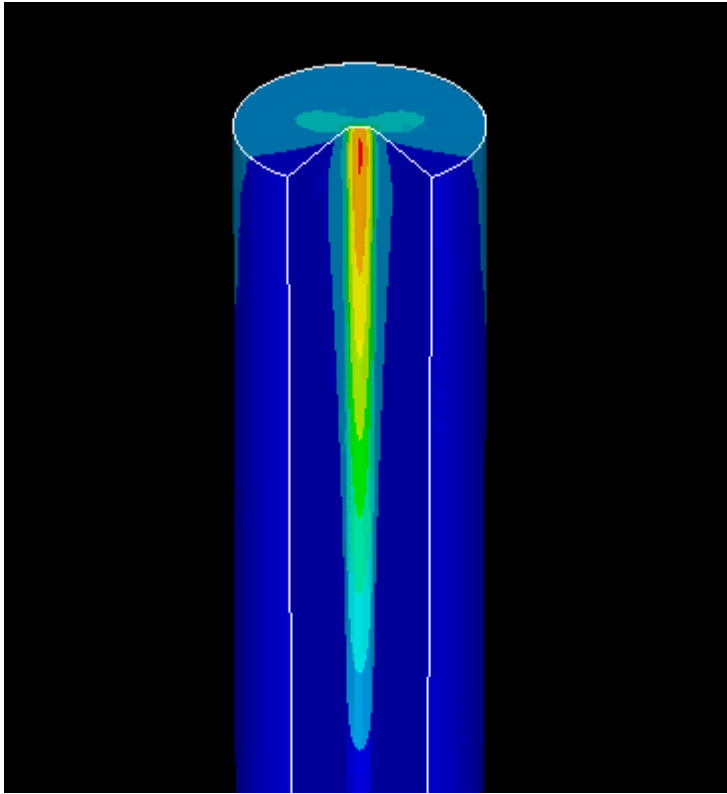
Figure 68: Stress distribution resulting from LC2

The stress distribution shown in *Figure 68*, shows correlation between the stress data obtained by Ballett [99] and the analysis of this thesis, contrary to what classical beam theory would suggest the point of maximum stress i.e. the hot spot is not on the upper surface but instead a small distance away, since our considered focus paths both emanate from the notch bisector on the upper surface it makes sense that focus path 2 would result in more fatigue damage as it captures higher stress extent from this stress distribution. In the investigation by Ballett et al.[75][99] these samples were assessed by applying the TCD with the maximum principle stress criterion which resulted in very conservative estimates. This level of conservatism could be ascribed to the fact that the maximum principle stress on its own cannot correctly account for the degree of multiaxiality of the local stress field unlike the MWCM.

6.4.2. Set 2, Holed shafts subjected to biaxial loading:

In this section the accuracy of our approach is tested considering the HCF strength of components containing very small stress concentrators. Endo and Ishimoto tested cylindrical samples with a 0.5mm diameter and depth are subjected to combined tension and torsion *Figure 69* [150]. The tested samples were made of S35C steel which has the following material properties [150][152]: Uniaxial fatigue limit $\sigma_0 = 233 MPa \ @ \ R = -1$, torsional fatigue limit $\tau_0 = 145 MPa \ @ \ R = -1$, critical distance $L = 0.246 \ mm$, and a mean stress sensitivity index $m = 1$. The samples were tested with the load signals being proportional ($\delta = 0°$) and non-proportional ($\delta = 90°$) both being fully reversed, and also considering different values of nominal biaxiality ratio, λ , where $\lambda = \tau_{nom,a}/\sigma_{nom,a}$. As mentioned earlier in this section, the assessed stress fields close to the hole were determined by the analytical solutions of Kirsch [151]. The crack paths are assumed to emanate from the edge of the hole and are characterised by the by the angle, ζ , as shown in *Figure 69*.
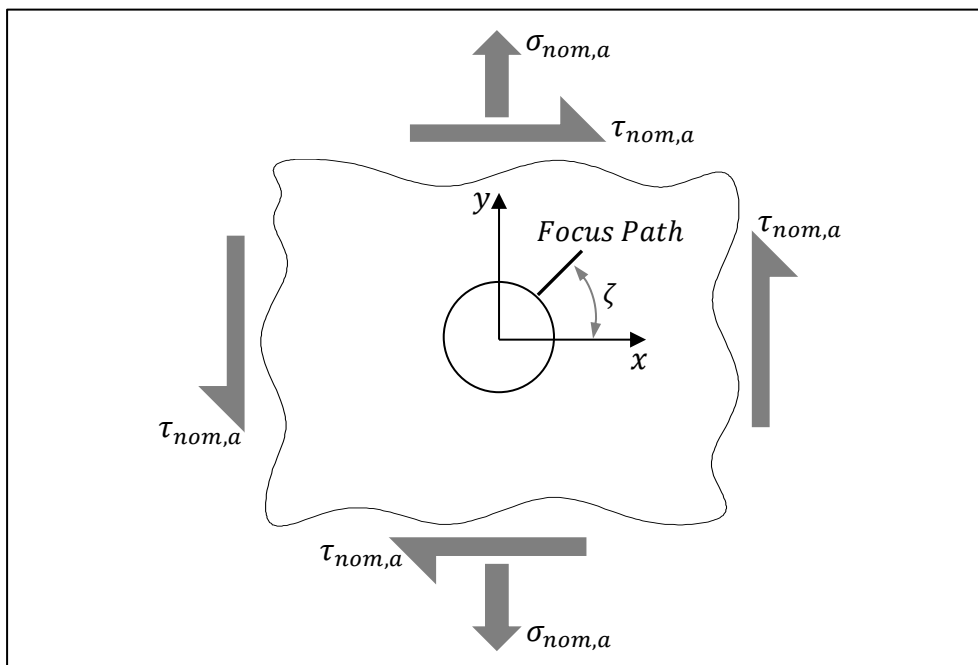
Figure 69: Micro hole subjected to combined tension and torsion [150]

The values of τ_a, $\tau_{a,eq}$, ρ_{eff} and φ_{HCF} as the angle ζ varies are plotted in *Figure 70*. Both graphs are plotted for the same nominal biaxiality value equal to 0.5 whereby the first graph is generated under proportional loading and the second is generated under non-proportional loading. It can be seen for both proportional and non-proportional loading that the focus path experiencing the maximum fatigue damage was at an angle, $\zeta = 35°$.
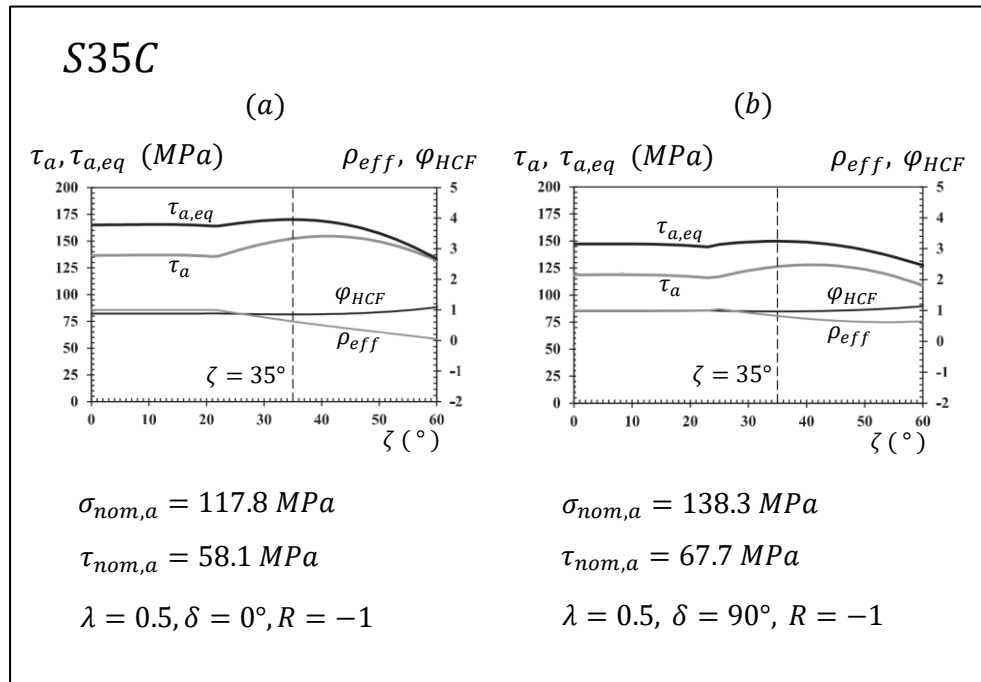
Figure 70: In-phase and out-of-phase variations of τ_a, $\tau_{a,eq}$, ρ_{eff} and φ_{HCF} with angle ζ

To conclude the evaluation of micro holes, the τ_a vs ρ_{eff} diagram of *Figure 71* provides validation of our approach in modelling the detrimental effects of micro-holes subjected to multiaxial loading with estimates typically falling in an error interval of $\pm 20\%$, these results being achieved independent of the degree of multiaxiality. Such results confirm the ability of the MWCM with the TCD PM to account for the effects of scale in multiaxial fatigue loading.
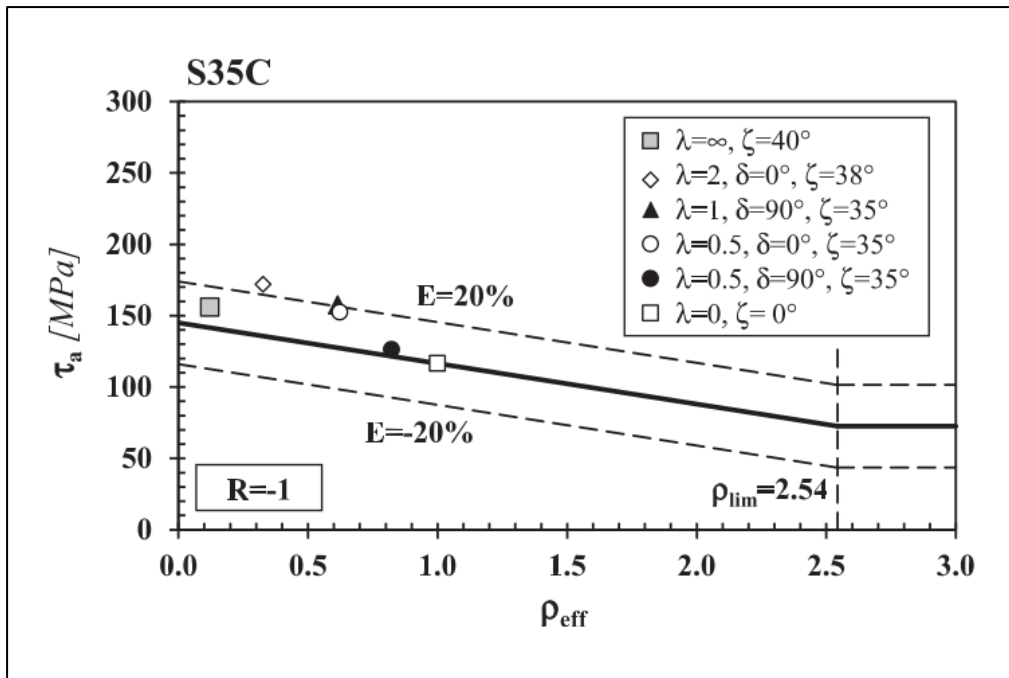
Figure 71: HCF strength estimated according to the MWCM for S35C samples

To follow on from this successful investigation on micro-holes experiencing multiaxial fatigue loading, our multiaxial fatigue assessment method was used to assess the macro-holed cylindrical samples *Figure 72* tested by Gough [142].
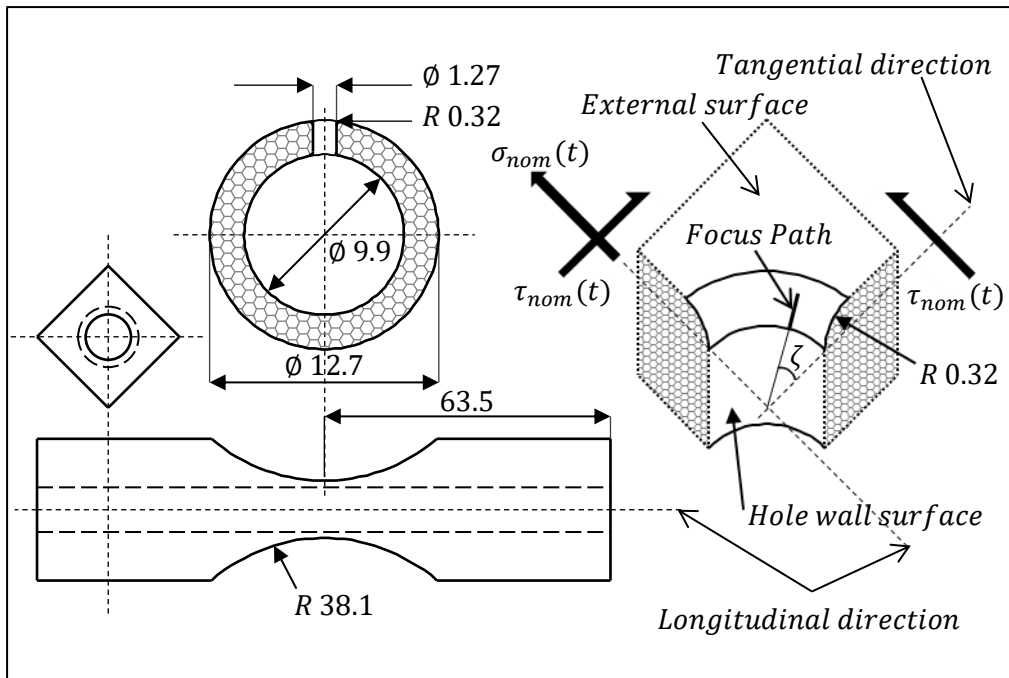
Figure 72: Macro-holed cylindrical samples subjected to combined bending and torsion [142]**, defining the focus path and angle** ζ

The samples are subjected to in-phase bending and torsion with and without superimposed static stress. The tested samples were made of S65A steel, S65A is a high strength steel which have the following material properties: $\sigma_{UTS} = 1000\,MPa$, $\sigma_Y = 946.3\,MPa$, uniaxial fatigue limit $\sigma_0 = 583.5 MPa\,@\,R = -1$, torsional fatigue limit $\tau_0 = 370.5 MPa\,@\,R = -1$, critical distance $L = 0.056\,mm$, and a mean stress sensitivity index $m = 0.41$ [61][142]. The stress data was calculated via FE software ANSYS®, the stress distribution showed that the point of maximum stress was at the intersection between the fillet and the hole wall surface, for these reasons the focus paths were chosen to emanate from the fillet and hole wall intersection, as shown in *Figure 72* the focus paths being described through angle ζ. The estimated fatigue damage for any load configuration was achieved by exploring different focus paths characterised by varying the angle ζ from 0-50°.

It can be seen in *Table 16*, that as the degree of multiaxiality of the applied load changes, the position of the critical focus path, the one experiencing the maximum fatigue damage, changed. The critical focus paths under pure bending and pure torsion are defined by $\zeta = 0°$ and $\zeta \approx 43°$ respectively.

Table 16: Accuracy in estimating the experimental results generated by Gough testing holed samples [142] – **also see *Figure 72***

$\sigma_{nom,a}$ (MPa)	$\sigma_{nom,m}$ (MPa)	$\tau_{nom,a}$ (MPa)	$\tau_{nom,m}$ (MPa)	τ_a (MPa)	ρ_{eff}	$\zeta(°)$	Error (%)
259.4	0	0	0	339.6	1.078	0.0	14.6
237.8	266.3	0	0	311.3	1.574	0.0	17.5
259.4	0	0	169.8	338.7	1.177	2.9	16.4
236.2	266.3	0	169.8	347.7	1.566	2.9	27.1
0	0	180.6	0	310.7	1.110	42.9	7.5
0	266.3	169.8	0	291.5	1.352	40.0	7.4
0	0	173.7	169.8	298.8	1.557	42.9	13.7
0	266.3	172.9	169.8	296.8	1.779	40.0	17.9
174.5	0	115.8	0	329.7	1.078	25.8	11.9
159	266.3	106.5	0	301.8	1.492	25.8	13.2
166.8	0	111.2	169.8	315.4	1.464	28.6	16.2
142	266.3	94.2	169.8	268.2	1.891	25.8	12.6
219.2	0	61.8	0	316.1	1.077	14.3	8.2
86.5	0	171.4	0	344.9	1.072	34.3	15.9

To conclude this section on macro-holed samples experiencing multiaxial loading with and without static imposed stresses, it is evident from *Table 16* and the τ_a vs ρ_{eff} diagram in *Figure 73* that the MWCM with the TCD PM is successful in estimating the HCF strength of macro holed samples with estimates typically falling within error intervals of $\pm 20\%$.
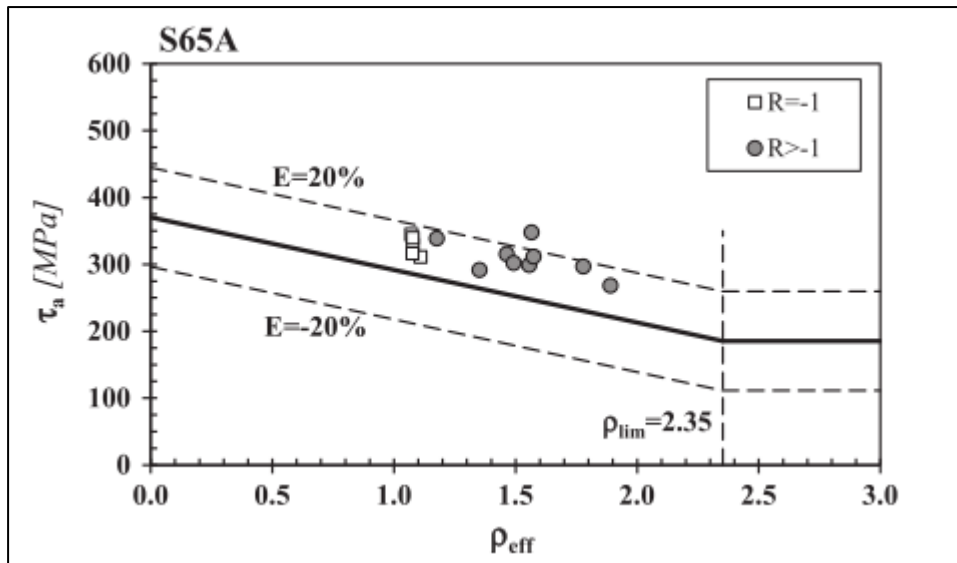
Figure 73: HCF strength estimated according to the MWCM for S65A macro-holed samples

6.4.3. Set 3, Deep splined shaft under bending and torsion:

The geometry shown in *Figure 74* depicts the deep splined shafts tested by Gough [142] under combined bending and torsion with and without superimposed static stresses. The tested samples were made of S65A steel, the same steel used to make the samples in previous sections. In *Figure 74* the origin of the investigated focus paths are given by markers A-D, in order to determine the critical focus path each of the four were assessed for each loading condition. *Table 17*, and the τ_a vs ρ_{eff} diagram of *Figure 75* shows that the effects of deep splined shafts are captured by our method, obtaining accurate results independent of loading including the presence of superimposed static stresses, returning high cycle fatigue estimates within an error interval of $\pm 20\%$.
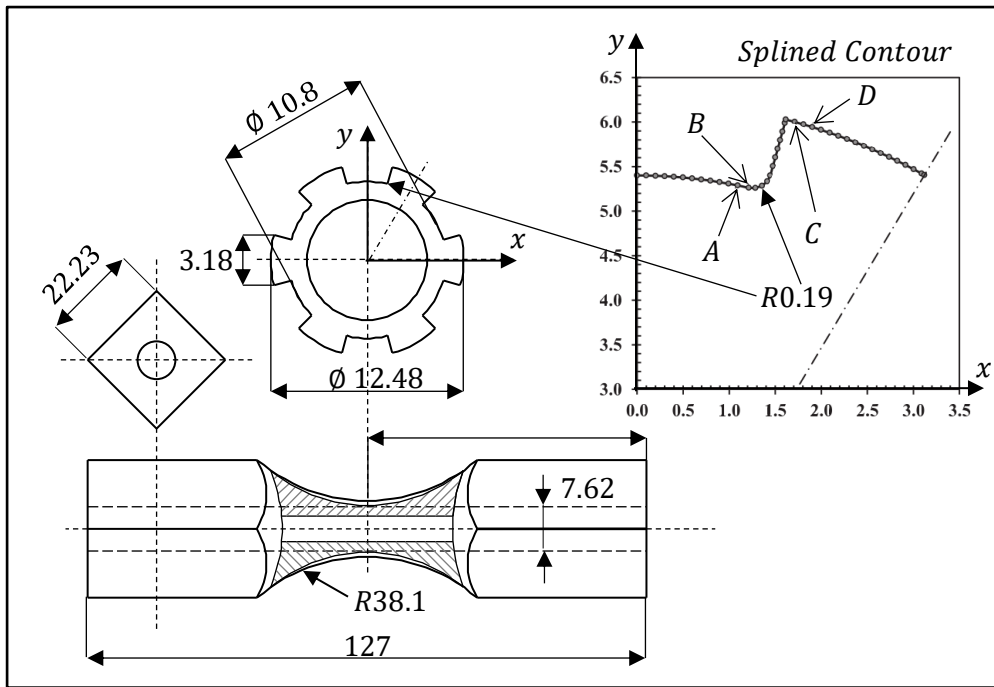
Figure 74: Splined shaft subjected to combined bending and torsion [142] **Origins of explored focus paths A,B,C and D**

Looking at *Table 17*, in particular the column indicating the calculated critical location, it was observed by Gough himself that the cracking behaviour of the splined shafts tested under pure bending was *"… failure did not occur due to the stress concentration effect of the splined contour"* [142]. Consistent with the observed cracking behaviour, our method correctly predicted under pure bending that the point experiencing the greatest amount of fatigue damage was positioned on the upper part of the spline contour indicated by points C and D in *Figure 74*. In situations of combined bending and torsion and pure torsion, the stress concentration effect was seen to prevail, resulting in the critical locations being positioned at the end of the bottom fillet indicated by markers A and B in *Figure 74*.

To conclude this section, it can be said that our methods accuracy in predicting the HCF strength of Goughs' splined shafts confirms that our method is capable of performing the fatigue assessment in situations where the position of the critical locations changes significantly as a result of variations in the multiaxiality of the applied load history.

Table 17: Accuracy in estimating the experimental results generated by Gough by testing splined shafts [142]-also see *Figure 74*.

$\sigma_{nom,a}$ (MPa)	$\sigma_{nom,m}$ (MPa)	$\tau_{nom,a}$ (MPa)	$\tau_{nom,m}$ (MPa)	τ_a (MPa)	ρ_{eff}	Critical location	Error (%)
563.6	0	0	0	311.0	0.971	C	4.6
537.3	266.3	0	0	296.5	1.169	C	4.9
534.2	0	0	169.8	287.3	1.128	D	1.5
540.4	266.3	0	169.8	290.7	1.328	D	6.7
0	0	185.3	0	281.9	0.014	A	-23.6
0	266.3	188.4	0	286.6	0.374	A	-14.7
0	0	177.6	169.8	270.1	0.020	A	-26.7
0	266.3	173.7	169.8	264.3	0.406	A	-20.0
264	0	176	0	296.6	0.443	A	-10.5
247	266.3	163.7	0	253.8	0.879	B	-12.8
253.2	0	168.3	169.8	283.8	0.605	A	-10.6
25.1	266.3	166.8	169.8	281.1	0.629	A	-10.8
501.8	0	142	0	324.6	0.769	A	4.0
95.7	0	189.9	0	291.2	0.165	A	-17.9
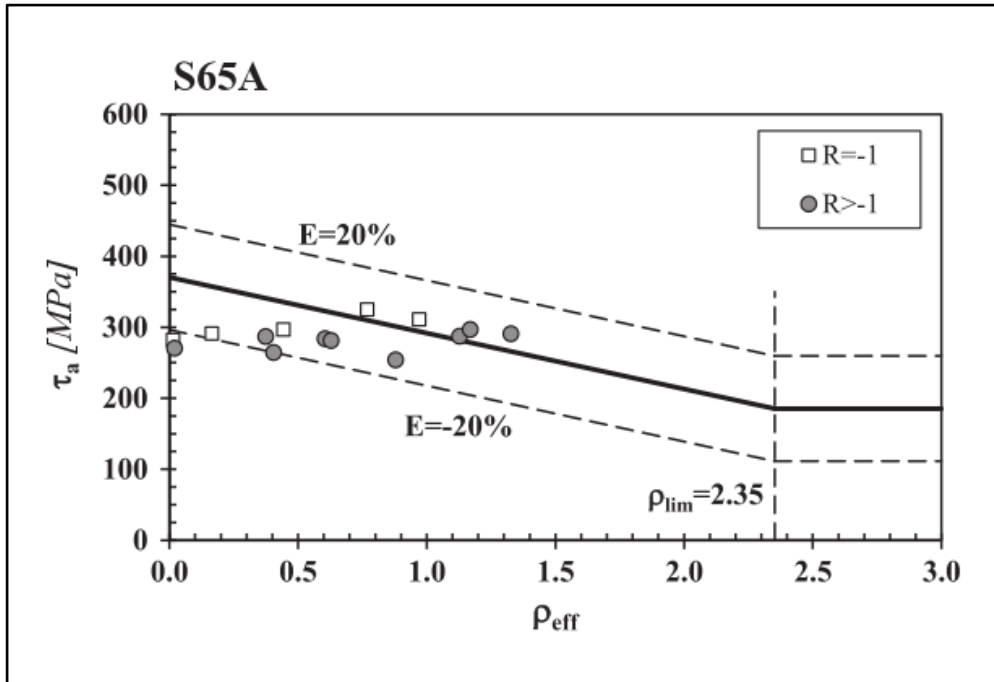
Figure 75: HCF strength estimated according to the MWCM for S65A splined samples

6.4.4. Set 4, Complex geometries tested under pure bending and combined tension and torsion

This final section of this validation exercise involves 3D angular stress concentrators *Figure 76* and *Figure 78*, the presence of 3D angular notches can produce under multiaxial loading a change in the hot-spot location. The point of maximum stress in these types of notches will experience significant stress gradients in all directions from that location.

The first specimens considered were the notched square cross-section specimens tested by Bellet et al. [75][99] shown in *Figure 76*. These samples were made of low-carbon steel En3B (BS040A12) and had the following mechanical properties [66]: $\sigma_{UTS} = 410\ MPa$, $\sigma_0 = 273\ MPa$, $\tau_0 = 171\ MPa$, $L = 0.2\ mm$ and $m = 1$. These specimens were tested under three-point bending as shown in *Figure 76*, the point of maximum stress being located at the tip of the notch.
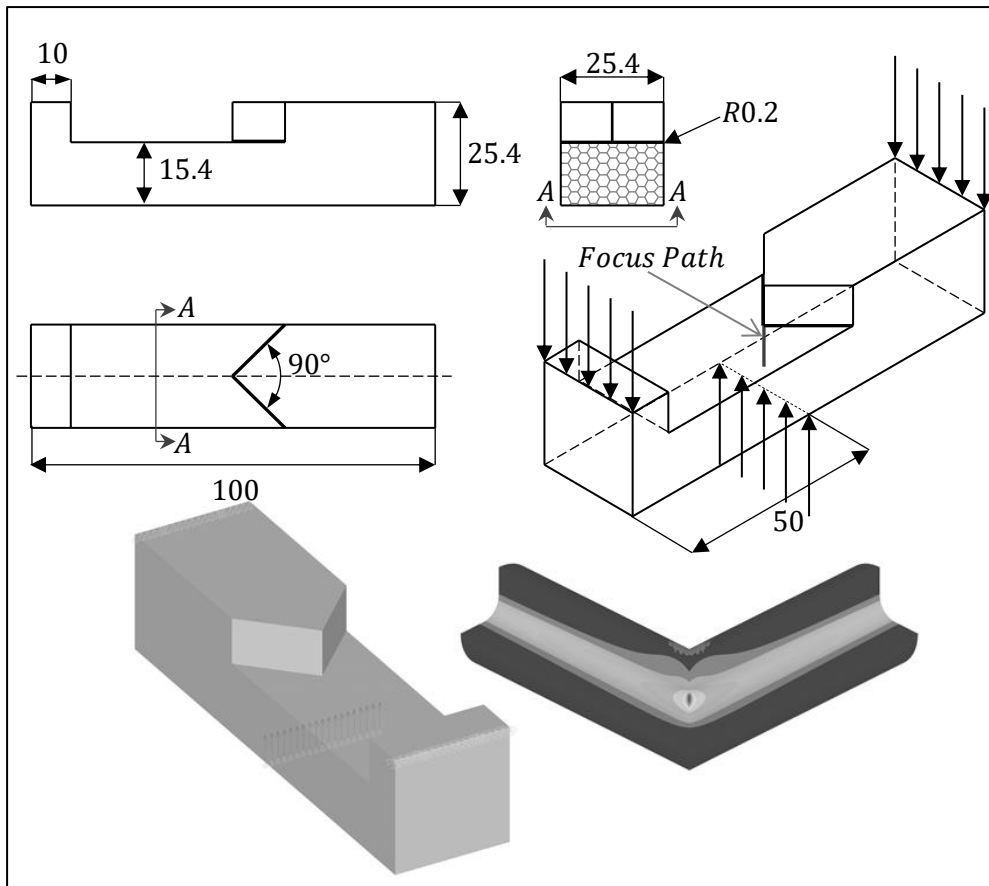
Figure 76: 3D notch in a square cross-section specimen loaded in three-point bending [75][99] **with Global and final sub-model stress plot.**

After close inspection of the geometrical features of the stress raising feature, the hypothesis can be formed where the fatigue cracks initiate at the tip of the notch itself [99]. Thus the focus path is assumed to emanate from the point where the notch fillet intersects the net section as shown in *Figure 76*, such a path following a perpendicular direction to the net section surface. The τ_a vs ρ_{eff} shown in *Figure 77* shows that our multiaxial methodology estimated a result with 15.8% error which supports the validity of our method.
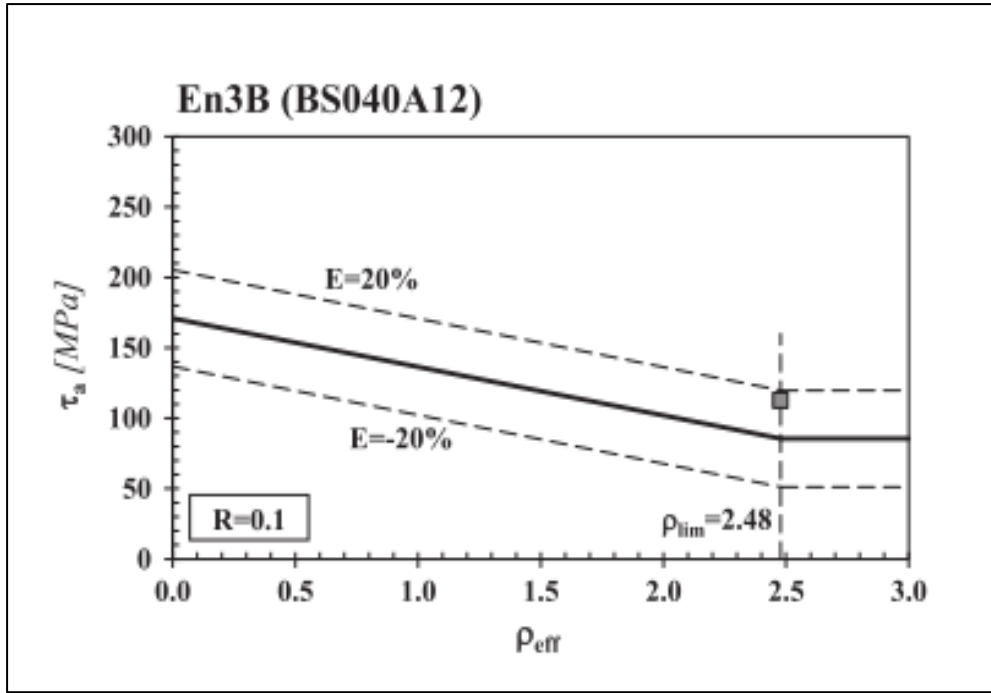
Figure 77: High-Cycle Fatigue strength estimated according to the MWCM

Thus far, the accuracy of our methodology has been validated by estimating fatigue damage in the presence of complex 3D stress raising features failing in the high-cycle fatigue regime. In order to provide a complete validation of our method, the final validation section will consider complex notched components failing in the finite lifetime fatigue regime.

In more detail, the samples shown in *Figure 78* were tested by Capetta et al. [141], the experimental program included in-phase and 90° out-of-phase axial and torsional loading. The cylindrical samples containing angular notches were made of En3B, for this low-carbon steel the MWCM's governing equations as well as the L_M vs N_f were taken as follows [68]:

$$k_\tau(\rho_{eff}) = 1 \cdot \rho_{eff} + 18.7 \quad (for\ \rho_{eff} \leq \rho_{lim} = 1.407)$$

$$\tau_{A,Ref}(\rho_{eff}) = -95.3 \cdot \rho_{eff} + 268.3 \quad (for\ \rho_{eff} \leq \rho_{lim} = 1.407)$$

$$m = 0.22, \qquad L_M(N_f) = 118.9 \cdot N_f^{-0.565}$$

171
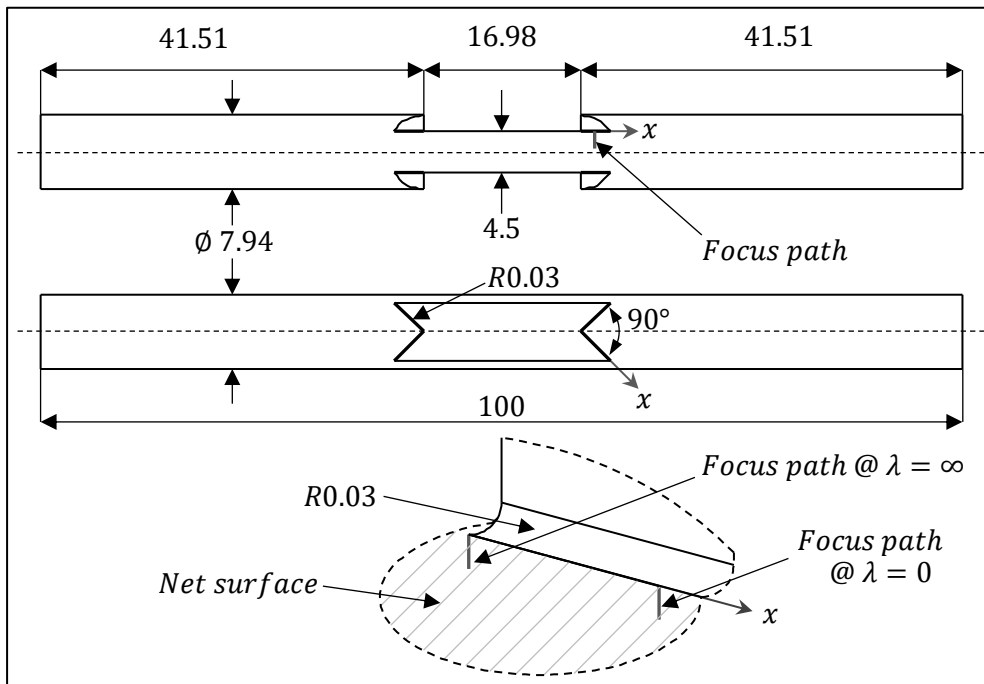
Figure 78: Cylindrical specimens containing 3D notches and subjected to in-phase and 90° out-of-phase axial and torsional loading [141]

It was observed by Capetta et al. [141] that the stress analysis performed using FE software ANSYS®, depending on the degree of multiaxiality and non-proportionality of the applied load, changed the position of the hot-spot stress, it was seen to move longitudinally along the notch fillet. As shown in *Figure 79*, the stress distribution under uniaxial loading results in the hot-spot being located at the notch tip whilst pure torque loading resulted in the hot-spot moving to approximately half way along the notch.
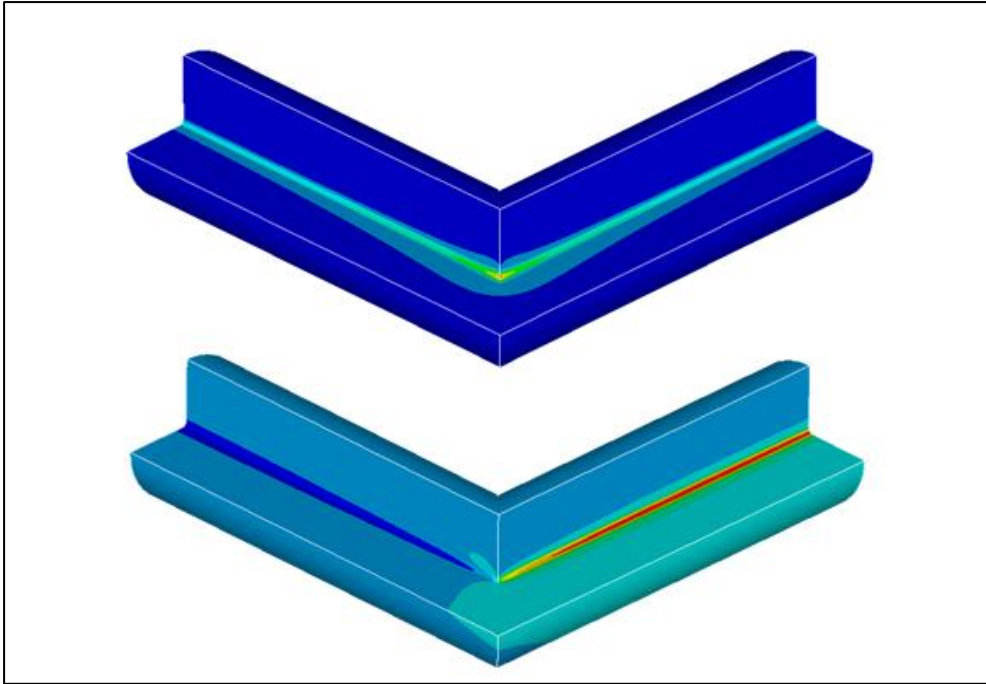
Figure 79: Elastic stress plot of sub-model under axial and torque loading

With this in mind, the focus paths were assumed to emanate from the end of the fillet, the fillet toe, all of them following a perpendicular direction to the free surface at the origin of the focus path, following the linear coordinate x having its origin at the notch tip, as shown in *Figure 78*. The focus path referred to as NTOE in *Figure 80,* is the focus path with the least amount of error or the largest fatigue damage, this justifying the selection of the focus path.

The experimental, N_f, vs estimated, $N_{f,e}$, finite fatigue lifetime diagram shown in *Figure 81*, confirms that the proposed method is capable of calculating estimates that are on the conservative side and mainly fall within the outer limits of the uniaxial and torsional scatter bands obtained by the fully-reversed plain fatigue curves used to calibrate the MWCM. The level of accuracy obtained confirms that our method is capable of giving highly accurate results, since from a statistical point of view, you cannot ask for a higher level of accuracy than the data used to calibrate the method itself. The value or range of coordinate x are listed in the legend of *Figure 81*, and indicate the position of the different focus paths used to make the estimations.
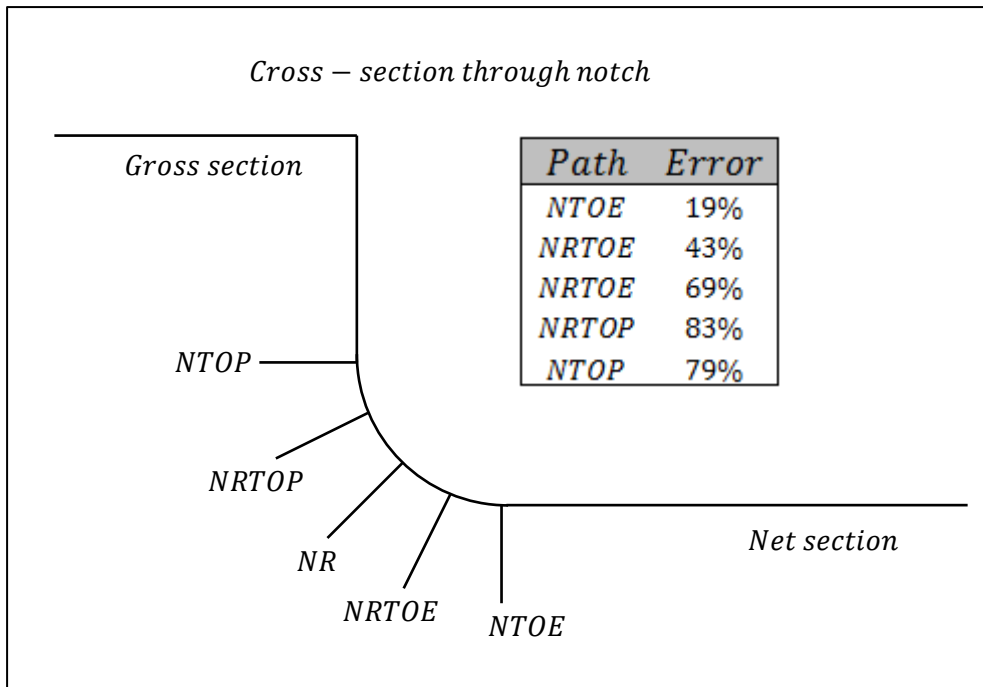
Figure 80: Focus path selection

Such a high level of accuracy was obtained by efficiently modelling the fact that the location of the crack initiation point varied with the variations of load history applied to the specimen [141]. Also it can be seen in *Figure 81* that given the profile of the load history, the hot-spot position varied slightly as the number of cycles to failure changed.

The level of conservatism obtained by applying our method could be ascribed to the fact that although the materials had the same designation and nominal chemical composition, the base material for the manufacture of the samples used to obtain the un-notched fatigue properties [68] and the material used to manufacture the notched samples assessed in this section came from two different batches. Further the 3D notched samples will of required considerably more machining which can have an effect on the material properties. λ δ ∞

Table 18: Summary of experimental data taken from Capetta et al. [141]

Series	Loading conditions			NO. data
	λ	δ	R	
Uniaxial	∞	0°	-1	15
Torsional	0	0°	-1	16
Biaxial in-phase	1	0°	-1	13
Biaxial out-of-phase	1	90°	-1	11
Biaxial in-phase	$\sqrt{3}$	0°	-1	8
Biaxial out-of-phase	$\sqrt{3}$	90°	-1	7
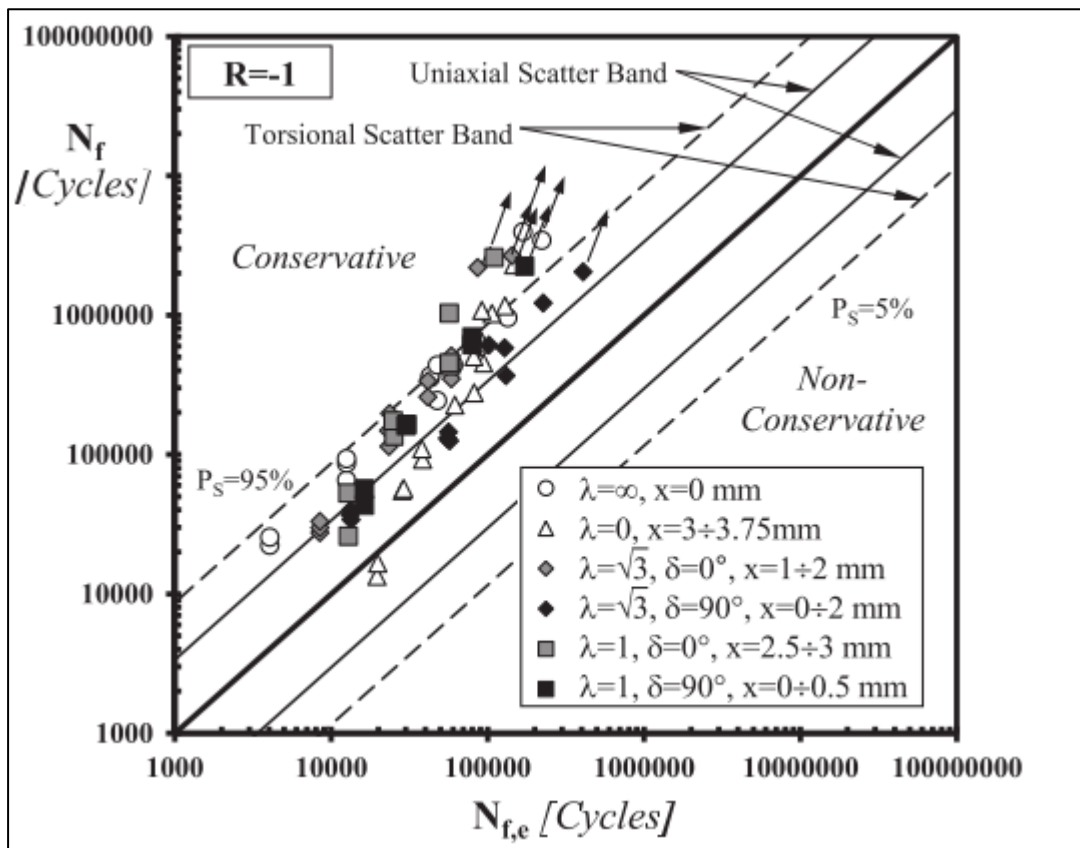
Figure 81: Finite lifetime estimations according to the MWCM

6.5.Conclusions

This chapter has reported on the validation exercise conducted and confirms that fatigue strength of components experiencing uniaxial or multiaxial fatigue loading can be accurately estimated according to the TCD by evaluating the focus path experiencing the largest damage extent.

The MWCM used in conjunction with the TCD PM has been shown to be successful in designing metallic components that exhibit severe stress gradients resulting from complex stress concentration phenomena against fatigue, including situations involving the presence of not only non-zero mean stresses but also non-proportional loading.

The proposed methodology has been shown to be capable of accurately modelling the fact that, given complex geometries, the position of the critical location can vary as the degree of multiaxiality and non-proportionality of the applied load history changes.

The MWCM applied with the TCD PM is effective in efficiently taking into account the size effect in fatigue through the varying micro/macro holed samples. More work is required to further investigate the methods accuracy in taking into account the volume/scale effect.

The proposed methodology achieved a high level of accuracy which is very promising, the fact that the methodology post-processes the stress results obtained from linear-elastic FE models make the design approach suitable for being used in engineering situations of practical interest.

7. Concluding summary

Chapters 2 and 3 of this thesis provide an insight into the engineering field of fracture and fatigue. It is clear that this engineering problem has received considerable attention by the engineering and scientific community. The problems associated with accurately predicting the fracture and fatigue strength of engineering components containing stress raising features are highly complex. It is suggested that the Theory of Critical Distances is capable of assessing notched engineering components with a high level of accuracy, this holding true independent of the complexity of the load history and geometry. The TCD's *modus operandi* suggests post-processing the entire stress field ahead of a stress raising feature using a material dependent scaled length parameter. The industrial led objectives proposed three applications of the TCD to be investigated, the results of such investigations have been detailed and will now be summarised.

The assessment of components against static loads is not a trivial one; the effects of stress raising features on the materials mechanical failure characteristics can be complex and difficult to quantify. The conventional application of the TCD to assess static loads on notched components requires additional experimentally determined material properties, for the additional work however a significant level of accuracy is achieved. The design engineer concerned with designing a notched component to resist a static load would commonly use the HSSM, the attractiveness of the HSSM is influenced by the fact that it is relatively quick and simple to implement. These two methods are hampered by two limiting factors; the TCD can return large non-conservative errors in certain situations involving plain components, whilst the HSSM can return significantly large conservative errors when assessing components containing sharp stress raising features. A reformulation of the TCD's *modus operandi* and the way in which the required material parameters are calculated provided a solution to the need for additional testing by using readily available material parameters,

and by assuming that the inherent strength parameter is equal to the materials ultimate tensile strength means that the reformulation would be suitable for the assessment of notched and plain components.

- The proposed reformulation was validated using 1744 data taken from technical literature.

- The simplified TCD PM offered a magnitude of improvement compared to the HSSM across the same set of data, the average error produced by the TCD PM was less than 30% compared to the HSSM which had an average error greater than 300%.

- The simplified TCD PM provides an efficient alternative to the HSSM to be used in practical design problems.

- Further experimental work is required to investigate and the mechanical behaviour of notched metallic components.

The second industry objective detailed was to investigate the use of the conventional linear-elastic TCD in the high-cycle fatigue regime to assess notched components experiencing in-service elevated temperatures. This investigation required experimental data to be generated, two sets of samples were manufactured, one set were machined from A319-T7 and the other from C45 steel, following specimen measuring each specimen was tested using a servo-hydraulic uniaxial test machine. In addition to the generated fatigue data, data was also taken from technical literature and assessed using the proposed methodology.

- The use of the linear-elastic TCD to design notched components against high-cycle fatigue and that experience in-service elevated temperatures was validated with predictions falling within an error interval of $\pm20\%$.

- At elevated temperature, the linear-elastic TCD can be used to design notched metallic components working in the high-cycle fatigue regime. The required material length parameter being treated as a material property independent of the components geometry.

- Further work is required to advance the use of this methodology to the medium-cycle regime or to find a relationship between temperature and the critical distance.

The final investigation detailed in this thesis regards the use of the TCD in conjunction with the MWCM to accurately assess engineering components that have complex geometries and experience uniaxial and multiaxial medium/high-cycle fatigue load histories. Conventional stress based assessment methods employed to assess complex geometries typically return conservative estimates usually in the order of 2.

The proposed use of the TCD in conjunction with the MWCM was proven to accurately estimate the fatigue strength and fatigue lifetime of components containing complex stress raising features which experience uniaxial and multiaxial load histories, including loads characterised as having non-zero mean stresses and non-proportionality.

- The proposed method efficiently assessed the size effect by accurately predicting the fatigue strength of components containing micro and macro holes. Further work is required to investigate the methods accuracy in assessing the volume/scale effect.

- Further work is needed to validate the method in situations involving variable amplitude fatigue loading.

This thesis has detailed specific investigations to solve three problems proposed by industry by extending the proven applications of the Theory of Critical Distances, in each instance the new application was seen to offer an increase in accuracy and efficiency.

8. Further work

The method proposed in chapter 4 was validated using the available data. To improve confidence in the method it is suggested that more experimental data is required. Specifically, the results obtained by testing ductile metallic samples loaded by mixed-mode I+II and I+III would improve confidence limits.

The application of the linear-elastic TCD to assess high-cycle fatigue was done so assuming constant amplitude load cycles, the method could be advanced by considering variable amplitude load cycles. The experimental investigation considered Mode I loaded samples, further investigations could include other load modes as well as multiaxial load scenarios.

The final investigation concerned with complex load histories and stress raising features was also validated using constant amplitude load cycles an extension to include variable amplitude loading would enable the method to be incorporated with real time monitoring.

10.   References

[1]   R. E. Peterson, *Stress Concentration Factors*. New York: John Wiley & Sons Ltd, 1973.

[2]   The Institution of Mechanical Engineers, *A general introduction to fracture mechanics*. London: Mechanical Engineering Publications Limited, 1978.

[3]   Y. Murakami, *Stress Intesnity Factors Handbook*, First. Oxford: Pergamon Press, 1987.

[4]   A. A. Griffith, "The Phenomena of Rupture and Flow in Solids." J STOR, London, pp. 163–198, 1921.

[5]   G. Irwin, "Fracture Dynamics," in *Fracturing of Metals, ASM*, 1947, pp. 147–166.

[6]   H. Tada, P. C. Paris, and G. R. Irwin, *The Stress Analysis of Cracks Handbook*, 3rd ed. New York: ASME Press, 2000.

[7]   G. R. Irwin, P. C. Paris, and H. Tada, *The Stress Analysis of Cracks Handbook*, Third. ASME Press, 2000.

[8]   W. Albert, *Uber Treibseile am Harz.*, vol. 10. Archiv fur Mineralogie, Georgnosie: Bergbau and Huttenkunde, 1837.

[9]   A. Wohler, "Versuche zur Ermittlung der auf die Eisenbahnwagwnachsen einwirkenden Krafte and di Widerstandsfahigkeit der Wagen-Achsem," pp. 583–616, 1860.

[10]   L. Spangenburg, *The fatigue of metals under repeated strains*. New York: D. Van Nostrand Publisher, 1876.

[11]   W. Schutz, "Pergamon A history of fatigue" vol. 54, no. 2, pp. 263–300, 1996.

[12]   L. Susmel and D. Taylor, "A novel formulation of the theory of critical distances to estimate lifetime of notched components in the medium-cycle fatigue regime," *Fatigue Fract. Eng. Mater. Struct.*, vol. 30, no. 7, pp. 567–581, 2007.

[13]   C. M. Sonsino, "Course of SN-curves especially in the high-cycle fatigue regime with regard to component design and safety," *Int. J. Fatigue*, vol. 29, no. 12, pp. 2246–2258, 2007.

[14]   R. W. Hertzberg, *Deformation and Fracture Mechanics of Engineering Materials*, 4th Editio. New York.

[15]   M. W. Brown and K. J. Miller, *Biaxial and Multiaxial Fatigue EGF Pub3*. 1989.

[16]   K. J. Miller and M. W. Brown, *Multiaxial Fatigue STP 853*. 1982.

[17]   B. Atzori, F. Berto, P. Lazzarin, and M. Quaresimin, "Multi-axial fatigue behaviour of a severely notched carbon steel," *Int. J. Fatigue*, vol. 28, no. 5–6, pp. 485–493, May 2006.

[18]   J. Marin, "Interpretation of Fatigue Strengths for Combined Stresses," in *International conference on Fatigue of Metals*, London: Institute of Mechanical Engineering, 1956, pp. 184–194.

[19]   L. Susmel, R. Tovo, and P. Lazzarin, "The mean stress effect on the high-cycle fatigue strength from a multiaxial fatigue point of view," *Int. J. Fatigue*, vol. 27, no. 8, pp. 928–943, Aug. 2005.

[20]   N. Frost, K. Marsh, and L. Pook, *Metal Fatigue*. Oxford: Clarendon Press, 1974.

[21]   S. S. Manson, "Behavior of materials under conditions of thermal stress," 1954.

[22]   L. F. Coffin, "The problem of thermal stress fatigue in austenitic steels at elevated

temperatures," *Am. Soc. Test. Mater.*, p. 31, 1954.

[23] L. F. Coffin, "A study of the effects of cyclic thermal stresses on a ductile metal," *ASTM*, vol. 76, pp. 931–950, 1954.

[24] R. Piascik, R. Gangloff, and A. Saxena, *Elevated Temperature Effects on Fracture and Fatigue*. Philadelphia: ASTM STP 1297, 1997.

[25] M. Verrilli and M. Castelli, *Thermomechanical Fatigue Behavior of Materials*. Philadelphia: ASTM STP 1263, 1996.

[26] R. Viswanathan, *Damage Mechanisms and Life Assessment of High Temperature Component*. ASM International, 1989.

[27] A. Carden, A. McEvily, and C. Wells, *Fatigue at elevated temperatures*. Philadelphia: ASTM STP520, 1973.

[28] S. S. Manson and G. R. Halford, *Fatigue and Durability of Metals at High Temperatures*. 2009.

[29] P. Domas and S. Antolovich, "An Integrated Local Energy Density Approach To Notch Low Cycle Fatigue," *Eng. Fract. Mech.*, vol. 21, no. I, pp. 187–202, 1985.

[30] T. Hasebe, M. Sakane, and M. Ohnami, "High Temperature Low Cycle Fatigue and Cyclic Constitutive Relation of MAR-M247 Directionally Solidified Superalloy," *J. Eng. Mater. Technol.*, vol. 114, no. April 1992, p. 162, 1992.

[31] T. Inoue, M. Sakane, Y. Fukuda, T. Igari, M. Miyahara, and M. Okazaki, "Fatigue-creep life prediction for a notched specimen of steel at 600°C," *Nucl. Eng. Des.*, vol. 150, no. 1, pp. 141–149, 1994.

[32]   P. J. Hurley, M. T. Whittaker, S. J. Williams, and W. J. Evans, "Prediction of fatigue initiation lives in notched Ti 6246 specimens," *Int. J. Fatigue*, vol. 30, no. 4, pp. 623–634, 2008.

[33]   M. Nozaki, S. Zhang, M. Sakane, and K. Kobayashi, "Notch effect on creep–fatigue life for Sn–3.5Ag solder," *Eng. Fract. Mech.*, vol. 78, no. 8, pp. 1794–1807, 2011.

[34]   a. R. S. Ponter, H. Chen, M. R. Willis, and W. J. Evans, "Fatigue-creep and plastic collapse of notched bars," *Fatigue. Fract. Eng. Mater. Struct.*, vol. 27, no. 4, pp. 305–318, 2004.

[35]   M. WHITTAKER, W. EVANS, P. HURLEY, and D. FLYNN, "Prediction of notched specimen behaviour at ambient and high temperatures in Ti6246," *Int. J. Fatigue*, vol. 29, no. 9–11, pp. 1716–1725, 2007.

[36]   M. Filippini, "Notched fatigue strength of single crystals at high temperature," *Procedia Eng.*, vol. 10, pp. 3787–3792, 2011.

[37]   D. Leidermark, J. Moverare, M. Segersäll, K. Simonsson, S. Sjöström, and S. Johansson, "Evaluation of fatigue crack initiation in a notched single-crystal superalloy component," *Procedia Eng.*, vol. 10, no. 1, pp. 619–624, 2011.

[38]   Q. Chen, N. Kawagoishi, and H. Nisitani, "Evaluation of notched fatigue strength at elevated temperature by linear notch mechanics," *Int. J. Fatigue*, vol. 21, no. 9, pp. 925–931, 1999.

[39]   G. Sines and R. E. Peterson, *Metal Fatigue*. New York; London; McGraw-Hill, 1959.

[40]   H. Neuber, *Theory of Notch Stresses*, Second. Heidelberg: Springer-Verlag, 1958.

[41]   Y. Lee, J. Pan, R. Hathaway, and M. Barkey, *Fatigue Testing and Analysis*. 2005.

[42] M. G. Natrella, "Experimental Statistics," *Methods in molecular biology (Clifton, N.J.)*. 1963.

[43] T. Matake, "An Explanation on Fatigue Limit under Combined Stress," *Bull. JSME*, vol. 20, no. 141, p. 257, 1977.

[44] L. Mcdiarmid, "A shear stress based critical-plane criterion of multiaxial fatigue failure for design and life prediction" vol. 17, no. 12, pp. 1475–1484, 1995.

[45] I. Papadopoulos, "Critical Plane Approaches in High-Cycle Fatigue: on the Definition of the Amplitude and Mean Value of the Shear Stress Acting on the Critical Plane," *Fatigue Fract. Eng. Mater. …*, pp. 269–285, 1998.

[46] L. Susmel, *Multiaxial notch fatigue, From nominal to local stress/strain quantities*. Woodhead & CRC, 2009.

[47] I. Papadopoulos, "A comparative study of multiaxial high-cycle fatigue criteria for metals," *Int. J. Fatigue*, vol. 19, no. 3, pp. 219–235, 1997.

[48] J. Lemaitre and J.-L. Chaboche, *Mechanics of Solid Materials*. Cambridge: Cambridge University Press, 1990.

[49] C. a. Gonçalves, J. a. Araújo, and E. N. Mamiya, "Multiaxial fatigue: A stress based criterion for hard metals," *Int. J. Fatigue*, vol. 27, no. 2, pp. 177–187, 2005.

[50] N. Zouain, E. N. Mamiya, and F. Comes, "Using enclosing ellipsoids in multiaxial fatigue strength criteria," *Eur. J. Mech. A/Solids*, vol. 25, no. 1, pp. 51–71, 2006.

[51] B. Li, L. T. Santos, and M. De Freitas, "A computerized procedure for long-life fatigue assessment under complex multiaxial loading," *Fatigue Fract. Eng. Mater. Struct.*, vol. 24, no.

3, pp. 165–177, 2001.

[52]   L. Susmel, "A simple and efficient numerical algorithm to determine the orientation of the critical plane in multiaxial fatigue problems," *Int. J. Fatigue*, vol. 32, no. 11, pp. 1875–1883, Nov. 2010.

[53]   L. Susmel, R. Tovo, and D. F. Socie, "Estimating the orientation of Stage I crack paths through the direction of maximum variance of the resolved shear stress," *Int. J. Fatigue*, vol. 58, pp. 94–101, Jan. 2014.

[54]   L. Susmel and P. Lazzarin, "A bi-parametric Wöhler curve for high cycle multiaxial fatigue assessment," *Fatigue Fract. Eng. …*, pp. 63–78, 2002.

[55]   P. Lazzarin and L. Susmel, "A stress-based method to predict lifetime under multiaxial fatigue loadings," *Fatigue. Fract. Eng. Mater. Struct.*, vol. 26, no. 12, pp. 1171–1187, Dec. 2003.

[56]   L. Susmel and N. Petrone, "Multiaxial fatigue life estimations for 6082-T6 cylindrical specimens under in-phase and out-of-phase biaxial loadings," in *Biaxial and Multiaxial Fatigue and Fracture*, A. Carpinteri, M. Freitas, and A. Spagnoli, Eds. Elsevier and ESIS, 2003, pp. 83–104.

[57]   K. Kanazawa, K. J. Miller, and W. Brown, M, "Low-cycle fatigue under out-of-phase loading conditions," *J. Eng. Mater. Technol.*, pp. 222–228, 1977.

[58]   D. F. Socie and G. Marquis, *Multiaxial Fatigue*. Warrendale: SAE, 2000.

[59]   L. Susmel, "Multiaxial fatigue limits and material sensitivity to non-zero mean stresses normal to the critical planes," pp. 1–22, 2008.

[60]   R. Kaufman and T. Topper, "The influence of static mean stresses applied normal to the maximum shear planes in multiaxial fatigue," in *Biaxial and Multiaxial Fatigue and Fracture*, A. Carpinteri, M. Freitas, and A. Spagnoli, Eds. Elsevier and ESIS, 2003, pp. 123–143.

[61]   L. Susmel, "Multiaxial fatigue limits and material sensitivity to non-zero mean stresses normal to the critical planes," *Fatigue Fract. Eng. Mater. Struct.*, vol. 31, no. 3–4, pp. 295–309, Mar. 2008.

[62]   J. a. Araújo, L. Susmel, D. Taylor, J. C. T. Ferro, and J. L. a. Ferreira, "On the prediction of high-cycle fretting fatigue strength: Theory of critical distances vs. hot-spot approach," *Eng. Fract. Mech.*, vol. 75, no. 7, pp. 1763–1778, May 2008.

[63]   L. Susmel, "Three different ways of using the Modified W??hler Curve Method to perform the multiaxial fatigue assessment of steel and aluminium welded joints," *Eng. Fail. Anal.*, vol. 16, no. 4, pp. 1074–1089, 2009.

[64]   L. Susmel, "Estimating fatigue lifetime of steel weldments locally damaged by variable amplitude multiaxial stress fields," *Int. J. Fatigue*, vol. 32, no. 7, pp. 1057–1080, Jul. 2010.

[65]   L. Susmel, C. M. Sonsino, and R. Tovo, "Accuracy of the Modified Wöhler Curve Method applied along with the rref=1mm concept in estimating lifetime of welded joints subjected to multiaxial fatigue loading," *Int. J. Fatigue*, vol. 33, no. 8, pp. 1075–1091, Aug. 2011.

[66]   L. Susmel and D. Taylor, "Two methods for predicting the multiaxial fatigue limits of sharp notches," *Fatigue Fract. Eng. Mater. Struct.*, vol. 26, no. 9, pp. 821–833, Sep. 2003.

[67]   L. Susmel, "A unifying approach to estimate the high-cycle fatigue strength of notched components subjected to both uniaxial and multiaxial cyclic loadings," *Fatigue. Fract. Eng.*

Mater. Struct., vol. 27, no. 5, pp. 391–411, May 2004.

[68]   L. Susmel and D. Taylor, "The Modified Wöhler Curve Method applied along with the Theory of Critical Distances to estimate finite life of notched components subjected to complex multiaxial loading paths," *Fatigue Fract. Eng. Mater. Struct.*, vol. 31, no. 12, pp. 1047–1064, Dec. 2008.

[69]   L. Susmel and D. Taylor, "A critical distance/plane method to estimate finite life of notched components under variable amplitude uniaxial/multiaxial fatigue loading," *Int. J. Fatigue*, vol. 38, pp. 7–24, May 2012.

[70]   D. Taylor, *The Theory of Critical Distances: A New Perspective in Fracture Mechanics*. Oxford: Elsevier Science, 2007.

[71]   K. Tanaka, "Engineering Formulae For Fatigue Strength Reduction Due To Crack-Like Notches," *Int. J. Fatigue*, vol. 22, no. 4, pp. 39–46, 1983.

[72]   J. M. Whitney and R. J. Nuismer, "Stress Fracture Criteria for Laminated Composites Containing Stress Concentrations," *J. Compos. Mater.*, vol. 8, no. 3, pp. 253–265, Jan. 1974.

[73]   P. Lazzarin, R. Tovo, and G. Meneghettit, "Fatigue crack initiation and propagation phases near notches in metals with low notch sensitivity," vol. 19, pp. 647–657, 1997.

[74]   D. Taylor, "Geometrical effects in fatigue: a unifying theoretical model," *Int. J. Fatigue*, vol. 21, no. 5, pp. 413–420, May 1999.

[75]   D. Bellett, D. Taylor, S. Marco, E. Mazzeo, J. Guillois, and T. Pircher, "The fatigue behaviour of three-dimensional stress concentrations," *Int. J. Fatigue*, vol. 27, no. 3, pp. 207–221, Mar. 2005.

[76]   L. Susmel and D. Taylor, "The theory of critical distances to predict static strength of notched brittle components subjected to mixed-mode loading," *Eng. Fract. Mech.*, vol. 75, no. 3–4, pp. 534–550, Feb. 2008.

[77]   J. Araujo, L. Susmel, D. Taylor, J. Ferro, and E. Mamiya, "On the use of the Theory of Critical Distances and the Modified Wöhler Curve Method to estimate fretting fatigue strength of cylindrical contacts," *Int. J. Fatigue*, vol. 29, no. 1, pp. 95–107, Jan. 2007.

[78]   L. Susmel, "The theory of critical distances: a review of its applications in fatigue," *Eng. Fract. Mech.*, vol. 75, no. 7, pp. 1706–1724, May 2008.

[79]   H. Kitagawa and S. Takahashi, "Application of fracture mechanics to very small cracks or the cracks in the early stage," in *Second International Conference on Mechanical Behaviour of Materials*, 1976, pp. 627–630.

[80]   E. T. Bowman and L. Susmel, "The Theory of Critical Distances to Model the Short- to Long-crack Transition in Geological Materials Subjected to Mode I Static Loading," *Procedia Mater. Sci.*, vol. 3, no. 0, pp. 562–567, 2014.

[81]   B. Atzori and P. Lazzarin, "Notch sensitivity and defect sensitivity under fatigue loading.pdf," *International Journal of Fracture*, vol. 107. pp. 3–8, 2000.

[82]   T. Yin, a. Tyas, O. Plekhov, a. Terekhina, and L. Susmel, "A novel reformulation of the Theory of Critical Distances to design notched metals against dynamic loading," *Mater. Des.*, vol. 69, pp. 197–212, 2015.

[83]   L. Susmel and D. Taylor, "An Elasto-Plastic Reformulation of the Theory of Critical Distances to Estimate Lifetime of Notched Components Failing in the Low/Medium-Cycle Fatigue Regime,"

J. Eng. Mater. Technol., vol. 132, no. April 2010, p. 021002, 2010.

[84]   L. Susmel and D. Taylor, "A novel formulation of the theory of critical distances to estimate lifetime of notched components in the medium-cycle fatigue regime," *Fatigue Fract. Eng. Mater. Struct.*, vol. 30, no. 7, pp. 567–581, Jul. 2007.

[85]   D. Taylor, "Predicting the fracture strength of ceramic materials using the theory of critical distances," *Eng. Fract. Mech.*, vol. 71, no. 16–17, pp. 2407–2416, Nov. 2004.

[86]   D. Taylor, "Applications of the theory of critical distances to the prediction of brittle fracture in metals and non-metals," *Ecf15*, 2004.

[87]   L. Susmel and D. Taylor, "On the use of the Theory of Critical Distances to predict static failures in ductile metallic materials containing different geometrical features," *Eng. Fract. Mech.*, vol. 75, no. 15, pp. 4410–4421, Oct. 2008.

[88]   L. Susmel and D. Taylor, "The Theory of Critical Distances to estimate the static strength of notched samples of Al6082 loaded in combined tension and torsion. Part II: Multiaxial static assessment," *Eng. Fract. Mech.*, vol. 77, no. 3, pp. 470–478, Feb. 2010.

[89]   L. Susmel and D. Taylor, "The Theory of Critical Distances as an alternative experimental strategy for the determination of KIc and ΔKth," *Eng. Fract. Mech.*, vol. 77, no. 9, pp. 1492–1501, Jun. 2010.

[90]   L. Susmel and D. Taylor, "The Theory of Critical Distances to estimate the static strength of notched samples of Al6082 loaded in combined tension and torsion. Part I: Material cracking behaviour," *Eng. Fract. Mech.*, vol. 77, no. 3, pp. 452–469, Feb. 2010.

[91]   D. Taylor and G. Wang, "The validation of some methods of notch fatigue analysis," *Fatigue*

Fract. Eng. ..., no. March, pp. 387–394, 2000.

[92]   L. Susmel and D. Taylor, "Fatigue design in the presence of stress concentrations," *J. Strain Anal. Eng. Des.*, vol. 38, no. 5, pp. 443–452, 2005.

[93]   L. Susmel and D. Taylor, "Can the Conventional High-Cycle Multiaxial Fatigue Criteria Be Re-Interpreted in Terms of the Theory of Critical Distances ?," vol. 2, no. 2, pp. 91–108, 2006.

[94]   L. Susmel and D. Taylor, "Non-propagating cracks and high-cycle fatigue failures in sharply notched specimens under in-phase Mode I and II loading," *Eng. Fail. Anal.*, vol. 14, no. 5, pp. 861–876, 2007.

[95]   G. Meneghetti, L. Susmel, and R. Tovo, "High-cycle fatigue crack paths in specimens having different stress concentration features," *Eng. Fail. Anal.*, vol. 14, no. 4, pp. 656–672, 2007.

[96]   D. Taylor, "A mechanistic approach to critical-distance methods in notch fatigue," *Fatigue Fract. Eng. Mater. Struct.*, vol. 24, no. 4, pp. 215–224, 2001.

[97]   X. Yang, J. Wang, and J. Liu, "High temperature LCF life prediction of notched DS Ni-based superalloy using critical distance concept," *Int. J. Fatigue*, vol. 33, no. 11, pp. 1470–1476, Nov. 2011.

[98]   D. Bellett and D. Taylor, "The effect of crack shape on the fatigue limit of three-dimensional stress concentrations," *Int. J. Fatigue*, vol. 28, no. 2, pp. 114–123, Feb. 2006.

[99]   D. Bellett, "The Fatigue Behaviour of Three-Dimensional Stress Concentrations," Trinity College Dublin, 2002.

[100]   A. A. H. Ameri, J. B. Davison, and L. Susmel, "On the use of linear-elastic local stresses to

design load-carrying fillet-welded steel joints against static loading," *Eng. Fract. Mech.*, vol. 136, pp. 38–57, 2015.

[101]   F. Pukelsheim, "The Three Sigma Rule," vol. 48, no. 2, pp. 88–91, 2016.

[102]   F. J. Gómez, M. Elices, F. Berto, and P. Lazzarin, "Local strain energy to assess the static failure of U-notches in plates under mixed mode loading," *Int. J. Fract.*, vol. 145, no. 1, pp. 29–45, Aug. 2007.

[103]   F. J. Gómez, M. Elices, F. Berto, and P. Lazzarin, "Fracture of V-notched specimens under mixed mode (I + II) loading in brittle materials," *Int. J. Fract.*, vol. 159, no. 2, pp. 121–135, Sep. 2009.

[104]   F. J. Gómez, M. Elices, F. Berto, and P. Lazzarin, "Fracture of U-notched specimens under mixed mode: Experimental results and numerical predictions," *Eng. Fract. Mech.*, vol. 76, no. 2, pp. 236–249, Jan. 2009.

[105]   F. J. Gómez, M. Elices, and J. Planas, "The cohesive crack concept: application to PMMA at −60°C," *Eng. Fract. Mech.*, vol. 72, no. 8, pp. 1268–1285, May 2005.

[106]   F. Berto, D. a. Cendon, P. Lazzarin, and M. Elices, "Fracture behaviour of notched round bars made of PMMA subjected to torsion at −60°C," *Eng. Fract. Mech.*, vol. 102, pp. 271–287, Apr. 2013.

[107]   M. R. Ayatollahi and A. R. Torabi, "Tensile fracture in notched polycrystalline graphite specimens," *Int. J. Carbon*, vol. 48, no. 8, pp. 2255–2265, Jul. 2010.

[108]   M. R. Ayatollahi and a. R. Torabi, "Experimental verification of RV-MTS model for fracture in soda-lime glass weakened by a V-notch," *J. Mech. Sci. Technol.*, vol. 25, no. 10, pp. 2529–

2534, Oct. 2011.

[109] Z. Yosibash, A. Bussiba, and I. Gilad, "Failure criteria for brittle elastic materials," *Int. J. Fract.*, vol. 125, no. 1957, pp. 307–333, 2004.

[110] F. Berto, P. Lazzarin, and C. Marangon, "Brittle fracture of U-notched graphite plates under mixed mode loading," *Mater. Des.*, vol. 41, pp. 421–432, Oct. 2012.

[111] P. Lazzarin, F. Berto, and M. R. Ayatollahi, "Brittle failure of inclined key-hole notches in isostatic graphite under in-plane mixed mode loading," *Fatigue Fract. Eng. Mater. Struct.*, vol. 36, no. 9, pp. 942–955, Sep. 2013.

[112] F. J. Gómez and M. Elices, "Fracture of components with V-shaped notches," *Eng. Fract. Mech.*, vol. 70, no. 14, pp. 1913–1927, Sep. 2003.

[113] F. J. Gomez, M. Elices, and A. Valiente, "Cracking in PMMA containing U-shaped notches," *Fatigue Fract. Eng. Mater. Struct.*, vol. 23, no. 9, pp. 795–803, Sep. 2000.

[114] M. R. Ayatollahi, a. R. Torabi, and P. Azizi, "Experimental and Theoretical Assessment of Brittle Fracture in Engineering Components Containing a Sharp V-Notch," *Exp. Mech.*, vol. 51, no. 6, pp. 919–932, Aug. 2010.

[115] F. Berto and M. R. Ayatollahi, "Fracture assessment of Brazilian disc specimens weakened by blunt V-notches under mixed mode loading by means of local energy," *Mater. Des.*, vol. 32, no. 5, pp. 2858–2869, May 2011.

[116]   a. R. Torabi and S. Amininejad, "Fracture assessment of VO-notches under mode II loading: Experiments and theories," *Theor. Appl. Fract. Mech.*, Nov. 2014.

[117] S. Cicero, V. Madrazo, and I. a. Carrascal, "Analysis of notch effect in PMMA using the Theory of Critical Distances," *Eng. Fract. Mech.*, vol. 86, pp. 56–72, May 2012.

[118] F. Berto, M. Elices, P. Lazzarin, and M. Zappalorto, "Fracture behaviour of notched round bars made of PMMA subjected to torsion at room temperature," *Eng. Fract. Mech.*, vol. 90, pp. 143–160, Aug. 2012.

[119] A. Seweryn and A. Łukaszewicz, "Verification of brittle fracture criteria for elements with V-shaped notches," *Eng. Fract. Mech.*, vol. 69, no. 13, pp. 1487–1510, Sep. 2002.

[120] F. Berto and A. Campagnolo, "Fracture tests under mixed mode I / III loading : An assessment based on the local energy," pp. 1–14, 2016.

[121] P. S. Shinde, K. K. Singh, V. K. Tripathi, P. K. Sarkar, and P. Kumar, "Fracture Toughness of Thin Aluminum Sheets Using Modified Single Edge Notch Specimen," *Int. J. Eng. Innov. Technol.*, vol. 1, no. 5, pp. 283–288, 2012.

[122] F. J. Gómez, M. Elices, and A. Valiente, "Fracture of a high strength steel containing u-notches," *ECF13*, 2013.

[123] K. Taghizadeh, F. Berto, and E. Barati, "Local strain energy density applied to martensitic steel plates weakened by U-notches under mixed mode loading," *Theor. Appl. Fract. Mech.*, vol. 59, no. 1, pp. 21–28, Jun. 2012.

[124] F. Berto and E. Barati, "Fracture assessment of U-notches under three point bending by means of local energy density," *Mater. Des.*, vol. 32, no. 2, pp. 822–830, Feb. 2011.

[125] F. Berto, P. Gallo, and P. Lazzarin, "High temperature fatigue tests of un-notched and notched specimens made of 40CrMoV13.9 steel," *Mater. Des.*, vol. 63, no. 1, pp. 609–619, 2014.

[126] N. Kawagoishi, Q. Chen, and H. Nisitani, "Fatigue strength of Inconel 718 at elevated temperatures," *Fatigue Fract Engng Mater Struct*, no. 23, pp. 209–216, 2000.

[127] D. Q. Shi, X. a. Hu, J. K. Wang, H. C. Yu, X. G. Yang, and J. Huang, "Effect of notch on fatigue behaviour of a directionally solidified superalloy at high temperature," *Fatigue Fract. Eng. Mater. Struct.*, vol. 36, no. 12, pp. 1288–1297, 2013.

[128] F. Berto, P. Lazzarin, and P. Gallo, "High-temperature fatigue strength of a copper-cobalt-beryllium alloy," *J. Strain Anal. Eng. Des.*, vol. 49, no. 4, pp. 244–256, 2014.

[129] P. Gallo, F. Berto, P. Lazzarin, and P. Luisetto, "High Temperature Fatigue Tests of Cu-be and 40CrMoV13.9 Alloys," *Procedia Mater. Sci.*, vol. 3, pp. 27–32, 2014.

[130] F. Berto and P. Gallo, "Extension of linear elastic strain energy density approach to high temperature fatigue and a synthesis of Cu-Be alloy experimental tests," *Eng. Solid Mech.*, vol. 3, no. 2, pp. 111–116, 2015.

[131] D. Leidermark, J. Moverare, K. Simonsson, and S. Sjöström, "A combined critical plane and critical distance approach for predicting fatigue crack initiation in notched single-crystal superalloy components," *Int. J. Fatigue*, vol. 33, no. 10, pp. 1351–1359, 2011.

[132] H. Christ and C. K. Wamukwamba, "The effect of mean stress on the high-temperature fatigue behaviour of SAE 1045 steel," *Mater. Sci. Eng. A*, vol. A, pp. 382–385, 1997.

[133] Y. Xiaoguang, H. Jia, S. Duoqi, H. Xiaoan, and D. Chengli, "LCF behavior and life modeling of DZ125 under complicated load condition at high temperature 1 Introduction," 2013.

[134] P. Lazzarin and R. Tovo, "A unified approach to the evaluation of linear elastic stress fields in the neighborhood of cracks and notches," *Int. J. Fract.*, vol. 78, no. 1, pp. 3–19, 1996.

[135] L. Susmel, *Multiaxial Notch Fatigue: from nominal to local stress-strain quantities.* Cambridge: Woodhead & CRC, 2009.

[136] Y. A. T, K. J. Y, and K. T, "Damage Progression Behavior under High Temperature Creep and Fatigue Conditions," *ICF10, Honolulu, Hawaii - 2001*, 2001.

[137] N. E. Dowling, *Mechanical Behavior of Materials*. New Jersey: Prentice-Hall, 1993.

[138] R. Jones, L. Molent, and S. A. Barter, "Calculating crack growth from small discontinuities in 7050-T7451 under combat aircraft spectra," *Int. J. Fatigue*, vol. 55, pp. 178–182, 2013.

[139] P. Lazzarin and R. Zambardi, "The equivalent strain energy density approach re-formulated and applied to sharp V-shaped notches under localized and generalized plasticity," *Fatigue Fract. Eng. Mater. Struct.*, vol. 25, no. 10, pp. 917–928, 2002.

[140] E. Robinson, "Effect of Temperature Variation on the Long-Time Strength of Steels," *ASME*, vol. 74, p. 777, 1952.

[141] S. Capetta, R. Tovo, D. Taylor, and P. Livieri, "Numerical evaluation of fatigue strength on mechanical notched components under multiaxial loadings," *Int. J. Fatigue*, vol. 33, no. 5, pp. 661–671, May 2011.

[142] H. J. Gough, "Engineering steels under combined cyclic and static stresses," *Inst. Mech. Eng.*, p. 417, 1949.

[143] H. J. Gough and H. V Pollard, "The strength of metals under combined alternating stresses," *Proc Inst Mech Eng*, vol. 131, no. 3, pp. 3–103, 1935.

[144] K. Dang Van, B. Griveau, and O. Messagge, "On a New Multiaxial Fatigue Limit Criterion:

Theory and Application," in *Biaxial and Multiaxial Fatgue EGF3*, M. Brown and K. J. Miller, Eds. London: Mechanical Engineering Publications, 1989, pp. 479–96.

[145] I. V. Papadopoulos, "a High-Cycle Fatigue Criterion Applied in Biaxial and Triaxial Out-of-Phase Stress Conditions," *Fatigue Fract. Eng. Mater. Struct.*, vol. 18, no. 1, pp. 79–91, 1995.

[146] K. Liu, "A Method Based on Virtual Strain-Energy Parameters for Multiaxial Fatigue Life Prediction," in *Advances in Multiaxial Fatigue, ASTM STP 1191*, D. McDowell and R. Ellis, Eds. 1993, pp. 67–84.

[147] A. Fatemi and D. F. Socie, "Critical Plane Approach To Multiaxial Fatigue Damage Including Out-of-Phase Loading.," *Fatigue Fract. Eng. Mater. Struct.*, vol. 11, no. 3, pp. 149–165, 1988.

[148] M. W. Brown and K. J. Miller, "A theory for fatigue failure under multiaxial stress–strain conditions," *Arch. Proc. Inst. Mech. Eng. 1847-1982 (vols 1-196)*, vol. 187, no. 1973, pp. 745–755, 2006.

[149] L. Susmel and D. Taylor, "Fatigue design in the presence of stress concentrations," *J. Strain Anal. Eng. Des.*, vol. 38, no. 5, pp. 443–452, Jan. 2003.

[150] M. Endo and I. Ishimoto, "The fatigue strength of steels containing small holes under out-of-phase combined loading," *Int. J. Fatigue*, vol. 28, no. 5–6, pp. 592–597, May 2006.

[151] G. Kirsch, *Die Theorie der Elastizität und die Bedürfnisse der Festigkeitslehre*. Zeitschrift des Vereins deutscher Ingenieure, 1898.

[152] A. Carpinteri, L. Montanari, A. Spagnoli, and S. Vantadori, "Size and load effects on the biaxial fatigue resistance of holed structural components," 2011, pp. 147–155.

11. Annex A - Static data

The 1744 test samples reassessed in the validation of the proposed static assessment tool.

Data set B1
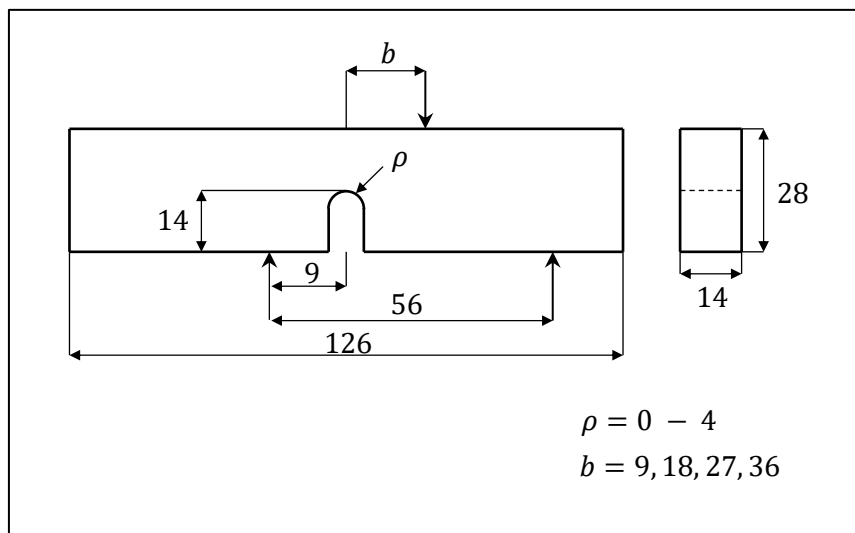
Figure 82: B1 [102]

Local strain energy to assess the static failure of U-notches in plates under mixed mode loading

F. J. Gómez · M. Elices · F. Berto · P. Lazzarin

Ref	Rho	Geometry	b (mm)	Fail load (N)	Load Mode
B1.1.1	0	TPB-U	9	1170	I+II
B1.1.2	0.2	TPB-U	9	1308	I+II

B1.1.3	0.3	TPB-U	9	1945	I+II
B1.1.4	0.5	TPB-U	9	2188	I+II
B1.1.5	1	TPB-U	9	2729	I+II
B1.1.6	2	TPB-U	9	3589	I+II
B1.1.7	4	TPB-U	9	4182	I+II
B1.2.1	0	TPB-U	18	1459	I+II
B1.2.2	0.2	TPB-U	18	1548	I+II
B1.2.3	0.3	TPB-U	18	2349	I+II
B1.2.4	0.5	TPB-U	18	2561	I+II
B1.2.5	1	TPB-U	18	3511	I+II
B1.2.6	2	TPB-U	18	4081	I+II
B1.2.7	4	TPB-U	18	5107	I+II
B1.3.1	0	TPB-U	27	1956	I+II
B1.3.2	0.2	TPB-U	27	2127	I+II
B1.3.3	0.3	TPB-U	27	3172	I+II
B1.3.4	0.5	TPB-U	27	3458	I+II
B1.3.5	1	TPB-U	27	4391	I+II
B1.3.6	2	TPB-U	27	5052	I+II
B1.3.7	4	TPB-U	27	6430	I+II
B1.4.1	0	TPB-U	36	2713	I+II
B1.4.2	0.2	TPB-U	36	3289	I+II
B1.4.3	0.3	TPB-U	36	4636	I+II
B1.4.4	0.5	TPB-U	36	4716	I+II
B1.4.5	1	TPB-U	36	6064	I+II
B1.4.6	2	TPB-U	36	7786	I+II
B1.4.7	4	TPB-U	36	9714	I+II

Data set B2
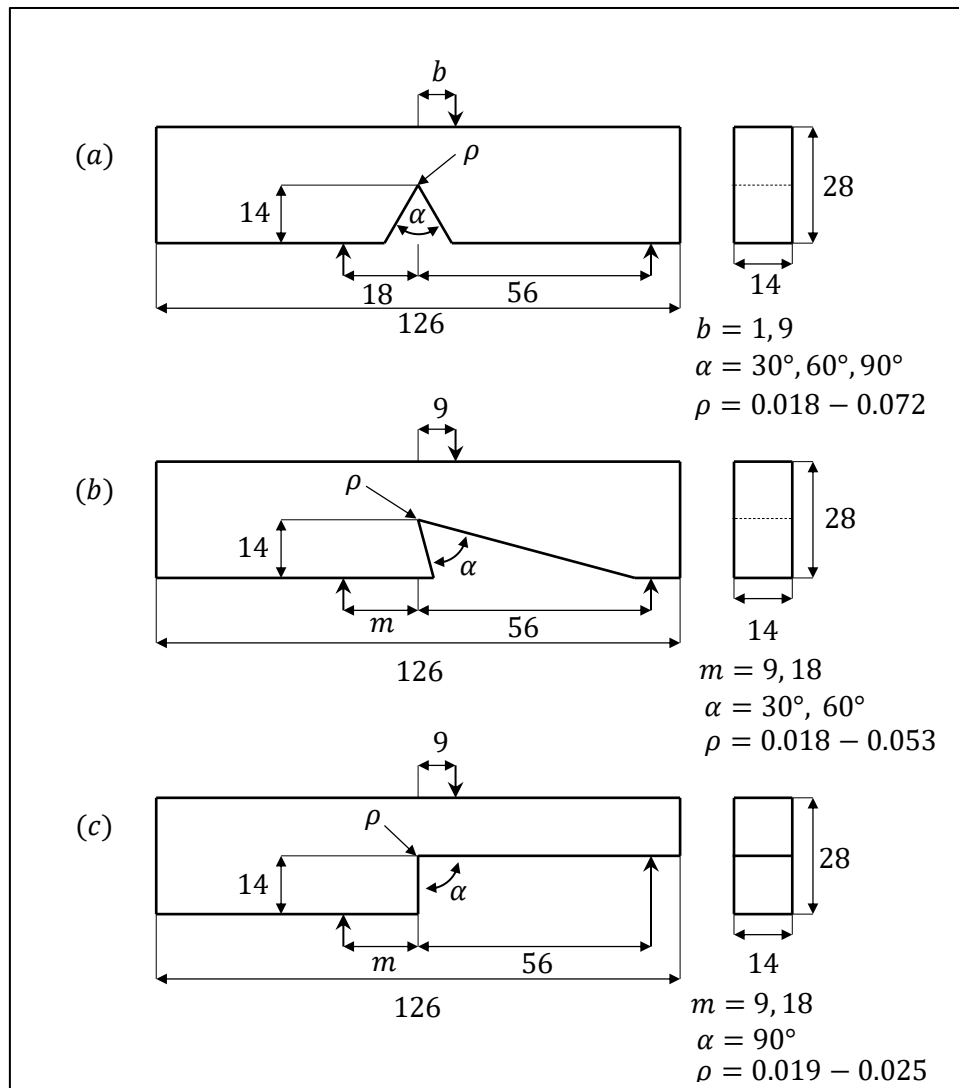
Figure 83: B2 [103]

Fracture of V-notched specimens under mixed mode (1+2) loading in brittle materials

F. J. Gómez · M. Elices · F. Berto · P. Lazzarin

Ref	Rho	Geometry	b (mm)	Fail load (N)	Load Mode
B2.1.1	0.045	TPB-V	1	813	I+II
B2.1.2	0.044	TPB-V	1	840	I+II
B2.1.3	0.032	TPB-V	1	860	I+II
B2.1.4	0.044	TPB-V	1	1047	I+II
B2.1.5	0.048	TPB-V	1	1017	I+II
B2.1.6	0.056	TPB-V	1	986	I+II
B2.1.7	0.032	TPB-V	1	856	I+II
B2.1.8	0.022	TPB-V	1	897	I+II
B2.1.9	0.02	TPB-V	1	894	I+II
B2.1.10	0.04	TPB-V	9	826	I+II
B2.1.11	0.044	TPB-V	9	940	I+II
B2.1.12	0.046	TPB-V	9	921	I+II
B2.1.13	0.066	TPB-V	9	1080	I+II
B2.1.14	0.072	TPB-V	9	1023	I+II
B2.1.15	0.063	TPB-V	9	1013	I+II
B2.1.16	0.018	TPB-V	9	923	I+II
B2.1.17	0.018	TPB-V	9	994	I+II
B2.1.18	0.023	TPB-V	9	961	I+II

Ref	Rho	Geometry	m	Fail load (N)	Load Mode
B2.2.1	0.026	TPB-V	9	2198	I+II
B2.2.2	0.016	TPB-V	9	2259	I+II
B2.2.3	0.033	TPB-V	9	2228	I+II
B2.2.4	0.05	TPB-V	9	3437	I+II
B2.2.5	0.053	TPB-V	9	3138	I+II
B2.2.6	0.052	TPB-V	9	3221	I+II
B2.2.7	0.022	TPB-V	9	3979	I+II
B2.2.8	0.016	TPB-V	9	5166	I+II
B2.2.9	0.018	TPB-V	9	4345	I+II
B2.2.10	0.028	TPB-V	18	1401	I+II
B2.2.11	0.03	TPB-V	18	1256	I+II

B2.2.12	0.022	TPB-V	18	1369	I+II
B2.2.13	0.045	TPB-V	18	1430	I+II
B2.2.14	0.041	TPB-V	18	1476	I+II
B2.2.15	0.042	TPB-V	18	1410	I+II
B2.2.16	0.019	TPB-V	18	1525	I+II
B2.2.17	0.022	TPB-V	18	1676	I+II
B2.2.18	0.025	TPB-V	18	1567	I+II

Data set B3
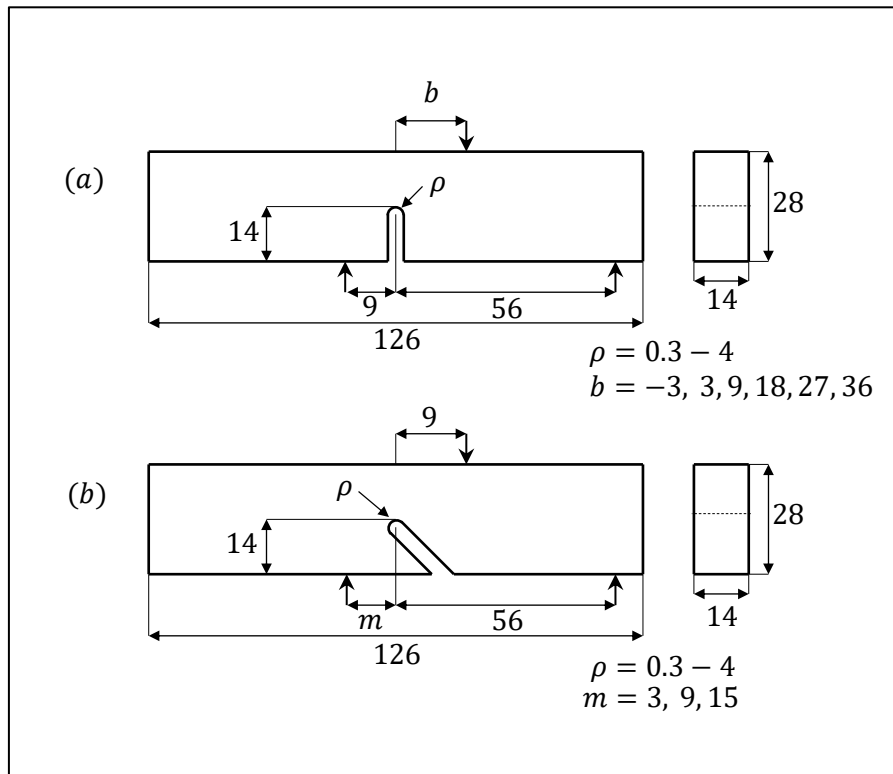
Figure 84: B3 [104]

Fracture of U-Notched specimens under mixed mode experimental results and numerical predictions

F. J. Gómez · M. Elices · F. Berto · P. Lazzarin

Ref	Rho	Geometry	b	Fail load (N)	Load Mode
B3.1.1	0	TPB-U	-3	2202	I+II
B3.1.2	0.3	TPB-U	-3	3168	I+II
B3.1.3	0.5	TPB-U	-3	3625	I+II
B3.1.4	1	TPB-U	-3	4605	I+II
B3.1.5	2	TPB-U	-3	6027	I+II
B3.1.6	4	TPB-U	-3	7003	I+II
B3.2.1	0	TPB-U	3	1419	I+II

Ref	Rho	Geometry	m	Fail load (N)	Load Mode
B3.2.2	0.3	TPB-U	3	2192	I+II
B3.2.3	0.5	TPB-U	3	2535	I+II
B3.2.4	1	TPB-U	3	2874	I+II
B3.2.5	2	TPB-U	3	3798	I+II
B3.2.6	4	TPB-U	3	4668	I+II
B3.3.1	0	TPB-U	9	1170	I+II
B3.3.2	0.3	TPB-U	9	1949	I+II
B3.3.3	0.5	TPB-U	9	2188	I+II
B3.3.4	1	TPB-U	9	2729	I+II
B3.3.5	2	TPB-U	9	3589	I+II
B3.3.6	4	TPB-U	9	4182	I+II
B3.4.1	0	TPB-U	18	1459	I+II
B3.4.2	0.3	TPB-U	18	2349	I+II
B3.4.3	0.5	TPB-U	18	2561	I+II
B3.4.4	1	TPB-U	18	3511	I+II
B3.4.5	2	TPB-U	18	4081	I+II
B3.4.6	4	TPB-U	18	5107	I+II
B3.5.1	0	TPB-U	27	1956	I+II
B3.5.2	0.3	TPB-U	27	3172	I+II
B3.5.3	0.5	TPB-U	27	3458	I+II
B3.5.4	1	TPB-U	27	4391	I+II
B3.5.5	2	TPB-U	27	4984	I+II
B3.5.6	4	TPB-U	27	6430	I+II
B3.6.1	0	TPB-U	36	2713	I+II
B3.6.2	0.3	TPB-U	36	4636	I+II
B3.6.3	0.5	TPB-U	36	4716	I+II
B3.6.4	1	TPB-U	36	6064	I+II
B3.6.5	2	TPB-U	36	7786	I+II
B3.6.6	4	TPB-U	36	9714	I+II

Ref	Rho	Geometry	m	Fail load (N)	Load Mode
B3.7.1	0.3	TPB-U	3	4307	I+II
B3.7.2	0.5	TPB-U	3	4523	I+II
B3.7.3	1	TPB-U	3	5201	I+II
B3.7.4	2	TPB-U	3	6105	I+II

B3.7.5	4	TPB-U	3	6434	I+II
B3.8.1	0.3	TPB-U	9	2421	I+II
B3.8.2	0.5	TPB-U	9	2418	I+II
B3.8.3	1	TPB-U	9	3166	I+II
B3.8.4	2	TPB-U	9	3775	I+II
B3.8.5	4	TPB-U	9	4294	I+II
B3.9.1	0.4	TPB-U	15	1757	I+II
B3.9.2	0.5	TPB-U	15	1784	I+II
B3.9.3	1	TPB-U	15	2345	I+II
B3.9.4	2	TPB-U	15	2921	I+II
B3.9.5	4	TPB-U	15	3409	I+II

Data set B4
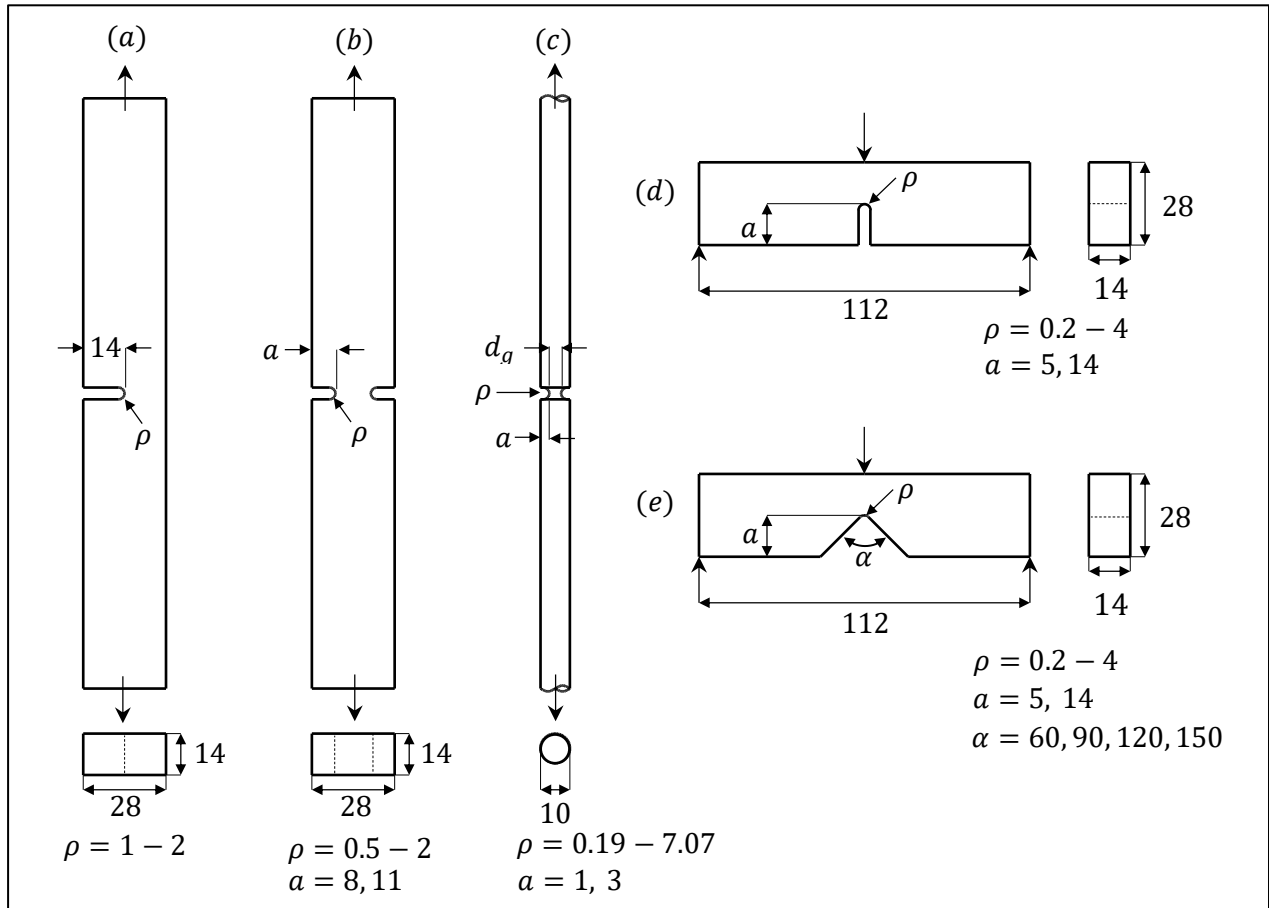
Figure 85: B4 [105]

The Cohesive crack concept : Application to PMMA at -60C

F.J. Gomez, M.Elices, J Planas

Ref	Rho	Geometry	Fail load (N)	Load Mode
B4.1.1	0.97	SENT	2860	I
B4.1.2	1.47	SENT	2900	I
B4.1.3	1.99	SENT	3900	I
B4.2.1	0.53	DENT	6400	I
B4.2.2	0.97	DENT	7600	I
B4.2.3	1.46	DENT	8940	I
B4.2.4	1.91	DENT	9890	I

207

B4.2.5	0.52	DENT	4000	I
B4.2.6	1.01	DENT	5000	I
B4.2.7	1.46	DENT	5700	I
B4.2.8	1.96	DENT	7000	I
B4.3.1	0.19	RNC	2500	I
B4.3.2	2.13	RNC	4680	I
B4.3.3	4.06	RNC	5200	I
B4.3.4	7.07	RNC	5200	I
B4.3.5	2.1	RNC	1460	I
B4.3.6	4	RNC	1450	I
B4.3.7	7.05	RNC	1580	I
B4.4.1	0.19	UN-TPB	1080	I
B4.4.2	0.34	UN-TPB	1690	I
B4.4.3	0.52	UN-TPB	1840	I
B4.4.4	0.94	UN-TPB	2220	I
B4.4.5	1.47	UN-TPB	2510	I
B4.4.6	1.97	UN-TPB	2670	I
B4.4.7	3.98	UN-TPB	3200	I
B4.4.8	0.18	UN-TPB	430	I
B4.4.9	0.34	UN-TPB	690	I
B4.4.10	0.53	UN-TPB	730	I
B4.4.11	0.93	UN-TPB	920	I
B4.4.12	1.46	UN-TPB	1060	I
B4.4.13	1.97	UN-TPB	1150	I
B4.4.14	3.98	UN-TPB	1300	I
B4.5.1	0.04	VN-TPB	460	I
B4.5.2	0.05	VN-TPB	1190	I
B4.5.3	0.06	VN-TPB	770	I
B4.5.4	0.04	VN-TPB	510	I
B4.5.5	0.47	VN-TPB	660	I
B4.5.6	0.84	VN-TPB	880	I
B4.5.7	0.06	VN-TPB	190	I
B4.5.8	0.06	VN-TPB	570	I
B4.5.9	0.43	VN-TPB	830	I
B4.5.10	0.83	VN-TPB	960	I

B4.5.11	0.06	VN-TPB	990	I
B4.5.12	2	VN-TPB	1400	I
B4.5.13	2.4	VN-TPB	1500	I

Data set B5
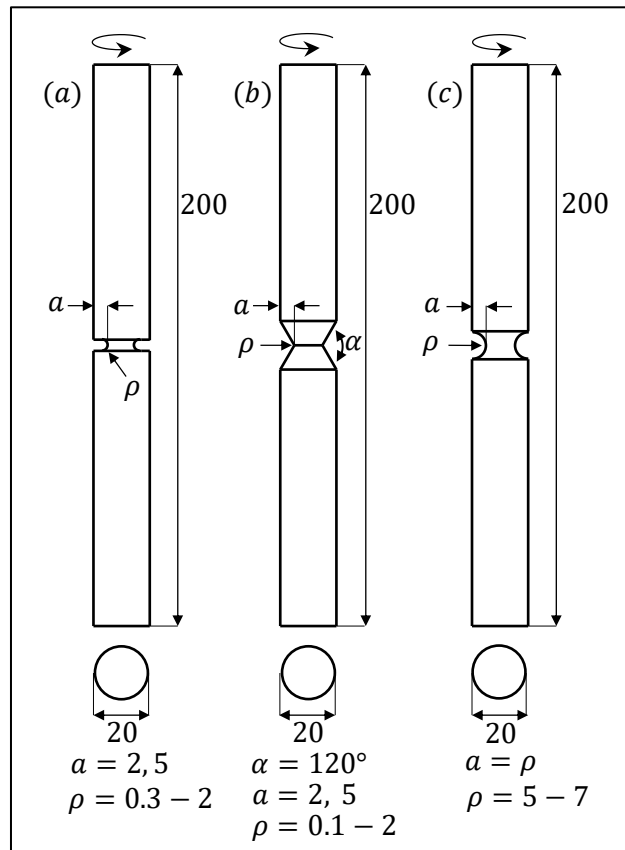
Figure 86: B5 [106]

Fracture behaviour of notched round bars made of PMMA subjected to torsion at -60 degrees C

F. Berto, D.A. Cendon, P. Lazzarin, M. Elices

Ref	Rho	Geometry	Fail load (Nm)	Load Mode
B5.1.1	0.3	RNC-U	20	III
B5.1.2	0.5	RNC-U	27	III

B5.1.3	1	RNC-U	30	III
B5.1.4	2	RNC-U	32	III
B5.1.5	0.3	RNC-U	106	III
B5.1.6	0.5	RNC-U	111	III
B5.1.7	1	RNC-U	105	III
B5.2.1	0.1	RNC-V	26	III
B5.2.2	0.3	RNC-V	21	III
B5.2.3	0.5	RNC-V	19	III
B5.2.4	1	RNC-V	32	III
B5.2.5	2	RNC-V	32	III
B5.2.6	0.1	RNC-U	105	III
B5.2.7	0.3	RNC-U	84	III
B5.2.8	0.5	RNC-U	77	III
B5.2.9	1	RNC-U	107	III
B5.3.1	5	RNC-U	29	III
B5.3.2	6	RNC-U	16	III
B5.3.3	7	RNC-U	7	III

Data set B6
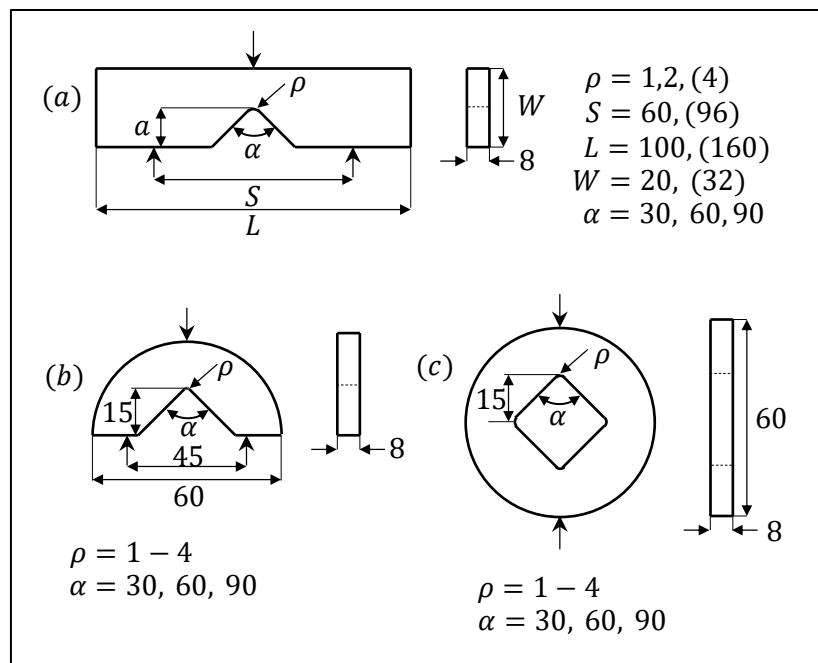
Figure 87: B6 [107]

Tensile Fracture in notched polycrystalline graphite specimens

M,R, Ayatollahi. A,R. Torabi

Ref	Rho	Geometry	Fail load (N)	Load Mode
B6.1.1	1	RV-TPB	158	I
B6.1.2	2	RV-TPB	188	I
B6.1.3	4	RV-TPB	290	I
B6.1.4	1	RV-TPB	169	I
B6.1.5	2	RV-TPB	207	I
B6.1.6	4	RV-TPB	321	I
B6.1.7	1	RV-TPB	166	I

B6.1.8	2	RV-TPB	201		I
B6.1.9	4	RV-TPB	315		I
B6.2.1	1	RV-SCB	541		I
B6.2.2	2	RV-SCB	613		I
B6.2.3	4	RV-SCB	680		I
B6.2.4	1	RV-SCB	490		I
B6.2.5	2	RV-SCB	579		I
B6.2.6	4	RV-SCB	731		I
B6.2.7	1	RV-SCB	517		I
B6.2.8	2	RV-SCB	584		I
B6.2.9	4	RV-SCB	633		I
B6.3.1	1	RV-BD	1902		I
B6.3.2	2	RV-BD	2023		I
B6.3.3	4	RV-BD	2095		I
B6.3.4	1	RV-BD	1439		I
B6.3.5	2	RV-BD	1646		I
B6.3.6	4	RV-BD	1722		I
B6.3.7	1	RV-BD	910		I
B6.3.8	2	RV-BD	993		I
B6.3.9	4	RV-BD	1140		I

Data sets B7, Q-B3 and Q-B4

Reference	D	a	t	α	β
B7 [7]	80	20	6	30°, 60°, 90°	0° − 35°
QB3 [8]	80	20	10	30°, 60°, 90°	0° − 35°
QB4 [9]	80	20	10	30°, 60°, 90°	0° − 35°

Figure 88: B7 [108]**, QB3** [114]**, QB4** [115]

Experimental verification of RV-MTS model for fracture in soda-lime glass weakened by a V-notch

M,R, Ayatollahi. A.R Torabi.

Ref	Rho	Geometry	2alpha (Load angle)	Fail load (N)	Load Mode
B7.1.1	1	V-BD	30 (0)	1730	I
B7.1.2	2	V-BD	30 (0)	2100	I

B7.1.3	4	V-BD	30 (0)	2460	I
B7.1.4	1	V-BD	30 (5)	1680	I+II
B7.1.5	2	V-BD	30 (5)	1810	I+II
B7.1.6	4	V-BD	30 (5)	2005	I+II
B7.1.7	1	V-BD	30 (10)	1780	I+II
B7.1.8	2	V-BD	30 (10)	2003	I+II
B7.1.9	4	V-BD	30 (10)	2080	I+II
B7.1.10	1	V-BD	30 (15)	1600	I+II
B7.1.11	2	V-BD	30 (15)	1810	I+II
B7.1.12	4	V-BD	30 (15)	2150	I+II
B7.1.13	1	V-BD	30 (20)	1580	I+II
B7.1.14	2	V-BD	30 (20)	1910	I+II
B7.1.15	4	V-BD	30 (20)	2001	I+II
B7.1.16	1	V-BD	30 (25)	1980	II
B7.1.17	2	V-BD	30 (25)	1890	II
B7.1.18	4	V-BD	30 (25)	2111	II
B7.2.1	1	V-BD	60 (0)	1280	I
B7.2.2	2	V-BD	60 (0)	1680	I
B7.2.3	4	V-BD	60 (0)	2125	I
B7.2.4	1	V-BD	60 (5)	1200	I+II
B7.2.5	2	V-BD	60 (5)	1653	I+II
B7.2.6	4	V-BD	60 (5)	1860	I+II
B7.2.7	1	V-BD	60 (15)	1280	I+II
B7.2.8	2	V-BD	60 (15)	1680	I+II
B7.2.9	4	V-BD	60 (15)	1730	I+II
B7.2.10	1	V-BD	60 (20)	1550	I+II
B7.2.11	2	V-BD	60 (20)	1730	I+II
B7.2.12	4	V-BD	60 (20)	1900	I+II
B7.2.13	1	V-BD	60 (25)	1654	I+II
B7.2.14	2	V-BD	60 (25)	1860	I+II
B7.2.15	4	V-BD	60 (25)	1910	I+II
B7.2.16	1	V-BD	60 (30)	1930	II
B7.2.17	2	V-BD	60 (30)	1935	II
B7.2.18	4	V-BD	60 (30)	2030	II
B7.3.1	1	V-BD	90 (0)	850	I

Ref		Geometry	2alpha (Load angle)	Fail load (N)	Mode
B7.3.2	2	V-BD	90 (0)	1095	I
B7.3.3	4	V-BD	90 (0)	1365	I
B7.3.4	1	V-BD	90 (5)	901	I+II
B7.3.5	2	V-BD	90 (5)	1116	I+II
B7.3.6	4	V-BD	90 (5)	1210	I+II
B7.3.7	1	V-BD	90 (15)	1072	I+II
B7.3.8	2	V-BD	90 (15)	1080	I+II
B7.3.9	4	V-BD	90 (15)	1320	I+II
B7.3.10	1	V-BD	90 (20)	1220	I+II
B7.3.11	2	V-BD	90 (20)	1280	I+II
B7.3.12	4	V-BD	90 (20)	1485	I+II
B7.3.13	1	V-BD	90 (30)	1700	I+II
B7.3.14	2	V-BD	90 (30)	1910	I+II
B7.3.15	4	V-BD	90 (30)	1930	I+II
B7.3.16	1	V-BD	90 (35)	2233	II
B7.3.17	2	V-BD	90 (35)	2280	II
B7.3.18	4	V-BD	90 (35)	2250	II

Experimental and Theroretical Assessment of Brittle Fracture in Engineering Components Containing a Sharp V-notch

M,R, Ayatollahi. A.R Torabi. P, Azizi

Ref	Rho	Geometry	2alpha (Load angle)	Fail load (N)
Q-B3.1.1	0.053	SV-BD	5129	I
Q-B3.1.2	0.056	SV-BD	5462	I
Q-B3.1.3	0.057	SV-BD	5485	I
Q-B3.1.4	0.054	SV-BD	6016	I+II
Q-B3.1.5	0.053	SV-BD	6776	I+II
Q-B3.1.6	0.056	SV-BD	6160	I+II
Q-B3.1.7	0.053	SV-BD	5960	I+II
Q-B3.1.8	0.055	SV-BD	6024	I+II
Q-B3.1.9	0.06	SV-BD	6446	I+II
Q-B3.1.10	0.054	SV-BD	5784	I+II
Q-B3.1.11	0.053	SV-BD	5504	I+II

Q-B3.1.12	0.053	SV-BD	4684	I+II
Q-B3.1.13	0.056	SV-BD	5462	II
Q-B3.1.14	0.057	SV-BD	5440	II
Q-B3.1.15	0.053	SV-BD	5393	II
Q-B3.2.1	0.056	SV-BD	3211	I
Q-B3.2.2	0.054	SV-BD	3328	I
Q-B3.2.3	0.056	SV-BD	4251	I
Q-B3.2.4	0.057	SV-BD	3720	I+II
Q-B3.2.5	0.058	SV-BD	3759	I+II
Q-B3.2.6	0.052	SV-BD	4511	I+II
Q-B3.2.7	0.059	SV-BD	3883	I+II
Q-B3.2.8	0.063	SV-BD	3470	I+II
Q-B3.2.9	0.061	SV-BD	4336	I+II
Q-B3.2.10	0.054	SV-BD	5027	I+II
Q-B3.2.11	0.057	SV-BD	5426	I+II
Q-B3.2.12	0.058	SV-BD	5214	I+II
Q-B3.2.13	0.058	SV-BD	6448	II
Q-B3.2.14	0.056	SV-BD	6513	II
Q-B3.2.15	0.05	SV-BD	6604	II
Q-B3.3.1	0.056	SV-BD	2093	I
Q-B3.3.2	0.057	SV-BD	1989	I
Q-B3.3.3	0.058	SV-BD	2223	I
Q-B3.3.4	0.054	SV-BD	2129	I+II
Q-B3.3.5	0.054	SV-BD	2306	I+II
Q-B3.3.6	0.056	SV-BD	2335	I+II
Q-B3.3.7	0.056	SV-BD	3704	I+II
Q-B3.3.8	0.057	SV-BD	3226	I+II
Q-B3.3.9	0.065	SV-BD	3317	I+II
Q-B3.3.10	0.056	SV-BD	6770	I+II
Q-B3.3.11	0.057	SV-BD	6842	I+II
Q-B3.3.12	0.058	SV-BD	6128	I+II
Q-B3.3.13	0.053	SV-BD	7425	II
Q-B3.3.14	0.058	SV-BD	8303	II
Q-B3.3.15	0.056	SV-BD	7358	II

Fracture assessment of Brazilian disc specimens weakened by blunt V-notches under mixed mode loading by means of local energy

F, Berto. M.R, Ayatollahi

Ref	Rho	Geometry	Load angle (°)	Fail load (N)	Load Mode
Q-B4.1.1	1	RV-BD	0	5300	I
Q-B4.1.2	1	RV-BD	5	4780	I+II
Q-B4.1.3	1	RV-BD	10	4300	I+II
Q-B4.1.4	1	RV-BD	15	4500	I+II
Q-B4.1.5	1	RV-BD	20	4200	I+II
Q-B4.1.6	1	RV-BD	25	4500	II
Q-B4.1.7	2	RV-BD	0	5900	I
Q-B4.1.8	2	RV-BD	5	5600	I+II
Q-B4.1.9	2	RV-BD	10	5700	I+II
Q-B4.1.10	2	RV-BD	15	5600	I+II
Q-B4.1.11	2	RV-BD	20	5180	I+II
Q-B4.1.12	2	RV-BD	25	5200	II
Q-B4.1.13	4	RV-BD	0	6100	I
Q-B4.1.14	4	RV-BD	5	5900	I+II
Q-B4.1.15	4	RV-BD	10	6400	I+II
Q-B4.1.16	4	RV-BD	15	6150	I+II
Q-B4.1.17	4	RV-BD	20	5400	I+II
Q-B4.1.18	4	RV-BD	25	5800	II
Q-B4.2.1	1	RV-BD	0	4000	I
Q-B4.2.2	1	RV-BD	5	3900	I+II
Q-B4.2.3	1	RV-BD	10	3800	I+II
Q-B4.2.4	1	RV-BD	15	3800	I+II
Q-B4.2.5	1	RV-BD	25	4700	I+II
Q-B4.2.6	1	RV-BD	30	5500	II
Q-B4.2.7	2	RV-BD	0	4800	I
Q-B4.2.8	2	RV-BD	5	4400	I+II
Q-B4.2.9	2	RV-BD	10	4700	I+II
Q-B4.2.10	2	RV-BD	15	4500	I+II
Q-B4.2.11	2	RV-BD	25	4500	I+II
Q-B4.2.12	2	RV-BD	30	5200	II
Q-B4.2.13	4	RV-BD	0	5200	I

Q-B4.2.14	4	RV-BD	5	5100	I+II
Q-B4.2.15	4	RV-BD	10	5100	I+II
Q-B4.2.16	4	RV-BD	15	5100	I+II
Q-B4.2.17	4	RV-BD	25	5400	I+II
Q-B4.2.18	4	RV-BD	30	6100	II
Q-B4.3.1	1	RV-BD	0	2200	I
Q-B4.3.2	1	RV-BD	5	2200	I+II
Q-B4.3.3	1	RV-BD	10	2400	I+II
Q-B4.3.4	1	RV-BD	20	3100	I+II
Q-B4.3.5	1	RV-BD	25	4100	I+II
Q-B4.3.6	1	RV-BD	35	7600	II
Q-B4.3.7	2	RV-BD	0	2900	I
Q-B4.3.8	2	RV-BD	5	2900	I+II
Q-B4.3.9	2	RV-BD	10	3200	I+II
Q-B4.3.10	2	RV-BD	20	3400	I+II
Q-B4.3.11	2	RV-BD	25	4000	I+II
Q-B4.3.12	2	RV-BD	35	6100	II
Q-B4.3.13	4	RV-BD	0	3500	I
Q-B4.3.14	4	RV-BD	5	3700	I+II
Q-B4.3.15	4	RV-BD	10	3900	I+II
Q-B4.3.16	4	RV-BD	20	4300	I+II
Q-B4.3.17	4	RV-BD	25	4500	I+II
Q-B4.3.18	4	RV-BD	35	6800	II

Data set B8
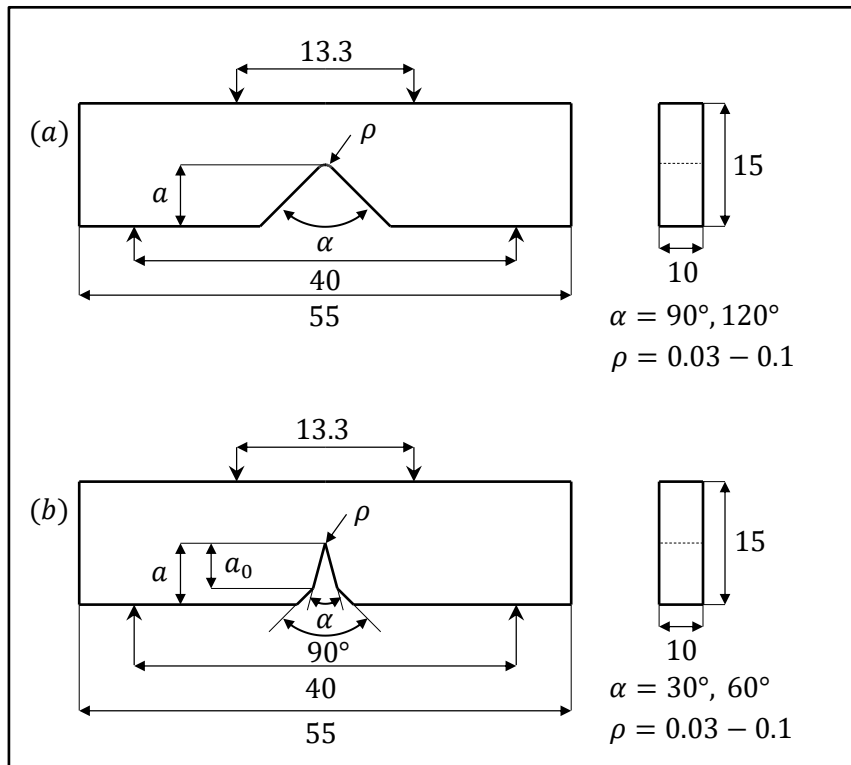
Figure 89: B8 [109]

Failure criteria for brittle elastic materials

Z. Yosibash, A. Bussiba, I Gilad

Ref	Rho	Geometry	Opening angle	Fail load (N)	Load Mode
B8.1.1	0.031	FPB-V	30	1815	I
B8.1.2	0.034	FPB-V	30	1933	I
B8.1.3	0.04	FPB-V	30	1799	I
B8.1.4	0.041	FPB-V	30	1628	I
B8.1.5	0.041	FPB-V	30	1942	I
B8.1.6	0.041	FPB-V	30	2060	I
B8.1.7	0.041	FPB-V	30	1942	I

B8.1.8	0.043	FPB-V	30	1662	I
B8.1.9	0.06	FPB-V	30	1628	I
B8.1.10	0.06	FPB-V	30	1628	I
B8.1.11	0.06	FPB-V	30	1560	I
B8.1.12	0.06	FPB-V	30	1717	I
B8.1.13	0.1	FPB-V	30	1844	I
B8.1.14	0.1	FPB-V	30	1805	I
B8.1.15	0.1	FPB-V	30	1991	I
B8.1.16	0.1	FPB-V	30	1962	I
B8.1.17	0.04	FPB-V	30	1594	I
B8.1.18	0.04	FPB-V	30	1436	I
B8.1.19	0.06	FPB-V	30	1439	I
B8.1.20	0.06	FPB-V	30	1413	I
B8.2.1	0.055	FPB-V	60	1874	I
B8.2.2	0.055	FPB-V	60	1962	I
B8.2.3	0.055	FPB-V	60	1953	I
B8.2.4	0.06	FPB-V	60	1972	I
B8.2.5	0.06	FPB-V	60	1753	I
B8.2.6	0.06	FPB-V	60	1701	I
B8.2.7	0.06	FPB-V	60	1721	I
B8.2.8	0.06	FPB-V	60	1658	I
B8.2.9	0.06	FPB-V	60	1603	I
B8.2.10	0.06	FPB-V	60	1526	I
B8.2.11	0.06	FPB-V	60	1680	I
B8.2.12	0.07	FPB-V	60	1895	I
B8.2.13	0.1	FPB-V	60	1785	I
B8.2.14	0.1	FPB-V	60	1903	I
B8.2.15	0.1	FPB-V	60	1913	I
B8.2.16	0.055	FPB-V	60	1736	I
B8.3.1	0.028	FPB-V	90	2080	I
B8.3.2	0.033	FPB-V	90	1810	I
B8.3.3	0.034	FPB-V	90	1884	I
B8.3.4	0.034	FPB-V	90	1785	I
B8.3.5	0.035	FPB-V	90	1853	I
B8.3.6	0.037	FPB-V	90	1821	I

B8.3.7	0.041	FPB-V	90	1805	I
B8.3.8	0.042	FPB-V	90	1847	I
B8.3.9	0.042	FPB-V	90	1838	I
B8.3.10	0.05	FPB-V	90	1878	I
B8.3.11	0.06	FPB-V	90	1974	I
B8.3.12	0.06	FPB-V	90	2144	I
B8.3.13	0.06	FPB-V	90	2167	I
B8.3.14	0.06	FPB-V	90	2244	I
B8.3.15	0.06	FPB-V	90	2478	I
B8.3.16	0.067	FPB-V	90	1292	I
B8.3.17	0.1	FPB-V	90	1523	I
B8.3.18	0.1	FPB-V	90	1642	I
B8.3.19	0.1	FPB-V	90	1461	I
B8.3.20	0.1	FPB-V	90	1724	I
B8.4.1	0.06	FPB-V	120	2551	I
B8.4.2	0.062	FPB-V	120	2580	I
B8.4.3	0.068	FPB-V	120	2442	I
B8.4.4	0.08	FPB-V	120	2659	I
B8.4.5	0.08	FPB-V	120	2266	I
B8.4.6	0.08	FPB-V	120	2931	I
B8.4.7	0.08	FPB-V	120	2655	I
B8.4.8	0.083	FPB-V	120	2928	I
B8.4.9	0.096	FPB-V	120	2892	I
B8.4.10	0.1	FPB-V	120	1962	I
B8.4.11	0.1	FPB-V	120	1927	I
B8.4.12	0.1	FPB-V	120	1805	I
B8.4.13	0.1	FPB-V	120	1958	I
B8.4.14	0.1	FPB-V	120	1893	I
B8.4.15	0.1	FPB-V	120	2053	I

Data set B9
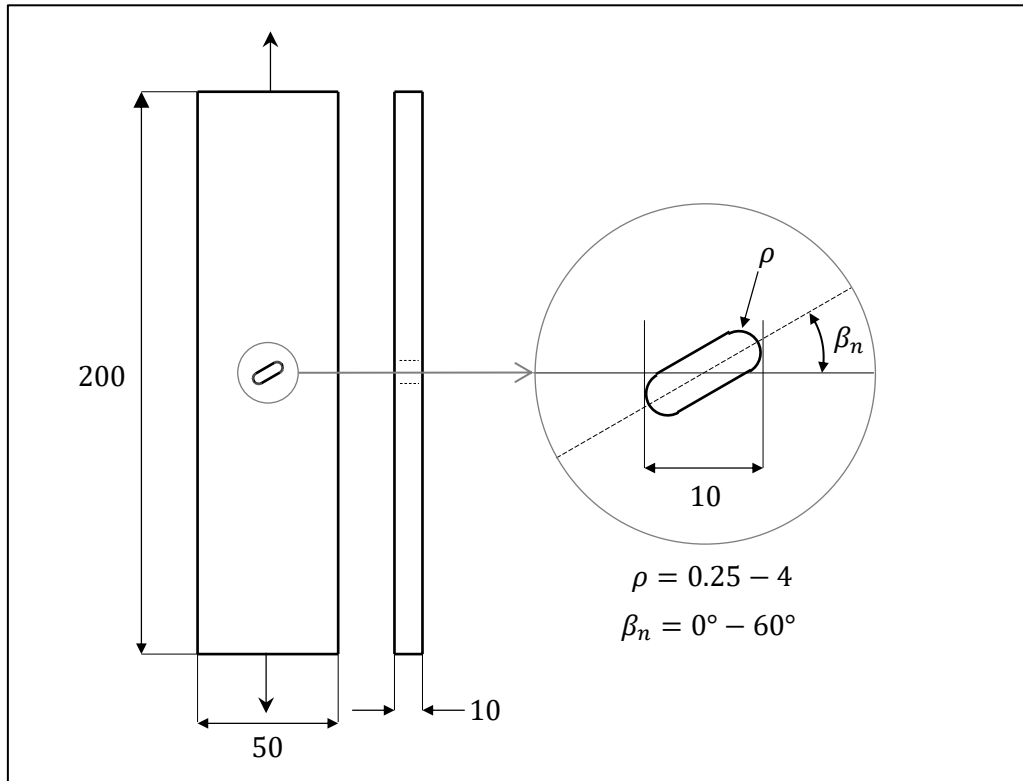
Figure 90: B9 [110]

Brittle fracture of U-notched graphite plates under mixed mode loading

F. Berto, P. Lazzarin, C. Marangon

Ref	Rho	Geometry	Notch Angle	Fail load (N)	Load Mode
B9.1.1	0.25	IB-T	0	4426	I
B9.1.2	0.5	IB-T	0	4505	I
B9.1.3	1	IB-T	0	4814	I
B9.1.4	2	IB-T	0	5516	I
B9.1.5	4	IB-T	0	6789	I
B9.2.1	0.25	IB-T	30	4034	I+II
B9.2.2	0.5	IB-T	30	4349	I+II

B9.2.3	1	IB-T	30	4824	I+II
B9.2.4	2	IB-T	30	5916	I+II
B9.2.5	4	IB-T	30	6886	I+II
B9.3.1	0.25	IB-T	45	3927	I+II
B9.3.2	0.5	IB-T	45	4261	I+II
B9.3.3	1	IB-T	45	4777	I+II
B9.3.4	2	IB-T	45	5606	I+II
B9.3.5	4	IB-T	45	6862	I+II
B9.4.1	0.25	IB-T	60	3942	I+II
B9.4.2	0.5	IB-T	60	4551	I+II
B9.4.3	1	IB-T	60	4779	I+II
B9.4.4	2	IB-T	60	5455	I+II
B9.4.5	4	IB-T	60	6749	I+II

Data set B10
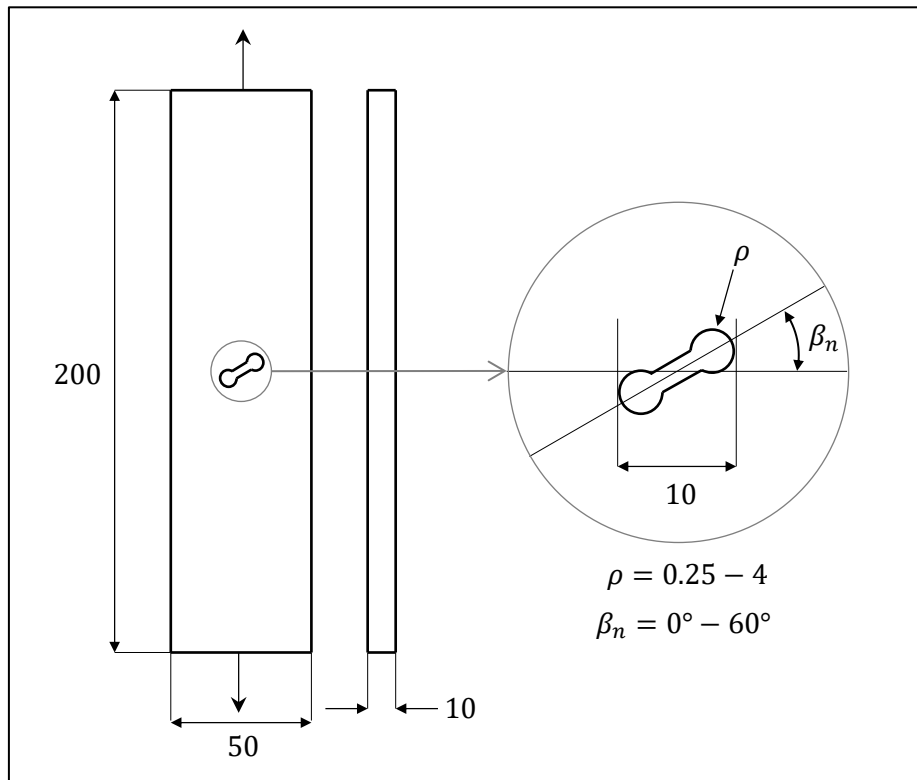
Figure 91: B10 [111]

Brittle Failure of inclined key-hole notches in isostatic graphite under in-plane Mixed mode loading
P. Lazzarin, F. Berto and M.R. Ayatollahi

Ref	Rho	Geometry	Notch Angle	Fail load (N)	Load Mode
B10.1.1	0.25	KH-T	0	3967	I
B10.1.2	0.5	KH-T	0	4059	I
B10.1.3	1	KH-T	0	3998	I
B10.1.4	2	KH-T	0	4967	I
B10.1.5	4	KH-T	0	4910	I
B10.2.1	0.25	KH-T	30	3991	I+II
B10.2.2	0.5	KH-T	30	4022	I+II

B10.2.3	1	KH-T	30	4125	I+II
B10.2.4	2	KH-T	30	4609	I+II
B10.2.5	4	KH-T	30	4775	I+II
B10.3.1	0.25	KH-T	45	3786	I+II
B10.3.2	0.5	KH-T	45	3892	I+II
B10.3.3	1	KH-T	45	4121	I+II
B10.3.4	2	KH-T	45	4972	I+II
B10.3.5	4	KH-T	45	4777	I+II
B10.4.1	0.25	KH-T	60	3995	I+II
B10.4.2	0.5	KH-T	60	3856	I+II
B10.4.3	1	KH-T	60	4114	I+II
B10.4.4	2	KH-T	60	4496	I+II
B10.4.5	4	KH-T	60	4553	I+II

Data set Q-B1

a (mm) table:

	a (mm)	α (°)	D (mm)
Set 1	14	15, 30, 60, 90, 120, 150	28
Set 2	5, 10, 14, 20	90	28
Set 3	4.5, 8,14, 28	90	9, 16, 28, 56
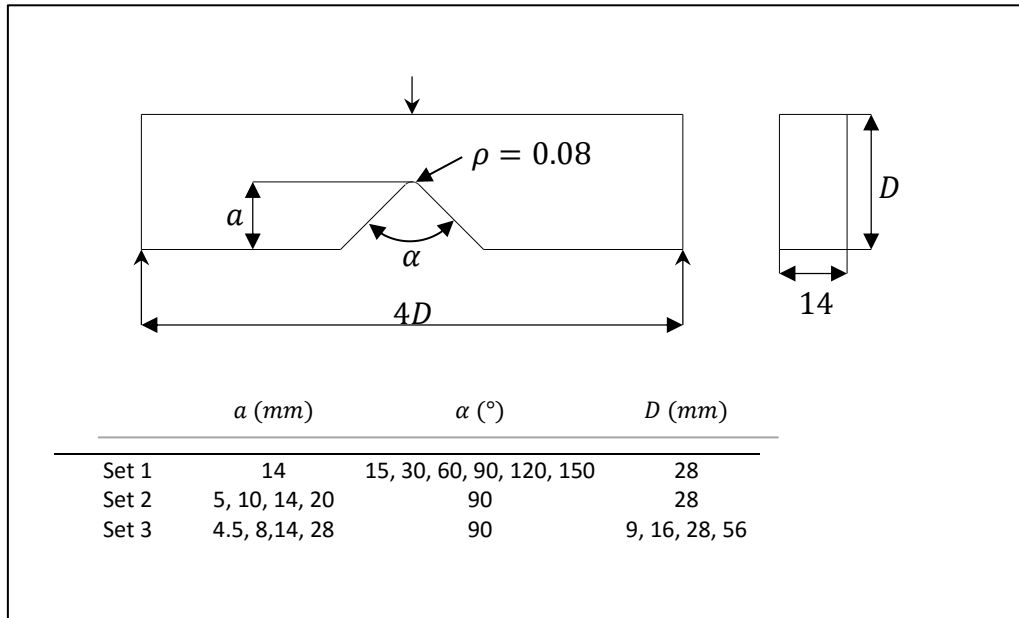
Figure 92: QB1 [112]

Fracture of Components with V-shaped notches

F.J. Gomez, M.Elices

Ref	Rho	Geometry	Fail load (N)	Load Mode
Q-B1.1.1	0.08	TPB-V	190	I
Q-B1.1.2	0.08	TPB-V	240	I
Q-B1.1.3	0.08	TPB-V	210	I
Q-B1.1.4	0.08	TPB-V	240	I
Q-B1.1.5	0.08	TPB-V	490	I
Q-B1.1.6	0.08	TPB-V	800	I
Q-B1.2.1	0.08	TPB-V	650	I
Q-B1.2.2	0.08	TPB-V	440	I
Q-B1.2.3	0.08	TPB-V	240	I
Q-B1.2.4	0.08	TPB-V	124	I

Q-B1.3.1	0.08	TPB-V	139	I
Q-B1.3.2	0.08	TPB-V	190	I
Q-B1.3.3	0.08	TPB-V	240	I
Q-B1.3.4	0.08	TPB-V	390	I

Data set Q-B2
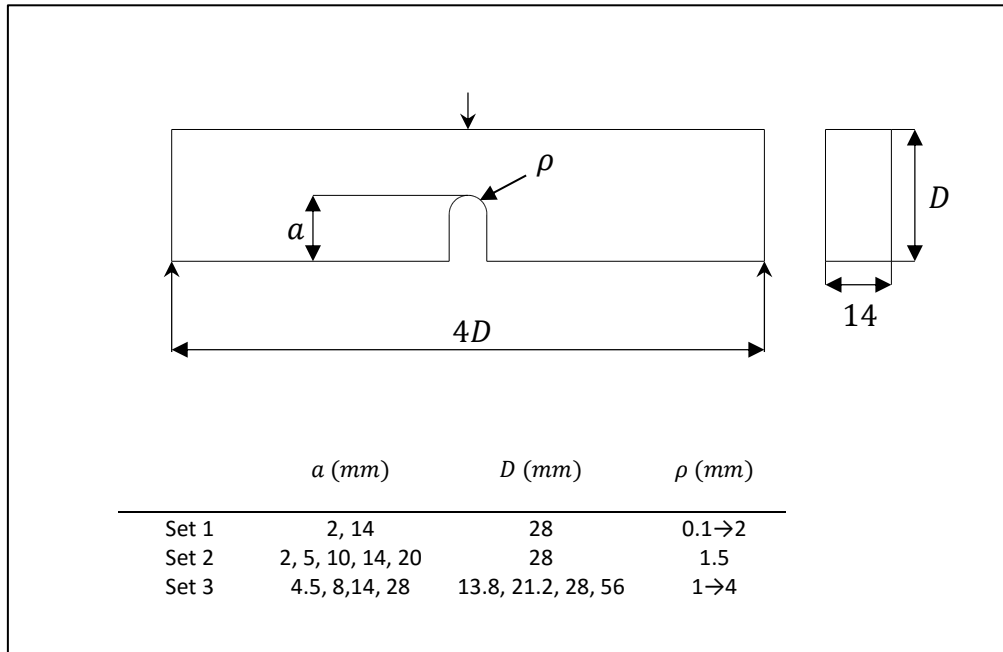
Figure 93: QB2 [113]

Cracking in PMMA containning U-shaped notches

F.J. Gomez, M.Elices. A. Valiente

Ref	Rho	Geometry	Fail load (N)	Load Mode
Q-B2.1.1	0.5	TPB-U	1900	I
Q-B2.1.2	1	TPB-U	2700	I
Q-B2.1.3	2	TPB-U	3000	I
Q-B2.1.4	0.11	TPB-U	350	I
Q-B2.1.5	0.13	TPB-U	340	I
Q-B2.1.6	0.2	TPB-U	410	I
Q-B2.1.7	0.5	TPB-U	600	I
Q-B2.1.8	1	TPB-U	710	I
Q-B2.1.9	1.5	TPB-U	800	I
Q-B2.1.10	2	TPB-U	920	I
Q-B2.2.1	1.5	TPB-U	2700	I
Q-B2.2.2	1.5	TPB-U	2000	I

Q-B2.2.3	1.5	TPB-U	1100	I
Q-B2.2.4	1.5	TPB-U	800	I
Q-B2.2.5	1.5	TPB-U	310	I
Q-B2.3.1	1	TPB-U	510	I
Q-B2.3.2	1.5	TPB-U	810	I
Q-B2.3.3	2	TPB-U	920	I
Q-B2.3.4	4	TPB-U	2200	I

Data set Q-B5
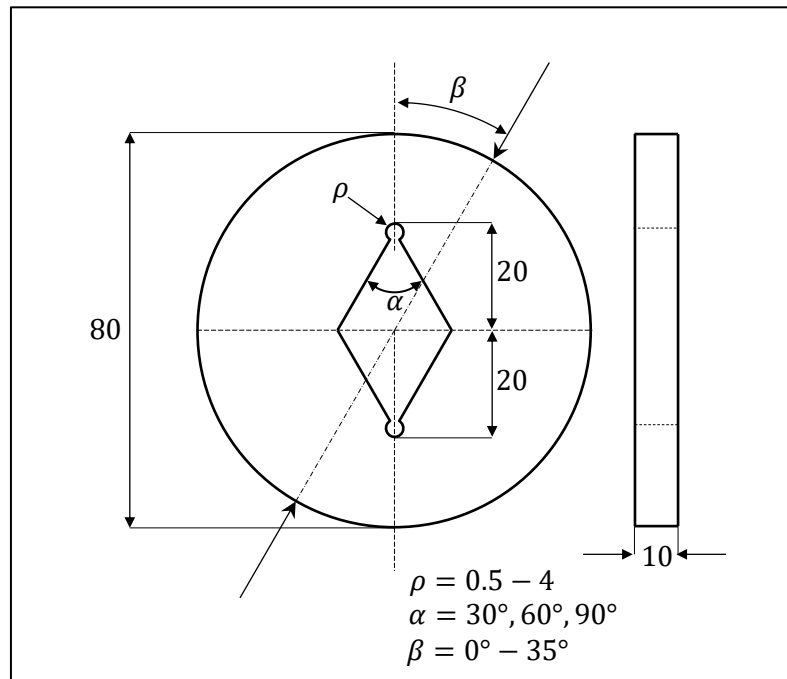
Figure 94: QB5 [116]

Fracture assessment of VO-notches under mode II loading: Experiments and theories

A.R. Torabi, SH. Amininejad Fracture

Ref	Rho	Geometry	Load angle (°)	Fail load (N)	Load Mode
Q-B5.1.1	0.5	VO-BD	0	5545	I
Q-B5.1.2	1	VO-BD	0	5314	I
Q-B5.1.3	2	VO-BD	0	6322	I
Q-B5.1.4	4	VO-BD	0	6752	I
Q-B5.2.1	0.5	VO-BD	0	3738	I
Q-B5.2.2	1	VO-BD	0	4232	I
Q-B5.2.3	2	VO-BD	0	5173	I
Q-B5.2.4	4	VO-BD	0	5866	I

Q-B5.3.1	0.5	VO-BD	0	2377	I
Q-B5.3.2	1	VO-BD	0	2476	I
Q-B5.3.3	2	VO-BD	0	2951	I
Q-B5.3.4	4	VO-BD	0	3899	I
Q-B5.4.1	0.5	VO-BD	25	4079	II
Q-B5.4.2	1	VO-BD	25	4479	II
Q-B5.4.3	2	VO-BD	25	5253	II
Q-B5.4.4	4	VO-BD	25	5897	II
Q-B5.5.1	0.5	VO-BD	28	4859	II
Q-B5.5.2	1	VO-BD	28	4199	II
Q-B5.5.3	2	VO-BD	28	4909	II
Q-B5.5.4	4	VO-BD	28	5535	II
Q-B5.6.1	0.5	VO-BD	34	5583	II
Q-B5.6.2	1	VO-BD	34	5173	II
Q-B5.6.3	2	VO-BD	34	5089	II
Q-B5.6.4	4	VO-BD	34	4903	II

Data set Q-B6
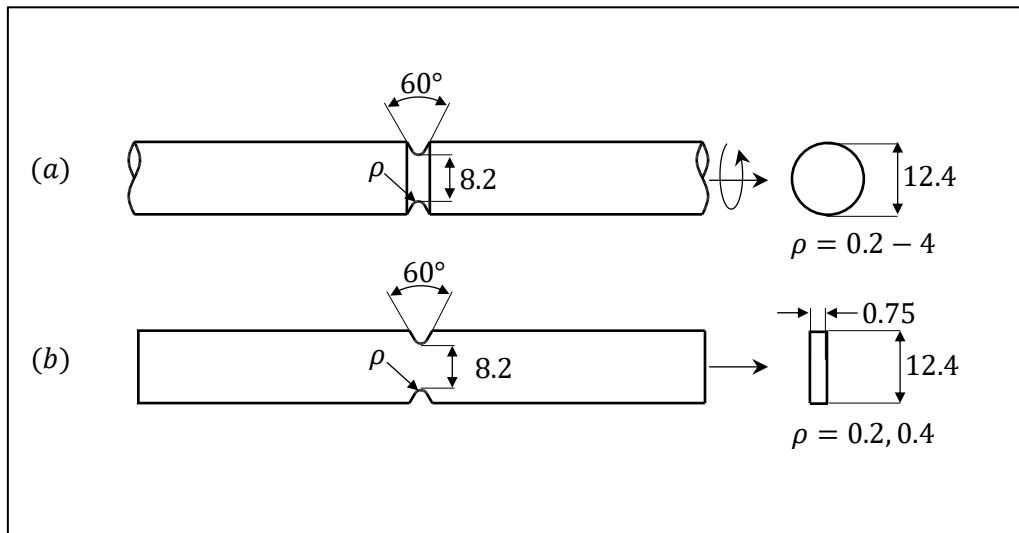
Figure 95: QB6 [76]

The Theory of critical distances to predict static strength of notched brittle components subjected to mixed-mode loading

L. Susmel, D. Taylor.

Ref	Rho	Geometry	σ_nom / τ_nom	Fail loads (KN / (Nm))	Load Mode
Q-B6.1.1	0.2	RNC	∞	1.78 / (0)	I
Q-B6.1.2	0.4	RNC	∞	2.23 / (0)	I
Q-B6.1.3	1.2	RNC	∞	2.78 / (0)	I
Q-B6.1.4	4	RNC	∞	2.83 / (0)	I
Q-B6.2.1	0.2	RNC	1	1.53 / (5.55)	I+III
Q-B6.2.2	0.4	RNC	1	1.71 / (5.03)	I+III
Q-B6.2.3	1.2	RNC	1	2.17 / (6.14)	I+III
Q-B6.2.4	4	RNC	1	2.52 / (6.77)	I+III
Q-B6.3.1	0.2	RNC	0.55	1.34 / (6.45)	I+III
Q-B6.3.2	0.4	RNC	0.55	1.34 / (6.45	I+III
Q-B6.3.3	1.2	RNC	0.55	1.26 / (6.80)	I+III
Q-B6.3.4	4	RNC	0.55	1.40 / (7.00)	I+III
Q-B6.4.1	0.2	RNC	0.23	0.72 / (6.90)	I+III

Q-B6.4.2	0.4	RNC	0.23	0.74 / (6.57)	I+III
Q-B6.4.3	1.2	RNC	0.23	0.77 / (7.41)	I+III
Q-B6.4.4	4	RNC	0.23	0.71 / (7.27)	I+III
Q-B6.5.1	0.2	RNC	0	0 / (9.60)	III
Q-B6.5.2	0.4	RNC	0	0 / (10.05)	III
Q-B6.5.3	1.2	RNC	0	0 / (10.73)	III
Q-B6.5.4	4	RNC	0	0 / (6.76)	III
Q-B6.6.1	0.2	DENT-V	∞	0.16 / (0)	I
Q-B6.6.2	0.4	DENT-V	∞	0.20 / (0)	I

Data set Q-B7
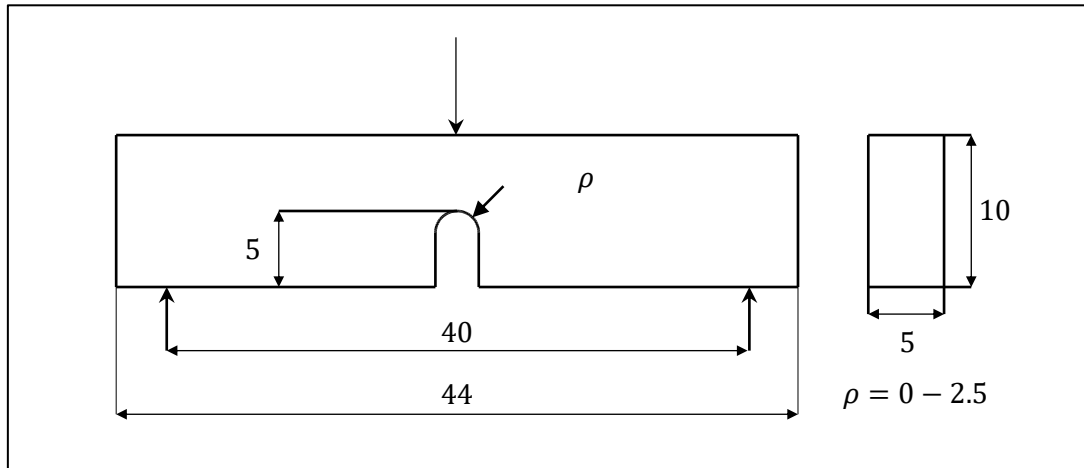
Figure 96: QB7 [117]

Analysis of notch effect in PMMA using the Theory of Critical Distances

S. Cicero, V. Madrazo, I.A. Carrascal

Ref	Rho	Geometry	Fail loads (N)	Load Mode
Q-B7.1.1	0	TPB-U	130.0	I
Q-B7.1.2	0	TPB-U	83.0	I
Q-B7.1.3	0	TPB-U	131.2	I
Q-B7.1.4	0.25	TPB-U	114.0	I
Q-B7.1.5	0.32	TPB-U	110.3	I
Q-B7.1.6	0.5	TPB-U	127.0	I
Q-B7.1.7	1	TPB-U	207.3	I
Q-B7.1.8	1.5	TPB-U	199.4	I
Q-B7.1.9	2	TPB-U	252.5	I
Q-B7.1.10	2.5	TPB-U	251.7	I

Data set Q-B8
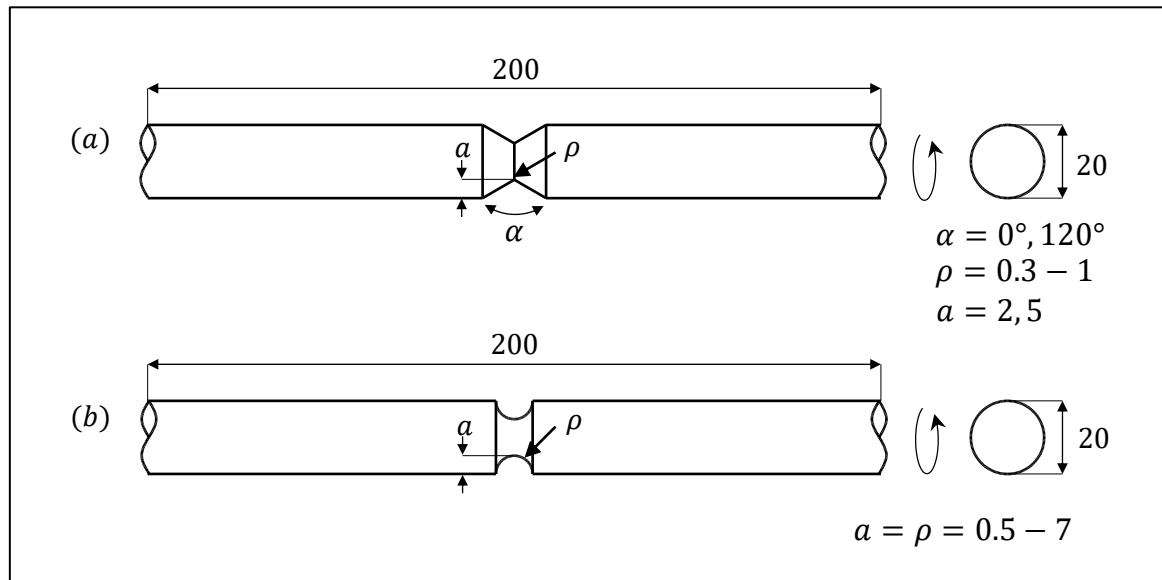
Figure 97: QB8 [118]

Fracture behaviour of notched round bars made of PMMA subjected to torsion at room temperature

F. Berto, M. Elices, P. Lazzarin, M. Zappalorto

Ref	Rho	Geometry	Notch Depth (mm)	Fail loads (Nm)	Load Mode
Q-B8.1.1	0.3	RNC-U	5	16.0	III
Q-B8.1.2	0.5	RNC-U	5	16.7	III
Q-B8.1.3	1	RNC-U	5	17.3	III
Q-B8.1.4	2	RNC-U	5	17.7	III
Q-B8.1.5	0.3	RNC-U	2	65.4	III
Q-B8.1.6	0.5	RNC-U	2	65.3	III
Q-B8.1.7	1	RNC-U	2	66.4	III
Q-B8.2.1	0.1	RNC-V	5	16.4	III
Q-B8.2.2	0.3	RNC-V	5	17.4	III
Q-B8.2.3	0.5	RNC-V	5	17.4	III
Q-B8.2.4	1	RNC-V	5	17.3	III

Q-B8.2.5	2	RNC-V	5	17.0	III
Q-B8.2.6	0.1	RNC-V	2	65.8	III
Q-B8.2.7	0.3	RNC-V	2	66.2	III
Q-B8.2.8	0.5	RNC-V	2	67.2	III
Q-B8.2.9	1	RNC-V	2	66.3	III
Q-B8.3.1	0.5	RNC-U	0.5	98.4	III
Q-B8.3.2	1	RNC-U	1	91.9	III
Q-B8.3.3	2	RNC-U	2	67.0	III
Q-B8.3.4	4	RNC-U	4	29.1	III
Q-B8.3.5	5	RNC-U	5	15.3	III
Q-B8.3.6	6	RNC-U	6	7.2	III
Q-B8.3.7	7	RNC-U	7	2.6	III

Data set Q-B9
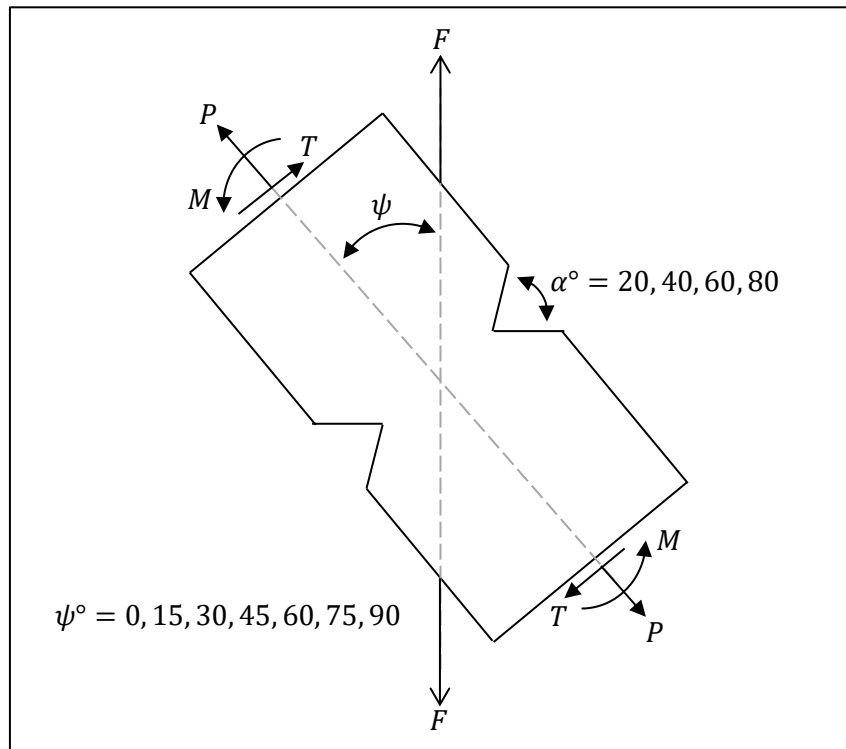
Figure 98: QB9 [119]

BRITTLE FRACTURE IN PLANE ELEMENTS WITH SHARP NOTCHES UNDER MIXED-MODE LOADING

Seweryn, A

Ref	Rho	Geometry	Notch angle (°)	Load angle (°)	Fail loads (kN)	Load Mode
Q-B9.1.1	0.01	DENT	20	0	2.24	I
Q-B9.1.2	0.01	DENT	20	0	2.12	I
Q-B9.1.3	0.01	DENT	20	0	1.82	I
Q-B9.1.4	0.01	DENT	40	0	1.82	I
Q-B9.1.5	0.01	DENT	40	0	2.07	I
Q-B9.1.6	0.01	DENT	40	0	2.11	I

Q-B9.1.7	0.01	DENT	60	0	2.09	I
Q-B9.1.8	0.01	DENT	60	0	1.62	I
Q-B9.1.9	0.01	DENT	60	0	1.94	I
Q-B9.1.10	0.01	DENT	80	0	2.72	I
Q-B9.1.11	0.01	DENT	80	0	2.36	I
Q-B9.1.12	0.01	DENT	80	0	2.62	I
Q-B9.2.1	0.01	DENT	20	15	2.12	I+II
Q-B9.2.2	0.01	DENT	20	15	2.30	I+II
Q-B9.2.3	0.01	DENT	20	15	1.95	I+II
Q-B9.2.4	0.01	DENT	40	15	1.94	I+II
Q-B9.2.5	0.01	DENT	40	15	2.10	I+II
Q-B9.2.6	0.01	DENT	40	15	2.00	I+II
Q-B9.2.7	0.01	DENT	60	15	1.72	I+II
Q-B9.2.8	0.01	DENT	60	15	1.86	I+II
Q-B9.2.9	0.01	DENT	60	15	2.15	I+II
Q-B9.2.10	0.01	DENT	80	15	2.62	I+II
Q-B9.2.11	0.01	DENT	80	15	2.52	I+II
Q-B9.2.12	0.01	DENT	80	15	2.46	I+II
Q-B9.3.1	0.01	DENT	20	30	2.28	I+II
Q-B9.3.2	0.01	DENT	20	30	2.44	I+II
Q-B9.3.3	0.01	DENT	20	30	2.62	I+II
Q-B9.3.4	0.01	DENT	40	30	2.48	I+II
Q-B9.3.5	0.01	DENT	40	30	2.05	I+II
Q-B9.3.6	0.01	DENT	40	30	1.92	I+II
Q-B9.3.7	0.01	DENT	60	30	2.34	I+II
Q-B9.3.8	0.01	DENT	60	30	1.95	I+II
Q-B9.3.9	0.01	DENT	60	30	2.00	I+II
Q-B9.3.10	0.01	DENT	80	30	2.44	I+II
Q-B9.3.11	0.01	DENT	80	30	2.40	I+II
Q-B9.3.12	0.01	DENT	80	30	2.60	I+II
Q-B9.4.1	0.01	DENT	20	45	2.56	I+II
Q-B9.4.2	0.01	DENT	20	45	2.58	I+II
Q-B9.4.3	0.01	DENT	20	45	2.71	I+II
Q-B9.4.4	0.01	DENT	40	45	2.40	I+II
Q-B9.4.5	0.01	DENT	40	45	2.60	I+II

Q-B9.4.6	0.01	DENT	40	45	2.68	I+II
Q-B9.4.7	0.01	DENT	60	45	2.70	I+II
Q-B9.4.8	0.01	DENT	60	45	2.62	I+II
Q-B9.4.9	0.01	DENT	60	45	2.50	I+II
Q-B9.4.10	0.01	DENT	80	45	3.04	I+II
Q-B9.4.11	0.01	DENT	80	45	2.98	I+II
Q-B9.4.12	0.01	DENT	80	45	3.20	I+II
Q-B9.5.1	0.01	DENT	20	60	2.67	I+II
Q-B9.5.2	0.01	DENT	20	60	2.86	I+II
Q-B9.5.3	0.01	DENT	20	60	2.82	I+II
Q-B9.5.4	0.01	DENT	40	60	2.56	I+II
Q-B9.5.5	0.01	DENT	40	60	2.75	I+II
Q-B9.5.6	0.01	DENT	40	60	2.66	I+II
Q-B9.5.7	0.01	DENT	60	60	3.2	I+II
Q-B9.5.8	0.01	DENT	60	60	2.56	I+II
Q-B9.5.9	0.01	DENT	60	60	3.14	I+II
Q-B9.5.10	0.01	DENT	80	60	3.72	I+II
Q-B9.5.11	0.01	DENT	80	60	3.55	I+II
Q-B9.5.12	0.01	DENT	80	60	3.44	I+II
Q-B9.6.1	0.01	DENT	20	75	3.04	I+II
Q-B9.6.2	0.01	DENT	20	75	3.02	I+II
Q-B9.6.3	0.01	DENT	20	75	2.83	I+II
Q-B9.6.4	0.01	DENT	40	75	3.36	I+II
Q-B9.6.5	0.01	DENT	40	75	2.95	I+II
Q-B9.6.6	0.01	DENT	40	75	3.26	I+II
Q-B9.6.7	0.01	DENT	60	75	3.28	I+II
Q-B9.6.8	0.01	DENT	60	75	3.02	I+II
Q-B9.6.9	0.01	DENT	60	75	3.55	I+II
Q-B9.6.10	0.01	DENT	80	75	5.8	I+II
Q-B9.6.11	0.01	DENT	80	75	4.95	I+II
Q-B9.6.12	0.01	DENT	80	75	3.75	I+II
Q-B9.7.1	0.01	DENT	20	90	2.98	II
Q-B9.7.2	0.01	DENT	20	90	3	II
Q-B9.7.3	0.01	DENT	20	90	3.24	II
Q-B9.7.4	0.01	DENT	40	90	4.17	II

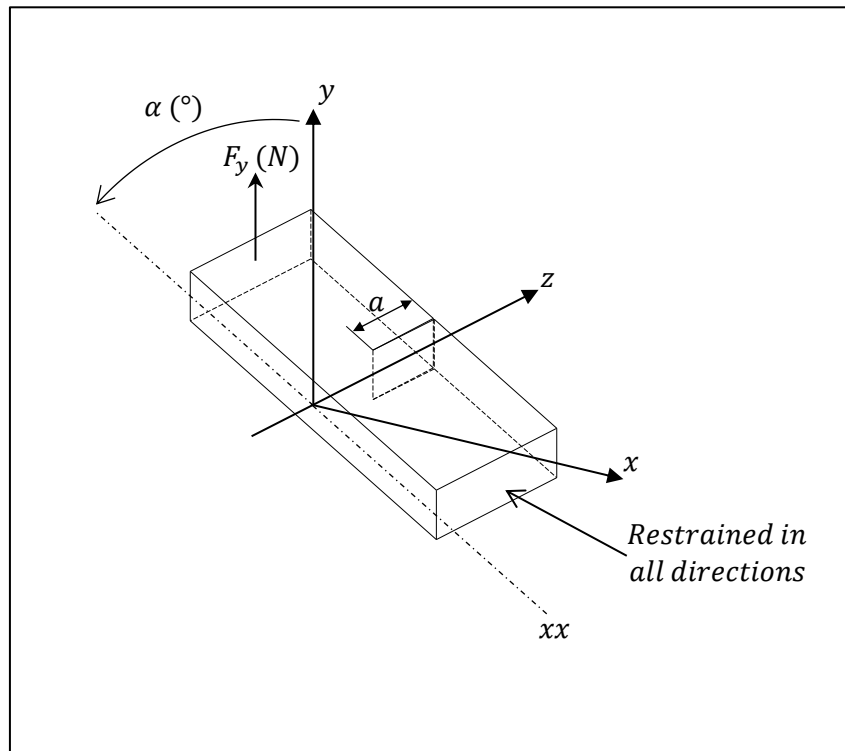|						
Q-B9.7.5	0.01	DENT	40	90	3.8	II
Q-B9.7.6	0.01	DENT	40	90	4.11	II
Q-B9.7.7	0.01	DENT	60	90	5.3	II
Q-B9.7.8	0.01	DENT	60	90	4.6	II
Q-B9.7.9	0.01	DENT	60	90	4.9	II
Q-B9.7.10	0.01	DENT	80	90	9.45	II
Q-B9.7.11	0.01	DENT	80	90	10.2	II
Q-B9.7.12	0.01	DENT	80	90	9.7	II

Data set Q-B10

Figure 99: QB10[120]

Fracture tests under mixed mode I / III loading : An assessment based on the local energy

Berto, F.   Campagnolo, A.

Ref	Rho	Geometry	Load angle (α°)	Crack length (a) (mm)	Fail load (N)	Load Mode
Q-B10.1.1	0	SENT	0	10.4	451.3	I
Q-B10.1.2	0	SENT	0	10.0	502.8	I
Q-B10.1.3	0	SENT	0	10.2	505.2	I
Q-B10.1.4	0	SENT	40	10.2	488.0	I+III
Q-B10.1.5	0	SENT	40	10.2	480.4	I+III
Q-B10.1.6	0	SENT	40	10.0	443.9	I+III
Q-B10.1.7	0	SENT	65	10.1	597.1	I+III

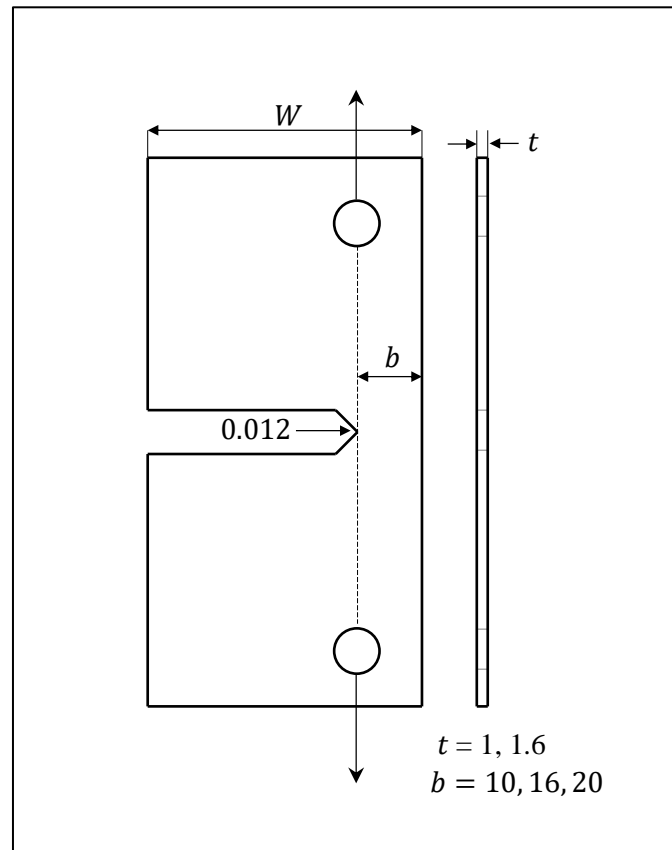|						
Q-B10.1.8	0	SENT	65	10.3	577.5	I+III
Q-B10.1.9	0	SENT	65	10.0	571.6	I+III
Q-B10.1.10	0	SENT	78	10.3	656.1	I+III
Q-B10.1.11	0	SENT	78	10.2	661.1	I+III
Q-B10.1.12	0	SENT	78	10.0	693.7	I+III
Q-B10.1.13	0	SENT	90	10.0	741.9	III
Q-B10.1.14	0	SENT	90	10.1	686.7	III
Q-B10.1.15	0	SENT	90	10.0	781.1	III

Data set M1

Figure 100: M1 [121]

Fracture Toughness of Thin Aluminium Sheets using modified single edge notch specimen

S. Prakash, K. Shinde, V Tripathi

Ref	Rho	Geometry	Thickness (mm)	Ligament length (mm)	Fail load (N)	Load Mode
M1.1.1	0.012	SENT	1.6	10	3001	I
M1.1.2	0.012	SENT	1.6	10	2799	I
M1.1.3	0.012	SENT	1.6	10	2947	I
M1.1.4	0.012	SENT	1.6	10	2900	I
M1.1.5	0.012	SENT	1.6	10	2893	I

| M1.1.6	0.012	SENT	1.6	16	3912	I
M1.1.7	0.012	SENT	1.6	16	4010	I
M1.1.8	0.012	SENT	1.6	16	3925	I
M1.1.9	0.012	SENT	1.6	16	3921	I
M1.1.10	0.012	SENT	1.6	16	3607	I
M1.1.11	0.012	SENT	1.6	20	4733	I
M1.1.12	0.012	SENT	1.6	20	4655	I
M1.1.13	0.012	SENT	1.6	20	4475	I
M1.1.14	0.012	SENT	1.6	20	4669	I
M1.1.15	0.012	SENT	1.6	20	4620	I
M1.2.1	0.012	SENT	1	10	1748	I
M1.2.2	0.012	SENT	1	10	1780	I
M1.2.3	0.012	SENT	1	10	1862	I
M1.2.4	0.012	SENT	1	10	1693	I
M1.2.5	0.012	SENT	1	10	1862	I
M1.2.6	0.012	SENT	1	16	2300	I
M1.2.7	0.012	SENT	1	16	2336	I
M1.2.8	0.012	SENT	1	16	2374	I
M1.2.9	0.012	SENT	1	16	2186	I
M1.2.10	0.012	SENT	1	16	2155	I
M1.2.11	0.012	SENT	1	20	2727	I
M1.2.12	0.012	SENT	1	20	2773	I
M1.2.13	0.012	SENT	1	20	3006	I
M1.2.14	0.012	SENT	1	20	2763	I
M1.2.15	0.012	SENT	1	20	2716	I

Data set M2
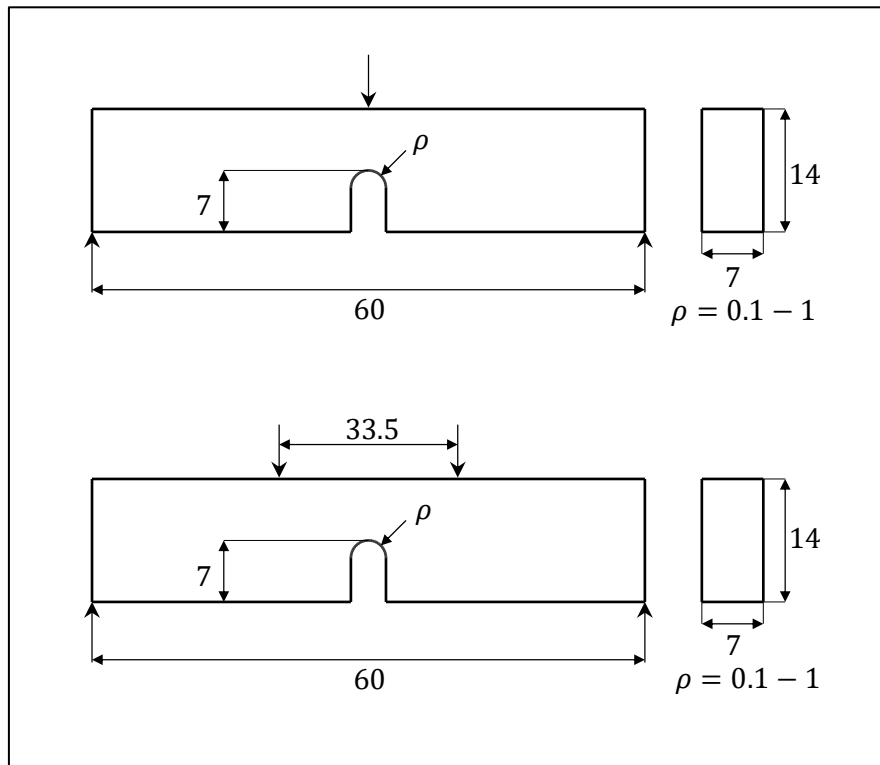
Figure 101: M2 [122]

FRACTURE OF A HIGH STRENGTH STEEL CONTAINING U-NOTCHES

F.J. Gómez, M. Elices and A. Valiente.

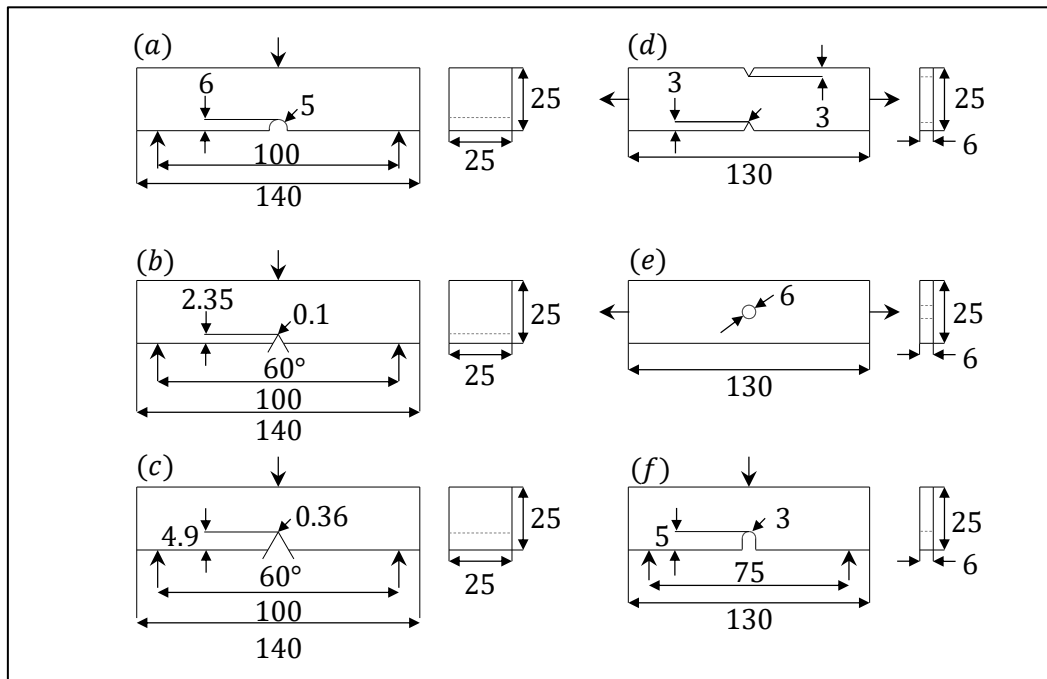| Ref	Rho	Geometry	Fail load (N)	Load Mode
M2.1.1	0.101	TPB-U	8900	I
M2.1.2	0.171	TPB-U	7100	I
M2.1.3	0.505	TPB-U	5100	I
M2.1.4	1	TPB-U	5100	I
M2.2.1	0.106	FPB-U	16900	I
M2.2.2	0.171	FPB-U	14200	I
M2.2.3	0.498	FPB-U	11100	I
M2.2.4	1	FPB-U	9800	I

Data set M3

Figure 102: M3 [87]

On the use of the Theory of Critical Distances to predict static failures in ductile metallic materials containing different geometrical features

L. Susmel, D. Taylor

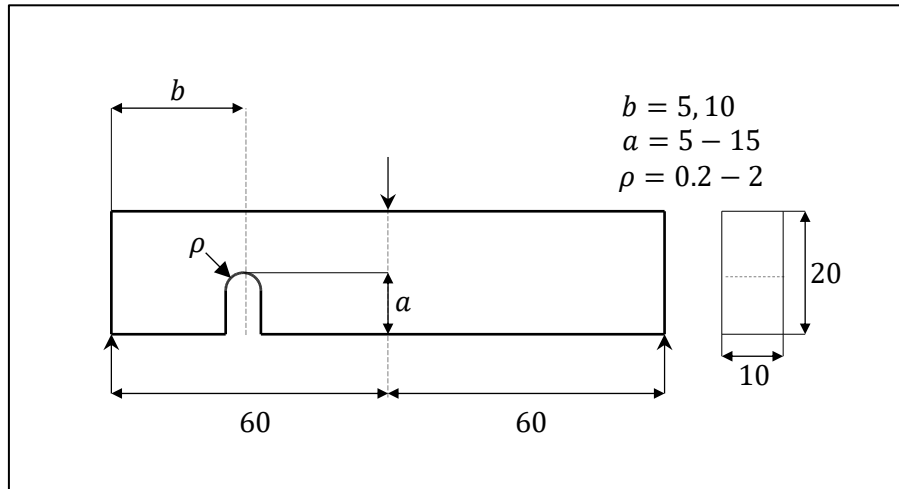| Ref	Rho	Geometry	Fail load (kN)	Load Mode
M3.1.1	5	TPB-U	95.17	I
M3.1.2	0.1	TPB-V	119.4	I
M3.1.3	0.3	TPB-V	96.45	I
M3.2.1	3	IB-T	83.6	I
M3.2.2	0.1	DENT	91.48	I
M3.2.3	3	TPB-U	33	I

Data set M4

Figure 103: M4 [123]

Local strain energy density applied to martensitic steel plates weakened by U-notches under mixed mode loading

K. Taghizadeh, F. Berto, E. Barati

Ref	Rho	Geometry	Notch depth (mm)	Distance, b (mm)	Fail load (N)	Load Mode
M4.1.1	0.2	TPB-U	5	5	18847	I+II
M4.1.2	0.5	TPB-U	5	5	29222	I+II
M4.1.3	1	TPB-U	5	5	40133	I+II
M4.1.4	2	TPB-U	5	5	51475	I+II
M4.1.5	0.2	TPB-U	7.5	5	16652	I+II
M4.1.6	0.5	TPB-U	7.5	5	25670	I+II
M4.1.7	1	TPB-U	7.5	5	32918	I+II
M4.1.8	2	TPB-U	7.5	5	43647	I+II
M4.1.9	0.2	TPB-U	10	5	13305	I+II
M4.1.10	0.5	TPB-U	10	5	18835	I+II
M4.1.11	1	TPB-U	10	5	25763	I+II

M4.1.12	2	TPB-U	10	5	33955	I+II
M4.1.13	0.2	TPB-U	15	5	6347	I+II
M4.1.14	0.5	TPB-U	15	5	9537	I+II
M4.1.15	1	TPB-U	15	5	12368	I+II
M4.1.16	2	TPB-U	15	5	14915	I+II
M4.2.1	0.2	TPB-U	5	10	15925	I+II
M4.2.2	0.5	TPB-U	5	10	21448	I+II
M4.2.3	1	TPB-U	5	10	32653	I+II
M4.2.4	2	TPB-U	5	10	41457	I+II
M4.2.5	0.2	TPB-U	7.5	10	12817	I+II
M4.2.6	0.5	TPB-U	7.5	10	17068	I+II
M4.2.7	1	TPB-U	7.5	10	24533	I+II
M4.2.8	2	TPB-U	7.5	10	31477	I+II
M4.2.9	0.2	TPB-U	10	10	8720	I+II
M4.2.10	0.5	TPB-U	10	10	12845	I+II
M4.2.11	1	TPB-U	10	10	18330	I+II
M4.2.12	2	TPB-U	10	10	22823	I+II
M4.2.13	0.2	TPB-U	15	10	3352	I+II
M4.2.14	0.5	TPB-U	15	10	4952	I+II
M4.2.15	1	TPB-U	15	10	6517	I+II
M4.2.16	2	TPB-U	15	10	8162	I+II

Data set M5

ρ

d_n

$60°$

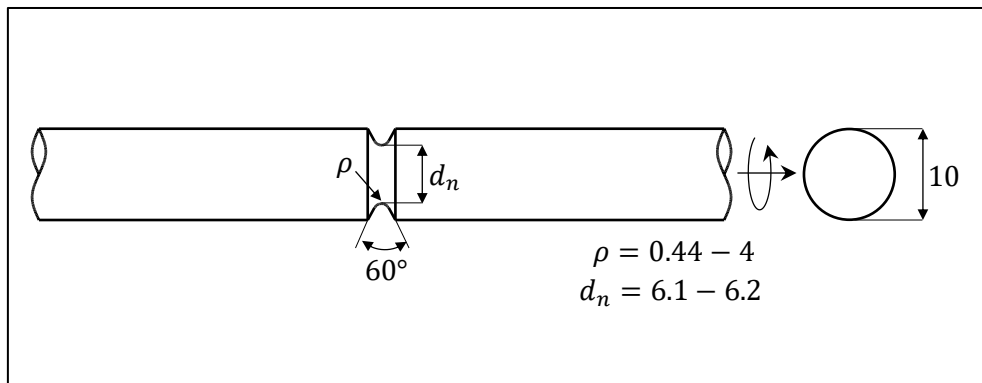$\rho = 0.44 - 4$
$d_n = 6.1 - 6.2$

10

Figure 104: M5 [88]

The Theory of Critical Distances to estimate the static strength of notched samples of Al6082 loaded in combined tension and torsion. Part II: Multiaxial static assessment

Luca Susmel, David Taylor

Ref	Rho	Geometry	σ_nom / τ_nom	Fail loads (MPa/ (MPa))	Load Mode
M5.1.1	0.44	RNC-V	∞	537.3 / (0)	I
M5.1.2	0.5	RNC-V	∞	551.6 / (0)	I
M5.1.3	1.25	RNC-V	∞	523.7 / (0)	I
M5.1.4	4	RNC-U	∞	449.3 / (0)	I
M5.2.1	0.44	RNC-V	1	254.7 / (254.7)	I+III
M5.2.2	0.5	RNC-V	1	259.0 / (263.4)	I+III
M5.2.3	1.25	RNC-V	1	271.6 / (271.8)	I+III
M5.2.4	4	RNC-U	1	255.9 / (260.1)	I+III
M5.3.1	0.44	RNC-V	0.55	164.0 / (298.1)	I+III
M5.3.2	0.5	RNC-V	0.55	148.5 / (274.6)	I+III
M5.3.3	1.25	RNC-V	0.55	155.0 / (281.7)	I+III

M5.3.4	4	RNC-U	0.55	160.1 / (296.2)	I+III
M5.4.1	0.44	RNC-V	0.23	68.9 / (299.8)	I+III
M5.4.2	0.5	RNC-V	0.23	65.0 / (286.8)	I+III
M5.4.3	1.25	RNC-V	0.23	69.6 / (301.7)	I+III
M5.4.4	4	RNC-U	0.23	74.9 / (330.7)	I+III
M5.5.1	0.44	RNC-V	0	0 / (265.6)	III
M5.5.2	0.5	RNC-V	0	0 / (255.1)	III
M5.5.3	1.25	RNC-V	0	0 / (277.6)	III
M5.5.4	4	RNC-U	0	0 / (312.1)	III

Data set M6
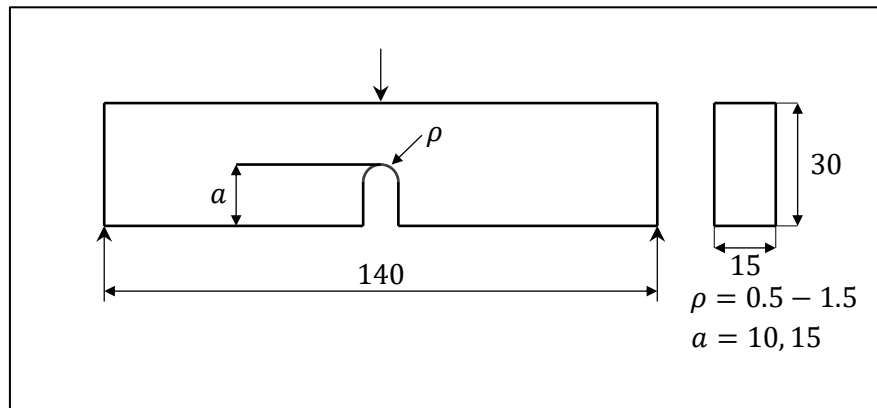
Figure 105: M6 [124]

Fracture assessment of U-notches under three point bending by means of local energy density.

F. Berto, E. Barati

Ref	Rho	Geometry	Notch depth (mm)	Fail loads (N)	Load Mode
M6.1.1	0.5	TPB-U	10	2248	I
M6.1.2	1	TPB-U	10	2510	I
M6.1.3	1.5	TPB-U	10	2783	I
M6.1.4	0.5	TPB-U	15	1405	I
M6.1.5	1	TPB-U	15	1723	I
M6.1.6	1.5	TPB-U	15	2075	I

Data set M7
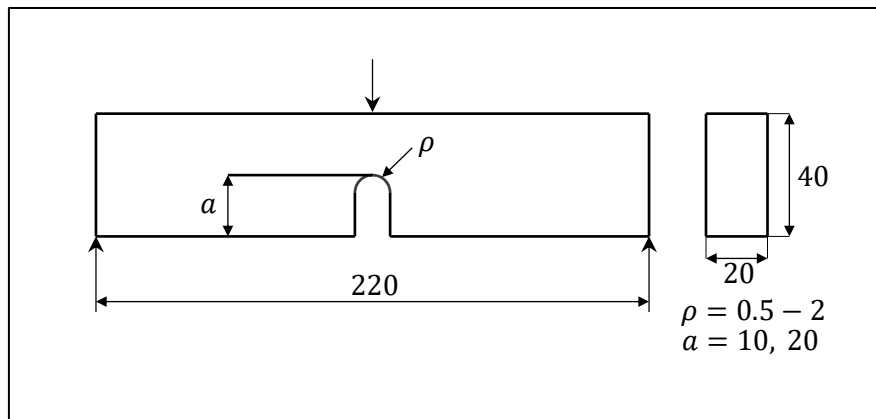
Figure 106: M7 [124]

Fracture assessment of U-notches under three point bending by means of local energy density.

F. Berto, E. Barati

Ref	Rho	Geometry	Notch depth (mm)	Fail loads (N)	Load Mode
M7.2.1	0.5	TPB-U	10	7730	I
M7.2.2	1	TPB-U	10	9140	I
M7.2.3	1.5	TPB-U	10	10800	I
M7.2.4	2	TPB-U	10	11690	I
M7.2.5	0.5	TPB-U	20	4010	I
M7.2.6	1	TPB-U	20	4450	I
M7.2.7	1.5	TPB-U	20	5570	I
M7.2.8	2	TPB-U	20	5830	I

12.   Annex B – Complete static assessment error results
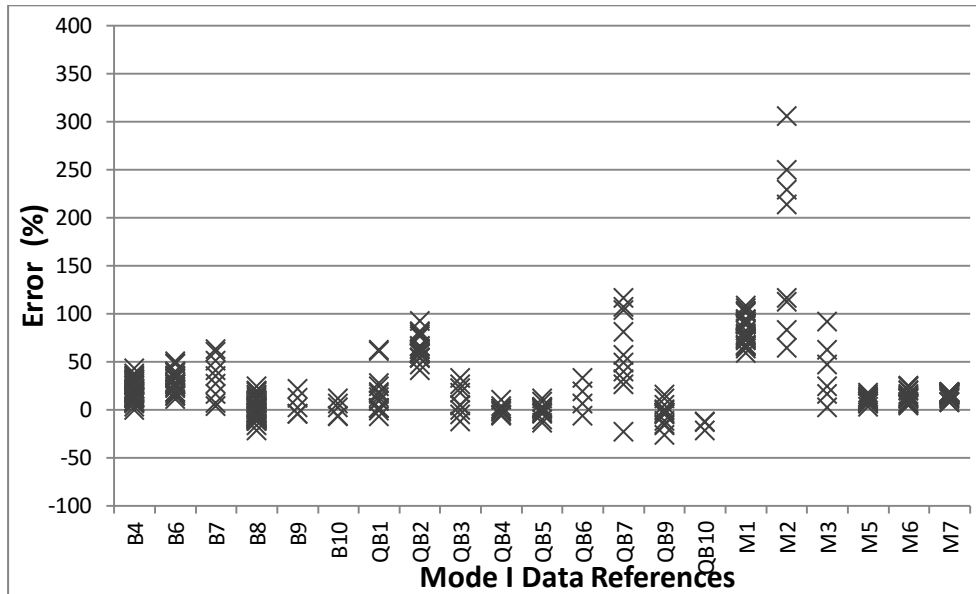
Figure 107: Mode I data (Table 2) and associated error results calculated according to the TCD PM using Maximum Principal Stress as effective stress
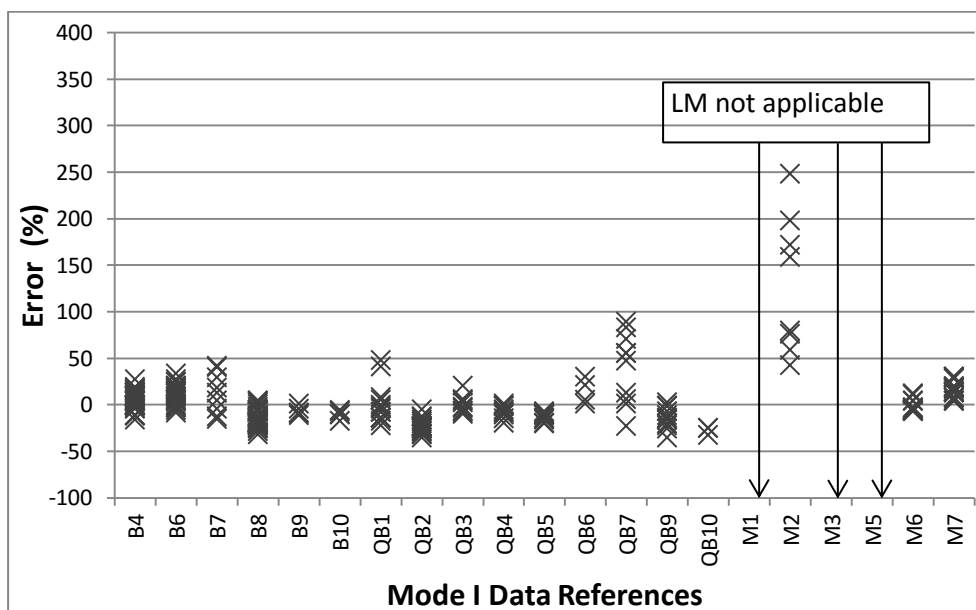
Figure 108: Mode I data (Table 2) and associated error results calculated according to the LM and the Maximum Principal Stress as effective stress
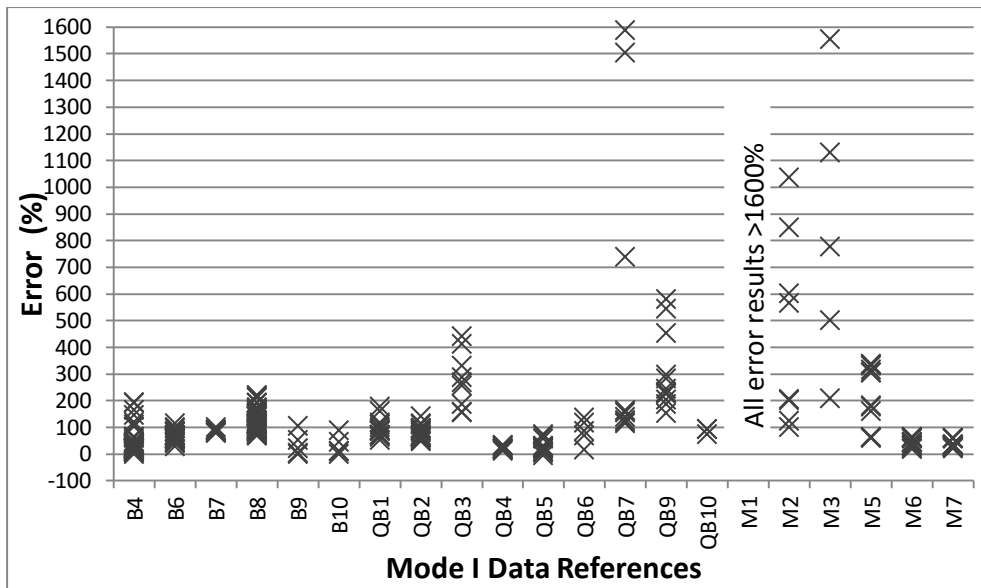
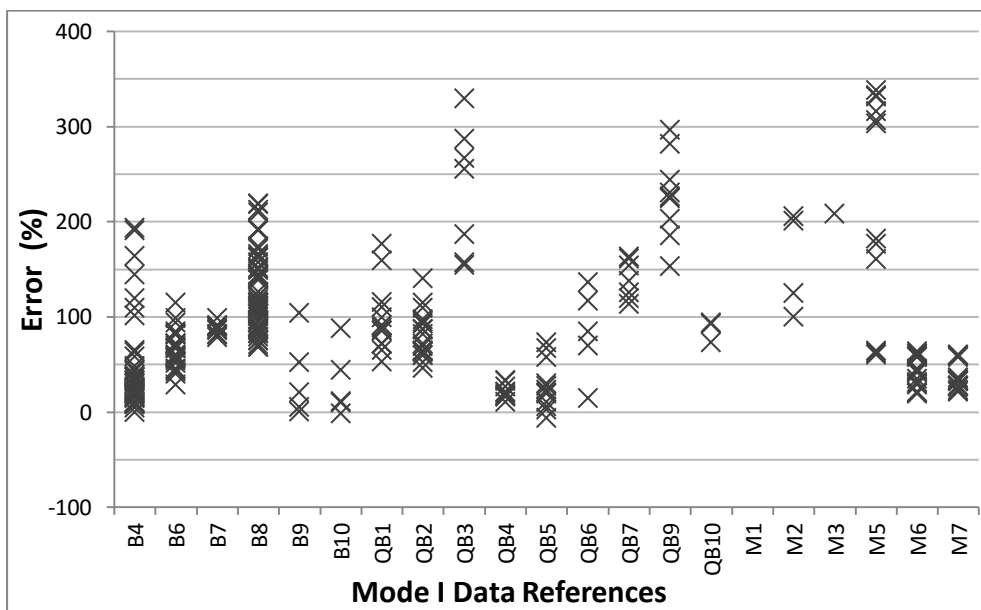**Figure 109: Mode I data (Table 2) and associated error calculated using the HSSM and Maximum Principal Stress**

Figure 110: Mode I data (Table 2) and associated error calculated using the HSSM and Maximum Principal Stress
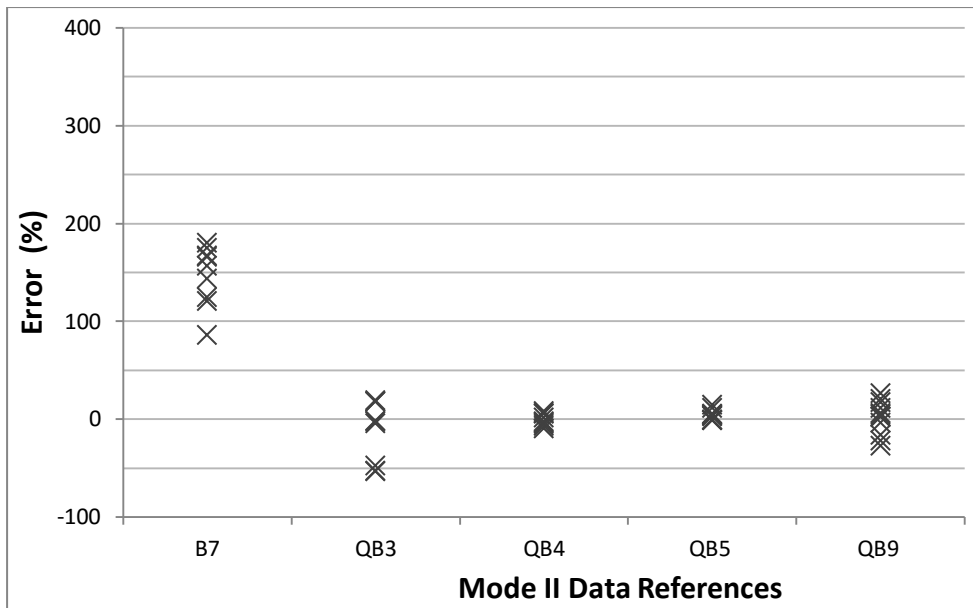
258

Figure 111: Mode II data (Table 2) and associated error results for Maximum Principal stress as effective stress in accordance with the engineering reformulation of the PM
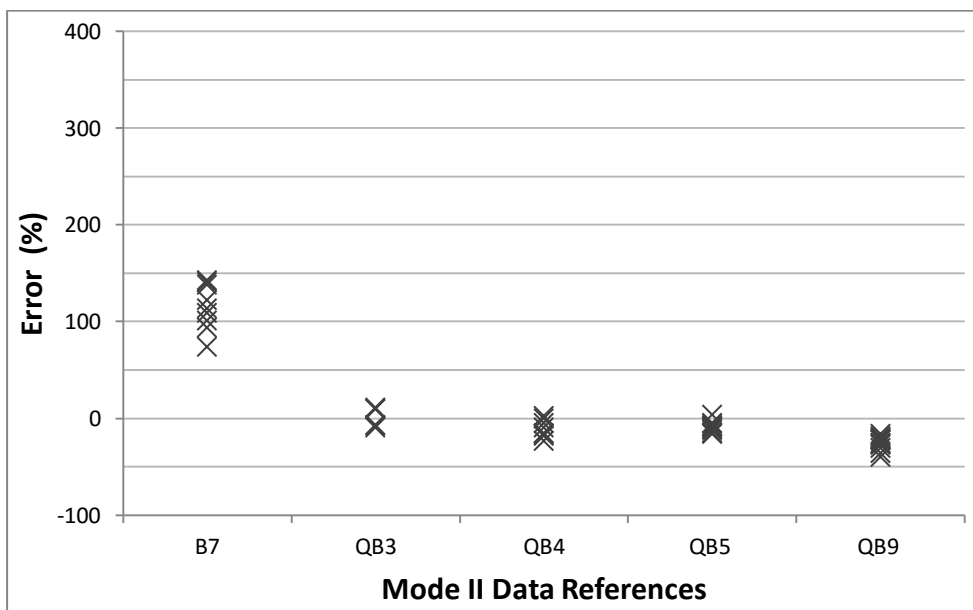

Figure 112: Mode II data (Table 2) and associated error results for Maximum Principal Stress as effective stress and the TCD LM
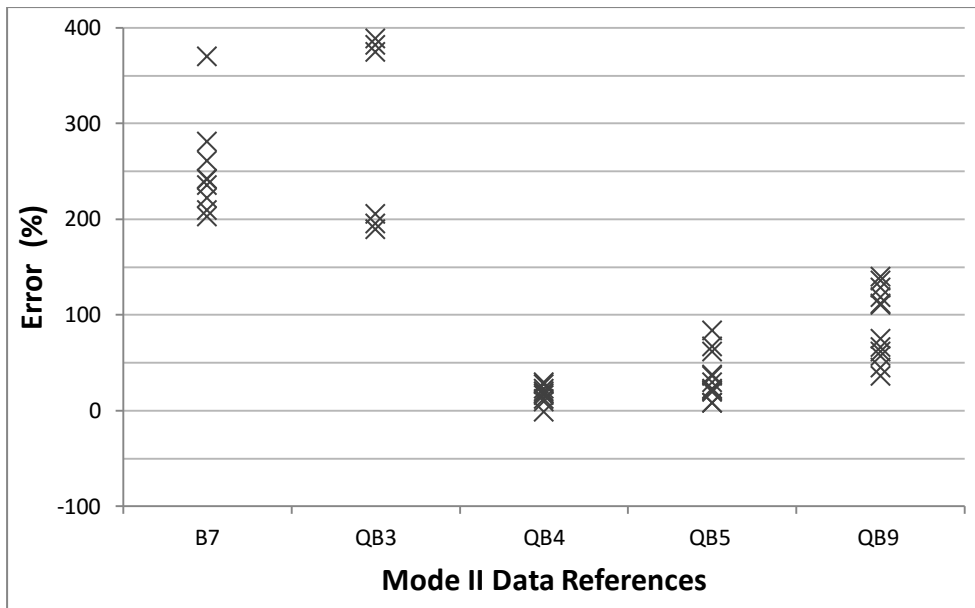
Figure 113: Mode II data (Table 2) and associated error calculated using the Maximum Principal Stress and the HSSM
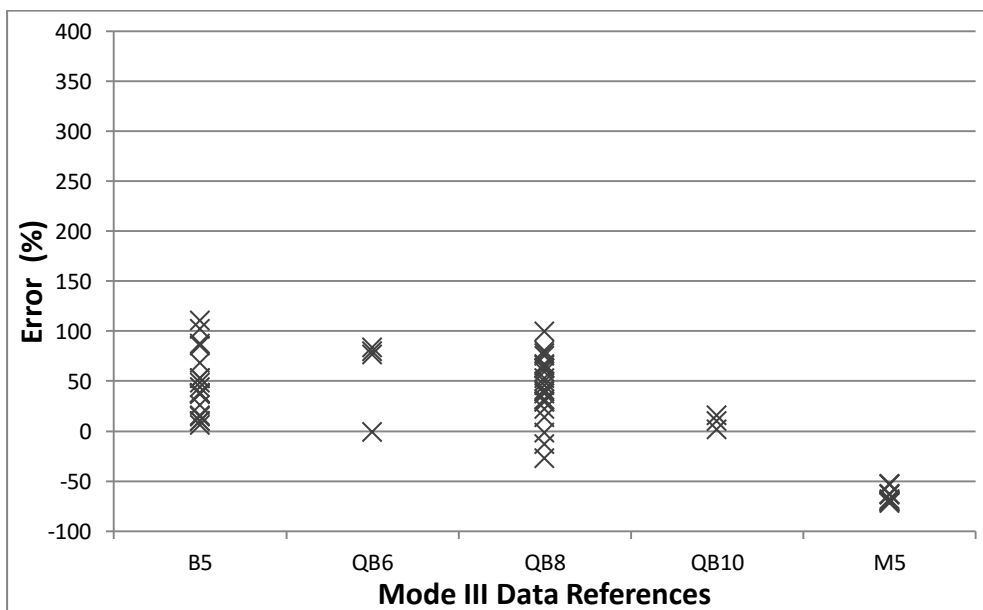

Figure 114: Mode III data (Table 2) and associated error results calculated using the Maximum Principal Stress and the TCD PM
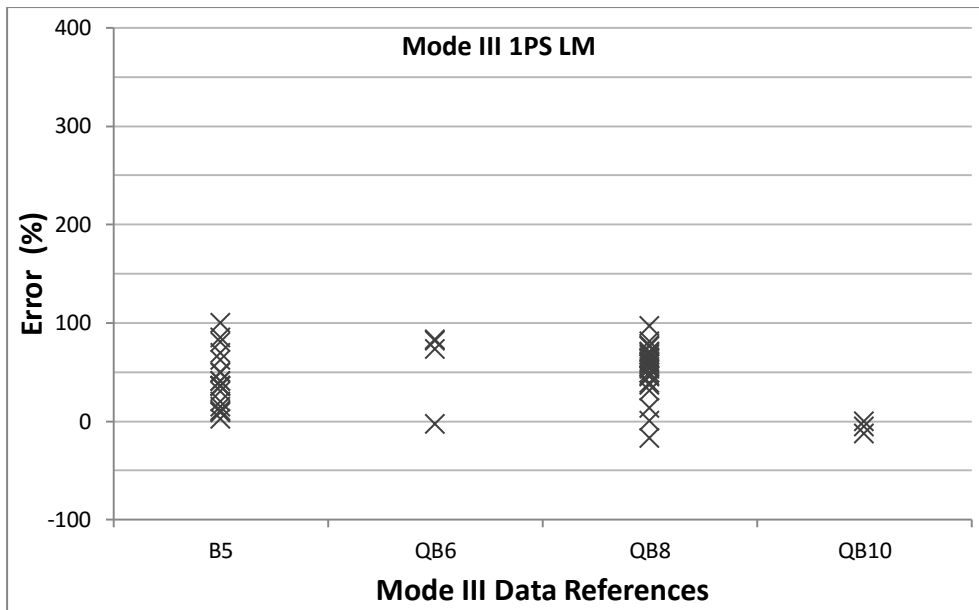
Figure 115: Mode III data (Table 2) and associated error results calculated using the Maximum Principal Stress and the TCD LM
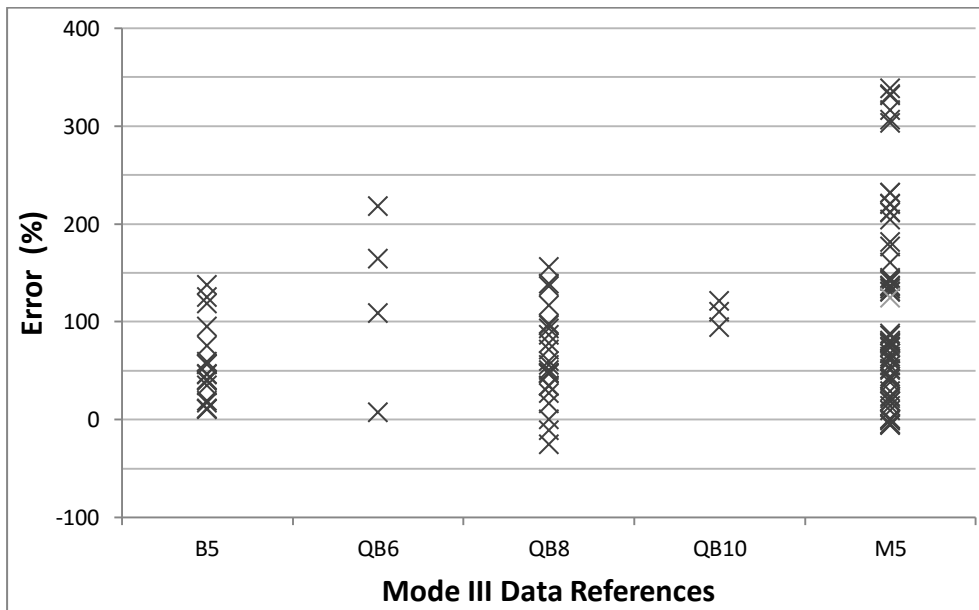

Figure 116: Mode III data (Table 2) and associated error results calculated using the Maximum Principal Stress and the HSSM
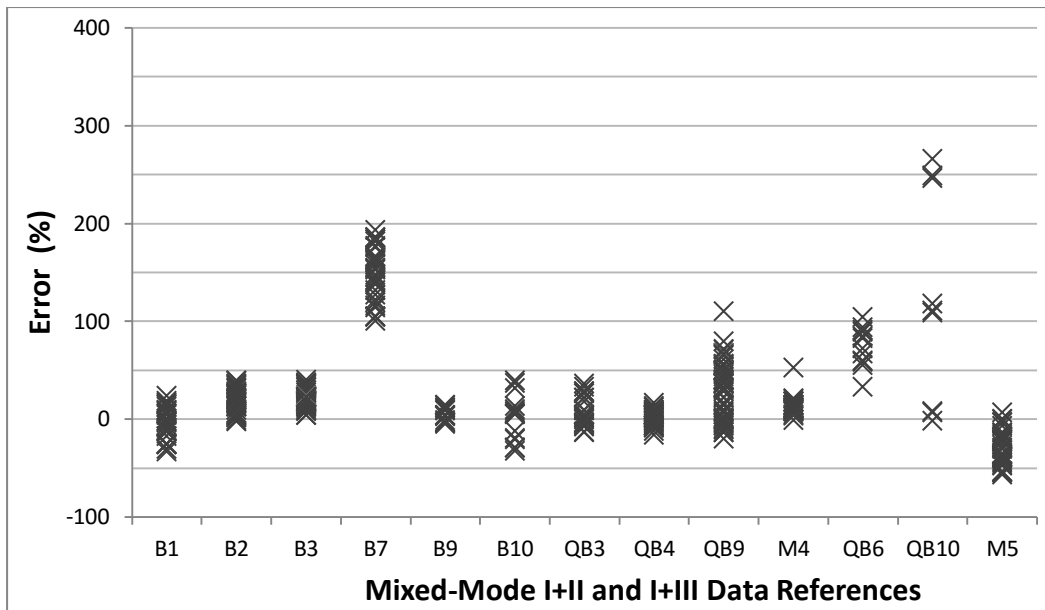
Figure 117: Mixed-Mode I+II and I+III data (Table 2) and associated error calculated using the Maximum Principal Stress and the TCD PM

Figure 118: Mixed-Mode I+II and I+III data (Table 2) and associated error calculated using the Maximum Principal Stress and the TCD LM
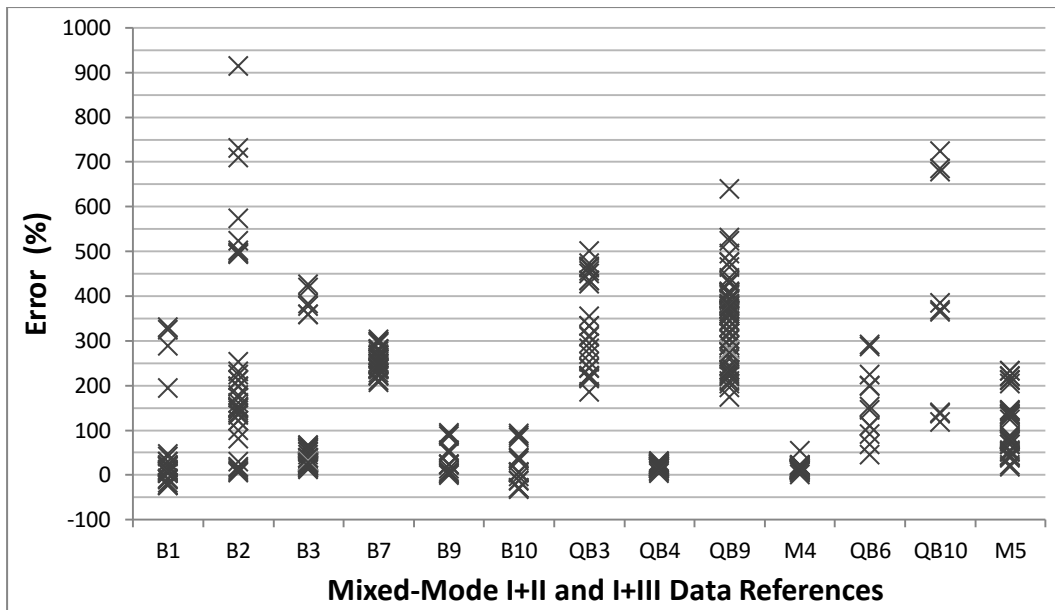
Figure 119: Mixed-Mode I+II and I+III data (Table 2) and associated error calculated using the Maximum Principal Stress and the HSSM
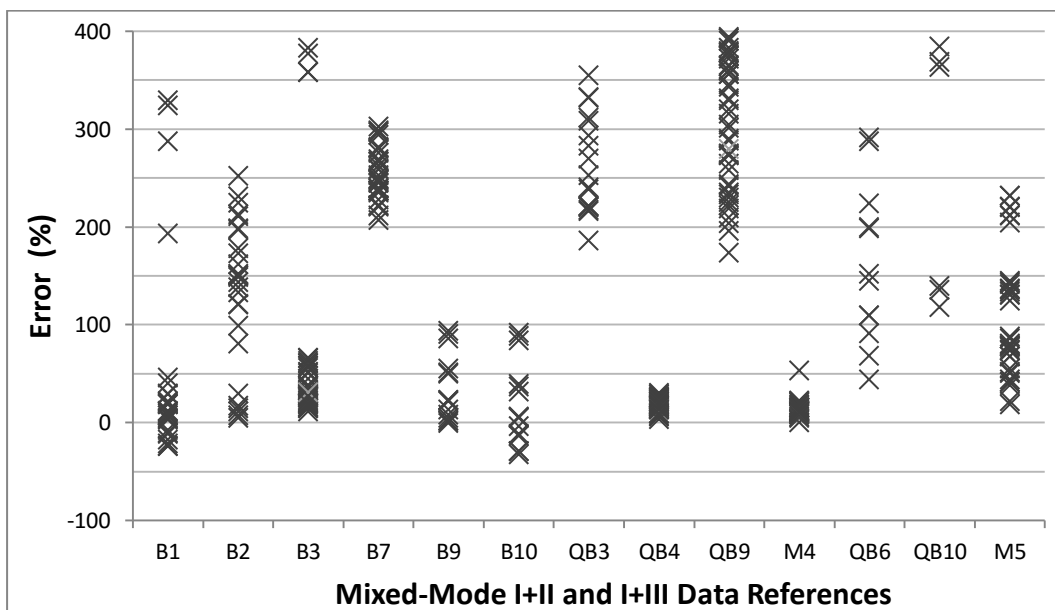
Figure 120: Mixed-Mode I+II and I+III data (Table 2) and associated error calculated using the Maximum Principal Stress and the HSSM
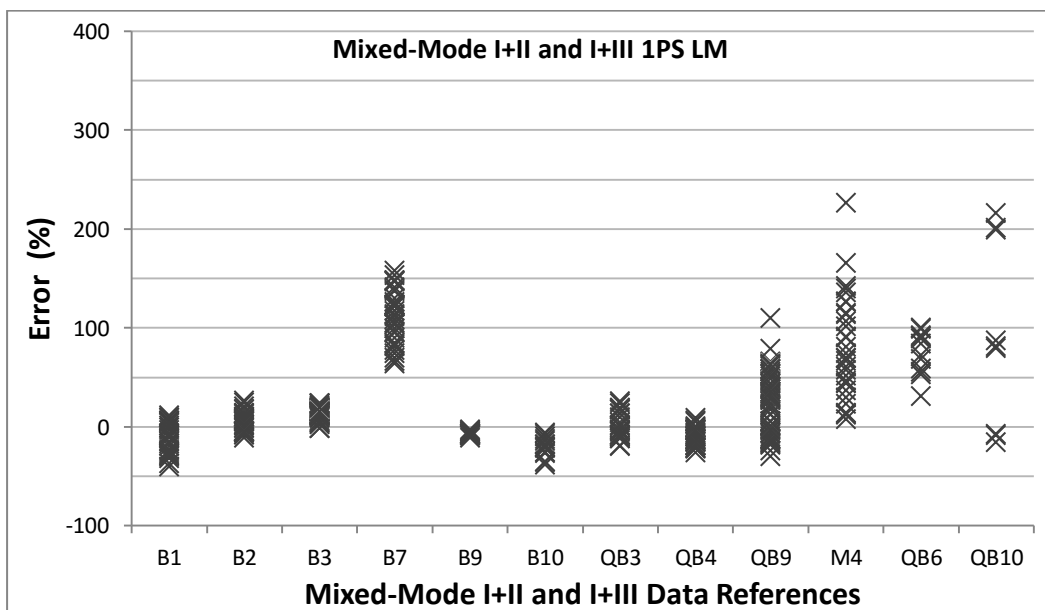
263
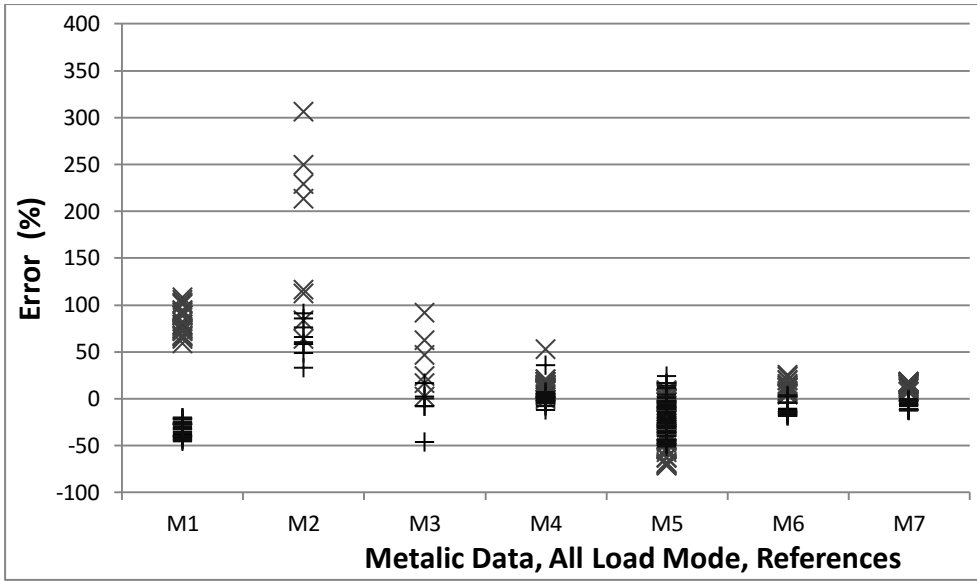
Figure 121: Metallic data (Table 2) and associated error using the TCD PM MPS (X) and VMS (+)
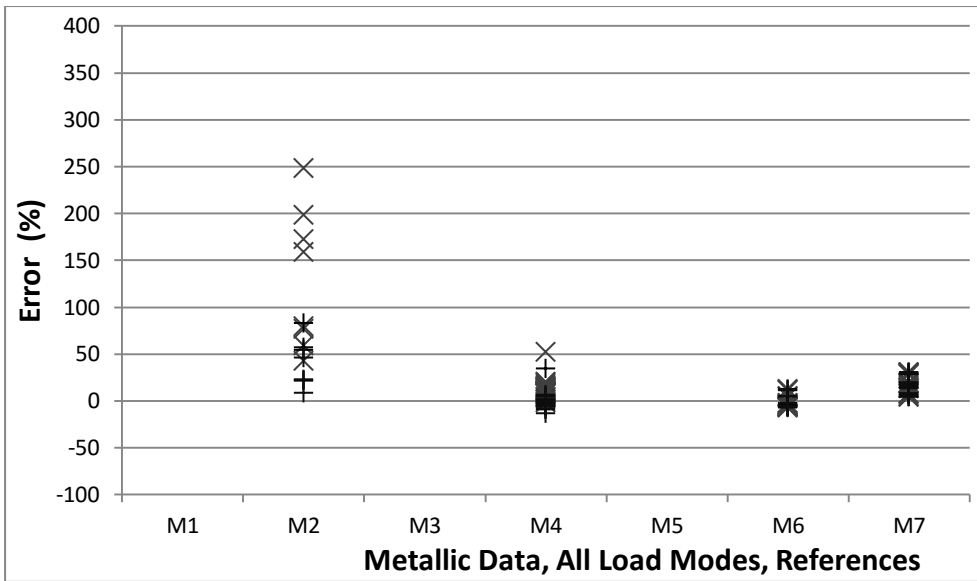
Figure 122: Metallic data (Table 2) and associated error using the TCD LM MPS (X) and VMS (+)

Figure 123: Metallic data (Table 2) and associated error using the HSSM MPS (X) and VMS (+)
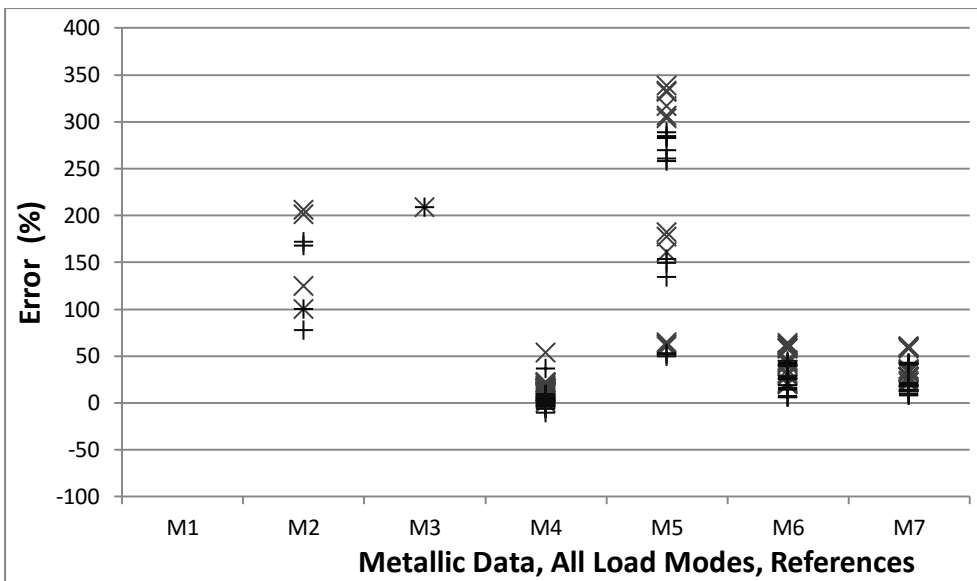
Figure 124: Metallic data (Table 2) and associated error using the HSSM MPS (X) and VMS (+)

13. Annex B – Elevated temperature fatigue data

Elevated temperature fatigue test results A319-T7 then C45.

Table 19: A319-T7 Plain samples

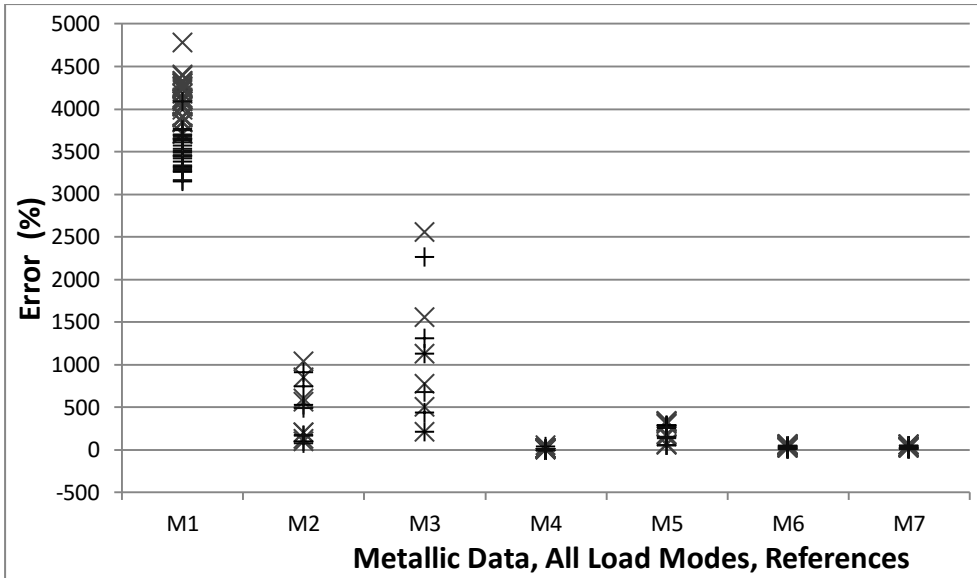| Code	R	N_f [Cycles]	$\Delta\sigma_{net}$ [MPa]
C-P	0.5	9738	120
F-P	0.5	83618	112.8
E-P	0.5	220631	110
B-P	0.5	271035	110
H-P	0.5	380484	106
J-P	0.5	432998	96.8
D-P	0.5	1004543	99.1
G-P	0.5	3120296	96.8
I-P	0.5	10000000	88.4
A-P	0.5	10000000	86

Table 20: A319-T7 U-Notch Samples

Code	r_n [mm]	w_n [mm]	R	N_f [Cycles]	$\Delta\sigma_{net}$ [MPa]
IU	2.175	19.9	0.5	64738	60
KU	2.202	20	0.5	72929	60
CU	2.223	19.82	0.5	80865	50
EU	2.201	20.2	0.5	111045	50
GU	2.148	19.94	0.5	470900	40
BU	2.196	19.9	0.5	547535	40
JU	2.192	20.04	0.5	556990	38
HU	2.154	19.8	0.5	5968886	36
AU	2.202	20	0.5	10000000	38
LU	2.201	19.98	0.5	10000000	30

Table 21: A319-T7 V-Notch Samples

Code	r_n [mm]	w_n [mm]	R	N_f [Cycles]	$\Delta\sigma_{net}$ [MPa]
BV	0.067	19.98	0.5	26987	40
HV	0.068	19.94	0.5	34581	40
CV	0.076	19.95	0.5	104453	30
IV	0.069	19.98	0.5	894817	22
JV	0.073	19.96	0.5	940341	22
DV	0.075	20.02	0.5	2046349	18
EV	0.07	20.02	0.5	2257475	18
GV	0.066	19.96	0.5	5278889	16.6
FV	0.067	20	0.5	8710132	15.4
KV	0.07	19.99	0.5	10000000	15

Table 22: C45 Plain Samples

Plain Samples					
		Thickness = 4.98mm		$\Delta\sigma_{net}$	Nf
Reference	r_n (mm)	W_n (mm)	R	(Mpa)	(Cycles)
P4	125	5	0.1	266	110000
P5	125	5	0.1	258	105000
P6	125	5	0.1	258	97975
P12	125	5	0.1	252	100665
P7	125	5	0.1	250	241720
P8	125	5	0.1	244	224652
P11	125	5	0.1	242	157193
P10	125	5	0.1	241	2001000
P3	125	5	0.1	238	2557717
P9	125	5	0.1	238	2001000
P2	125	5	0.1	210	2275047

Table 23: Blunt U-Notch Samples

Blunt U-Notch Samples					
		Thickness = 4.98mm		$\Delta\sigma$net	Nf
Reference	r_n (mm)	W_n (mm)	R	(Mpa)	(Cycles)
BU1	2.97	13.29	0.1	190.00	1750
BU2	2.97	13.28	0.1	100.00	15939
BU4	2.97	13.28	0.1	85.00	29540
BU5	2.97	13.28	0.1	75.00	35375
BU6	2.95	13.22	0.1	65.00	57211
BU7	2.97	13.24	0.1	60.00	88839
BU9	2.95	13.28	0.1	59.00	139996
BU10	2.96	13.25	0.1	58.00	119258
BU8	2.98	13.18	0.1	57.50	2001000
BU3	2.97	13.29	0.1	55.00	2001000

Table 24: C45 Sharp U-Notch Samples

Sharp U-Notch Samples					
Reference	r_n (mm)	Thickness = 4.98mm	R	$\Delta\sigma$net	Nf
		W_n (mm)		(Mpa)	(Cycles)
SU8	0.98	14.17	0.1	70.00	17160
SU1	0.98	14.13	0.1	60.00	55825
SU7	0.98	14.12	0.1	49.24	56313
SU10	0.98	14.11	0.1	45.00	81349
SU9	0.99	14.13	0.1	45.00	95374
SU2	0.97	14.17	0.1	40.00	130869
SU6	0.96	14.13	0.1	39.30	184079
SU3	0.96	14.19	0.1	32.00	2001000
SU4	0.97	14.16	0.1	35.00	2001000
SU5	0.96	14.17	0.1	38.19	2001000

Table 25: C45 V-Notch Samples

V-Notched Samples					
Reference	r_n (mm)	Thickness = 4.98mm	R	$\Delta\sigma net$	Nf
		W_n (mm)		(Mpa)	(Cycles)
V7	0.15	13.37	0.5	60	16900
V10	0.16	13.41	0.5	65	18916
V2	0.16	13.34	0.5	60	21776
V1	0.12	13.37	0.5	40	43733
V8	0.13	13.40	0.5	40	50150
V5	0.13	13.41	0.5	29.4	111522
V3	0.14	13.49	0.5	20.5	207502
V9	0.16	13.41	0.5	30	223753
V4	0.14	13.48	0.5	29.4	326112
V6	0.15	13.44	0.5	18	2001000